Analysing diffusion of biological colloids in glycan rich extracellular matrices – experimental and theoretical tools

Abigail Rose Edlinger Roberts

Submitted in accordance with the requirements for the degree of

Doctor of Philosophy

The University of Leeds

School of Biomedical Sciences

March 2024

I confirm that the work submitted is my own and that appropriate credit has been given where reference has been made to the work of others.

This copy has been supplied on the understanding that it is copyright material and that no quotation from the thesis may be published without proper acknowledgement.

The right of Abigail R. E. Roberts to be identified as Author of this work has been asserted by Abigail R. E. Roberts in accordance with the Copyright, Designs and Patents Act 1988.

Acknowledgements

I would like to start out my acknowledgements by thanking my supervisors Dr Ralf Richter and Dr Jessica Kwok. Thank you for providing guidance throughout this project and acting as my mentors, I really appreciate that you spent the time to train me for this project but also to train me to be a good scientist. I would like to thank all members of the Richter and Kwok labs, especially Itzel, Laia, Sumitra, Xiaoli, Chunyue, Lynda, and Ashleigh, as well as former members of these labs. Especially Dr Saikat Jana, who played a critical role in my training of microscopy techniques and with microscopy analysis. I would also like to thank Dr Delphine Débarre and Dr Oksana Kirichuck, at the Université Grenoble Alpes, for their help with RICM and model matrices on glass surfaces through the links between my project and theirs.

At the University of Leeds, I would like to thank the Bioimaging facility including Sally and Ruth. You provided critical help with training on the confocal. I would like to thank the members of the Schools of Physics and Astronomy, and Biomedical sciences including my previous assessors Dr Lars Jeuken (currently Leiden University and Dr Aleks Ponjavic.

I would like to thank our collaborators at the University of Osnabrück, Dr Jacob Piehler and Dr Changjiang You, for crucial materials.

I would also like to thank Jelizaveta Pavljuk for giving me the opportunity to teach and pass on my knowledge, as well as the contributions she made to this thesis. Knowing that Jelizaveta is continuing this work means I know that this project is in safe hands.

Many thanks to my friends and family for their support throughout my PhD process. Especially to my father, Stefan, thanks for always showing an interest in my work and for always having confidence in me. Also, to my partner, Liam, for all the encouragement and reassurance.

Statement on the Contributions of Other Researchers

Abigail R. E. Roberts is the sole author of this thesis. However, other researchers have contributed to selected data acquisition and analysis, as follows:

Chapter 3: Ralf P. Richter produced the fluorescently labelled EUVs (Section 3.2.6). Jelizaveta Pavljuk performed the QCM-D experiments involving the application of fluorescently labelled EUVs to a SAv monolayer and HA films (Section 3.3.3).

Chapter 4: Ralf P Richter performed the DLS analysis of fluorescently labelled EUVs (Sections 4.2.4 and 4.3.3.1).

Chapter 5: James Warren started the work on an analytical model of colloid diffusion as part of his MPhys dissertation (co-supervised by Abigail R. E. Roberts and Ralf P. Richter), however, the analytical model presented in Chapter 5 has undergone significant changes in comparison to the model presented in James Warren's MPhys dissertation.

Many thanks to these researchers for contributing vital work to this thesis.

Statement on the Impact of the COVID-19 Pandemic

The COVID-19 pandemic had a substantial effect on the work flow and output of this PhD project. The pandemic resulted in ~5 months of lost lab time during the first government required lock down. Following the reopening of the lab, there was a reduction in lab time in comparison to normal and a significant reduction in the amount of supervised training in order to accommodate the COVID safe working rules (social distancing etc.). This had multiple impacts on the project. Under normal circumstances, certain data artefacts would likely have been identified much earlier and troubleshooting in the technique development would have been more efficient leading to a project outcome more aligned with the original project plan. Overall, this led to some unanticipated changes to the project focus.

Publications Produced Throughout the PhD Project

Throughout her PhD project, Abigail R. E. Roberts has made contributions to several research papers, listed below. These do not reflect the core of the work presented in this thesis, though cover related topics.

Kirichuk O, Srimasorn S, Zhang X, **Roberts ARE**, Coche-Guerente L, Kwok JCF, Bureau L, Débarre D, Richter RP . Competitive Specific Anchorage of Molecules onto Surfaces: Quantitative Control of Grafting Densities and Contamination by Free Anchors. *Langmuir.* 2023; 39(50), pp 18410-18423. PMID: 38049433

Gray AL, Karlsson R, **Roberts ARE**, Ridley AJL, Pun N, Khan B… Dyer, DP. Chemokine CXCL4 interactions with extracellular matrix proteoglycans mediate widespread immune cell recruitment independent of chemokine receptors. *Cell Reports*. 2023; 42(1), Article No: 111930. PMID: 36640356

Srimasorn S, Souter L, Green DE, Djerbal L, Goodenough A, Duncan JA, **Roberts ARE**, Zhang X, Débarre D, De Angelis PL, Kwok JCF, Richter RP. A quartz crystal microbalance method to quantify the size of hyaluronan and other glycosaminoglycans on surfaces. *Scientific Reports.* 2022; 12, Article No: 10980. PMID: 3576846.

Abstract

The extracellular matrix provides a crucial framework in multicellular organisms. Matrix composition varies between tissues and different physiological states, but glycosaminoglycans are a quintessential feature. Glycosaminoglycans are polymer chains consisting of repeated disaccharides with a high degree of polydispersity and negative charge. Biological colloids distribute within the extracellular matrix and are impacted by glycosaminoglycans, either through site-specific interactions or by generation of a physical and electrostatic barrier. For example, chemokines and growth factors have well documented interactions with glycosaminoglycans required for their biological functions. Other glycans, as part of glycosphingolipids, interact with toxins, such as shiga toxin, as they similarly traverse the extracellular matrix. Our current mechanistic understanding of diffusion processes in the extracellular matrix is limited, however, largely due to the lack of methods to probe such processes in a controlled environment. The aim of this thesis was to develop experimental and theoretical tools to probe and understand the molecular mechanisms that define the diffusion of biological colloids in glycan rich extracellular matrices.

Model extracellular matrices were generated and refined to recreate features to investigate the interaction between biological colloids and glycosaminoglycans. These colloids include the chemokine CXCL12, shiga toxin, and unilamellar vesicles. Glycan-binding ability was adversely affected by fluorescent labelling of the glycan binding molecules. Furthermore, the bespoke method of Plane sphere confinement microscopy (PSCM) was developed to directly probe the rate of diffusion of biological colloids within glycan-rich model matrix films without interference of exchange processes with the bulk solution. Finally, an analytical model to describe diffusion of biological colloids within a sticky polymer matrix was derived using knowledge of diffusion in solution and binding kinetics. These methods can be used to analyse diffusion and mobility of polymer binding molecules in polymer rich extracellular matrices and the impact of diffusion on functions in biological systems.

List of Abbreviations

AF	Alexa Fluor
AMD	Areal Mass Density
BODIPY	Boron-dipyrromethene
BSA	Bovine Serum Albumin
CD	Cluster of Differentiation
CS	Chondroitan Sulfate
CT	Cholera Toxin
DLS	Dynamic Light Scattering
DNA	Deoxyribonucleic Acid
DOPC	1,2-dioleoyl-sn-glycero-3-phosphocholine
DOPE-CAP-B	1,2-dioleoyl-sn-glycero-3-phosphoethanolamine-N-(Cap Biotinyl)
DS	Dermatan Sulfate
ECM	Extracellular Matrix
EDTA	Ethylenediaminetetraacetic acid
EUVs	Extruded Unilamellar Vesicles
FGF	Fibroblast Growth Factor
FGFR	Fibroblast Growth Factor Receptor
FRAP	Fluorescence Recovery After Photobleaching
GAG	Glycosaminoglycan
Gal	Galactose
GalNAc	N-acetylgalactosamine
Gb_3	Globotriaosylceramide
Gdn HCl	Guanidine hydrochloride
GFP	Green Fluorescent Protein
GlcA	Glucuronic acid
GlcNAc	N-acetylglucosamine
GTA	Gluteraldehyde
HA	Hyaluronan
HEPES	4-(2-hydroxyethyl)-1-piperazineethanesulfonic acid
His	Histidine
HN	Heparosan
HP	Heparin
HS	Heparan sulfate

IdoA	Iduronic acid
KS	Keratan sulfate
LAP	Linear Assignment Problem
LB	Laemmli Broth
LED	Light Emitting Diode
LoG	Laplacian of Gaussian
MSD	Mean Square Displacement
PAGE	Polyacrylamide Gel Electrophoresis
PCR	Polymerase Chain Reaction
PSCM	Plane Sphere Confinement Microscopy
QCM-D	Quartz Crystal Microbalance with Dissipation Monitoring
RICM	Reflection Interference Contrast Microscopy
RMS	Root Mean Squared
SAv	Streptavidin
SDS	Sodium Dodecyl-sulfate
SE	Spectroscopic Ellipsometry
SLB	Supported Lipid Bilayer
SPT	Single Particle Tracking
STxB	Shiga toxin B sub unit
SUVs	Small Unilamellar Vesicles
TAE	Tris-Acetate-EDTA

List of Figures

Figure 1. **The Structure of the Extracellular Matrix**... 4
Figure 2. **The Possible Disaccharide Units for Different GAG Types**. 6
Figure 3. **The Major Glycosphingolipids.** 8
Figure 4. **Ribbon Structure of Chemokines and their Dimers** 10
Figure 5. **CXCL5 in Complex with HS, CS, and DS** 11
Figure 6. **Structure of Fibroblast Growth Factors** 12
Figure 7. **FGF2 in Complex with Heparin** 13
Figure 8. **Structures of AB_5 Toxins** 15
Figure 9. **Types of Extracellular Vesicles** 17
Figure 10. **Formation of a Model ECM** 25
Figure 11. **Illustration of QCM-D Mode of Operation**. 27
Figure 12. **Formation of a GAG film followed by QCM-D** 29
Figure 13. **SE on Thin Flims** 31
Figure 14. **Principles and design of fluorescence microscopy** 32
Figure 15. **Fluorescence Recovery After Photobleaching** 34
Figure 16. **Reflection Caused By Spherical Objects** 36
Figure 17. ***Map of Plasmid pRSET*** 44
Figure 18. **The Formation of a Model HS Rich Glycocalyx Monitored by QCM-D** 56
Figure 19. **Purification of Biotinylated HS** 60
Figure 20. **Modulating 33 kDa HS Surface Coverage** 62
Figure 21. **Formation of a High Molecular Weight Hyaluronan Brush** 63
Figure 22. **Formation of SLB and SAv Layers on Silica Wafers** 65
Figure 23. **The RMS Anchor Distance Between Different Size HA Chains** 66
Figure 24. **The Formation of Films of Mucin-like Structures, Monitored by QCM-D** 67
Figure 25. **Production and Strategy for Labelling CXCL12** 71
Figure 26. **QCM-D Responses of HisCXCL12γ Binding to an HS Film** 72
Figure 27. **QCM-D Responses of Different CXCL12α Forms Binding to an HS Film** 74
Figure 28. **QCM-D Responses for Different Molar Ratios of OG488:HisCXCL12α Binding to HS Films.** 75
Figure 29. **Nonspecific Binding of OG488•HisCXCL12α to SAv**. 76
Figure 30. **QCM-D Response for CXCL12α-AF647 Binding to an HS film** 78
Figure 31. **Nonspecific Binding of CXCL12α-AF647 to SAv**. 79
Figure 32. **STxB and its Binding Sites for Gb_3.** 81
Figure 33. **QCM-D Response of Different STxB Forms Binding to a Mucin-like Film** 82
Figure 34. **Fluorescent EUVs Bind to SAv Monolayers.** 85
Figure 35. **Fluorescent EUVs Do Not Bind HA-b dp15 Surfaces** 85
Figure 36. **Airyscan Confocal Images of CXCL12α 'Clusters'** 87
Figure 37. **Epifluorescence Microsocopy Analyses of OG488•HisCXCL12α on Glass.** 89
Figure 38. **The Types of Diffusion Measured in Standard Microscopy on Thin Films, and How PSCM Enables Analysis of In-Film Diffusion** 97
Figure 39. **The PSCM Motorised Cantilever** 99
Figure 40. **The PSCM Stage Insert** 106
Figure 41. **Resting Forces Are Set by a Counter-Weight-Balance System** 107
Figure 42. **Epifluorescence Micrographs of Functionalised Surfaces after Plane-Sphere Contact Formation Reveal Defects**. 109
Figure 43. **GTA crosslinks SAv Monolayers.** 110

Figure 44. **Epifluorescence Micrographs Reveal Transfer of SAv from the Planar to the Curved Surface** 111
Figure 45. **The Addition of a Motorised Cantilever to the PSCM Unit** 112
Figure 46. **The Effective Height as a Function of the Set Resting Force is not Affected by the Cantilever** 113
Figure 47. **Damage to Functionalised Surfaces is Reduced with the Motorised Cantilever**. 114
Figure 48. **The Focus Position Has a Minor Effect on the Effective Height Measured by RICM** 115
Figure 49. **Surface Coverings Cause Changes to the Appearance of Newtonian Rings** 116
Figure 50. **The Effect of Surface Coatings on the Effective Height Extracted from RICM Images** 118
Figure 51. **The Effect of Subsequent Rod Drops on the Effective Height Extracted from RICM Images.** 120
Figure 52. **Changes to the Appearance of the Contact Point Following Subsequent Contacts** 121
Figure 53. **Workflow for SPT in PSCM** 122
Figure 54. **An Overview of an Example Data Set** 124
Figure 55. **The Pre-Processing of Time Series for SPT** 126
Figure 56. **Validation of the Processing of MSDAnalyser Output** 127
Figure 57. **MSD Plot of Single Particle Tracking Data** 128
Figure 58. **ε^2 and D Values Do not Correlate in the selected ε^2 range.** 129
Figure 59. **The Distribution of ε^2 Values** 130
Figure 60. ***DLS Analysis of the Size of EUVs*** 132
Figure 61. **Effect of Confinement on the Diffusion of EUVs**. 134
Figure 62. **Population Analysis of Diffusion of EUVs in the Bulk Solution** 134
Figure 63. **ε^2 / $4Dt_{exposure}$ as a function of gap height** 135
Figure 64. **Distribution of Tracks within the Confined Space.** 136
Figure 65. **Height of HA Brush and Control Surfaces, as Measured by RICM**. 138
Figure 66. **Effect of an HA Brush on the Diffusion of EUVs.** 139
Figure 67. **Population Analysis of Diffusion of EUVs above (and within) the HA Brush**. 141
Figure 68. **The Diffusion Process in a Sticky Polymer Matrix**.. 149
Figure 69. **The Effect of c_{bs} and K_d on D_{eff}/D_{matrix}.** 157
Figure 70. **Effective Diffusion Coefficients of CXCL12α and CXCL12γ as a Function of the Concentration of HS** 159
Figure 71. **The Effect of the Concentration of Binding Sites the Effective Diffusion Coefficient of Halo FGF1 in an HS Model Matrix** 161
Figure 72. **Fluorescence Recovery After Photobleaching of FGF2 on an HS Film and HaCAT Cells** . 162
Figure 73. **Effective Diffusion Coefficient of FGF2 in Descement's Membrane as a Function of the Concentration of HS Sites.** 166

Table of Contents

Acknowledgements III
Statement on the Contributions of Other Researchers IV
Statement on the Impact of the COVID-19 Pandemic V
Publications Produced Throughout the PhD Project VI
Abstract VII
List of Abbreviations VIII
List of Figures X
Table of Contents XII
Chapter 1: General Introduction 1
1.1 General Outline 2
1.2 The Extracellular Matrix 2
1.3 Diffusion 4
1.4 Glycosaminoglycans 5
1.5 Other Glycans 7
1.5.1 Glycosphingolipids 7
1.6 Biological Colloids 9
1.6.1 Signalling Proteins 9
1.6.1.1 Chemokines 9
1.6.1.2 Fibroblast Growth Factors 12
1.6.2 Toxins 13
1.6.2.1 AB_5 toxins 14
1.6.3 Extracellular Vesicles 15
1.7 Diffusion of Biological Colloids through ECMs 17
1.8 Project Aims 19
1.9 Outline of Thesis 20
Chapter 2: Introduction to Relevant Methods 21
2.1 Outline 22
2.1.1 Model Extracellular Matrices and their Benefits 22
2.1.2 Formation of Model Extracellular Matrices 23
2.1.3 Quartz Crystal Microbalance (QCM-D) 25
2.1.3.1 A QCM-D Application 27
2.1.4 Spectroscopic Ellipsometry 29
2.1.5 Fluorescence Microscopy 31
2.1.5.1 Applications of Fluorescent Microscopy to Model ECMs 32

2.1.6 Reflection Interference Contrast Microscopy 34
Chapter 3: Development of Model Glycocalyces and Labelling Glycan Binding Molecules - Advancements and Pitfalls 38
3.1 Introduction 39
3.2 Methods 42
3.2.1 Protein and Plasmid sources 42
3.2.2 Protein Labelling 42
3.2.3 Sub-cloning of DNA Constructs 43
3.2.3.1 Polymerase Chain Reaction (PCR) 45
3.2.3.2 Restriction Digest 45
3.2.3.3 Ligation Reaction 46
3.2.3.4 Agarose Gel Electrophoresis 46
3.2.3.5 DNA Mini Preparations: Plating, Selections, and Culture 46
3.2.4 Protein Production 46
3.2.5 Production of Small Unilamellar Vesicles (SUV) 48
3.2.6 Production of Extruded Unilamellar Vesicles (EUVs) 49
3.2.7 Model Glycocalyx Formation 49
3.2.7.1 Surface Functionalisation for Anchorage of Biotinylated Glycopolymers 49
3.2.7.2 Anchorage of Biotinylated Glycopolymers to Form Model Glycocalyx Films 50
3.2.8 Quartz Crystal Microbalance with Dissipation Monitoring (QCM-D) 51
3.2.9 Optical Microscopy 51
3.2.10 Spectroscopic Ellipsometry (SE) 52
3.2.11 Calculation of the Number of Disaccharides from QCM-D Data 54
3.3 Results 55
3.3.1 Creating Bespoke Model Glycocalyces 55
3.3.1.1 Modelling an HS Glycocalyx to Probe Diffusion of Proteins Binding to Sulfated GAGs 55
3.3.1.1.1 Post-chromatographic Analysis of Biotinylated HS by QCM-D 56
3.3.1.1.2 Controlling the Concentration of HS on the Surface 60
3.3.1.2 Modelling a Thick and Open Glycocalyx for Passive Diffusion Analyses 62
3.3.1.3 Models Inspired by Mucin-rich Glycocalyces 66
3.3.2 Fluorescent Labelling of Diffusion Colloids 68
3.3.2.1 Requirements on Colloids and Labels for Model Glycocalyx Binding and Diffusion Analyses 68
3.3.2.2 CXCL12 Chemokines 68
3.3.2.2.1 Labelling of CXCL12 on the N terminus Affects HS binding 68

3.3.2.2.1.1 Successful production and purification of CXCL12α and CXCL12γ 68
3.3.2.2.1.2 HisCXCL12γ shows modified HS binding compared to CXCL12γ..... 71
3.3.2.2.1.3 HisCXCL12α and CXCL12α bind similarly to HS films 72
3.3.2.2.1.4 Fluorescent labelling via the His_6 tag impairs HS binding of CXCL12α 73
3.3.2.2.2 Labelling of CXCL12α on the C terminus Affects HS binding 76
3.3.2.3 Shiga Toxin 79
3.3.2.3.1 Labelling of STxB via NHS Ester Affects Gb_3 Binding..... 80
3.3.2.3.2 Labelling of STxB via C-terminal Polyhistidine Tag Affects Gb_3 Binding 80
3.3.3 Fluorescently Labelled EUVs 82
3.3.4 Minute Defects in SLBs on Glass Affect the Interpretation of Protein Distribution Data 85
3.4 Discussion..... 90
3.4.1 Generation of Different Glycocalyces 90
3.4.2 Molecular Mechanisms for Altered Binding 91
3.4.3 The Importance of Defects in SLBs 92
Chapter 4: Plane Sphere Confinement Microscopy to probe Diffusion within Model Glycocalyces ... 94
4.1 Introduction 95
4.2 Methods 98
4.2.1 Materials 98
4.2.2 Manufacture of Glass Rods with Hemi-spherical Caps 98
4.2.3 Assembly of a Motorised Cantilever for Gentle Plane-Sphere Approach..... 98
4.2.4 Dynamic Light Scattering (DLS) 99
4.2.5 Cleaning and Functionalisation of Surfaces 99
4.2.6 Optical Microscopy 100
4.2.6.1 Fluorescence Microscopy..... 100
4.2.6.2 Reflection Interference Contrast Microscopy..... 100
4.2.6.3 Confocal Microscopy and Fluorescence Recovery After Photobleaching 100
4.2.7 Height analyses from RIC micrographs 101
4.2.7.1 Analyses of the thickness of surface coatings..... 101
4.2.7.2 Quantifying the grafting distance of HA brushes from the brush thickness..... 102
4.2.7.3 Analysis of the effective height of plane-sphere contact in PSCM 102
4.2.8 Determination of the Gap Height Profile in Plane-Sphere Confinement 102
4.2.9 Relating Effective Height to Resting Force in PSCM 103
4.2.10 Tracking of Diffusion of Fluorescent EUVs..... 103
4.2.10.1 Pre-processing of Image Time Series 103
4.2.10.2 Determination of EUV Diffusion Tracks 103

4.2.10.3 Mean Square Displacement (MSD) Analysis of Diffusion Tracks 103
4.3 Results 105
4.3.1 Development of a PSCM Stage Insert with Improved Interface Stability and Quality 105
4.3.1.1 The New PSCM Stage Insert 105
4.3.1.2 Mitigating Damage to Functionalised Surfaces upon Plane-Sphere Contact Formation 107
4.3.1.2.1 Stabilising the Functional Surface by Streptavidin Crosslinking 108
4.3.1.2.2 Reducing the Rate of Approach of the Curved Surface 111
4.3.1.3 Reliability of the Calculated Effective Height 114
4.3.1.4 Surface Coverage Impacts on the RICM Image and the Impact on the Effective Height 115
4.3.1.4.1 The Effect Model Matrix Surface Functionalisation Decreases Effective Height 116
4.3.1.4.2 Subsequent Contacts Results in a Decreased Effective Heights for GAG Films 118
4.3.2 Developing a Workflow for Single Particle Tracking in PSCM 121
4.3.2.1 Overview of the Data Analysis Steps 122
4.3.2.2 Establishing an Example Data Set 122
4.3.2.3 Pre-processing of Image Time Series 124
4.3.2.4 Extraction of Diffusion Tracks and their Mean Square Displacement Analysis 126
4.3.2.5 Curation of the MSD Analysis Output 128
4.3.3 Proof-of-Principle Application: Analysing EUV Diffusion in Confined Solution and in HA Brushes 130
4.3.3.1 Quantifying the Hydrodynamic Size of EUVs 131
4.3.3.2 Analysis of EUVs in Confined Solution 132
4.3.3.2.1 Quantifying EUV Diffusion in Confined Solution 132
4.3.3.2.2 Estimating Number Distributions of EUVs in Confined Solution 135
4.3.3.3 Analysis of EUVs in an HA Brush 136
4.3.3.3.1 HA Brush Design 136
4.3.3.3.2 Quantifying Diffusion of EUVs in an HA Brush 138
4.4 Discussion 142
4.4.1 Further Improvements 142
4.4.2 Implications on the Impact of an HA brush on Diffusion 143
4.4.3 Future Applications 144
Chapter 5: An Analytical Model for Biological Colloid Diffusion in a Sticky Polymer Matrix 145
5.1 Introduction 146
5.2 Results 149
5.2.1 An analytical model of macromolecular diffusion in a sticky polymer matrix 149

5.2.1.1 Defining the interaction scenario 149
5.2.1.2 Defining the interaction between macromolecule and polymer 149
5.2.1.3 Defining diffusion in plain solution and in the polymer matrix 150
5.2.1.4 A Theoretical Model of Diffusion in a Sticky Matrix 151
5.2.1.5 Extensions to the Model 153
5.2.1.5.1 Effect of Steric Hindrance on Diffusion 153
5.2.1.5.2 Effect of High Concentration of Macromolecules on Diffusion 153
5.2.1.5.3 Effect of Multivalent Binding on Diffusion 153
5.2.2 Exploring Quantitative Predictions of the Analytical Model 154
5.2.2.1 Parameters for Stokes-Einstein Diffusion 154
5.2.2.2 Interaction Parameters 156
5.2.2.3 Relevant Ranges of K_d and c_{bs} in GAG-rich ECMs 156
5.2.3 Review of Literature Data in Light of the Analytical Model 157
5.2.3.1 Diffusion in Defined Model Matrices and Comparison to Experimental Data 157
5.2.3.1.1 Diffusion of CXCL12 Isoforms 157
5.2.3.1.2 Diffusion of Halo-FGF1 159
5.2.3.2 Comparison to Experimental Data: in vitro 162
5.2.3.2.1 Comparison to Experimental Data: CXCL13 diffusion in HS-rich lymphatic ECM 162
5.2.3.2.2 Comparison to Experimental Values: Fibroblast Growth Factor 164
5.2.3.2.2.1 FGF2 Diffusion in Endothelium Basement Membrane 164
5.2.3.2.3 Diffusion of FGF2 in the Fibroblast Pericellular Matrix 166
5.3 Discussion 170
5.3.1 Validity of the Model for Model Matrices 170
5.3.2 Validity of the Model for *In Vitro* Matrices 171
5.3.3 Experimental Design for Further Verification 172
5.3.3.1 The Effect of Varying the Concentration of Binding Sites on D_{eff} 172
5.3.3.2 The Effect of Multivalency on D_{eff} 172
Chapter 6: General Discussion and Conclusions 173
6.1 Summary of Results 174
6.2 Integrating Experimental and Theoretical Tools 175
6.3 Future Work in the Field 176
6.4 How to Label Glycan-binding Proteins Wisely? 176
6.4.1 What is the Pore Size in the Glycocalyx? 177
6.4.2 What is the Role of the Diffusion Coefficient in Gradient Formation? 177
6.5 Conclusions 178

References 179
Appendix 195
Supplementary Figures 195

Chapter 1: General Introduction

1.1 General Outline

The aim of this thesis is to develop experimental and analytical tools to measure the diffusion of biological colloids in glycan-rich extracellular matrix. This chapter will comprise of a review of the relevant literature and what is currently understood about the process of diffusion of biological colloids in the intercellular space, followed by defining the remaining knowledge gaps and the specific project aims of this thesis.

1.2 The Extracellular Matrix

The extracellular matrix (ECM) is a quintessential structure in multicellular organisms, it surrounds all cells and provides a specialised environment which is responsible for a range of mechanical properties such as elasticity (1-5). For example, the stiffness of tissues, as measured by the elastic modulus, can range from low kPa ranges, such as the basement membrane, to GPas, in tendons and bones (6). It also some biochemical properties such as the presentation of signalling and structural proteins and a buffering capability for the large amount of small molecules present by maintaining large amounts of water. The ECM is generated by the cells that exist within it, and is dynamic, constantly responding to the activities occurring within it and in the surrounding cells. For example, the shedding of certain molecules during inflamed states (7). Due to this, there are many different types of ECMs. Pericellular matrices are those that are in close proximity to cells. They play vital roles in the interaction between molecules within the matrix and cells themselves. (1-5).

The interstitial matrices surround cells in tissues and form a key part of the maintenance of tissue architecture due to its molecular organisation (1-5). The structures in the interstitial matrix have a large impact on the transport of biological molecules through it. Collagen fibres and extracellular proteoglycans, proteins with a covalently attached sugar components dominate the interstitial matrix. Overall, there are many types of matrices even in these sub classifications, and their components are highly specific and ever-changing. The cells that exist within matrix have key roles in the components of the matrix. Therefore, a pericellular matrix generated by a fibroblast vs generated by a keratinocyte will differ due to the individual differences in cellular output (8). The ECM has many protein components including collagen and fibronectin, which have many structural roles. Collagen that has associate with elastin exerts a limiting effect on the amount that the elastin can stretch, providing a structural backbone to the complex (2). The ECM also has many glycans, which are defined as polysaccharide molecules, components. For example, in a study focusing on ECMs derived from three different cell types, chondrocytes, bone marrow mesenchymal stromal cells, and synovium derived mesenchymal stromal cells, the glycans extracted from their ECMs had defined and distinct disaccharides compositions (9).The different components have key different roles, they form a

meshwork (Figure 1) that contains pores, and they also can provide a binding platform (1-5). Many ECM components interact specifically with proteins and other types of molecules, such as the specific binding of CXCL13 to matrix components which is distinct from the binding that occurs between CXCL13 and its cell receptors (10).

One specific type of ECM that is pertinent is the endothelial glycocalyx, a sugar rich ECM that is thinner than other forms of ECM and sits in close proximity to cellular surfaces in the vasculature (2, 4, 11).A variety of different studies place the thickness of the glycocalyx between 20 and 500 nm, depending on the type of vasculature under investigation (12). The rich glycan components of the glycocalyx can be said to form a forest, with components such as glycosaminoglycans which act as trees extending far out into the matrix and others like glycoproteins and glycolipids, acting as grass and bushes which are closer to the cell surface. One example of a glycocalyx, is the endothelial glycocalyx, the ECM that lines the lumen of blood vessels (12-15). The endothelial glycocalyx plays a key role in the extravasation of leukocytes into tissues during inflammation. Signalling molecules, pathogens, toxins, among other molecules interact specifically with the endothelial glycocalyx. Furthermore, if the glycocalyx becomes damaged, this can lead to damage to the cells forming the walls of vessels (14). This is due to the sheer stress caused by the flow of blood acting on the cell surfaces themselves rather than the intermediate glycocalyx layer.

In multicellular organisms, all intercellular signalling components must traverse the ECM. However, the complex interplay between these traversing materials and the ECM components is unclear. A review of the literature focusing on this interplay follows in this chapter, as the relationship between ECM components and other materials are key to understanding transport in the intercellular space.

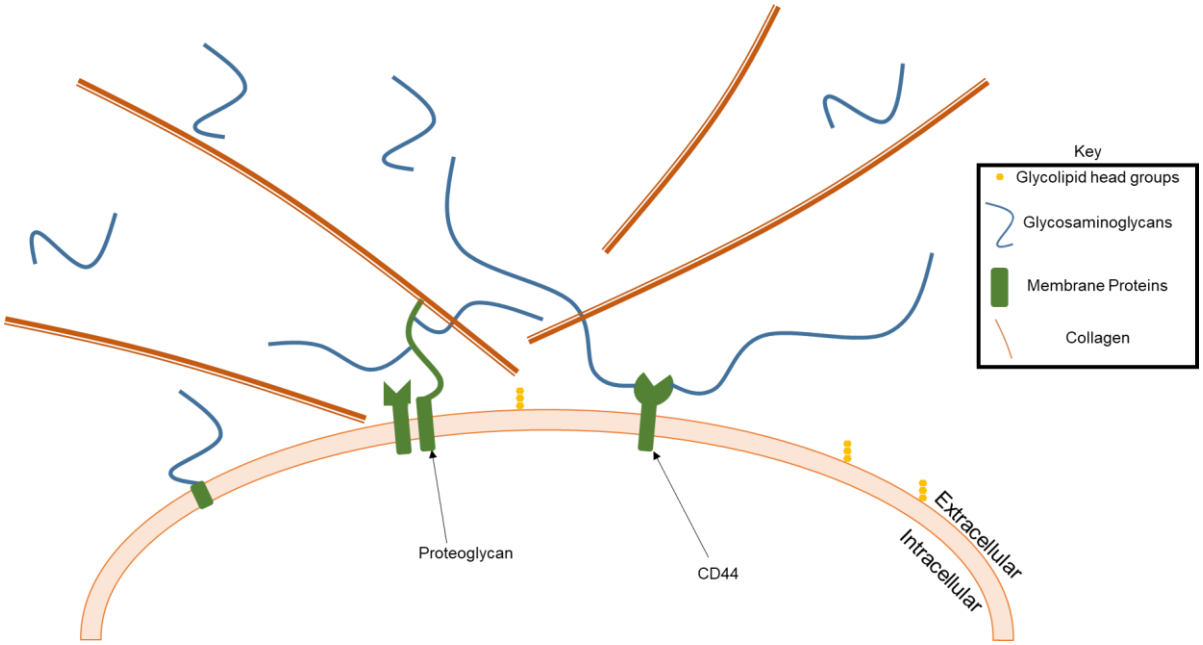


Figure 1. ***The Structure of the Extracellular Matrix****. A selection of ECM components and their organisation in the ECM. ECM components include proteoglycans, CD44 (a cell surface receptor with HA attached), glycan motifs from glycolipids, free GAGs, free collagen, and cell surface receptors. Adapted from Ref. (16)*

1.3 Diffusion

The theory of Brownian motion, states that colloids will move randomly in solution and in his PhD thesis, Einstein found that in relation to Brownian motion, diffusion is dependent on the free energy of the particle (k_BT), the viscosity of the solution (η), and the size of the particle (R_h, the hydrodynamic radius) ($D = \frac{k_BT}{6\pi\eta R_h}$)(17, 18). Diffusion can be defined as random, such as by Einstein, or as concentration dependent. In the latter case, this includes that a concentration gradient of a diffusing molecule is at play and that the diffusion is directed towards areas of lower concentration. In solution, particles will exhibit the diffusion that Einstein described in his thesis. But if a source and sink of a particle are present, the diffusion will be dictated by the concentration gradient (17, 18). This is described by Fick's law: $J = -D\frac{dc}{dx}$, where J represents the flux of the molecule and *c* is the molar concentration and x is the position (19).

Biological colloids distribute in the ECM and the mechanisms for their transport in the ECM must be diffusion based (20, 21). In multicellular organisms, the diffusion will be concentration dependent, as there will be a cellular source. However, a solely concentration based gradient seems unlikely considering the complex nature of the ECM. If diffusion was unconstrained, this could lead to the aberrant localisation of cells and other biological colloids, disrupting the intercellular functioning of multicellular organisms. The complex nature of the ECM must guide this process by providing a

meshwork and a binding platform that can constrain diffusion. However, the exact biophysical mechanisms that underpin this are not well understood (20, 21).

1.4 Glycosaminoglycans

Glycosaminoglycans (GAGs) are chains of repeating disaccharide units (2, 4, 22). The different types of GAGs are chondroitin sulfate (CS), dermatan sulfate (DS), heparan sulfate (HS), hyaluronan (HA), and keratan sulfate (KS) (Figure 2). Most GAGs are sulfated except for HA. Regardless, all GAGs carry a high negative charge, through carboxylate and sulfate groups, making them ideal molecules to maintain the hydrophilic properties of the ECM. GAGs, due to their length and location throughout the matrix (shown in Figure 1) and not just in close proximity to the cell surface, can be said to form the trees within the forest of glycocalyces. Proteoglycans, proteins with GAGs attached, may sit in the plasma membrane. HA may bind to plasma membrane proteins and receptors. Both proteoglycans and HA may exist freely in the ECM. Therefore, GAGs form a large amount of the glycan content of different ECMs (2, 4, 22).

Interactions between GAGs and their protein binding partners are vital for ECM function (23). A recent literature review found that HS and HP have over 800 different protein binding partners with data collected from a variety of different analysis techniques (24, 25). The interactions between GAGs and proteins are largely governed by electrostatics, with many GAG binding proteins carrying a positive charge. HS binding proteins can have a variety of functions such as growth factors, protein degradation and coagulation, metabolism, and ECM formation. This highlights the range of processes that HS, and GAGs at large, are involved in (23, 24).

The study of GAGs is highly complex due the degree of variability within them (22, 26). They are extremely heterogenous due to the different types of modifications, such as sulfation and epimerisation that they can undergo. This makes them difficult produce in a laboratory, as their production is not template driven. During DNA replication, an original strand of DNA is copied through enzymatic reactions and the resulting product is identical to the original copy. However, for GAG production, the involved enzymes are not copying an existing GAG, therefore, the GAG that results from this process is generated by the availability of certain enzymes and chemical groups only. The monosaccharides may undergo epimerisation, where the stereochemistry of the sugar may change. In addition, the amount of sulfation and where it occurs along the chain, as well as the type of sulfation (N-sulfated or O-sulfated, which relates to whether the sulfate is covalently bound to an oxygen or a nitrogen) further contribute to the complexity of GAG study (22). Due to these levels of variability, the most readily available GAGs are those in simpler forms. For example, HA due to its lack of sulfation and epimerisation is the most readily available commercial GAG and can be produced from bacteria.

Other GAGs, however, must be isolated from various different animal tissues. GAGs can be synthesised chemically, but there are still various limitations including being able to produce large amounts (22).

The GAG profile of different extracellular matrices is determined by the enzymes involved in their production and regulation (22, 27, 28). For example, the qualities of HS are regulated by heparinases, sheddases (which act on the proteoglycan core), and sulfatases (27) in conjugation with the enzymes that are required for its production. HS 6-O-sulfate is removed by endosulfatases on areas of high sulfation on HS chains. This type of sulfation is critical for the interaction of HS with many of its binding partners. A loss in function of one type of endosulfatase has been linked to an increased risk of secondary infections following sepsis (27). Furthermore, in the endothelial glycocalyx, GAGs are often shed during inflammatory states, impacting on the structure and binding capabilities of the glycocalyx (28).This highlights how the enzymatic processing of GAGs affects the interactions that they are capable of undertaking and how changes in the GAG profile of a tissue changes its functioning (27, 28). The production and regulation of GAGs highlight how the defining the GAG content of different ECMs is difficult.

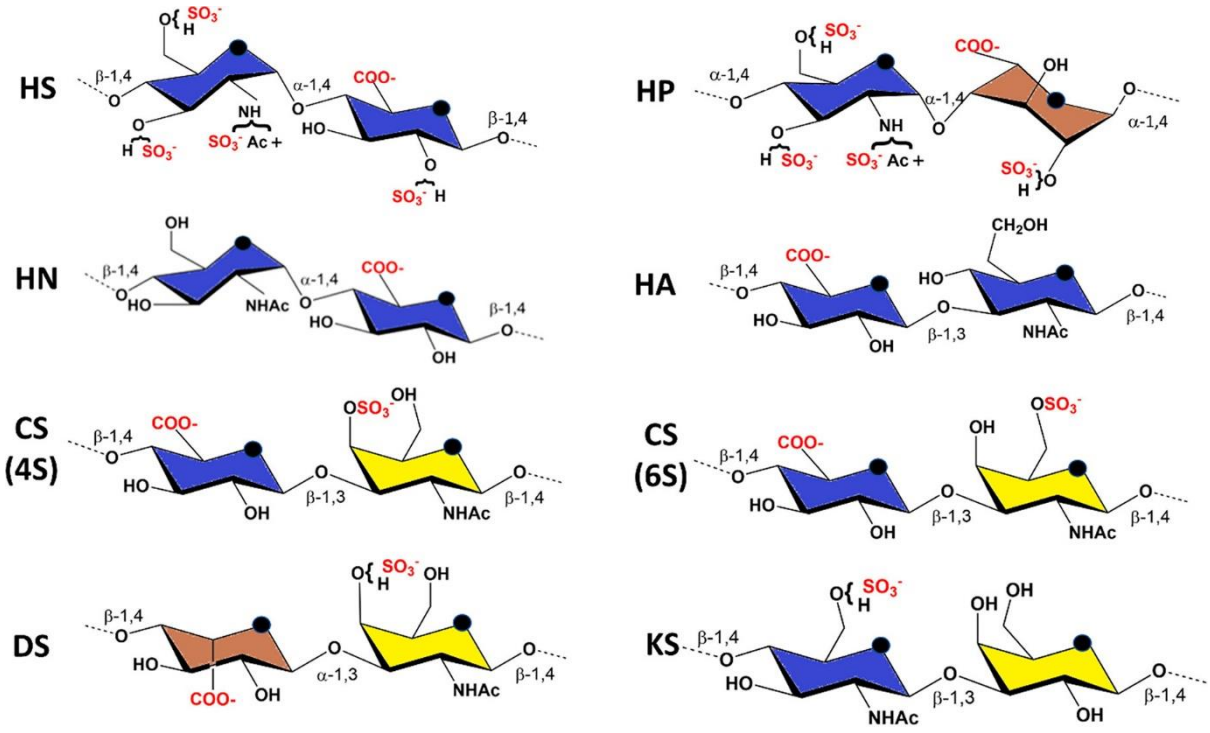


Figure 2. ***The Possible Disaccharide Units for Different GAG Types****. Components of disaccharide units: Heparan sulfate (HS) – N-acetylglucosamine (GlcNAc) and glucuronic acid (GlcA), Heparin (HP) – GlcNAc and iduronic acid (IdoA), Heparosan (HN) – GlcNAc and GlcA, Hyaluronan (HA) – GlcA and GlcNAc, Chondroitan sulfate (CS) – GlcA and N-acetylgalactosamine (GalNAc), Dermatan Sulfate (DS) – IdoA and GalNAc, Keratan Sulfate (KS) – GlcNAc and Galactose (Gal). The negative charges are indicated in red and the possible sulfation sites shown by braces with the sulfate in red. Blue*

monosaccharides represent glucose and its derivatives, yellow represents galactose and its derivatives, and brown iduronic acid and its derivatives. Taken from Ref. (22).

1.5 Other Glycans

Glycosaminoglycans are not the only glycans in the ECM, there are also glycoproteins and glycolipids (29, 30). Glycoproteins and glycolipids are shorter polysaccharides and, therefore, make up the grass and bushes of the forest of the glycocalyx (1-5).

1.5.1 Glycosphingolipids

There are different types of glycolipids, but the major type in mammals are glycosphingolipids. (29, 30). The lipid constituent, which sits inside the plasma membrane, consists of a sphingosine linked via an amide to a fatty acid. This constituent is called a ceramide and there are variations in its sphingosine and fatty acid, but the major differentiation between the glycosphingolipids is due to the sugar moiety that forms the head group of the lipid. The ceramide is first linked to either glucose or galactose, these sugars can then be further linked to additional saccharides (Figure 3). These additions occur enzymatically, with enzymes that are specific to glycosphingolipids (29, 30). However, some glycosyltransferases, enzymes that transfer sugar groups from nucleotide sugar donors, can act on both glycosphingolipids and glycoproteins. The enzymes responsible for glycosphingolipid synthesis, and the synthesis of the intermediate molecules, are under regulatory control through protein expression. This leads to the different cell types having distinct glycosphingolipid profiles (29, 30).

The different types of lipids in the plasma membranes are variable and glycosphingolipids can occupy anywhere from 5 to 20% (29, 30). In the central nervous system, myelin contains one of the highest percentages of glycosphingolipids. One of particular importance is galactosylceramide (GalCer), synthesised in the oligodendrocytes. GalCer stabilises myelin (31). Glycosphingolipids in plasma membranes often cluster together and form lipid rafts, micro domains in the plasma membrane. In the case of myelin, these lipid rafts control the distribution of myelin basic proteins, which plays a key role in the organisation of myelin. Furthermore, GalCer also has sulfated derivatives such as sulfatides that are produced by galactosylceramide sulfotransferase. The absence of this enzyme means that the sulfated derivatives of GalCer are not present and the resulting myelin has a reduced thickness (31).

Some glycosphingolipids have cluster of differentiation (CD) names due to their prevalence on the surface of immune cells (29, 30). Globotriaosylceramide (Gb_3) is also known as CD77 and initially discovered as a marker for B lymphocytes. Recently, Gb_3 has been designated as a potential marker for head and neck cancers (32). Most head and neck cancers are difficult to detect with 75% of patients diagnosed with them having some form of metastasis. Using a Gb_3 detecting antibody, this glycosphingolipid was detected in head and neck cancer cell lines, mouse models, and human samples.

Defining Gb_3 as a cell surface marker for this cancer adds to the different cell types that can be defined by presentation of this glycolipid on the surface, highlighting that different glycolipids can act as markers for multiple cell types (29, 30, 32).

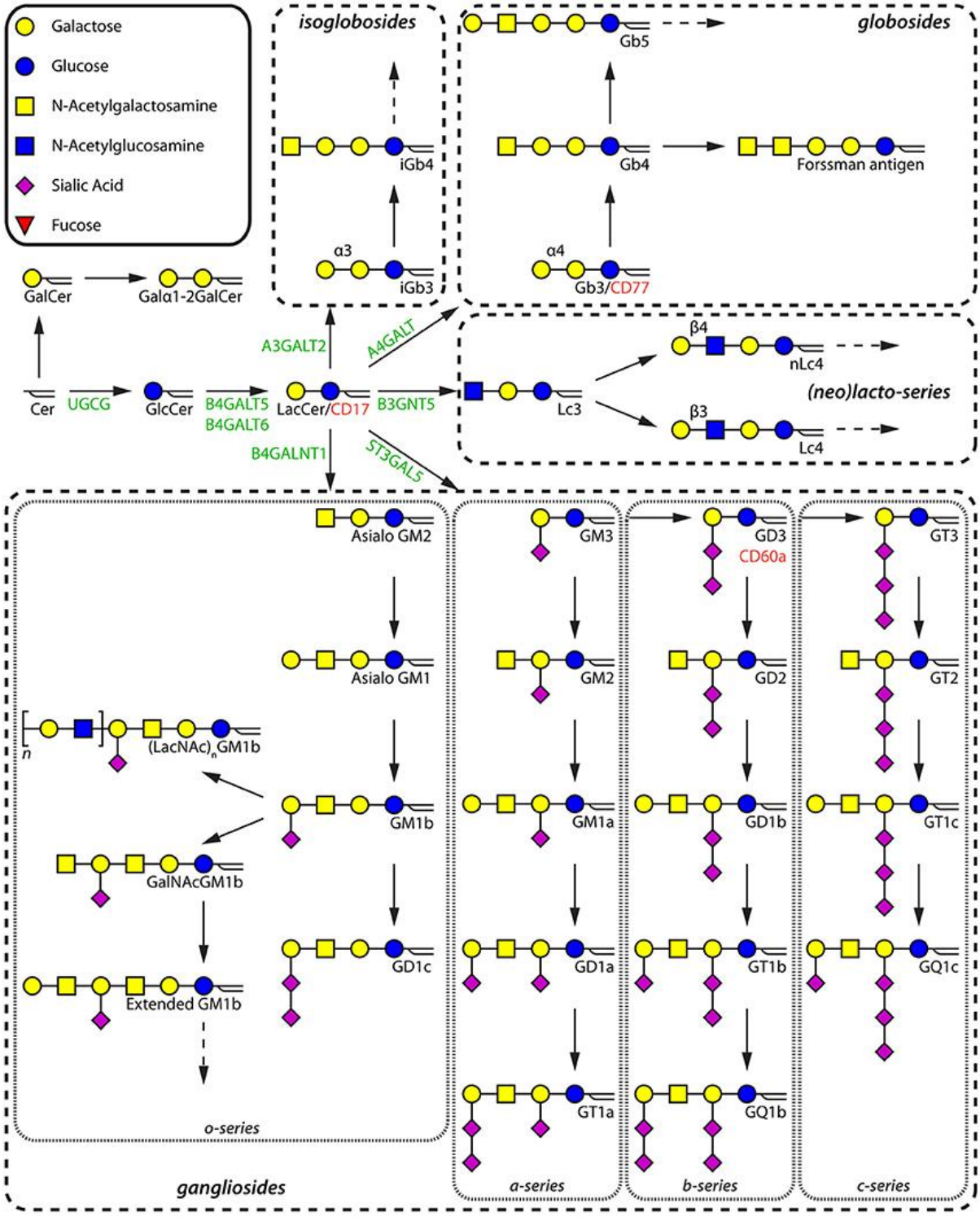


Figure 3. ***The Major Glycosphingolipids.*** *The key in the upper left hand corner denotes the sugar head groups of each glycosphingolipid. Subgroups are denoted by the dashed borders. Enzymes in the synthesis pathway are denoted in green. Taken from Ref. (29).*

1.6 Biological Colloids

A colloid is a solute particle ranging in hydrodynamic radius from 0.5 to 100 nm (33) and the movement of these particles are defined well by Brownian motion in dilute solution (17, 33). Biological colloids are colloids that have relevance in biological systems and range from inter and intra cellular proteins to vesicles (34). This is not the only definition of colloids in terms of size ranges and functions, but it the the most relevant within the context of this thesis. The ECM contains a variety of biological colloids, those of particular relevance here, due to their interaction with the glycan components of the ECM, include signalling proteins, toxins, and extracellular vesicles. The function of these biological colloids plays critical roles in a multicellular organism by governing cell communication. This section will focus on the biochemistry and functionality of these biological colloids within the ECM and the context of glycan binding and diffusion.

1.6.1 Signalling Proteins

The extracellular matrix acts a signalling platform as it exists in the space between cells where signalling proteins exist after excretion (1, 15, 35). There is a wealth of evidence placing signalling proteins in the ECM interacting with glycosaminoglycans, specifically heparan sulfate (36-41). Two particular groups of proteins that have been studied in this regard are chemokines, the signalling proteins involved in the immune system, and fibroblast growth factors, which have critical roles in development and tissue repair (41).

1.6.1.1 Chemokines

Chemokines (**chemo**tactic cyto**kines**) are a family of small signalling proteins that act as inflammatory cues to direct immune cells to areas of infection (42). Chemokines are classified according to the disulfide bonds between the structurally disordered N terminus and other areas of the protein. The cysteines within these disulphide bonds occur in a C, CC, CXC, or CXXXC pattern, providing the name for the different chemokine families. An X here represents any amino acid other than cysteine. Other notable structural features of chemokines (Figure 4A) are a C terminal α helix, a 3_{10} helix (an alternative helical secondary structure that is more tightly coiled than an α helix), and an antiparallel β sheet, which is essential for dimer formation in CXC chemokines (Figure 4B) (39, 42). The hydrodynamic radius of chemokines ranges from 1.5 to 2 nm (43).

The main function of chemokines within the immune system is to recruit immune cells. Different chemokines recruit different types of immune cells selectively. For example, CXCL4 recruits five different types of leukocytes, whereas CCL2 recruits monocytes alone (38). The presence of specific mixtures of chemokines can also impact on the recruitment of immune cells (44). Chemokines may also act homeostatically on immune cells and have essential roles in development (45). CXCL12 is a chemokine that is essential for life, a null mutation of CXCL12 is embryonic lethal due to the essential

role that it plays in cardiac development (46). It is also responsible for maintaining haematopoietic stem cells within the bone marrow, a necessary part of immune system maintenance (47). The different types of cell recruitment shown by different chemokines highlight that their regulation is important for the correct functioning of the immune system at a multicellular level.

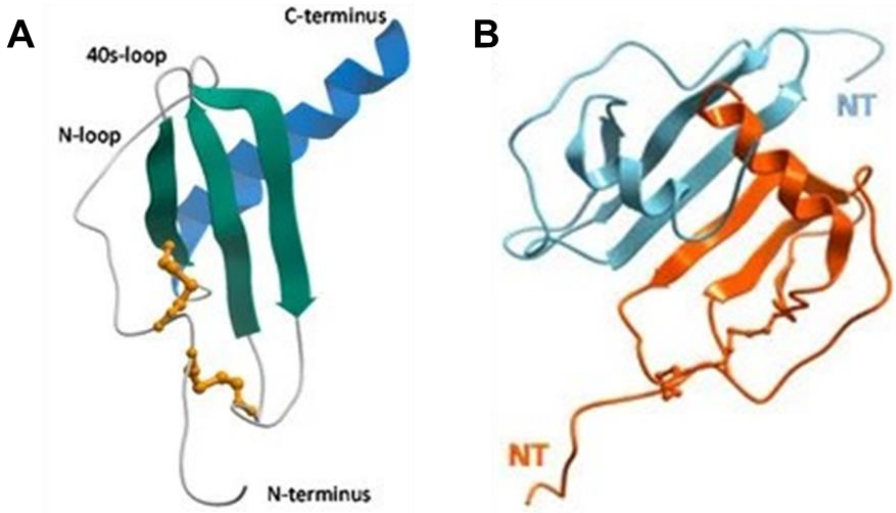


Figure 4. ***Ribbon Structure of Chemokines and their Dimers****. A) The ribbon structure of CXCL8, as a model chemokine, with the disulfide bonds shown in ball and stick configuration. B) The ribbon structure of a CXCL12 dimer, as a model chemokine dimer structure, blue and orange correspond to the individual monomers. Adapted from Ref. (39).*

Chemokine – GAG binding is a well established phenomenon, highlighting the relationship between chemokines and the ECM (38, 39, 48, 49). Chemokines may bind HS, CS, and DS, as exemplified by CXCL5 (Figure 5) (50). The interactions between chemokines and GAGs often relies on the presence of BBXB motifs in the amino acid sequence, two basic residues separated from an additional basic residue by an amino acid of any type (46). Figure 5 highlights the involvement of these basic residues in the interactions between chemokines and GAGs. Therefore, the interaction between chemokines and GAGs is often guided by electrostatic factors, but it is not limited to this type of interaction (39). In the context of GAG binding, chemokines can often form dimers, chemokine dimers can bind than one GAG chain, resulting in GAG cross-linking (41).

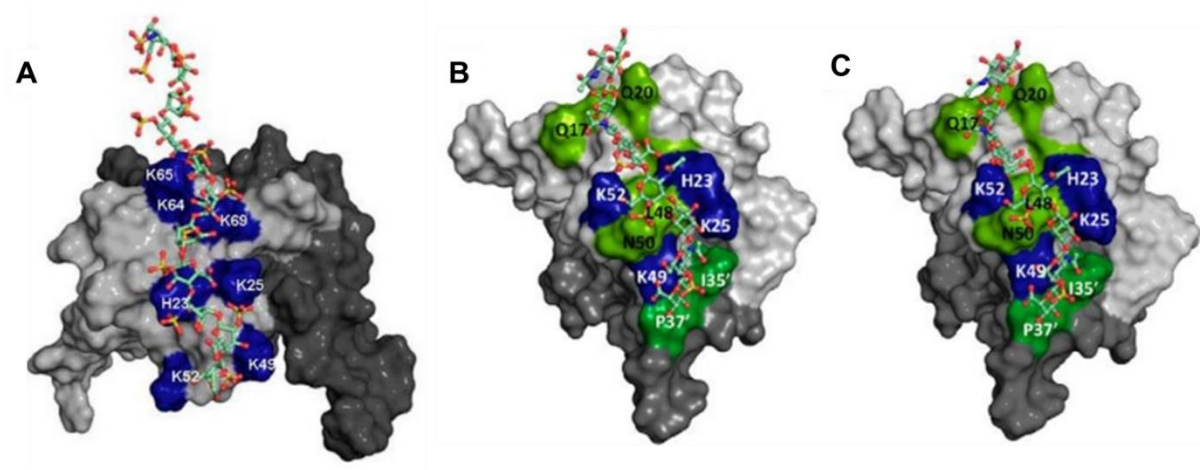


Figure 5. ***CXCL5 in Complex with HS, CS, and DS.*** *A-C) CXCL5 dimers (light and dark grey) in complex with HS (N sulfated and 2 O sulfated) (A), CS (4 sulfated) (B), and DS (4 sulfated). GAGs are shown in stick and ball configuration. Residues involved in the interaction are coloured blue (basic) and green (polar) (light and dark represent individual monomers of CXCL5). Adapted from Ref. (50).*

The importance of GAGs in chemokine distribution and function has been shown through experimental investigation such as the importance of HS in leukocyte migration (51). In heparanase expressing mice, the heparan sulfate chains of the ECM have a decreased length. Neutrophils in venules moved in random directions, decreasing their ability to migrate to the infected site. The impact of this immune functioning was demonstrated by the limited ability of these mice to clear infections when compared to the wild- type mice. Furthermore, less fluorescently labelled chemokine was observed on the endothelium in these mutant mice than in wild-type mice (51).

Mutagenesis has also been used to investigate the importance of HS-chemokine interactions, particularly through creating mutant model organisms. A mutant mouse model with CXCL12 lacking certain HS binding regions has been used to investigate the impact of HS binding on CXCL12 function (52). These mice had increased amounts of CXCL12 in their serum along with increased circulating white blood cells. Upon the inducement of ischemia, inadequate blood supply, the CXCL12 mutants had a decrease in the amount of haematopoietic stem cells in the ischemic muscle but an increase in these cells circulating the vasculature. Furthermore, the revascularisation in the ischemic muscle was significantly decreased. Application of wild-type CXCL12 could restore the muscle, therefore, the ability of CXCL12 to bind HS is required for the recovery of this muscle injury (52). This indicated that HS binding is required for the correct distribution and localisation of the chemokine in order to activate responses (52).

Previously, chemokines were thought to form chemotactic gradients, that is, gradients of chemoattractants that are free to diffuse in solution. However, there is gathering evidence that

chemokines may form haptotactic gradients, that is, gradients in which the chemoattractant is attached to an immobile matrix (53-56). One such example is Weber *et al.,* a study on dendritic cell migration from the interstitial tissue to the lymphatic system (55). A CCL21 gradient was visualised with immunohistochemistry and the amount of the chemokine decreased over distance away from the lymphatic vessel. A heparinase treatment resulted in a flattening of the CCL21 gradient, therefore, the presence of HS was required in order for the correct gradient to form. This study provided i*n situ* evidence to support haptotactic gradients as the mechanism of directed immune cell movement (55).

1.6.1.2 Fibroblast Growth Factors

Fibroblast Growth Factors (FGFs) are a group of signalling proteins with a paramount role in growth and development in animals and also have a close relationship, similar to that of chemokines, with GAGs (57-59). There are 23 FGF proteins and their common structure consists of 12 antiparallel β sheets (Figure 6). FGFs bind their cognate receptors, FGFRs, and may activate a variety of downstream signalling pathways dependent on cell type. For example, RAS/MAP kinase pathway, which is a sequence of phosphorylation events that causes changes to protein expression and often drives cell division. There are three main outcomes: proliferation, migration, or differentiation. For example, FGF2 results in proliferation when detected by endothelial cells, but when detected in astrocytes will result in cell migration (59). There are a variety of conditions that are caused by deregulation of FGFs and their receptors, making these molecules of keen interest in therapeutic developments (57-59).

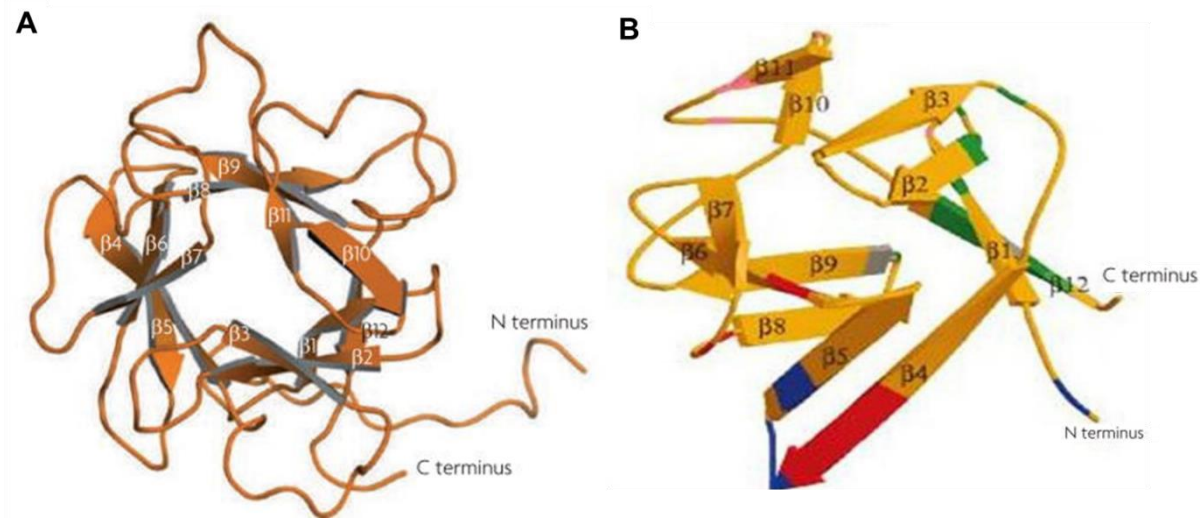


Figure 6. ***Structure of Fibroblast Growth Factors.*** *A) The ribbon structure of FGF1. B) The ribbon structure of FGF2. Adapted from Ref. (57) and (58) respectively.*

FGFs typically act through paracrine signalling, remaining in close proximity to the cells they are produced in. HS binding has a role in FGF2 signalling by acting as a coreceptor with FGFR (58). Heparin binds to FGFs via the face of the protein with β sheets 1 and 2, and 10 through 12 (Figure 7). The

hydrodynamic radius of FGFs is comparable with that of chemokines (60). However, each FGF has a distinct method of interaction with GAGs with varying affinities and a varying number of binding sites (41, 61). For example, FGF1 and FGF2 have distinct differences in their interaction with HS. FGF1 has a μM affinity for HS, whereas FGF2 has at least two binding sites, one with a high nM affinity and another with a low nM affinity (61). Therefore, there is some degree of multivalency in FGF-GAG interactions. FGF-HS interactions play an important role in downstream signalling activation, due to the role of HS as a coreceptor for FGFRs. For example, treatment of a B cell line derivative with FGF1 and FGF2 in combination with various sizes and sulfation levels of HS showed how different FGF-HS interactions have different biological results (62). FGF1 showed better activation for HS types with 6-O sulfation. FGF2 showed better activation for HS chains with a greater number of disaccharides. These results showed how differential types of HS had different impacts on the activity of the two different FGFs (62).

Some studies have investigated FGF transport in the ECM in the context of FGF-HS interactions (40, 63-65). One particular study, Sun *et al.,* found that FGF1 is less mobile in pericellular matrices of fibroblast cells than FGF2 and FGF6 (65). This is likely to be due to the interactions of these individual FGFs with HS as the study highlights that each FGF has a slightly different relationship to HS.

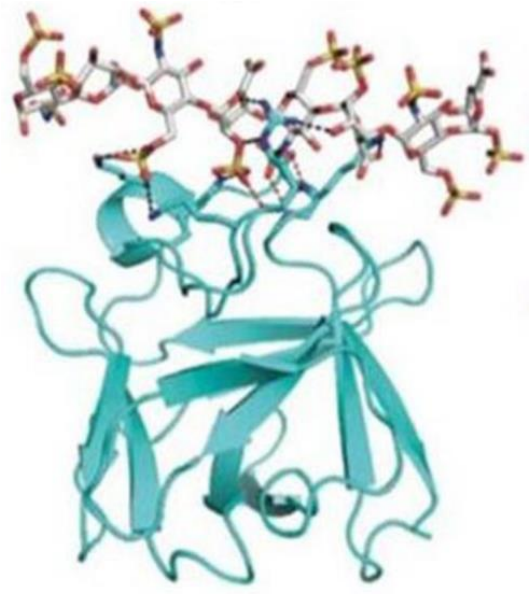


Figure 7. ***FGF2 in Complex with Heparin.*** *FGF2 in ribbon form in complex with heparin in ball and stick form. Taken from Ref. (58).*

1.6.2 Toxins

Endogenous proteins are not the only proteins that distribute in and interact with the extracellular matrix and its components. Upon bacterial invasion into multicellular organisms, bacteria and their toxins interact with material in the extracellular matrix and on cell surfaces in order to enter cells and

spread throughout the organism (66-68). Many gram-negative bacteria interact with ECM proteins such as fibronectin and laminin. Some toxins, such as AB_5 toxins, after their release from bacterial cells, interact specifically with the sugar components of the ECM (69).

1.6.2.1 AB_5 toxins

AB_5 toxins consist of two subunits (A and B). They are released from *Vibreo cholerae, Escherichia coli, Shigella dysenteriae, Bordetella pertussis, Bacillus anthracis,* and *Ricinus communis*, for example (69). Cholera toxin (CT) and Shiga toxin (STx) (Figure 8) interact with glycosphingolipids through the B subunit of the protein, a pentamer. Through this interaction, internalisation of the toxin is triggered resulting in the downstream effects within the cell. Typically, these toxins impact on cells in the intestinal epithelium, causing the cells to loose water, resulting in diarrhoea and dehydration (69). CT also has a secondary glycan binding site in the glycocalyx, it is able to bind to certain blood type antigens (70).

The pentameric B subunit of Shiga toxin (STxB) interacts specifically with the sugar components of the glycosphingolipid Gb_3 (71, 72). STxB can bind up to 15 molecules of Gb_3, with each subunit of the B pentamer containing three binding sites. One such site contains an oligonucleotide/oligosaccharide binding (OB) fold, this type of structure consists of a β barrel and an α helix that sits opposite the main binding site (73). The binding site for the sugar in this case are three loops, two between individual β sheets and one between a β sheet and the α helix. The other binding sites on the STxB monomer contact two β sheets directly or the N terminal end of the α helix (71). Each binding site has a varying affinity.

The interaction between STxB and Gb_3 causes significant changes to the plasma membrane as part of its mechanism for cell entry (72). Due to the binding between the toxin and the glycosphingolipid, the membrane and STxB become mechanically coupled which results in a clustering of these lipids on the membrane, which triggers endocytosis. Therefore, the interaction between these two molecules is essential in driving the bacterial infection. The diffusion of the toxin itself in the extracellular matrix until it meets Gb_3 would impact on the cell types that the toxin can infect, but there is not experimental data that measured this diffusion.

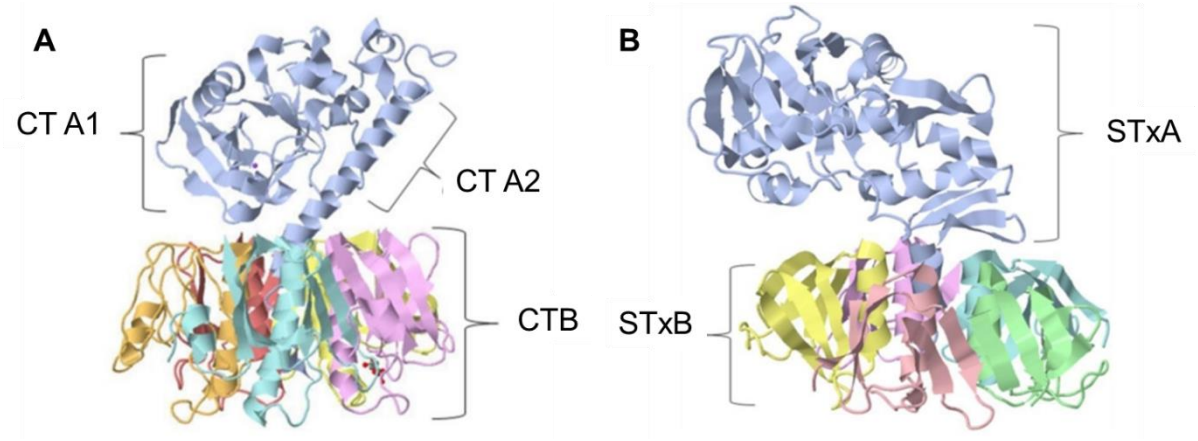


Figure 8. ***Structures of AB$_5$ Toxins.*** *A) The two subunits of Cholera toxin. B) The two subunits of Shiga toxin. The B subunits of these toxins are always pentamers. Adapted from Ref. (69).*

1.6.3 Extracellular Vesicles

Individual proteins and their oligomers are not the only biological colloids released by cells. Extracellular vesicles are lipid vesicles enclosing biological active molecules (74, 75). The lipid coatings are derived from the plasma membrane or individual cell organelle membranes, giving the vesicle itself a defined identity. Vesicles themselves can occur in a variety of sizes from 30 to 1000 nm (Figure 9). Typically, vesicle identity is defined by their size (Figure 9), including exosomes which originate from the endosomal reticulum, microvesicles and apoptotic bodies which originate from the plasma membrane. It is also possible to define vesicles by using antibodies against cell surface markers (76). Vesicles released from cells typically contain a large variety of cell surface markers highlighting the variety in functions as this would affect how they interact with the ECM.

Vesicles are a critical part of cell signalling and communication. For example, in the context of development and Hedgehog (Hh) signalling, extracellular vesicles are responsible for 50% of Hh signalling (77). Hh is a morphogen, a signalling molecule that impacts on cellular behaviour by forming concentration gradients, these would also fall under the definition of biological colloids (78). Hh undergoes palmitoylation, a lipid modification, and cholesterolation as an essential post translation modification for its signalling (79). The addition of cholesterol causes Hh to localise into structures within the ECM. This may be linked to extracellular vesicles or glycosaminoglycans, as Hh also has the ability to bind HS (79, 80). However, upon removal of cholesterol from Hh, the distance in which Hh is displaced decreases,indicating a reduced ability for the Hh to diffuse (77). There is also data to suggest that Sonic Hh, a vertebrate homolog of Hh, may form micelles or exosome-like structures in the ECM. Overall, Hh signalling and diffusion appears to be caused by a complex interplay between the role of lipid motifs and Hh binding to glycosaminoglycans.

Extracellular vesicles distribute in the interstitial matrix as a critical mechanism for their transport in multicellular organisms (74, 75). Transport in the interstitial matrix is often defined by the rate of flow of the interstitial fluid without considering the impact of the matrix pore size or affinity. However, due to markers, such as proteins or other membrane components, on the surfaces of vesicles, they have the potential to interact with the ECM, affecting their diffusion. Vesicles containing different levels of integrins, as a consequence of their cell of origin, distribute differently in different types of interstitial matrix (75). Furthermore, extracellular vesicles are large in comparison to the signalling proteins and toxins previously discussed (at a minimum five times greater in diameter). Due to the pore like structure of the extracellular matrix, there will be steric affects that impact on the diffusion of vesicles (74). The effects of pore size are not extensively studied and the diffusion of vesicles of a defined size as a function of the pore size of an ECM is not known. In synthetic matrices, there are often a range of pore sizes within the matrix, and there has been continuing development in order to improve this. In collagen-GAG synthetic matrices, the size range for pore sizes cover around 50 μm (81).However, the pore size is likely to have a profound effect on the way that vesicles carry out their functions in different types of matrices under different conditions. For example, in inflamed states when GAGs are shed, it is possible that this leads to an increase in the pore size of the matrix (7).

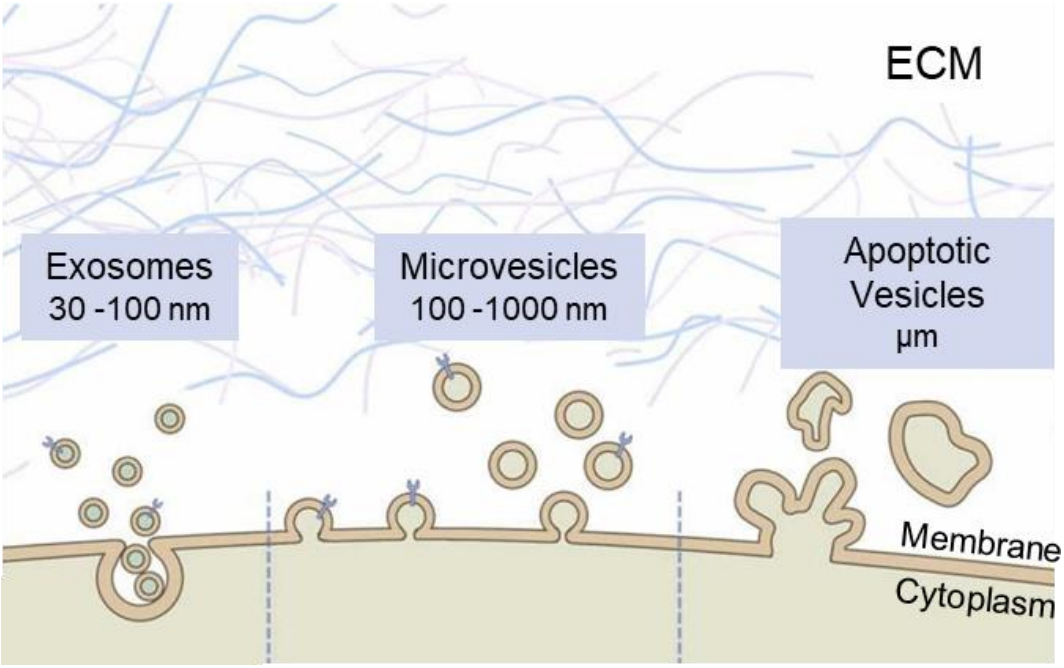


Figure 9. ***Types of Extracellular Vesicles.*** *The size ranges (tens of nm to tens of µm) of different types of extracellular vesicles released into the ECM from the plasma membrane. The vesicles of different size ranges are the result of different processes and are released with different mechanisms. Exosomes are generated within the cell and secreted by the fusion of one large vesicle with the plasma membrane. Microvesicles and apoptotic bodies are generated from the plasma membrane itself. Adapted from Ref. (74).*

1.7 Diffusion of Biological Colloids through ECMs

In this chapter, the components of the ECM and biological colloids that have been reviewed. Interactions between biological colloids and the ECM define the diffusivity and retention of biological colloids in the extracellular space. These interactions are typically transient, and may be biochemical, consisting of binding to the matrix, or physical, due to steric effects caused by the meshwork that the ECM provides. This leads to the question of how biochemical and physical interaction of biological colloids with the ECM impact on biological colloid diffusion.

There are a few studies that have analysed diffusion of such biological colloids through different types matrices. The study of nanoparticle diffusion in 3D gels has been an active area of study (82, 83). In one study, a polyacrylonitrile membrane with pore sizes ranging from 0.19 to 3.4 µm and the pore size assessed through scanning electron microscopy (82). Matrigel, a 3D gel that emulates the basement membrane, contains a number of proteins among which is collagen which has been chemically cross linked, a pore size of 0.14 µm has been achieved with this type of ECM-like gel (84). These studies can accurately describe the effects of steric interactions on the diffusion of inert molecules, but cannot describe biochemical interactions. However, these types of matrix gels have pore sizes, although they

are well defined, it is unknown if they reflect the true size of pores in the ECM due to the difficulty in defining the pore size (13). However, measurements through a variety of techniques would suggest that the pore size is on the order of nanometers instead of microns. Overall, these types of studies may not reflect biological situations well due to the differences between what is present in the model systems and the reality of biological ECMs. The model matrices introduced in Chapter 2 have a stringent formation method that allows for very well defined model matrices, in terms of the components and interactions between them, to be formed with the ability to form matrices with a precise pore size on the nanometer scale.

Studies of pericellular matrices may offer better insight into biological situations. Miller *et al.* have shown that the diffusion of chemokines in tissues can be measured using microscopy techniques Fluorescence Correlation Spectroscopy (FCS) and Fluorescence Recovery After Photobleaching (FRAP) (85). Sun *et al.* analysed the diffusion of different FGFs in fibroblast pericellular matrices, through FRAP, and found that different FGFs had different levels of mobility (65). Fibroblast pericellular matrices are rich in HS proteoglycans and the interaction between FGFs and HS is likely responsible for the varied level of diffusivity of the FGFs. However, the mechanism of diffusion that results from GAG-FGF interaction is unclear. Heterogeneous distribution of the FGFs within the pericellular matrix was observed, highlighting that the location of the FGFs as a result of the FGF-GAG interaction (65). Duchesne *et al.* utilised the same pericellular matrices but with a different diffusion tracking approach, single particle tracking (SPT), focusing on the diffusivity of FGF2 (40). This study found that the majority of FGF2 is confined on pericellular extracellular matrices. They went further and analysed the distribution of FGF2 binding sites on HS and considered that the organisation of these binding sites must influence the areas in which FGF2 is confined (40). This provides crucial data to indicate that this interaction is vital in defining GAG-binding protein distribution and diffusion in the ECM.

The common theme within these studies that remains elusive is how the interaction between the GAGs or other glycans and its binding partner impacts on the binding partner's diffusion. The heterogeneity of pericellular matrices and other tissues leaves many open questions about the pore size, GAG sulfation, GAG length, the exact number of binding sites, and the affinity of the GAG-binding protein to this specific GAG types, among others. Technique development in this area would allow the analysis of diffusion in a well defined matrix with a well understood interaction between all binding partners within the matrix. A technique that can easily be modified to change the matrix to address specified questions would increase the range of scenarios that can be investigated.

Table 1. ***Summary of Biological Colloids.*** *The different biological colloids discussed in this chapter and features that could impact on their ECM diffusion such as their size which impacts on Stokes-Einstein diffusion and their ECM interactions.*

Biological Colloid	Size		ECM Interaction Partner
	Molecular Weight (kDa)	Hydrodynamic Radius (nm)	
Chemokines	8-10 (45)	1.5 – 2 (43)	Glycosaminoglycans
Fibroblast Growth Factors	17-34 (59)	~ 3 (FGF2) (60)	Glycosaminoglycans
AB toxins	50 – 100 (69)	Unknown	Glycoproteins and glycolipids
Extracellular Vesicles	Variable	15 – 500	Variable

1.8 Project Aims

Although the current research can define many biological colloid interactions with matrix components and requirement of this interaction for function, the impact of these interactions on diffusion and distribution are unclear. There have been some studies that focus on addressing this question, but there are limited tools available to analyse and describe this phenomenon.

The overall aim of this thesis is to generate tools, both experimental and theoretical, to study how stickiness and porosity define the diffusion of biological colloids in model ECMs.

The specific objectives are:

1. To generate extracellular matrix models in which the pore size of the matrix and the biochemical and biophysical interactions between the model matrix and biological colloids are well defined. These includes tuning the models to reproduce the salient features of interest.
2. To explore how biological colloids may be labelled to enable their visualisation and tracking without the label impacting on the matrix-binding ability of the biological colloid.
3. To develop an experimental method to track the diffusion of biological colloids within model extracellular matrix films.
4. To explore the effect of pore size on the diffusion of biological colloids.
5. To develop a theoretical model that considers how stickiness regulates the diffusivity of biological colloids in model and *in vitro* extracellular matrices.

1.9 Outline of Thesis

Chapter 2 of this thesis will review the relevant established methods involved to address the thesis objectives. This includes the mechanisms underlying the techniques and the results that can be obtained from them. Chapter 3 will address objectives 1 and 2, Chapter 4, objectives 3 and 4, and Chapter 5, objective 5. Chapter 6 will bring the results from Chapters 3 through 5 together and address whether or not these objectives were achieved.

Chapter 2: Introduction to Relevant Methods

2.1 Outline

Considering the question that is to be addressed within this thesis, there are two important features of this research. Firstly, how to generate model glycan-rich matrix and secondly, how to measure diffusion of macromolecules. This includes a combination of preparative and analytical techniques. For the former, this involves the formation of GAG-rich model matrices. For the latter, this involves defining the exact properties of the model matrices that recapitulate the main features of interest of the *in vivo* extracellular matrix. Further analytical techniques are also required for measuring and predicting diffusion of biological colloids.

This chapter reviews the purpose and working principles of established methods which have been generated by other authors. A summary of these techniques is listed in Table 2. New methods that were developed in this doctoral work are outlined in their respective chapters. These new methods include plane sphere confinement microscopy (PSCM) on model matrices (Chapter 4) and an analytical model for prediction of diffusion of biological colloids in sticky polymer matrices (Chapter 5).

2.1.1 Model Extracellular Matrices and their Benefits

Extracellular matrices (ECMs) can be extracted from tissues, but cells applied to extracted ECMs often have differing behaviour in comparison to *in vivo* cell activities (2, 4, 86). Furthermore, the components of cellular ECMs are very varied and difficult to define. For example, although the disaccharide composition of glycosaminoglycans of different ECMs can be measured thoroughly by mass spectrometry, giving an insight into the types of GAGs that are present (9). The enzymatic process required for this analysis means that the GAGs are broken down into their subunits, meaning that information on the length and molecular weight is lost. Additionally, when considering the protein components of the ECM, many proteins are insoluble which can lead to them going undetected. Some proteins can become soluble in certain buffers and with reagents that remove non-covalently bound material. However, one study suggested that 75% of insoluble proteins remain even after this type of treatment (87). Proposed mechanisms as a result of analyses of data observed on cellular ECMs may be misguided by the current understanding of the components within them. For instance, an insoluble protein may be present, but has gone undetected and that results in the mechanisms missing this component. In order to separate out which components of the ECM are responsible for different experimental outcomes, a model matrix can be used (88).

Model ECMs can be reliably reproduced and are much simpler in comparison to cellular generated matrices. They are also two dimensional systems on a surface, further simplifying them from the three dimensional matrices of cellular systems and making the model matrices compatible with many different analytical techniques (88). The relative simplicity provided by 2D model systems, 3D cell

cultures have been critical in the testing of pharmaceutical products due to the ability to test these products in a close to life scenario (89). However, for mechanistic studies, additional complexity can result in unpredictable and more difficult to account for outcomes from experiments. In a 2D system, where the amount of parameters are reduced to a specified number then all experimental outcomes must be due to one of those. This allows for easier development of proposed mechanisms and the ability to build complexity over time. Eventually, 2D models will be compared with 3D models in order to allow the integration of different proposed mechanisms (90).

Within this work, the parts of the ECM that are replicated in model matrices are different types of glycan content (Sections 3.3.1.1, 3.3.1.2, and 3.3.1.3), pore size (Section 3.3.1.2), and fluidity (Section 4.3.1.2.1). These different facets of the model ECM are easily changed during its formation and are tailored to the specific question under investigation.

2.1.2 Formation of Model Extracellular Matrices

The formation of model extracellular matrices forms the foundation of this work, it allows for the generation of the model system that can be tuned and specified to answer the questions of interest (88, 91). These model surfaces are designed to recreate the quintessential features of the extracellular matrix that are relevant to the question of interest such as GAG type, size, sulfation and grafting density. These types of model matrices are formed using a bottom up approach, using individual biomolecules that can self-assemble to form layers of a model matrix. This self-assembly is reliant on the specific interactions between the biomolecules as a result of their basic features. A planar support is used to form a lipid membrane, generated from lipid vesicles and their interaction with each other and surfaces. The lipids contain a biotin on their polar head groups, Streptavidin (SAv) binds strongly to this. Biotinylated GAGs, or other molecules, can then bind to the SAv. In this manner the strong interaction between biotin and SAv is exploited to allow for self-assembly. All these molecules play specific roles in the formation of the model matrix (88, 91). This is not the only method of model matrix formation. GAG-collagen scaffold model matrices can be produced by freeze-drying different mixtures of components (81). Synthetic hydrogels that serve as model matrices can be formed from alginate containing peptides, a negatively charged polymer that can be cross-linked with calcium ions.

A schematic of the formation of model ECMs on planar surfaces through lipid membrane and in the SAv anchorage platform is presented in Figure 10. This system has three key functional features. The first, a supported lipid bilayer (SLB), a fluid surface with lateral mobility. The second a SAv monolayer to allow for the anchoring of specific molecules. Thirdly, biotinylated molecules with biotin acting as anchors to SAv. Small Unilamellar Vesicles (SUVs) are applied to surfaces to which they will adsorb (Figure 10, step 1). Once these SUVs reach a critical coverage on the surface, they will rupture and

form an SLB on the surface, the main driving force for this formation is the hydrophobic effect (Figure 10, step 2). This method of SLB formation is called the vesicle spreading method (92). This bilayer generates a homogenous layer that covers the entire surface and retains its nominal lateral mobility of a plasma membrane. This homogenous layer is due to the energetically favourable interaction between the charged head groups of the phospholipids with the silica surface and the solution and the hydrophobic lipid tails only interacting with each other. This homogeneity has been previously assessed through Atomic Force Microscopy (AFM) by Richter *et al.* (92) In this work, the typical types of lipids used to generate SLBs are DOPE-CAP-B (1,2-dioleoyl-sn-glycero-3-phosphoethanolamine-N-(Cap Biotinyl)) and DOPC (1,2-dioleoyl-sn-glycero-3-phosphocholine). The former contains a biotin molecule in its head group, at a defined molar percentage, which allows for the attachment of SAv the bilayer (Figure 10, step 3) (88).

The SAv monolayer acts as an intermediate layer in this model matrix, providing the linkage between the bilayer and the biotinylated molecules that will be added. The main feature of the extracellular matrix that the model is designed to recreate in this thesis is the abundance of GAGs. In order to achieve this, GAGs have been chemically modified with the conjugation of a biotin molecule at the reducing end of the sugar polymer (93). Biotinylation is a one-step chemical oxime ligation method which is well established and works for any GAG type. This allows the GAGs to bind the SAv monolayer with a defined orientation extending outward from the surface, similar to the presentation of GAG chains on a core protein in the endogenous environment (88). The benefits of this method are that the GAGs applied can have defined type, length, and sulfation (88, 91). GAGs that have been purified and assessed for their chemical composition are used in this process, these can be characterised to a high degree of certainty such as knowledge of the molecular weight within a few kDa. Furthermore, the formation of this model matrix can be monitored by different techniques to understand their structure and morphology (see Section 2.2.2, Figure 12), and these model matrices can be formed on different types of surfaces such as silica coated materials or glass allowing them to be utilised for multiple types of techniques (41). Characterisation techniques that can be applied to model matrices simply are not as easily adapted for use on cells, another advantage of using model matrices.

In this way, for these model matrices it is possible to know the exact molecules responsible for the results observed which is a substantial benefit of this technique (88, 91). As the aim of this thesis is to understand how the interactions between biological colloids and polymers in the ECM impacts on the

diffusion of biological colloids, limiting the model ECM to those molecules alone provides a much better methods for understanding.

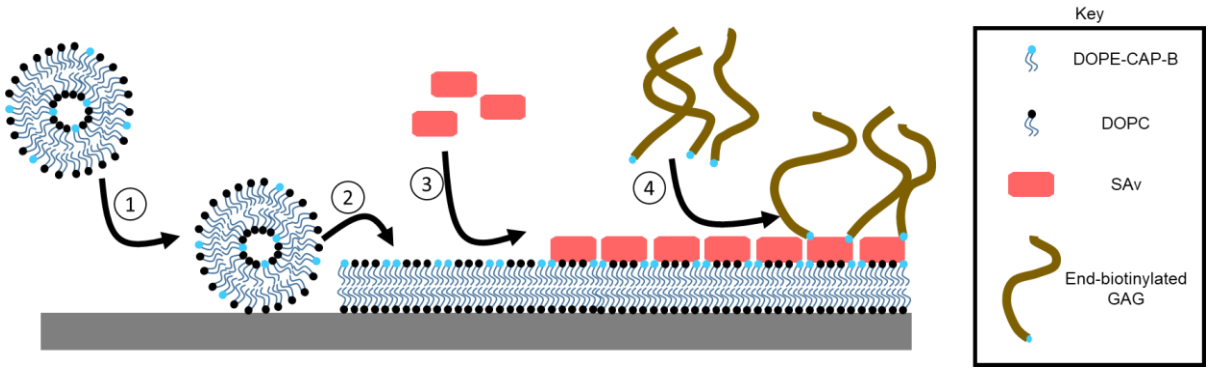


Figure 10. ***Formation of a Model ECM****. Including formation of an SLB and the binding of subsequent elements: ① Application and adsorption of SUVs to the surface. ② Vesicular rupture and the formation of an SLB. ③ Binding of SAv. ④ Binding of end-biotinylated GAGs. Molecules are not drawn to scale. In reality, the SAv monolayer and the lipid bilayer would be the same thickness and the lipid head groups would be smaller in relation to their lipid tails.*

2.1.3 Quartz Crystal Microbalance (QCM-D)

One of the main analytical techniques employed in this thesis is Quartz Crystal Microbalance with Dissipation monitoring (QCM-D). QCM-D provides quantitative measurements about the binding of different components to a surface and the viscoelastic properties of films on surfaces (94). In this work, QCM-D can be used to assess the formation of model extracellular matrices, their properties, and their interactions with other molecules in the system.

QCM-D is a biophysical technique that relies on the piezoelectric properties of the quartz crystal (94-96). When an alternating voltage is applied to a quartz crystal, the top and bottom parts of the crystal vibrate antiparallel to each other and generate a shear-mode oscillation, this can be seen in schematic form in Figure 11A. Not all quartz crystals oscillate in the shear mode, but the types involved in this technique are cut to allow for this. The AT-cut crystal is the most common crystal used in QCM applications and has the capability to oscillate in shear mode due to the angle of the crystal cut in comparison to the z axis (97). At resonance, a standing wave forms in the crystal which propagates into the adjacent medium. The resonance frequency and energy dissipation of the wave are affected by material immobilised to the sensor surface and the adjacent medium, and the ability of the quartz sensor to quantify such changes with high sensitivity is exploited for biophysical measurements. The frequency on which the crystal vibrates (the fundamental) also has multiples which are referred to as overtones (94-96).

QCM-D relies on the ring-down method specifically, where the externally applied voltage is discontinuous and when stopped, the oscillating wave decays over time on its own (98). From the decay curve, essential information may be extracted (Figure 11B) about the properties of the oscillation, such as the resonance frequency, *f*. For normalised frequency shifts, *F* is used. Resonance frequency can be determined with high accuracy from the inverse of the distance between peaks. In 1959, Sauerbrey found that changes in the resonance frequency are proportional to the changes in mass attached to the surface of the crystal when performed in air (99). This led to the formation of the Saubrey equation:

$$\Delta f = -\frac{n}{C}m = -\frac{n}{C}\rho h \qquad [2.1]$$

Where *m* is the areal mass density, *C* is the mass sensitivity constant, *n* is the overtone number, *ρ* is the density of the film on the surface of the crystal and *h* is the height. This equation is only applicable for certain film types. It was later shown that the attached mass must satisfy certain conditions in order to be directly proportional to the change in frequency, including that the attached mass must be rigid, evenly distributed across the crystal, and have a mass much smaller than the crystal itself. In most cases, and all cases relevant to this piece of work, a decrease in resonance frequency indicates adsorption of material to the crystal surface (94, 96).

The second parameter extracted from the decay curve is the energy dissipation, *D*. This is found from the curve fit to the decay in amplitude of the oscillating wave (Figure 11B) (94). The energy dissipation is a measure of how quickly electromechanical energy stored in the oscillating crystal is converted into heat and therefore, is a useful measurement in understanding the viscoelastic properties of the system (94). The energy dissipation is sensitive to the mechanical properties of the surface coating and the adjacent medium. Because changes in the mechanical (e.g. viscoelastic) properties of solvated films are often linked to morphological changes, the dissipation can be related to the morphology of material on the sensor surface.

At the start of an experiment, baseline measurements are acquired for *F* and *D*. All measurements throughout the course of an experiment are then referred to as Δ*F* and Δ*D*, as these are changes to the baseline measurements and reflect the changes to the surface.

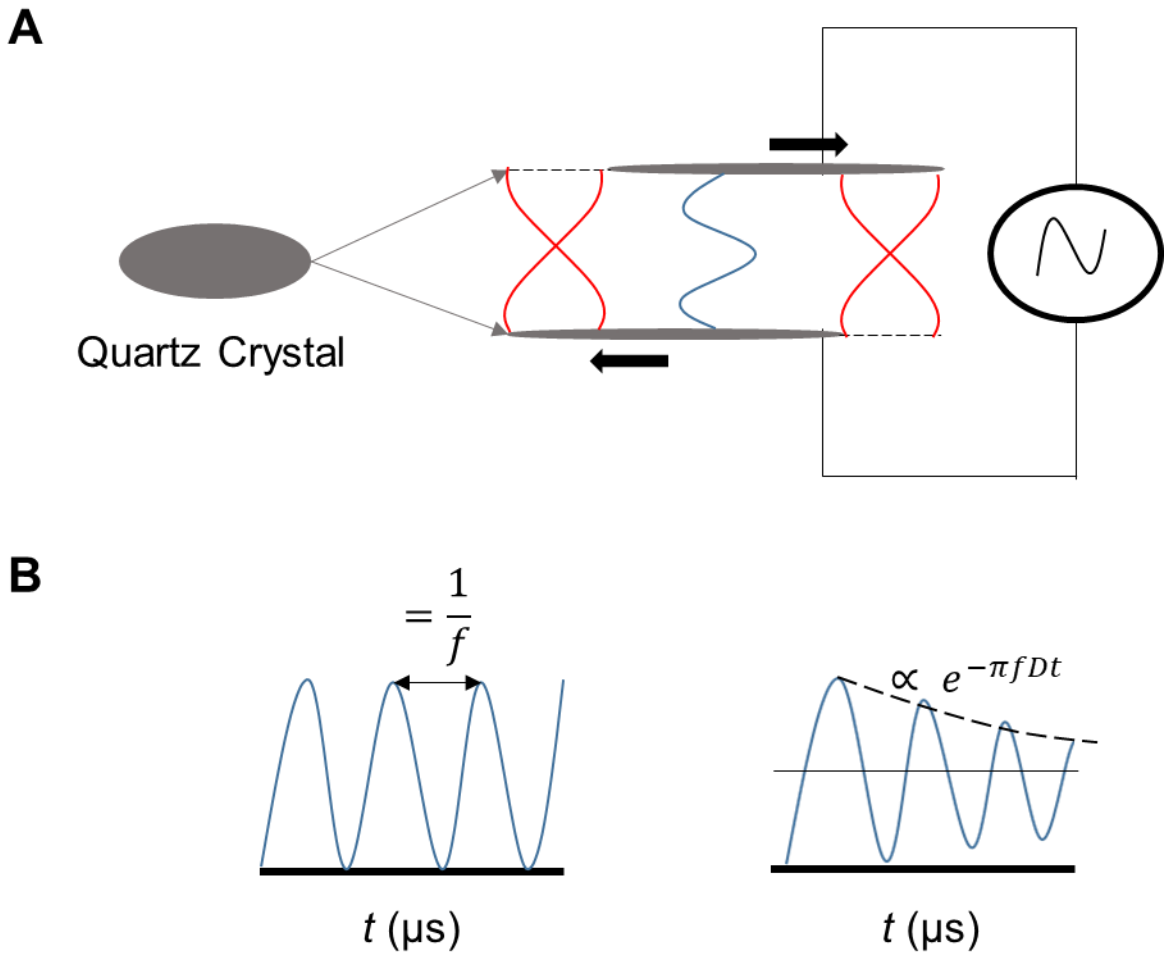


Figure 11. ***Illustration of QCM-D Mode of Operation****. A) The quartz crystal and the application of the oscillatory voltage resulting in the vibration of the two surfaces of the crystal in an antiparallel manner. The red waves represent the fundamental frequency, the blue waves represent the third overtone. B) How parameters describing the shear oscillation of the sensor are extracted from the decay curve obtained with the ring-down method. Here f represents resonance frequency, D represents energy dissipation, and t is time. Adapted from (94-96).*

2.1.3.1 A QCM-D Application

QCM-D has a number of uses in studying adherence of molecules to surfaces and the types of films generated. It has been used to investigate binding between different surfaces and ligands (41, 88, 100), the thickness and viscoelastic properties of different thin films (88, 92, 101), and to look at nanoparticle interactions (96).

To illustrate what information can be extracting from changes in frequency and dissipation upon binding of specific materials to QCM surfaces, the process of the formation of a model extracellular matrix (Section 2.2.1) on a QCM-D silica surface will be explained with the accompaniment of QCM-D data (Figure 12). The addition of biotinylated lipids in the form of SUVs to silica coated QCM-D sensors

results in the formation of an SLB on the silica surface; this is reflected in the decrease in frequency and subsequent increase resulting in a plateau at -25 ± 1 Hz, between time 15 and 22.5 min. A negative frequency shifts indicates an adherence of material to the surface. The reason for a greater decrease than the final plateau value is that the adsorption of many SUVs to the surface results in a larger change in the resonance frequency due to the entrapment of solvent molecules between and within the SUVs. Upon vesicular rupture, spreading and subsequent formation of lipid bilayer, the solvent molecules are excluded from the film and are no longer contributing to the QCM-D signal, this type of response is well defined in Richter *et al.* 2003 (102, 103). The final dissipation shift of bilayer formation is less than 0.5 ppm, this indicates a relatively rigid layer. The transient peak at 3 ppm is due to the vesicular layer on the surface, the vesicular layer is much softer than an SLB and this is reflected in the dissipation shift. SAv binding to the bilayer decreases the frequency by a further 27 ± 1 Hz and a dissipation shift of less than 0.5 ppm, between time 34 and 46 min. The small change in dissipation reflects that SAv as a globular protein does not impact on the rigidity of the surface. This highlights the sensitivity of the technique to both binding and film properties. SAv as a large globular protein causes a significant decrease in frequency, but as the globular protein does not change the properties of the surface, it does not impact on the dissipation. Therefore, the technique can separate effects due to binding and film properties. Biotinylated HS binding to the surface results in a frequency decrease of ~30 Hz and a dissipation increase of 6 ppm, between time 61 and 74 min. This large dissipation change indicates how the rigidity of the surface has changed; the addition of long polymers has resulted in a film that extends further above the surface with polymers that have a large degree of freedom via their own movement. This type of film formation of analysis of GAG films and materials that can bind to them is well established (88).

This type of analysis has been pioneered by the lab of Dr Ralf Richter and has been utilised in many protein-GAG film interaction studies (41, 88, 104). It has also been used for quantitative analysis of GAG species, such as for analysis of GAG sizes (101). This technique has since been adopted by other labs such as that of Professor Marta Bally for the use of interactions between viruses and different surface formations (105).

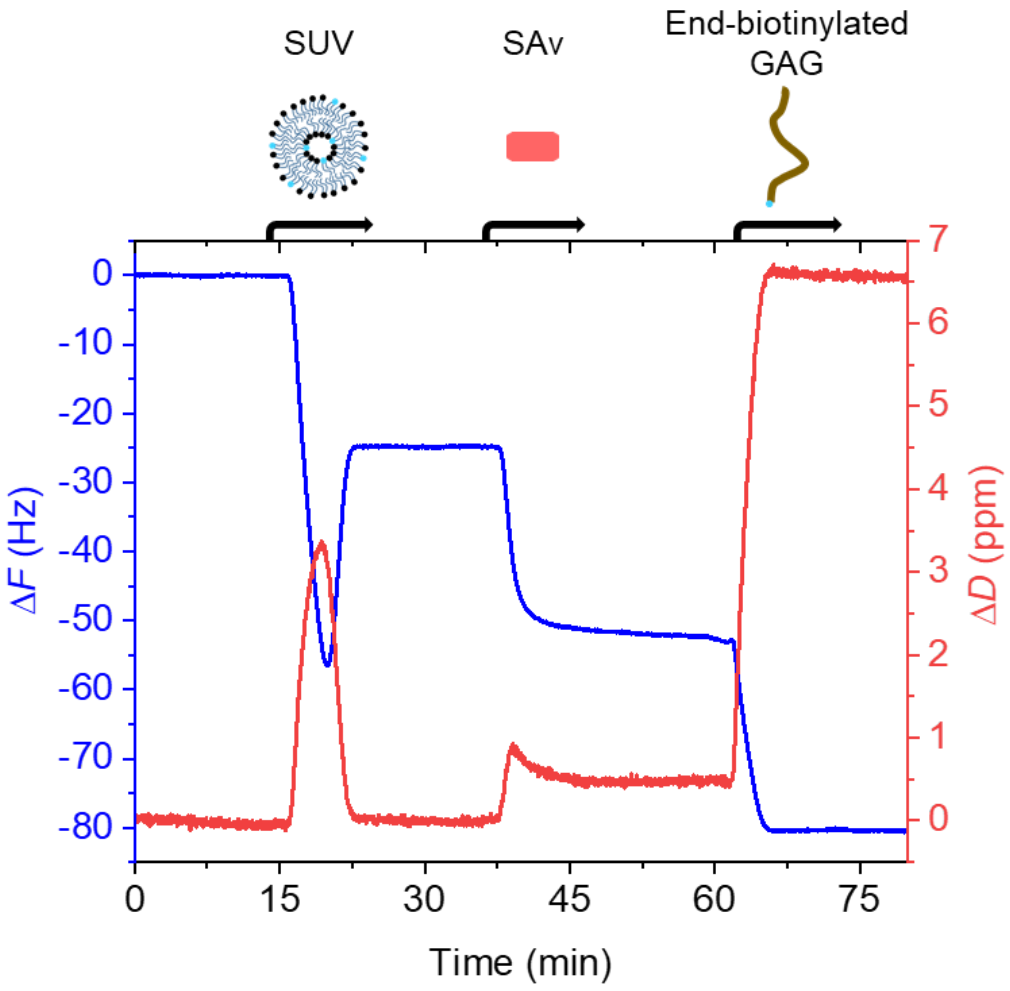


Figure 12. ***Formation of a GAG film followed by QCM-D.*** *Shown are the frequency (ΔF) and dissipation (ΔD) changes that accompany all steps of the surface functionalisation, starting from the formation of a supported lipid bilayer, followed by a SAv monolayer and the formation of an HS film. Start and duration of incubation of respective materials are indicated by arrows above the graph. Concentrations for incubation: SUV (5 mol-% DOPE-CAP-B + 95 mol-% DOPC) – 50 µg/ml, SAv – 20 µg/ml, biotinylated GAG (HS 33 kDa) – 10 µg/ml. The fifth overtone is presented here, data was qualitatively comparable across all overtones.*

2.1.4 Spectroscopic Ellipsometry

Spectroscopic ellipsometry (SE) is an optical technique that monitors changes in the properties of light as it is reflected off a surface (106-109). This technique is comparative with QCM-D as it can monitor model ECM formations and changes to the model ECM as a result of the interactions between the surface and other molecules. However, unlike QCM-D, SE results are not as sensitive to solvent effects and can provided more specific levels of analysis about surface components (106-109).

This technique relies on the specific properties of polarised light. The incidence light is linearly polarised, upon reflection from a surface the light becomes elliptically polarised (Figure 13). The light wave in linearly polarised light is in one plane that aligns with the direction of the light source, for elliptically polarised light, there are two light waves that are perpendicular to one another (110). This reflected polarised light can be defined by the ratio of its amplitudes and the phase difference in reference to the incident light. There are two ellipsometric angles which can be measured: Ψ, the amplitude ratio, and Δ, the difference in phase shift. By comparing the changes in Ψ and Δ for a surface that is bare and a surface with material in the form of a thin film, it is possible to extract the refractive index and thickness of the film (106-109).

In practice, reflection coefficients can be related to the two ellipsometric angles (106):

$$\frac{R_p}{R_s} = \tan(\psi)e^{i\Delta} \qquad [2.2]$$

where R_p and R_s are the reflection coefficients, sometimes referred to as the Fresnel coefficients, for light parallel and normal to the plane of incidence, respectively. These depend on the wavelength, the angle of incidence, and the properties of the reflecting surface (with its coating and surrounding medium). In practice, the extraction of the properties of the system is achieved by generating values for Ψ and Δ based on estimates of the refractive index and thickness of the film. This is an iterative process and is repeated until the generated values match the measured values from the experiment (106). A common method for calculating the optical properties is the Cauchy law, in which 3 different parameters can be varied and providing both thickness and optical properties nominally called A and B (108, 109, 111). In practice, this involves the building of an optical model of the surface, consisting of different layers each with a refractive index that is the same in all directions, termed optically isotropic. These models describe films that are optically transparent or Cauchy mediums, this fits well with buffer solutions and biomolecular layers. A Cauchy layer has parameters that can be defined including the refractive index and thickness. Using these parameters of each individual Cauchy layer, other information that can be gleaned including the areal mass density and molar surface densities (91).

Overall, SE can be applied to many studies on biomolecular interfaces, as different biomolecules and their interactions result in changes in the measured refractive index of the reflected light (Figure 13). It utilised to estimate the average distance between molecules on a surface (91), to determine the incorporation of proteins within thin films (104), and the calculation of dissociation constants (108).. Within this work, it has been used to characterise root mean square anchor distance of end grafted hyaluronan chains (see Chapter 4).

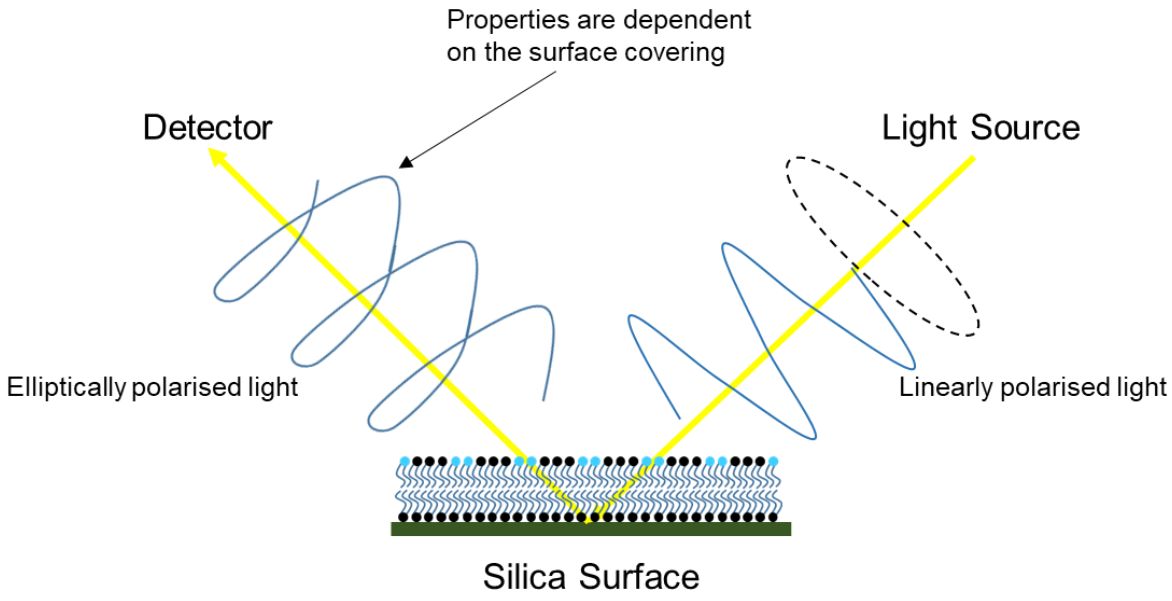


Figure 13. ***SE on Thin Flims.*** *Light passes from the source, through a quarter wave plate and becomes linear polarised light. It then passes through the film on the silica surface before reflection, upon which the light becomes elliptically polarised. Adapted from Ref. (107).*

2.1.5 Fluorescence Microscopy

Fluorescence microscopy is used in this work to observe distribution and movement of molecules including assessment of the homogeneity of SAv monolayers for film formation and the observation of fluorescently labelled biological colloids. Microscopy methods have frequently been applied in order to observe small scale structures through magnification (112, 113). Although this can provide a wealth of information, the specific form of microscopy utilised most throughout this body of work is fluorescence microscopy. This relies on fluorescent molecules; they have the ability to absorb and emit light of a specific wavelength. This is due to a phenomenon described in Figure 14, the Jablonski diagram, an electron in its ground state is capable of absorbing energy at a specific wavelength, and this causes the electron to jump to a higher state of energy. The electron gradually loses thermal energy until a photon is emitted, returning the electron to its ground state. The emitted light is always of a longer wavelength than the absorbed light. Therefore, these molecules are then visible under these defined wavelengths of excitation and emission. This phenomenon has been exploited to visualise typically nonvisible molecules by linking fluorescent molecules to proteins or other molecules of interest in order to be able to observe them in situations where they would not previously have been visible (112, 113).

Fluorescent molecules can be observed through epifluorescence or confocal microscopy by illumination with light at the excitation wavelength (112, 113). Epifluorescence microscopy (schematic

in Figure 14A) utilised a light source, usually a mercury lamp or a light emitting diode (LED), which passes through an excitation filter and beam splitter before illuminating the sample and emission from the sample is detected. Confocal microscopy (schematic in Figure 14B) utilises lasers as a light source, these are focused onto the sample. The light that is reflected passes through a pinhole lens and a pinhole before reaching the detector. The purpose of this is to remove out of focus light, reducing the light scatter that is captured in the image. A standard confocal microscope can reach diffraction limited resolution (approximately 250 nm). A further update to confocal microscopy called Airyscan, which uses an array of detectors, can further increase the resolution capabilities (112, 113).

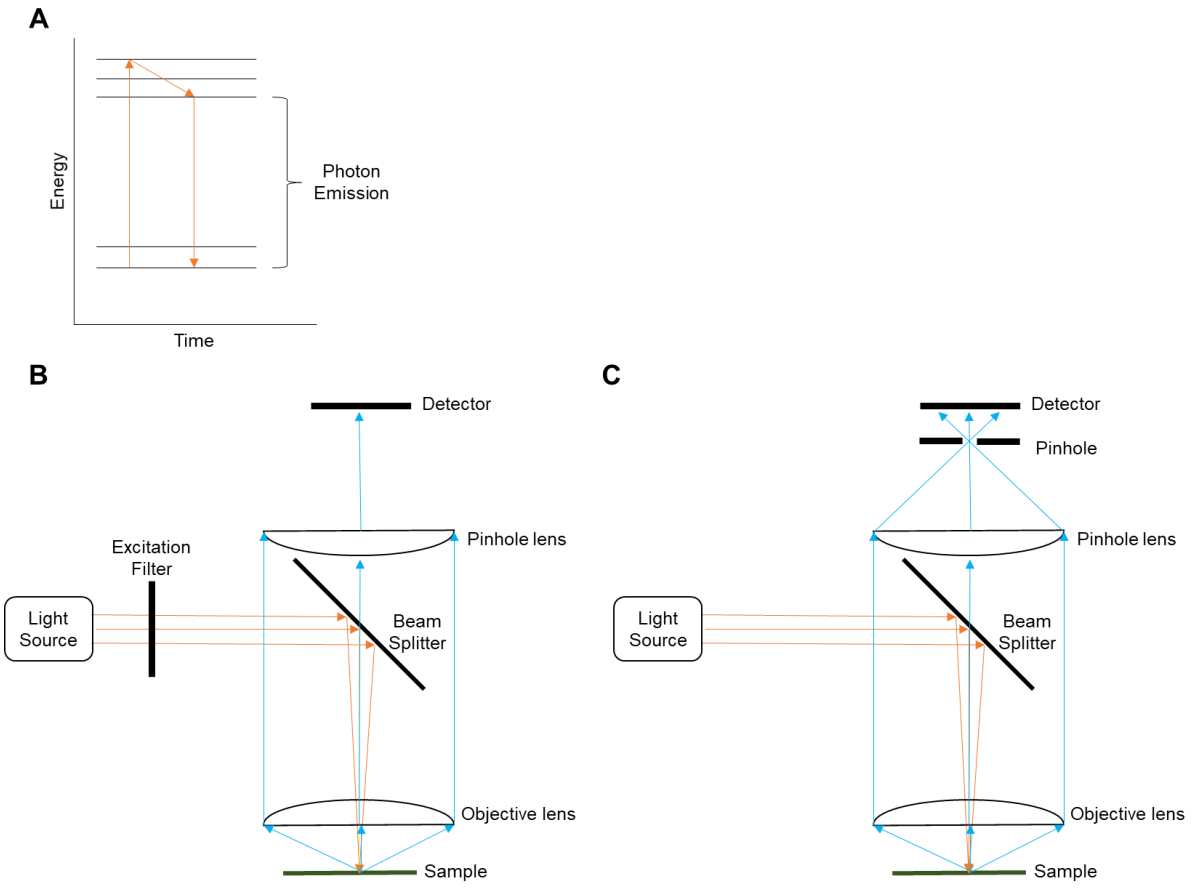


Figure 14. ***Principles and design of fluorescence microscopy.*** *A) The Jablonski diagram showing how molecules become excited, loose a small amount of energy and then return to their ground state by emitting a photon. B) The light path for epifluorescence microscopy. FC indicates filter cube. C) The light path for confocal microscopy. Adapted from (112, 113).*

2.1.5.1 Applications of Fluorescent Microscopy to Model ECMs

The model matrix described in Section 2.2.1 can be visualised in fluorescence microscopy due to the commercial availability of fluorescently labelled SAv (41). With the use of Fluorescent Recovery After Photobleaching (FRAP), it is possible to gather mobility information about the SAv and the other

molecules that it is attached to (114, 115). FRAP is a method in which a specific area of a surface with fluorescent molecules present is photobleached, resulting in a loss of fluorescence in that location (Figure 15). The phenomenon of photobleaching is due to the degradation of the fluorescent molecule. A fluorophore has a certain number of excitation/emission cycles that it can undergo before the molecule becomes degraded and can no longer fluoresce, resulting in the photobleached state. The degradation is a result of a chemical reaction that is dependent on the specific fluorophore. One example of a fluorophore degradation mechanism is a reaction with oxygen and the formation of reactive oxygen species (114, 115).

Monitoring the amount of fluorescence in the photobleached area over time gives an indication on the mobility of the fluorescent molecule. If the molecule is mobile, then the fluorescence intensity within the bleached area will recover over time. By tracking the fluorescence recovery over time, it is possible to extract a diffusion coefficient of the fluorescent molecule by using the diameter of the bleach area and the half time required for full recovery, called the Soumpasis method. Fluorescence intensity can be measured quantitatively (in arbitrary units, Figure 15B) allowing for the plotting of fluorescent recovery curves which enhance the mobility analysis of fluorescent materials. The data shown in Figure 15 is disc FRAP, the bleach region is circular, but line FRAP is also available. Line FRAP bleaches one line of an image of a defined width and length, typically the image acquisition involves only this line. This acquisition for line FRAP is much faster than disc FRAP which can be advantageous if the fluorophore under investigation is particularly mobile (114). FRAP has previously been performed on model ECMs in order to investigate if certain GAG binding molecules have properties which allow them to cross link GAGs and modify the ECM (38, 41, 100).

Single Particle Tracking (SPT) is the process of following a particle visible in microscopy images over time and extracting the mean square displacement (MSD) is another method of analysis for data acquired with fluorescent microscopy (116, 117). If a single fluorescent molecule is visible at the resolution that the images have been acquired at, it is possible to trace that molecule for a duration of sequentially taken images and extract how much the molecule has been displaced in the x-y plane (MSD). Specifically, the central coordinates of the particle for each frame are defined and the difference in position for a starting and finishing time point are calculated. These can be plotted as a function of time with the slope of this plot giving the diffusion coefficient (17, 116, 117).

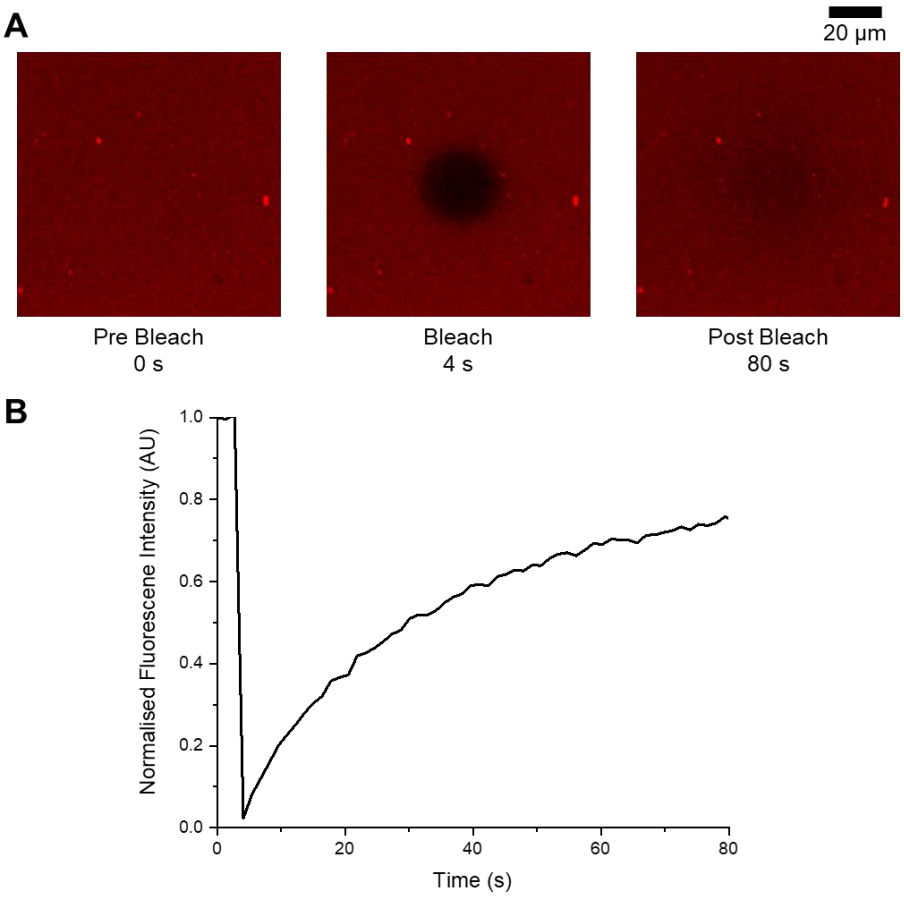


Figure 15. ***Fluorescence Recovery After Photobleaching.*** *A) Images of SAv-Atto-565 monolayer before and after photobleaching. The SAv monolayer is bound to an SLB consisting of 99.5:0.5 DOPC:DOPE-CAP-B molar ratio. B) A fluorescence recovery graph of the entire sequence of images represented in A. The Y axis is the normalised fluorescence intensity, setting the baseline fluorescence intensity as 1 and the bleached fluorescence intensity as 0.*

2.1.6 Reflection Interference Contrast Microscopy

Reflection Interference Contrast Microscopy (RICM) is a microscopy method that relies on the interference of light rays to provide spatial information about an object and the surface beneath it (118-120). An incident ray is projected onto the glass coverslip and the sample, a certain amount of light is reflected by the glass, but the remainder passes through and hits the sample, and this is again reflected (Figure 16). The two different rays of reflected light will interfere with each other, giving rise to an interference pattern. For spherical objects this is known as a Newtonian fringes (Figure 16). The given intensity of the interference can be represented as:

$$I = I_1 + I_2 + 2\sqrt{I_1 I_2}cos(2kh(x,y) + \phi) \qquad [2.3]$$

Where *I* represents intensity, I_1 and I_2 the reflection from the glass and the reflection from the sample respectively, *k* is a factor dependent on the refractive index and the wavelength, and φ is a phase shift. The most interesting factor here is *h(x,y)*, this is the height difference of the glass surface and the sample in accordance with its *(x,y)* position. This is how height information of an object can be obtained (118).

In practical terms, there are modifications to the standard microscopy set up in order to optimise RICM image acquisition and data extraction: an antiflex objective with an integrated rotatable quarter wave (λ/4) plate and a filter cube that contains crossed-polarisers (118, 120). Their purpose is to filter out any scattered light and resulting in the detection of only the reflected light. This is achieved by the light that has arrived at the objective (having already been linearly polarised before arrival) passing through the quarter wave plate and becoming circularly polarised. When the light is reflected back toward the objective, it will pass through the quarter wave plate again and become linearly polarised once more. Stray light is, therefore, not cross polarised and will not be detected, which enables a better quality image (118, 120).

Equation 2.3 does not contain any directly measurable factors, but can be modified, for spherical objects, in order to do so (121):

$$I(r) = A_1 e^{-\frac{r^2}{w_1^2}} + A_2 e^{-\frac{r^2}{w_2^2}} cos\left(\delta h(r) \frac{2\pi n_{buffer}}{\lambda} + \phi_0\right) \quad [2.4]$$

Where *r* is the distance from the bead centre, A_1 and A_2 are the amplitudes of the intensity at the centre of the sphere and the fringes, respectively, and w_1 and w_2 are factors that indicate how the amplitudes will decrease with the samples distance from the glass surface. $\delta h(r)$, the distance between the sample and the glass surface is then estimated through (121):

$$\delta h(r) \approx 2h(0) + \frac{r^2}{R} - \frac{3}{4}\frac{r^4}{R^3} \quad [2.5]$$

Where *R* is the radius of the spherical object.

RICM has been applied to study the distance of polystyrene beads from the surface that they are resting on; specifically, this can be used to calculate the height of polymer films grafted onto surfaces and hence other information that can be extracted from the height of such films (104, 121). Another application, is the calculation of gap heights from a hemispherical cap placed on a surface in Plane Sphere Confinement Microscopy (PSCM) (see Chapter 4) (122).

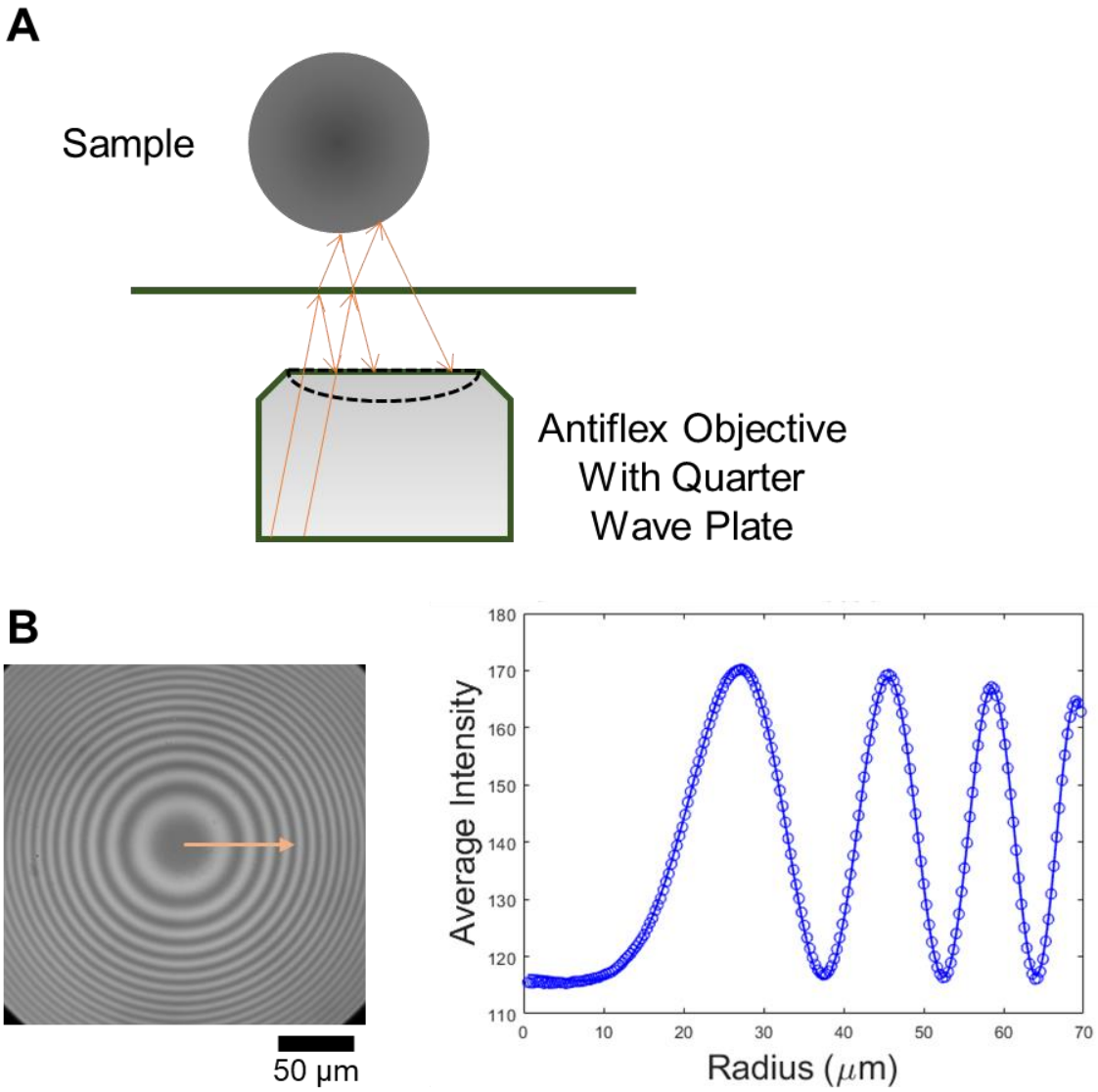


Figure 16. ***Reflection Caused By Spherical Objects.*** *A) Rays of light projected at the sample are reflected back and detected by the specific objective required for RICM. Adapted from (12). B) A 25 µm bead produces a Newtonian fringe pattern (left). From this, we can extract a radial intensity profile (right).The circles represent data points and the solid line the equation fit.*

Table 2. ***Summary of Techniques.***

Name	Abbreviation	Parameters Measured	Sensitivity
Quartz Crystal Microbalance with Dissipation Monitoring	QCM-D	Binding, Viscoelastic Properties	Senses binding to the surface and changes to properties of the film
Spectroscopic Ellipsometry	SE	Binding, Thickness, Areal Mass Density, Molar Surface Density	As QCM-D, but with increased sensitivity. Can estimate the number of molecules on a surface
Fluorescence Microscopy	N/A	Visualisation of Fluorescent Molecules	Can show the binding and structure of molecules on a surface
Fluorescence Recovery After Photobleaching	FRAP	Mobility of Fluorescent Molecules	Can show the movement of molecules on a surface
Single Particle Tracking	SPT	Mobility of Fluorescent Molecules	Can show the movement of molecules on a surface
Reflection Interference Contrast Microscopy	RICM	Distances (Height/Thickness)	Can determine height and thickness with 5 nm resolution

Chapter 3: Development of Model Glycocalyces and Labelling Glycan Binding Molecules - Advancements and Pitfalls

3.1 Introduction

The aim of this thesis is to generate a fluorescence microscopy based assay that will allow for the investigation into the diffusion of biological colloids (e.g. macromolecules and their assembly, and particles) within a glycosaminoglycan (GAG)-rich model matrix. This requires that the molecules of interest be labelled with a fluorescent tag that does not interfere with the salient GAG binding features of the macromolecule or particle and allows for the acquisition of good quality fluorescence microscopy data. It also requires a well-established ECM model designed to investigate the interactions between GAGs and colloids, in which the experiments will be performed.

A general model for an ECM selected for this study is well established for studies involving GAG binding proteins (38, 41, 88, 91, 93, 100, 101, 123). Details on its formation and features can be found in Section 2.1.1. Briefly, it consists of a supported lipid bilayer (SLB) with a certain molar percentage of biotinylated lipids, a streptavidin (SAv) monolayer, and a layer of end biotinylated GAGs or other glycans in order to capture the salient features of the ECM relevant to the parameters under investigation. The molar percentage of biotinylated lipids effects mobility of the bilayers and the number of binding sites for SAv. These matrices can be monitored by both QCM-D and microscopy and contained strictly defined parameters such as the number of GAG molecules on the surface and the mobility of these due to the addition of crosslinking agents or not, making them an ideal platform for study of the molecules that exist in the ECM (38, 41, 88, 91, 93, 100, 101, 123). This system allows for the generation of model ECMs with the same properties each time due to the homogeneity of the system. They contain multiple aspects that can be tuned, for example, the GAG type, its length and sulfation. This is controlled by the application of GAGs that have been purified and evaluated for their properties under stringent methods. The different types can be selected based on the question of interest. These films have been used routinely to study the interaction between GAGs and proteins, leading to the discovery of certain crosslinking molecules and which molecules may and may not bind the glycocalyx (38, 41, 100, 104, 124).

Within this chapter, new methods to better define specific aspects of the model matrices and to extract additional information are development. Specifically, the percentage coverage of molecules is modified to change the pore size of the matrix for large molecular weight HA, and the amount of GAG on the surface. The ECM is extremely heterogenous and therefore, the ability to replicate certain differences in the ECM in certain conditions is a desirable method in ECM research. For example, creating ECMs with HS with varying degrees of sulfation to reflect the changes in sulfation pattern of HS, as a consequence of the activity of sulfating enzymes such as Sulfs (27) would make it possible to study how interactions between different proteins and the ECM change under inflammatory conditions.

Chemokines are chemotactic cytokines, signalling proteins that distribute within different glycocalyces in order to perform their functions, including during development and in immune responses (45, 49). CXCL12α is a chemokine of 8 kDa and has a well defined relationship with heparan sulfate (HS) in terms of the mechanism of binding and the role of the interaction in CXCL12 function. It has previously been used in studies with the model ECMs to investigate the phenomenon of GAG crosslinking and the effects of oligomerisation of chemokines (41, 88, 100). These studies showed that the oligomerisation of CXCL12 increases its affinity to HS and results in the reduction in mobility of HS molecules within a model matrix. CXCL12 is a homeostatic chemokine that is involved in development of vascular and haematopoietic systems among others, mice with mutant CXCL12 resulting in a disrupted CXCL12-HS interaction have disrupted vasculature development (45, 47). CXCL12α is often used as a model chemokine due to its protein structure and interactions, with GAGs and with its canonical receptors, being typical of chemokines in general (47, 52). Understanding the way that CXCL12 is recruited and maintained at specific sites impacts on the understanding of homeostatic chemokine functions, such as the maintenance of hematopoietic stem cells within the bone marrow (125).

There is currently no known diffusion rate for CXCL12 in the ECM, highlighting the lack of research into this area. Although it has previously been investigated how the distribution of CXCL12 changes as its interaction with HS (52), implying that this interaction would have an effect on its diffusion, there have been no studies focused on this aspect of CXCL12. As one of the primary functions of chemokines is to direct cells to specific areas within organisms through a process called chemotaxis, this would require the diffusion of the molecule. The inability of CXCL12 to get to sites of injury results in poor wound healing (52). If the chemokine has not reached the site that it is required at, this indicates an aberration in the diffusion of the molecule. Understanding the diffusion of CXCL12 would provide insights into diseased and developmental states. Furthermore, as CXCL12 has a variety of isoforms which all bind heparan sulfate (HS) with different dissociation constants, it provides a variety of molecules to compare experimentally (46, 125, 126). Each isoform has additional amino acid residues added to its C terminus resulting in an increased affinity for HS, by comparing them, it would be possible to elucidate how the different residues alter the interaction with HS and consequently the diffusion coefficient of the molecule.

Shiga toxin B sub unit (STxB) provides another interesting case for diffusion in the ECM(71, 127). STxB is about 40 kDa and can be considered a model B type toxin, in the way that CXCL12 can be considered a model chemokine. Shiga toxin interacts with globotriaosylceramide (Gb_3) which is present on target cells and provides part of the mechanism for the toxin invasion. Gb_3 is a glycolipid that shares many similarities with glycosaminoglycans, namely that is contains a sugar moiety that consists of saccharide units (128). Until the toxin has bound Gb_3, it is diffusing through the extracellular matrix. Therefore,

the glycolipid must play a role in the way StxB diffuses and, therefore, a role in how the infection spreads inside an organism. The distance and speed with which STxB diffuses could be an indication of the mechanisms of the speed in which cells in a multicellular organisms are affected by the presence of STxB. Unlike CXCL12, it has been shown that STxB has fully reversible binding to a film displaying the sugar moieties of Gb_3, this would lead to a faster diffusion coefficient in a matrix containing this molecule (127). Therefore, if successfully labelled, STxB would make an interesting molecules to study in this context.

There are limited examples of commercially labelled proteins that bind GAGs, highlighting the difficulty in producing such material. However, this also provides a limit on the investigations possible. To date, there is no known investigation dedicated to the labelling of such molecules and the effect on their salient functions, and the production of them appears to be done on a case by case basis and usually not in the context of GAG binding. Highlighting the need for these techniques and investigations to be developed and made.

The first specific aim of this chapter are to generate model glycocalyces that can be used to investigate the diffusion of different permeation colloids. Firstly, colloids that interact specifically with glycans by altering and defining the types of glycans on the surface and the concentration of these motifs. Secondly, a glycocalyx of high molecular weight HA that has a specified pore size to allow the diffusion of large (tens of nm) colloids to be investigated. This was achieved with the techniques QCM-D and SE. The production of fluorescently labelled colloids was the second aim. The functionality of these colloids was tested in respect to their innate glycan binding capabilities and their nonspecific binding. Finally, the suitability of model colloids and model systems is investigated and the potential bias and influence these have on the interpretation of results.

3.2 Methods

3.2.1 Protein and Plasmid sources

Wild-type (WT) CXCL12α (8.1 kDa) was kindly provided by Professor Hugues Lortat-Jacob (Institut de Biologie Structurale, Grenoble, France). This was produced in BL21 (DE3) *E. coli* with a pET17b vector and purified by cation exchange and size exclusion chromatography with the purity assessed by mass spectrometry (126, 129). Polyhistidine (6× His) tagged CXCL12α (His-CXCL12α) (10 kDa) was produced and purified in house as detailed in Sections 3.2.3 and 3.2.4. CXCL12α with a C-terminal Alexa Fluor 647 tag (CXCL12α-AF647) (8.7 kDa) was purchased from Almac (Craigavon, Northern Ireland, UK).

Shiga toxin subunit B (STxB, 38.5 kDa) was kindly provided by Dr Laia Saltor Núñez and Professor Bruce Turnbull (University of Leeds, UK). STxB was expressed in BL21(DE3) *E. coli* already containing a vector, the protein was purified via affinity chromatography and purity assessed by sodium dodecyl-sulfate polyacrylamide gel electrophoresis (SDS PAGE) (127). Polyhistidine (6× His, located on the C terminus) tagged STxB (His-STxB) was kindly provided by enGenes Biotech GmbH (Vienna, Austria). His-STxB was produced in BL21(DE3) and enGenes-X-press V1 *E. coli* with pET30a-Cer and pSCS-T7×31 vectors (130), and purified by sequential nickel affinity chromatography and size exclusion chromatography, the latter was coupled with multi angle light scattering (MALS) and right angle light scattering (RALS) to assess the molecular weight of the construct. STxB exists as a pentamer in solution with a molecular weight of 45 kDa.

Wild-type streptavidin (SAv) and SAv labelled with an Atto 565 fluorophore (SAv-Atto565) were sourced from Sigma-Aldrich.

3.2.2 Protein Labelling

To obtain fluorescent STxB (STxB-AF488), STxB was labelled via primary amines with an NHS-Ester AlexaFluor 488 (Antibodies.com, Cambridge, UK) by Dr Laia Saltor Núñez following an established protocol (131). Briefly, protein stock was incubated with NHS-Ester AlexaFluor 488 in 5 times molar excess for 1 hour. A desalting column was used to remove excess dye from the solution. To assess the extent of labelling of STxB, High Resolution Mass Spectrometry (HRMS) was utilised in order to measure the differences in mass for the WT STxB and the labelled STxB-AF488. Differences in molecular mass indicated if the protein has been labelled and how many labels are present per monomer.

To obtain fluorescent CXCL12α, varied molar ratios of His-CXCL12α and Tris-NTA Oregon Green 488 (OG488) were added together and incubated at room temperature for 30 minutes. Following incubation, the mixture was used directly. Tris-NTA Oregon Green 488 was kindly provided by Dr Changjiang You and Professor Jacob Piehler (University of Osnabrück, Germany) (132).

3.2.3 Sub-cloning of DNA Constructs

The cDNA encoding CXCL12α was kindly provided by Professor Tracy Handel (University of California, San Diego, USA), and the cDNA encoding CXCL12γ was kindly provided by Professor Hugues Lortat-Jacob (Institut de Biologie Structurale, Grenoble, France), both in individual plasmids. cDNA was individually cloned into the same plasmid in order to ensure that the resulting proteins would have the same inserted amino acids at the N terminus. pRSET A (*Figure 17*) was chosen for cloning the CXCL12 constructs as it contains a hexahistidine (His_6) tag site. The restriction sites chosen for cloning were NcoI (CCATGG) at the 5' end (which can be seen in the multi cloning cite (MCS) in *Figure 17*) and NheI (GCTAGC) at the 3' end (not listed in the MCS, two codons down from the His_6 location). The gene sequences for both isoforms were amplified from their original plasmids by Polymerase Chain Reaction (PCR), 18 base pairs from the gene sequences were included in the primers with the final designs shown in Table 1.

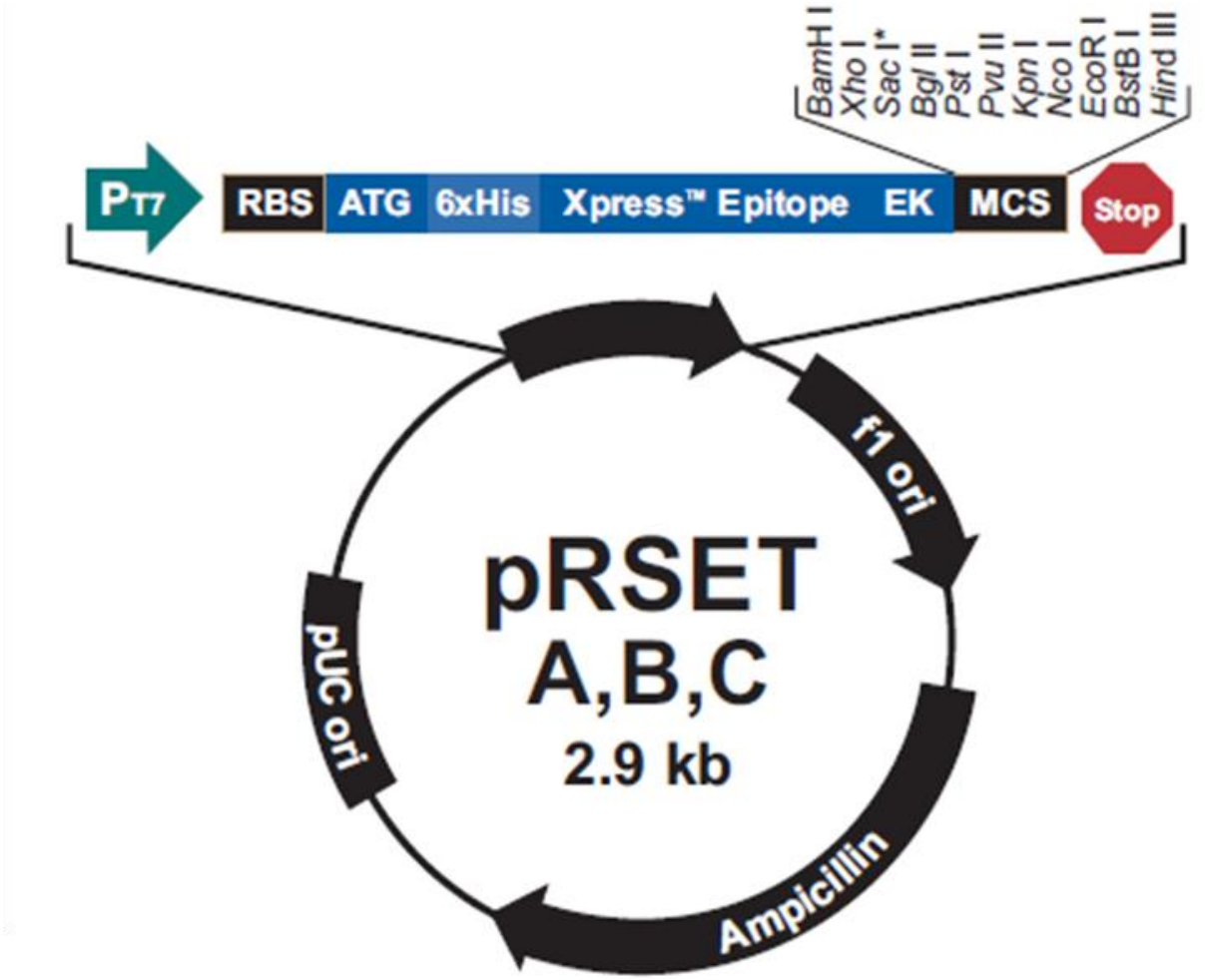


Figure 17. ***Map of Plasmid pRSET.*** *Indicated are the start codon (ATG), the His_6 tag (6xHis), the multi cloning site (MCS), listing some of the restriction enzyme sites (NheI is also present but not within the MCS, rather within the Xpress™ Epitope sequence), and the antibiotic resistance gene (ampicillin) in this bacterial plasmid. The different forms (A. B, and C) have different reading frames and results in slightly different lengths of the N terminus of the encoded proteins. Other features in this diagram include a promoter sequence sequence (P_{T7}), a ribosome binding site (RBS), an antibody detection site (Xpress™ Epitope), an enterokinase cleavage site (EK), a single stranded DNA rescue site (f1 ori), and a site to encourage high replication and growth rate in E. coli (pUC ori). Taken from Ref. (133).*

Table 3. ***Primers for CXCL12 Isoforms.*** *Red indicates the NheI restriction site, green indicates the NcoI restriction site, and the blue bases were added for efficiency in cutting with the restriction enzymes.*

Primer Name	**Sequence (5' to 3')**
CXCL12α forward	GGTGCTAGCATGAAACCGGTGAGCCTG
CXCL12α reverse	ACCCCATGGTTATTTGTTCAGCGCTTT
CXCL12γ forward	GGTGCTAGCATGAAACCAGTCAGCCTG
CXCL12γ reverse	ACCCCATGGCTAGTTTTTCCTTTTCTG

3.2.3.1 Polymerase Chain Reaction (PCR)

PCR was performed according to the Phusion® polymerase protocol from Thermo Fisher (134), annealing temperatures for each primer (Table 2) were calculated using the T_m calculator from Thermo Fisher (135). Following PCR, the samples were loaded onto a 1% agarose gel (with SYBER green (Thermo Fisher)) for visualisation and purification (Section 3.2.3.4 and 3.2.3.5). Purification was performed using a gel extraction kit from Qiagen™ following the manufacturer's instructions. Concentration and purify were measure using NanoDrop spectrometer.

*Table 4***. Annealing Temperatures for PCR Amplifications of CXCL12 genes.**

Gene Name	**Annealing Temperature (˚C)**
CXCL12α	70.3
CXCL12γ	68.4

3.2.3.2 Restriction Digest

Circular plasmid digestions were performed with 10 units of restriction enzymes, NheI and NcoI (New England Biolabs) and 1× CutSmart buffer (50 mM potassium acetate, 20 mM Tris-acetate, 10 mM magnesium acetate, 100 µg/ml bovine serum albumin (BSA), pH 7.9; New England Biolabs). 1 µg of pRSET A or 250 ng of PCR product were used for the digestion mixtures. The final volume of the reaction mixture was 25 µl. The reaction was performed at 37 ˚C for 1 h and then incubated at 80 ˚C for 20 minutes for enzyme inactivation. To prevent re-ligation, the plasmid digestion mixture was treated with alkaline phosphatase. 0.5 units of calf intestine alkaline phosphatase (Promega) was added to the digestion mixture, along with 1× alkaline phosphatase buffer (50 mM Tris-HCl, 1 mM $MgCl_2$, 0.1 mM $ZnCl_2$, 1 mM spermidine, pH 9.3; Promega). This was then incubated at 37 ˚C for 30 minutes. The reaction mixture was then loaded to an agarose gel for visualisation and purification (Section 3.2.3.4 and 3.2.3.5).

For diagnostic digest following DNA produced from minipreps, 5 units of enzymes and 750 ng of DNA were used in a 10 µl volume to test for positive plasmid clones. All other components were the same as stated previously.

3.2.3.3 Ligation Reaction

50 ng of purified digested vector and 125 ng of digested PCR product were added to 1 unit of T4 DNA ligase (Labolan) and T4 DNA ligase buffer (50 mM Tris-HCl, 10 mM MgCl2, 1 mM ATP, 10 mM DTT, pH 7.5; New England Biolabs). The mixture was incubated at room temperature for 3 h followed by a 10 min incubation at 65 ˚C. 5 µl of the reaction mixture was then transformed into competent cells.

3.2.3.4 Agarose Gel Electrophoresis

1 % (w/v) agarose gels were produced by adding 0.5 g agarose (Thermo Fisher) to 50 ml TAE buffer (40 mM Tris, 20 mM acetic acid, 1 mM EDTA; Lonza), the mixture was heated to allow the agarose to dissolve in the solution. SYBER green was added to the gel in order to stain the DNA for visualisation. DNA loading dye (New England Biolabs) was added to samples before loading them on the gel. Gels were run at 125 V in 1× TAE buffer on a Bio-Rad agarose gel apparatus until the loading dye reached the bottom. DNA in the gel was visualised using a Blue Light Transilluminator (Syngene). DNA was purified from agarose gels using a QIAquick Gel Extraction Kit (QIAGEN) (136). DNA concentration was measured using a Nanodrop 2000c Spectrophotometer (Thermo-Fisher Scientific) using Beer's Law and a mass extinction coefficient of 50 ng/µl cm^{-1}.

3.2.3.5 DNA Mini Preparations: Plating, Selections, and Culture

Ligation reactions were transformed into DH5α *E. coli* cells and plated onto LB agar plates containing 100 µg/ml ampicillin and grown at 37 ˚C overnight. Individual, isolated colonies were selected and transferred to 5 ml Lysogeny Broth (LB, Thermo Fisher Scientific) cultures. Miniprep cultures were grown overnight in a shaking incubator at 37 ˚C at 220 rpm. Bacteria were harvested in a benchtop micro centrifuge at 10,000 × *g* for 3 min. Plasmid DNA was isolated using a QIAprep Miniprep Kit (Qiagen) following the provider's instructions (137). DNA concentration was measured using a Nanodrop 2000c Spectrophotometer. Sequencing was performed by GeneWiz (Leipzig, Germany). 20 µl samples of 75 ng/µl of DNA were sent for sequencing with a T7 promoter primer.

3.2.4 Protein Production

Protein expression and production were performed in *E. coli* competent cells, followed by extraction from inclusion bodies in a denatured state and protein purification used nickel affinity chromatography. Proteins were refolding after the purification process.

The protein expression for the DNA constructs produced in Section 3.2.3 were as follows. Plasmids were transformedinto BL21 DE3 *E. coli* cells, single colonies selected and seeded into 10 ml starter cultures in LB with the same ampicillin concentration as above, and grown overnight at 37 ˚C with

shaking at 220 rpm. The culture was transferred into 100 ml LB and grown under the same conditions as the overnight cultures until OD_{600} reached a value of approximately 0.6. IPTG at 0.5 mM was used to induce protein expression and the culture was grown at these conditions for 3 hours.

From this point on purification was the same for all plasmids products. Bacteria were harvested by centrifugation at 6,500 × *g* for 15 min at 4 ˚C. The pellet was resuspended in lysis buffer (50 mM Tris (Sigma-Aldrich), pH 7.5, 300 mM NaCl (Sigma-Aldrich), 1% v/v Triton X-100 (Sigma-Aldrich)) and lysed by sonication for 4 min (duty cycle 2 s on / 8 s off) at 60% power. The resulting solution was centrifuged at 6,500 × *g* for 20 min at 4 ˚C. The supernatant was discarded, the resulting pellet resuspended in lysis buffer, and the above centrifugation was repeated. The resulting pellet was then resuspended in wash buffer (50 mM Tris, pH 7.5, 300 mM NaCl, 5% v/v Triton X-100) and centrifuged for 30 min at 6,500 × *g* and 4 ˚C. After discarding the supernatant, solubilisation of the inclusion bodies in the pellet was performed by resuspension in equilibration buffer (50 mM Tris, pH 8, 6 M guanidine hydrochloride (Gdn HCl; Sigma-Aldrich), 4 mM DTT (Sigma-Aldrich), which served to unfold proteins) and overnight incubation at 4 ˚C with constant agitation. This was followed by centrifugation at 8,000 × *g* for 30 min at 4 ˚C. Nickel affinity chromatography was then performed with Roche cOmplete His-Tag Purification Resin (Sigma-Aldrich), equilibrated with 10 times the resin volume of equilibration buffer. Once the solubilised inclusion bodies were passed over the column, the contents of the column were washed with 10 times resin volume wash buffer (50 mM MES (Sigma-Aldrich), pH 6, 6 M Gdn HCl, 4 mM DTT). Protein was eluted with elution buffer (50 mM acetate (Sigma-Aldrich), pH 4, 6 M Gdn HCl, 4 mM DTT) in 1 ml fractions.

Elution fractions (analysed with SDS PAGE) with the highest amount of CXCL12α were added dropwise to 10 times the volume of the combined elution fractions of refolding buffer (50 mM Tris, 500 mM arginine-HCl (AppliChem, Darmstadt, Germany), 1 mM EDTA (Sigma-Aldrich), 1 mM oxidised glutathione (Sigma-Aldrich), pH 7.5), this mixture was incubated at room temperature for 1 hour with gentle stirring. The refolding mixture was dialysed against 5 L of 20 mM Tris, 50 mM NaCl, pH 8 at 4 ˚C for 3 cycles of 8 hours. The resulting solution was centrifuged at 8,000 × *g* for 30 min to remove precipitated protein. The protein solution was then concentrated to a suitable concentration and amount using Pierce Protein Concentrator PES (Thermo-Fisher Scientific, Gloucester, UK) with a 3 kDa molecular weight cut off. Protein concentration was measured using a Nanodrop 2000c Spectrophotometer.

Samples collected from all steps throughout the protein purification process were analysed by sodium dodecyl sulfate polyacrylamide gel electrophoresis (SDS PAGE), this was performed with 12.5% Mini-PROTEAN TGX Precast Protein Gels (Bio-Rad, Watford, UK). Samples were mixed with 4 times volume

ratio of loading dye (250 mM Tris, 10% w/v SDS (Carl Roth, Karlsruhe, Germany), 0.008% bromophenol blue (Sigma-Aldrich), 5% β-mercaptoethanol (Sigma-Aldrich), 40% glycerol (Sigma-Aldrich)). Fractions containing 6 M Gdn HCl were diluted to 2 M with ultrapure water before the addition of loading dye to prevent the Gdn HCl from affecting the electrophoresis of the polypeptides. SeeBlue Pre-stained Protein Standard (Thermo-Fisher Scientific) was used as molecular weight markers. Gels were run at 30 mA in SDS Running Buffer (192 mM Glycine (Sigma-Aldrich), 25 mM Tris, 0.1% w/v SDS) until the loading dye was at the bottom of the gel, using a Bio-Rad SDS PAGE apparatus. The gel was then removed and washed in ultrapure water to remove residual SDS, and transferred to InstantBlue Protein Stain (Expedeon, Cambridge, UK) solution for 20 min with agitation at room temperature. Images of gels were obtained by scanning using a printer.

3.2.5 Production of Small Unilamellar Vesicles (SUV)

SUVs were made using a previously established protocol (92). The procedure consists of creating a mixture of desired lipids at a specified ratio in a suitable organic solvent to ensure homogenisation of the lipid mixture, followed by removal of the solvent, resuspension in aqueous solution and generation of small unilamellar vesicles via sonication. SUVs were made in two different ratios: 5 mol.% and 0.5 mol.% 1,2-dioleoyl-sn-glycero-3-phosphoethanolamine-N-(Cap Biotinyl) (DOPE-CAP-B) in a 1,2-dioleoyl-sn-glycero-3-phosphocholine (DOPC) background. These lipids were obtained as powders from Avanti, (Alabama, USA).

Lipid stock solutions in chloroform were prepared by adding approximately 1 ml of chloroform (Sigma-Aldrich) to the lipid powder. The concentrations were then calculated as follows:

$$V_{\mathrm{chloroform}} = \frac{m_{\mathrm{lipid\,+\,solvent\,+vial}} - m_{\mathrm{vial}} - (m_{\mathrm{lipid\,+\,box}} - m_{\mathrm{box}})}{\rho_{\mathrm{chloroform}}}, \quad [3.1]$$

$$C = \frac{m_{\mathrm{lipid\,+\,box}} - m_{\mathrm{box}}}{V_{\mathrm{chloroform}}}. \quad [3.2]$$

In Equations [3.1] and [3.2] the index 'vial' indicates the glass vial used for storage and the index 'box' indicates the glass bottle that the powdered lipid was provided in. This allows for the calculation of the exact solution volume $V_{\mathrm{chloroform}}$, and ultimately, the mass concentration C of the lipids. Chloroform lipid stocks were stored at -20˚C.

To make mixtures of defined lipid ratios, appropriate volumes of lipid stocks were calculated from the concentrations of the lipid stocks and the molecular weight of the lipids. The corresponding volumes were added to a glass tube and briefly mixed. Nitrogen gas was then gently blown into the tube while rotating it, to evaporate most of the solvent and to deposit a thin homogenous lipid film on the wall of the tube. The tube was then placed in a vacuum for a minimum of 1 hour to remove residual solvent. Then, an appropriate volume of HEPES buffered saline (HBS) (10 mM HEPEs (Sigma-Aldrich), 150 mM

NaCl, pH 7.4) was added to reach the desired lipid concentration. The lipid dispersion was then homogenised by 5 cycles of vortexing, freezing (in dry ice) and thawing (in warm water, approximately 40˚C). The homogenised lipid solution was then sonicated (with a tip sonicator, Fisher Scientific, Loughborough, UK) for 30 min (duty cycle 1 s on / 1 s off) at 70% power on ice water. After sonication, the solution was clear indicating that small unilamellar vesicles had been formed from the larger vesicles. This was followed by centrifugation at 15,000 × *g* in a bench top microcentrifuge for 10 minutes to remove any metal particles from the sonicator tip. The supernatant was then stored as 0.5 ml aliquots in Eppendorf tubes, topped up with nitrogen gas, at 4˚C.

3.2.6 Production of Extruded Unilamellar Vesicles (EUVs)

Liposomes were made in accordance with Section 3.2.5 consisting of 89 mol-% DOPC, 10 mol-% DOPS (Avanti) and 1 mol-% 2-(4,4-difluoro-5,7-dimethyl-4-bora-3a,4a-diaza-s-indacene-3-dodecanoyl)-1-hexadecanoyl-sn-glycero-3-phosphocholine (beta-BODIPY FL C12-HPC) (Life Technologies, Carlsbad, CA, USA). Liposomes were extruded with an Avestin Liposome Extruder (Avestin, Ottawa, Canada) through track-etch membranes of 50 nm or 30 nm pore size (Whatman, Maidstone, UK). These EUVs were generated by Dr Ralf P Richter.

3.2.7 Model Glycocalyx Formation

3.2.7.1 Surface Functionalisation for Anchorage of Biotinylated Glycopolymers

Films of biotinylated glycopolymers can be formed on silica coated QCM-D sensors (QSX303; Biolin Scientific, Västra Frölunda, Sweden), silicon SE wafers (University wafer, Boston, MA, USA), and glass coverslips (VWR, Radnor, PA, USA) (Piranha treated, 24 × 24 mm^2, #1.5). Surfaces were cleaned before addition of any reagents (see Sections 3.2.8 and 3.2.9). Surface functionalisation involves the formation of an SLB by applying SUVs with a defined percentage of DOPE-CAP-B in a DOPC background, addition of streptavidin forming a layer on top of the SLB, and the addition of a biotinylated molecule. Formation of these surfaces is explained in Section 2.2.1. SUVs were prepared as detailed in Section 3.2.5. For optical microscopy assays, SAv-Atto565 was used in place of plain SAv, to facilitate visualisation by fluorescence microscopy. Final concentrations of each component are listed in Table 3. On glass surfaces, concentrations were doubled in order to increase the binding rate in stagnant solution (88, 91).

Glycopolymers containing a backbone consisting of disaccharide groups can be biotinylated on the reducing end via oxime ligation (93). Biotinylated glycopolymers are generated by creating a reaction mixture of 5 mg/ml of glycopolymer, 50 mM sodium acetate, 20 mM aniline (Sigma), and EZ-link alkoxyamine PEG4-biotin (Thermo Fisher) in 3 times molar excess of the glycopolymer. The molar concentration of the glycopolymer was estimated from the concentration in mg/ml and the nominal molecular weight of the sample. The purpose of the sodium acetate is to act as a coupling buffer and

the analine can act as a hydrogen acceptor. This mixture was incubated overnight at 37 ˚C with 300 rpm in a thermomixer. The resulting solution was purified by Size Exclusion Chromatography (SEC) using Sephadex G-25 (5 kDa molecular weight cut-off) as the column medium. Elution fractions from this medium were tested by QCM-D to identify the fractions with the highest concentration and purity. This method has been validated to produce biotinylated glycopolymers without excess biotin in the solution (101). The use of the oxime ligation as opposed to hydrazone ligation is the increased stability of the resulting molecules in aqueous solution (93).

3.2.7.2 Anchorage of Biotinylated Glycopolymers to Form Model Glycocalyx Films

HA films were assembled as described in (101, 121). HA-b was quasi-monodispersed with sizes of 280, 520, and 840 kDa and provided by Hyalose (Oklahoma City, OK, USA). The HA was produced as described previously (138). HA-b was applied to a SAv monolayer at 20 µg/ml and the root mean square anchor distance was calculated via the areal mass density from spectroscopic ellipsometry ellipsometry data (Section 3.2.10).

HS films were assembled as described in Migliorini *et al*. (88). HS-b was applied to the SAv monolayer at the concentration specified in Table 3. Different batches of biotinylated HS were used: some 12 kDa HS was biotinylated and kindly provided by Dhruv Thakar (CNRS, Grenoble, France), further 12 kDa HS and also 33 kDa HS was biotinylated by myself with MBiol project student Jelizaveta Pavljuk (University of Leeds, UK), as described in Section 3.2.7.1. The polydispersity of both HS samples was 1.6, for 12 kDa HS there were 1.4 sulfates per disaccharide as measured by Dr Dhruv Thakar.

End-biotinylated HA-*g*-Gb_3 was produced by Dr Laia Saltor Núñez by grafting Gb_3 molecules to an HA chain via a copper-catalysed azide-alkyine cycloaddition between HA-*g*-propargyl and Gb_3-N_3 (127). Gb_3-N_3, a trisaccharide containing one glucose and two galactose molecules with an azide on the primary carbon of the glucose, was synthesised enzymatically from Lactose-N_3 and UDP-glucose with a glucose epimerase and a galactosyltransferase. HA-*g*-propargyl is hyaluronic acid with propargylamine attached via the carboxyl group of glucuronic acid, which provides a reactive alkyne for the click reaction. The HA-*g*-propargyl had a molecular weight of 140 kDa, and a polydispersity of 1.03. The copper-catalysed azide-alkyine cycloaddition reaction was performed with a mixture of copper sulfate, Tris((1-hydroxy-propyl-1H-1,2,3-triazol-4-yl)methyl)amine (THPTA), sodium ascorbate, HA-*g*-propargyl and Gb_3-N_3. The degree of substitution of the Gb_3-N_3 onto the HA was 35%. The chemical composition of products and intermediates were verified with proton NMR. HA-*g*-Gb_3 was biotinylated on the reducing end as described in Section 3.2.7.1. The resulting HA-*g*-Gb_3 had 30 disaccharide units and a molecular weight of 89 kDa. The final product was applied to the SAv monolayer at the concentration specified in Table 3.

Table 3. **Concentrations of Reagents for Glycocalyx Film Formation.** Each component of the model matrix was added to generate the final concentrations listed in the table below. These concentrations were selected due to the ability of the molecules to saturate the surface at this concentration within an appropriate time period. HA concentrations were selected to achieve specified surface density within selected times.

	On Silica surface (for QCM-D or SE analyses)	**On glass surface (for microscopy analyses)**
SUV	50 µg/ml	100 µg/ml
SAv	20 µg/ml	40 µg/ml
HS-b	10 µg/ml	10 µg/ml
b-HA-*g*-Gb$_3$	20 µg/ml	N/A
HA-b	20 µg/ml	20 µg/ml

3.2.8 Quartz Crystal Microbalance with Dissipation Monitoring (QCM-D)

Silica coated QCM-D sensors (QSX303; Biolin Scientific, Västra Frölunda, Sweden) were incubated in 2% w/v SDS for at least 30 minutes, thoroughly rinsed with water, blow dried with nitrogen gas, and treated in a UV/ozone chamber for 30 minutes before being placed into the QCM-D chambers. Measurements were obtained at room temperature using the Q-Sense E4 System with each sensor inside an individual Flow Chamber (Biolin Scientific). The flow rate of 20 µl/min was generated with a syringe pump (Legato; World Precision Instruments, Stevenage, UK) in a working buffer of HEPES buffered saline (HBS; 10 mM HEPES, 150 mM NaCl, pH 7.4). To ensure accurate and high quality measurements and to obtain baseline measurements, data were acquired at the fundamental (*n = 1*) and all overtones (*n = 3, 5, 7, 9, 11, 13*) prior to the beginning of the experiment. Data were acquired over these overtones throughout the course of the experiment. Before and between additions of materials for the formation of the model extracellular matrix, the surface was washed with HBS for 10 minutes. Each component was added for 15 minutes, or until an equilibrium was reached.

In cases where an alternative QCM-D set up was used with a peristaltic pump (IPC; Ismatec, Germany) (Figure 28), all other methods remained the same.

Q-Sense DFind (Biolin Scientific) software was used for data analysis. Figures were generated in OriginPro 2019b (OriginLab Corporation). Measurements were taken over all overtones, but the fifth overtone (*n = 5*) is presented here. Data was qualitatively comparable between all overtones.

3.2.9 Optical Microscopy

Glass coverslips 24 × 24 mm^2, #1.5 (VWR) used for confocal microscopy were Piranha treated, a 1:3 (*v*/*v*) mixture of hydrogen peroxide and concentrated sulfuric acid for 1 h at 100 ˚C, before rinsing with ultrapure water and drying with nitrogen gas. Immediately prior to use the slides were exposed to

UV/ozone for 30 minutes and attached to a Teflon base, containing four holes of 1 cm diameter, using Twinsil glue (Picodent, Wipperfürth, Germany). This creates four 50 µl wells on the Teflon base in which different types of functionalised surfaces can be formed. The Teflon base was cleaned prior to use by sonication in ultrapure water for 10 minutes and 100% Ethanol (Thermo Fisher Scientific) for 10 minutes, then blow dried with nitrogen gas. After the incubation of individual components, the glass surface was rinsed with HBS 10 times with 100 µl.

Confocal images were obtained at the University of Leeds Bioimaging Facility using a Zeiss LSM880 Inverted + Airyscan Confocal microscope and ZEISS ZEN microscope software. The objective typically used was a Plan-Apochromat 40×/1.4 Oil DIC M27. OG488•HisCXCL12α was excited with the 488 nm laser at 5% of maximal intensity. The pinhole size was set to 198 µm, corresponding to 5 Airy units. Airyscan images were obtained with the Plan-Apochromat 63×/1.4 Oil DIC M27 objective, and the pinhole set to 2.55 Airy units.

Epifluorescence images were obtained using a Zeiss Axio Observer 7 with an EC Plan NeoFluar 63x/1.25 Ph3 Antiflex Oil Objective. Sav-Atto565 was excited using the LED-module 555 nm with the 90 HE DAPI/GFP/Cy3/Cy5 reflector. OG488•HisCXCL12α was excited using the LED-module 475 nm with the 38 HE GFP reflector. Both had a scaling factor of 0.103 µm per pixel. Camera binning was 1,1.All microscopy images were analysed in Fiji (139).

3.2.10 Spectroscopic Ellipsometry (SE)

SE measurements were performed on pieces of cut silicon wafers (3×20 mm^2) in a custom-made open cuvette (approximately 100 µl volume) with glass windows using a spectroscopic rotating compensator ellipsometer (M-2000V; J. A. Woollam, Lincoln, Nebraska, USA). The custom made cuvette had an open top to allow for sample injection by pipette and stirring was achieved by a magnetic stirrer. It also contained inlet and outlet tubing attached to a peristaltic pump (IPC; Ismatec, Germany). Ellipsometric angles, Δ and Ψ, were acquired over the wavelength range λ = 370 to 1000 nm. The plane of incidence was horizontal and the angle of incidence was 70°.

Silicon wafers were treated in a similar way to QCM-D sensors with an incubation in 2% w/v SDS and UV/Ozone treatment (see Section 3.2.8). Samples were incubated on the silica surface within the cuvette in an HBS working buffer. Immediately following sample injection, the solution was typically stirred for 5 seconds with the remainder of the incubation being completed in still solution. This was to ensure even distribution of the material throughout the solution without causing any materials to loose functionaility. During the injection of SUVs, the solution was stirred throughout the entirety of the incubation period. Following sample incubation, the surface was rinsed, with stirring, with HBS at a rate of 5 ml/min using the peristaltic pump.

SE was used to quantify the surface density of HA-b in model glycocalyx films. SE data was acquired and analysed using CompleteEASE software (J. A. Woollam, Lincoln, NE, USA). Measured values for angles Δ and Ψ were related to the optical properties of the film as described in (91, 140). Briefly, data were first acquired in bulk solution on the plain silicon wafer (with native oxide film), to determine the optical properties of this surface. The native oxide film was treated as a Cauchy medium with a refractive index $n_{oxide} = A_{oxide} + B_{oxide}/(\frac{\lambda}{\mu m^2})$, where A was an adjustable parameter and B was set to 0.01591. The thickness was found to be 0.95 ± 0.03 nm and A was found to be 2.45 ± 0.14. The bulk solution was also treated as a transparent Cauchy medium with a refractive index: $n_{solvent}(\lambda) = 1.325 + 0.00322/(\frac{\lambda}{\mu m^2})$. The optical properties of the silica were then fixed for the analysis of subsequent binding processes. The biomolecular film on the silicon wafer was modelled as two optically isotropic layers; the first (index 1) encompassing the supported lipid bilayer and SAv monolayer, and the second (index 2) the hydrated HA brush. Each of the two layers was treated as a Cauchy layer with a thickness ($d_{1|2}$) and a refractive index ($n_{1|2}(\lambda) = A_{1|2} + B_{1|2}/\lambda^2$), where $A_{1|2}$ and $B_{1|2}$ are the Cauchy parameters. For both layers, parameter B was equal to the value of B in bulk solution ($B_{1|2} = B_{\mathrm{sol}} = 0.00322$). For the SLB-SAv layer, A was set to 1.4, which is a typical value for biomolecular films, and the thickness d_1 was the only adjustable parameter. This approach provided for robust fitting of thin (<10 nm) films. After fitting of the first layer, the values were fixed before fitting the second layer. For the HA layer, A_2 and d_2 were adjustable parameters. The areal mass density (*AMD*) was calculated with de Fejter's equation: $AMD = d(A - A_{\mathrm{sol}})/(\mathrm{d}n/\mathrm{d}c)$, where d*n*/d*c* is the refractive index increment (Table 4 (140)). The *AMD* was converted to molar surface density (Γ) by dividing by the molecular weight of the species: $\Gamma = \frac{AMD}{\mathrm{HA}\ M_w}$. This can then be converted to Root Mean Squared (RMS) anchor distance (d_{rms}) by $d_{\mathrm{rms}} = \frac{1}{\sqrt{(\Gamma \times \mathrm{N_A})}}$, where $\mathrm{N_A}$ is Avogadro's number. For films of these thickness, the RMS anchor distance can be taken as approximately equal to the mesh size of the film (141).

Table 4. **Refractive Index Increments for Different Layers in SE.** The d*n*/dc value for SAv is valid for most proteins to a good approximation.

	d*n*/d*c* (cm³/g)
Lipids	0.169
SAv	0.18
HA	0.15

3.2.11 Calculation of the Number of Disaccharides from QCM-D Data

The number of disaccharides was estimated from the Δ*D*/-Δ*F* ratio for QCM-D data from the 5th overtone at a coverage of Δ*F* = -2.5 Hz, as established in Reference (101), as follows:

$$n_{\mathrm{ds}} = \frac{\Delta D}{-\Delta f} \Big/ \frac{10^{-6}}{\mathrm{Hz}} \times \left(37.15 \frac{\mathrm{Hz}}{10^{-6}} \frac{\Delta D}{\Delta f} + 23.38\right) \frac{12.53 + \left(3.259 \frac{\mathrm{Hz}}{10^{-6}} \frac{\Delta D}{\Delta f}\right)^{-6.775}}{1 + \left(3.259 \frac{\mathrm{Hz}}{10^{-6}} \frac{\Delta D}{\Delta f}\right)^{-6.775}} \quad [3.3]$$

3.3 Results

3.3.1 Creating Bespoke Model Glycocalyces

This project revolves around the production of methods to trace diffusion of macromolecules in the ECM and investigate the factors within the matrix that impact on diffusion. In order to achieve this goal, the formation of thin films on surfaces that recapitulate the main features of the ECM within a glycocalyx model with defined grafting density and length of specified GAGs were used. These types of films are well documented in the literature (88, 91, 93, 101, 141), within this section, these techniques have been utilised to design and produce films that resemble the glycocalyx.

3.3.1.1 Modelling an HS Glycocalyx to Probe Diffusion of Proteins Binding to Sulfated GAGs

The first step was to reliably produce an HS film and to produce more biotinylated HS of good quality. Figure 18 shows the formation of an HS film. SUVs were applied to the surface and accumulate, reflected by a rapid decrease in frequency shit (-60 Hz), a critical mass is reached and causes the vesicles to rupture generating an SLB, increasing the frequency shift to -25 Hz. The dissipation increases to 3.5 ppm during the vesicular accumulation on the surface due to the inherent flexibility of a vesicular layer. After formation of an SLB, the dissipation falls to ≤ 0.5 ppm. These values are well aligned with the established process of SLB formation on silica surfaces showing that a continuous quality bilayer has been formed (92). The addition of SAv causes the frequency to fall by a further 25 Hz and an initial increase in dissipation of 1 ppm, decreasing to a final value of 0.6 ppm. This is the expected frequency shift for SAv binding to a film containing 5% biotinylated lipids (88). The stability of the frequency and dissipation shifts during the rinsing period indicate the stability of the surfaces. The decrease in frequency upon binding of HS-b to the SAv monolayer is 15 Hz. When comparing this value to that achieved on a comparable surface of SAv on SLB with a HS-b material with the same source and nominal molecule weight, it falls below the expected value of 33 Hz (88). Although the concentration of HS-b for the reference material was five times greater both final frequency shifts were reached within the first 5 minutes of the incubation period indicating that the surface was fully saturated within this time period and that an increased concentration would not have led to a larger decrease in frequency in Figure 18. The age of the HS-b used in this experiment was approximately 4 years, therefore, it is a possibility that the HS-b had degraded over time, causing a smaller change in frequency. This could be due to the HS chains becoming shorter leading to an alternative molecular weight.

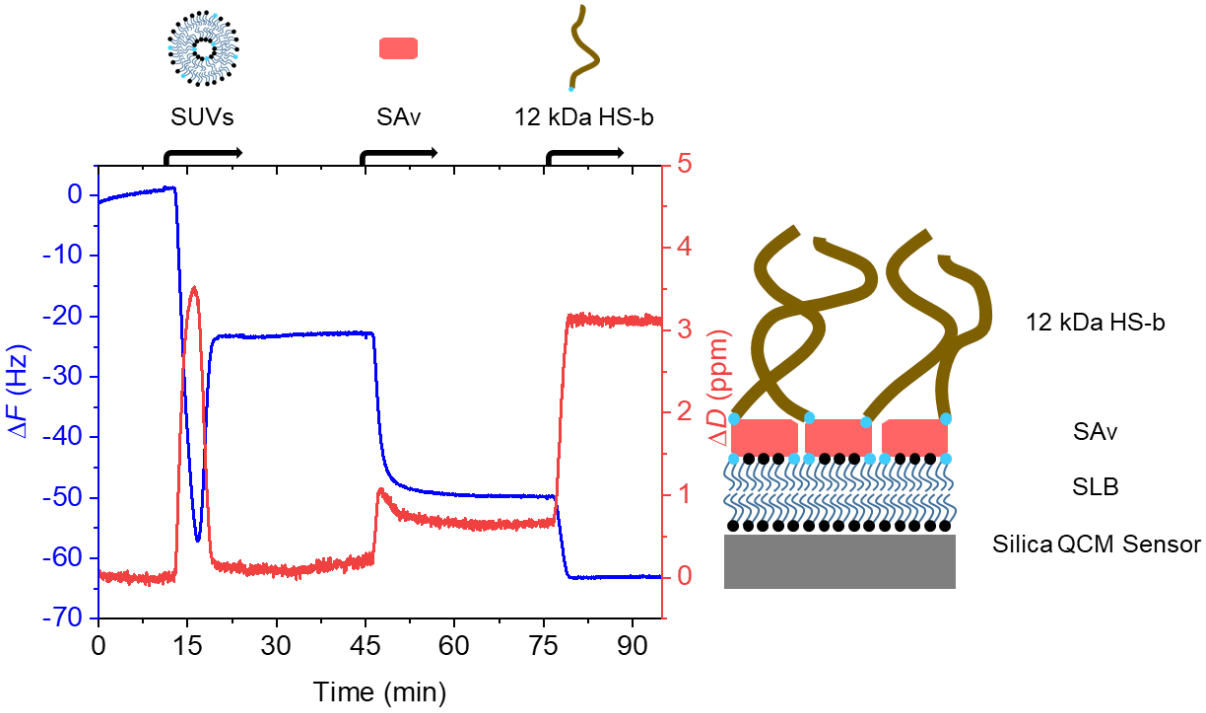


Figure 18. ***The Formation of a Model HS Rich Glycocalyx Monitored by QCM-D.*** *Shown are the frequency (ΔF) and dissipation (ΔD) changes that accompany all steps of the surface functionalisation, starting from the formation of a supported lipid bilayer, followed by a SAv monolayer and the formation of an HS film. Start and duration of incubation of respective materials are indicated by arrows above the graph. Concentrations for incubation: SUV (5 mol-% DOPE-CAP-B + 95 mol-% DOPC) – 50 µg/ml, SAv – 20 µg/ml, HS-b (nominal M_W = 12 kDa) – 10 µg/ml. The fifth overtone is presented here, data was qualitatively comparable across all overtones.*

3.3.1.1.1 Post-chromatographic Analysis of Biotinylated HS by QCM-D

A new aliquot of HS source material (from the same batch used earlier) was biotinylated at the reducing end by oxime ligation, and purified by size exclusion chromatography, according to the protocol in Section 3.2.7.1. The elution fractions resulting from the size exclusion chromatography were analysed by QCM-D to quantify the size, purity and concentration of the biotinylated HS (HS-b). This is a method recently developed in the Richter lab across multiple different projects including this one (101).

To this end, a small amount of each fraction was diluted and applied to a SAv-on-SLB film and the resulting frequency and dissipation shifts were monitored and analysed (Figure 19A-B). Only the first seven elution fractions produced appreciable changes in frequency and dissipation shifts. The remaining fractions produced no responses (data not shown) were discarded as they must contain either no or a very low concentration of HS-b.

The binding rates, as reflected in the frequency shifts in Figure 19A, provide a measure of the relative concentrations of HS-b. The highest rate of binding is seen for EF3 and EF4, indicating that these fractions contain the highest concentration of HS. The binding rates gradually decrease towards both earlier and later fractions, consistent with HS-b being eluted as a single 'peak' from the size exclusion column.

It is also notable that the elution fractions produce different final changes in frequency. All maximal frequency shifts (Figure 19C) are well below the 30 Hz that was shown in Migliorini *et al.*, this indicates that the GAG chains are likely shorter than those previously used and that the chains themselves have degraded over time. The negative frequency shifts at saturation, or maximal frequency shift, provide a measure of the purity of HS-b. The smaller the maximal frequency shift, the greater the contamination of free biotin (91). The later elution fractions (5 through 7) have frequency shifts of 10 Hz or less, it is not likely that the HS has halved in size between the fractions but rather that the excess biotin from the biotinylation reaction is present. This aligns with the known properties of Size Exclusion Chromatography, smaller molecules will take more time to travel through the chromatography column and appear in latter elutions. Therefore, fractions 5 through 7 are likely not pure biotinylated GAGs and would lead to a surface that is not saturated by GAGs, with some of the SAv sites being filled with biotin instead.

In order to select which fraction contains the HS that is most useful for the ongoing project, a sample of good purity and of a large molecular weight, a glycosaminoglycan sizing method was utilised (101). This involves creating a parametric plot of the ratio of change in dissipation to the change in negative frequency ($\Delta D/-\Delta F$) against the change in negative frequency ($-\Delta F$; Figure 19D). All elution fractions have a similar $\Delta D/-\Delta F$ ratio except for fraction 7, indicating that there is relatively consistent sizing within the sample. As discussed above, fraction 7 likely has a high degree of contamination with biotin and this could explain why it does not follow the same trend as the other fractions. Other than the expected noise at frequency shifts close to 0 Hz, all fractions show a $\Delta D/-\Delta F$ ratio that is virtually independent of coverage ($-\Delta F$) at around 0.2 ppm/Hz. This is achieved by calculating the number of disaccharides (see Section 3.2.11) from the $\Delta D/-\Delta F$ ratio at ΔF = -2.5 Hz using the standard curve established by Srimasorn *et al.* (101).

Most of the elution fractions have 7 and 10 disaccharides, this translates to estimated molecular weights between 4.0 and 5.7 kDa, this is much lower than expected so these fractions can be discarded. The estimated molecular weight was calculated by multiplying the number of disaccharides with the molecular weight of the heparin disaccharide, as this is a more sulphated form of HS, this is an estimate and may be slightly larger than the true molecular weight (142). Elution Fraction 3 had 17

disaccharides, which results in an estimated molecular weight of 9.8 kDa, this is far below the expected value, but should make a good platform to test for binding of HS binding molecules. Although this is quite different to the other fractions, it is clear to see that the $\Delta D/-\Delta F$ ratio for this fraction is markedly different to the others (Figure 19). This is likely due to degradation of the HS chain, resulting in the loss of disaccharides over time. This value also provides a good explanation for why the target frequency from the literature was not reached. However, these data highlight the depth of information that can be extracted from QCM-D data to define and quality control the properties of the model matrices.

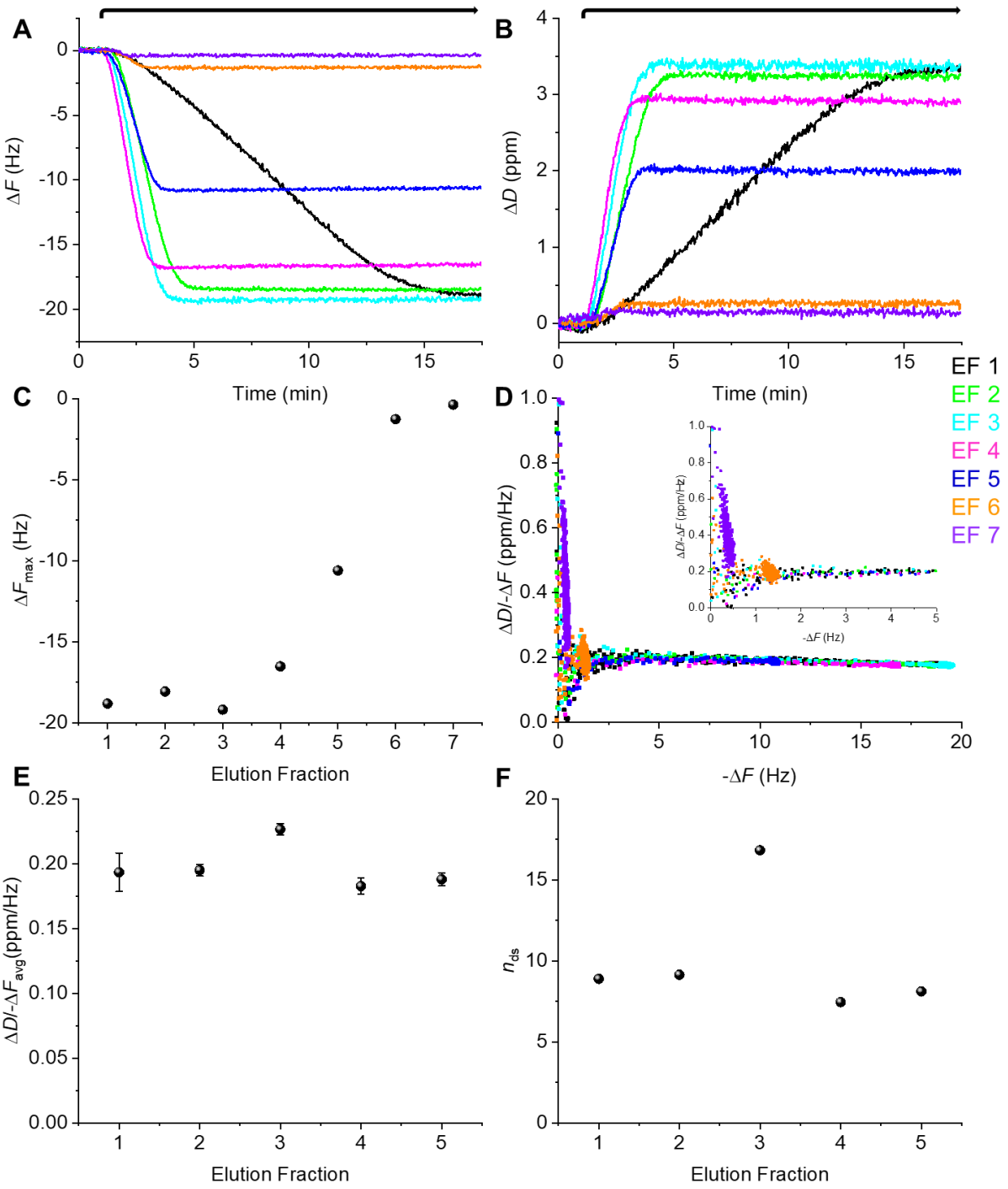

A
ΔF (Hz)
Time (min)
B
ΔD (ppm)
Time (min)
EF 1
EF 2
EF 3
EF 4
EF 5
EF 6
EF 7
C
ΔF_max (Hz)
Elution Fraction
D
ΔD/-ΔF (ppm/Hz)
-ΔF (Hz)
E
ΔD/-ΔF_avg (ppm/Hz)
Elution Fraction
F
n_ds
Elution Fraction

Figure 19. ***Purification of Biotinylated HS.*** *A) Frequency changes (ΔF) upon incubation of elution fractions of biotinylated HS purified by Size Exclusion Chromatography on a SAv monolayer. B) Dissipation changes (ΔD) upon incubation of elution fractions of biotinylated HS on a SAv monolayer. The SAv monolayer was formed as presented in Figure 18. C) The maximal frequency shifts of each elution fraction. D) A parametric plot of the ΔD/-ΔF ratio against the negative frequency change for each elution fraction. The inset shows the data between 0 and -5 Hz. E) The average ΔD/-ΔF between -2 and -3 Hz for all elution fractions that reached these values. Error bars represent standard deviation. F) The number of disaccharides (n_{ds}) of each elution fraction.*

3.3.1.1.2 Controlling the Concentration of HS on the Surface

Another facet of the model matrix that was varied within this project, is the concentration of HS chains on the surface. The concentration of HS on the surface is directly related to the percentage coverage of HS. This can be modulated by competitive adsorption with controlled molar ratios of HS-b and free biotin (91, 119, 121).

The first method is achieved by understanding how mass transport limited binding affects how quickly molecules of a defined hydrodynamic radius bind to a surface (91). By considering that the Stokes-Einstein relation and the concentration of the binding molecule will determine the time in which the maximal molar surface density ($\Gamma_{1,sat}$) is reached. When one molecule is present, $\Gamma_{1,sat}$ will equal the total molar density of binding sites (Γ_{as}) on the surface. If an additional molecule is present that would saturate the surface in the same manner then the following equation can be established (91):

$$\frac{c_2}{c_1} = \left(\frac{R_2}{R_1}\right)^{\frac{2}{3}} \left(\frac{\Gamma_{\mathrm{as}}}{\Gamma_{1,\mathrm{sat}}} - 1\right) \qquad [3.4]$$

Here, the indices 1 and 2 relate to the functional molecule and the free anchor molecule, respectively, *R* is the hydrodynamic radius, *c* is the molar concentration, and Γ_{sat} is the molar surface density at saturation. When $\frac{\Gamma_{\mathrm{as}}}{\Gamma_{1,\mathrm{sat}}}$ is equal to 2, this is equivalent to 50% coverage with the functional molecule, if it is equal to 4, this is equivalent to 25% coverage. In order to test this for a HS-b film, 33 kDa HS was used as the functioning molecule and biotin was used as contaminating molecule.

Equation 3.4 was used to calculate the mixing ratios. The hydrodynamic radius of biotin was used as determined previously (0.37 nm) and the hydrodynamic radius of 33 kDa HS was defined as $R_{\mathrm{HS}} \approx 0.05\ nm\ (n_{\mathrm{ds}})^{0.61}$ (91). The concentration of HS-b was kept at 10 µg/ml and the biotin concentrations varied at 0.23 µM and 0.69 µM, these were mixed thoroughly before addition. The nominal stock concentration of HS-b was estimated using the purification protocol, as 1 mg of material was eluted with 1 ml of buffer, and a comparison in binding rate to similar weight HS.

Mixing ratios of HS-b and free biotin were defined for target coverages of 25%, 50% and 100% HS-b, and these mixtures were tested for binding on a SAv film in QCM-D (Figure 20, A-B). The results for frequency shifts are -2.5 Hz, -6.0 Hz, and -27.5 Hz for predicted coverages of 25%, 50%, and 100% surface coverages, respectively. Surprisingly, the frequency shift at saturation did not scale linearly with the predicted HS surface coverage (Figure 20C). The theoretical prediction should result in a linear dependence and previous data on a similar system has indicated this (91). Instead, the frequency shifts for coverages below 100% fell consistently below expectations.

One reason for this could be that the concentration of HS is not correct. The concentration was estimated to be 10 µg/ml, however, this was estimated based on the concentrations used in the starting reactions for biotinylated and the volumes in the purification process, so there is room for error due to the starting concentrations. It is also possible that the hydrodynamic radius of the HS was incorrect, the method of estimation is not direct, but has been previously proved correct for chondroitin sulfate, which is a GAG of similar characteristics and so this method is reliable (91). It is also possible that the biotin concentration was incorrect as biotin solutions do not have a very long shelf life, however, solutions of biotin were produced fresh for each assay to avoid any inaccuracy in biotin concentration.

As the frequency shifts should scale linearly with percentage HS coverage, it is possible to modify the calculations of HS coverage with a range of HS concentrations, these are plotted against frequency shift at saturation in Figure 20C. The estimated HS concentrations of 1.67 and 2.49 µg/ml form the most linear trend with the data, therefore, the HS concentration must be between these two values. This is a novel method for calculating the concentration of a biotinylated GAG molecule. These calculated concentrations of the working concentration can be scaled up to 50 and 75 µg/ml for the stock HS concentration. Going forward, using the new concentration in the above equation, it would be possible to achieve a more accurate surface coverage.

These data demonstrate that different percentage coverages can be achieved although they did not achieve the desired percentage coverage of HS. Here, approximately 6% and 16% HS coverage was achieved, modulating the concentration to the same amount. If investigating the effect of HS concentration on interactions or other parameters, specific HS coverages are not required, but a variation, these data fulfil these requirements. Therefore, these surfaces can still be used for these types of analyses.

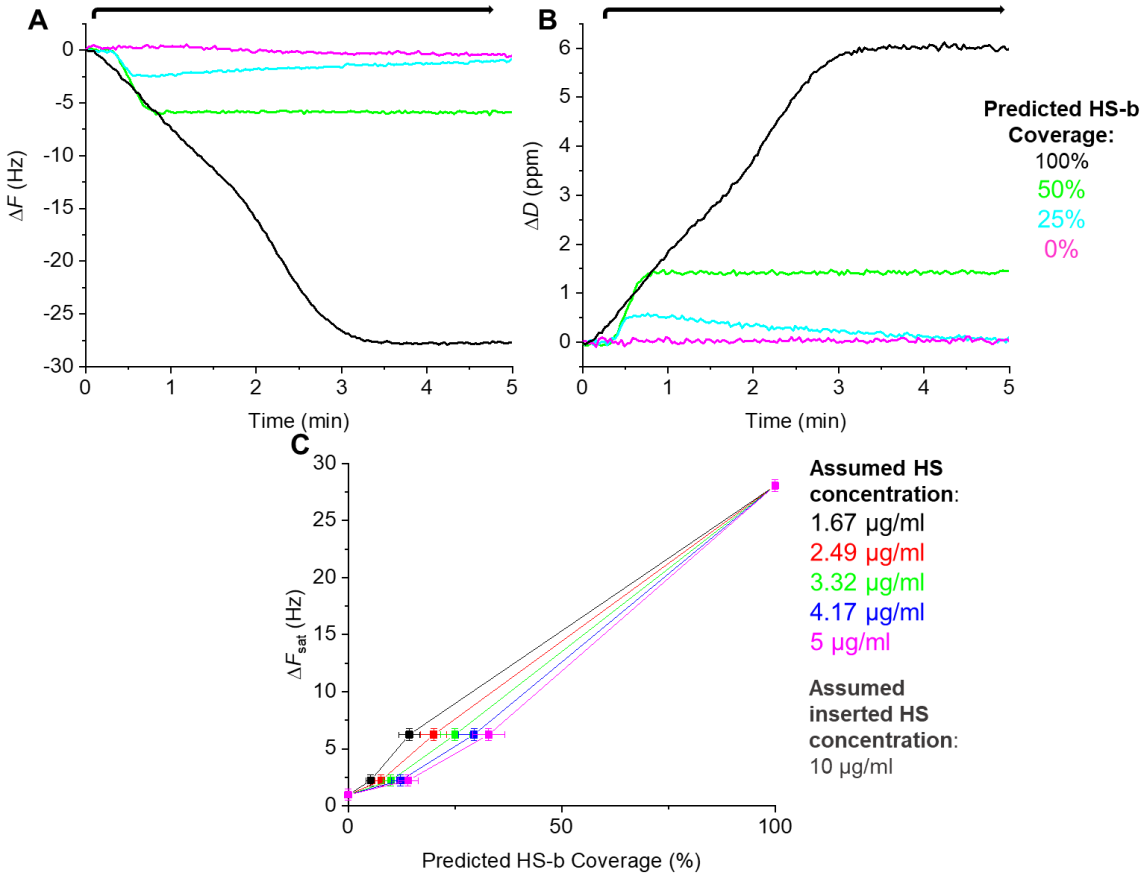


Figure 20. ***Modulating 33 kDa HS Surface Coverage****. A-B) Frequency (A) and dissipation (B) changes upon incubation of different ratios of HS and Biotin to a SAv monolayer. NB; for this incubation, the flow rate was 100 µl/min in order to maintain mass transport limited binding. Supported lipid bilayers and SAv monolayers for this set of experiments were formed as presented in Figure 18. C) A graph of the frequency shift at saturation against the predicted HS coverage. Error bars in x represent the error propagation due to pipetting error. Error bars in y account for fluctuations in frequency.*

3.3.1.2 Modelling a Thick and Open Glycocalyx for Passive Diffusion Analyses

The second method for modulating surface coverage uses the intrinsic properties of high molecular weight of HA (119, 121). Due to the length of HA molecules used in this study (n_{ds} ≈ 2095, contour length = 2095 nm (101)), the HA will rarely saturate all binding sites on the surface due to steric hindrance between the molecules. During the formation of a high molecular weight HA brush as followed by QCM-D (Figure 21B), the frequency shift decreases very slowly to only -4 Hz and does not plateau within the incubation period as opposed to the formation of films with much lower molecular weight GAGs (Section 3.3.1.1). There are multiple reasons for this. Firstly, the contour length of this material is on the micron scale, this would result in the chain projecting far from the silica surface, making the frequency less sensitive to the mass changes of this film (94, 141). Secondly, due to this large contour length and the natural repulsion between HA chains because of their negative charge,

the HA chains are spread out with many biotin binding sites between them (Figure 21A). The coverage of HA cannot be modulated by the addition of biotin to fill binding sites as this method relies on the binding being mass transport limited and the binding of high molecular weight HA is not.

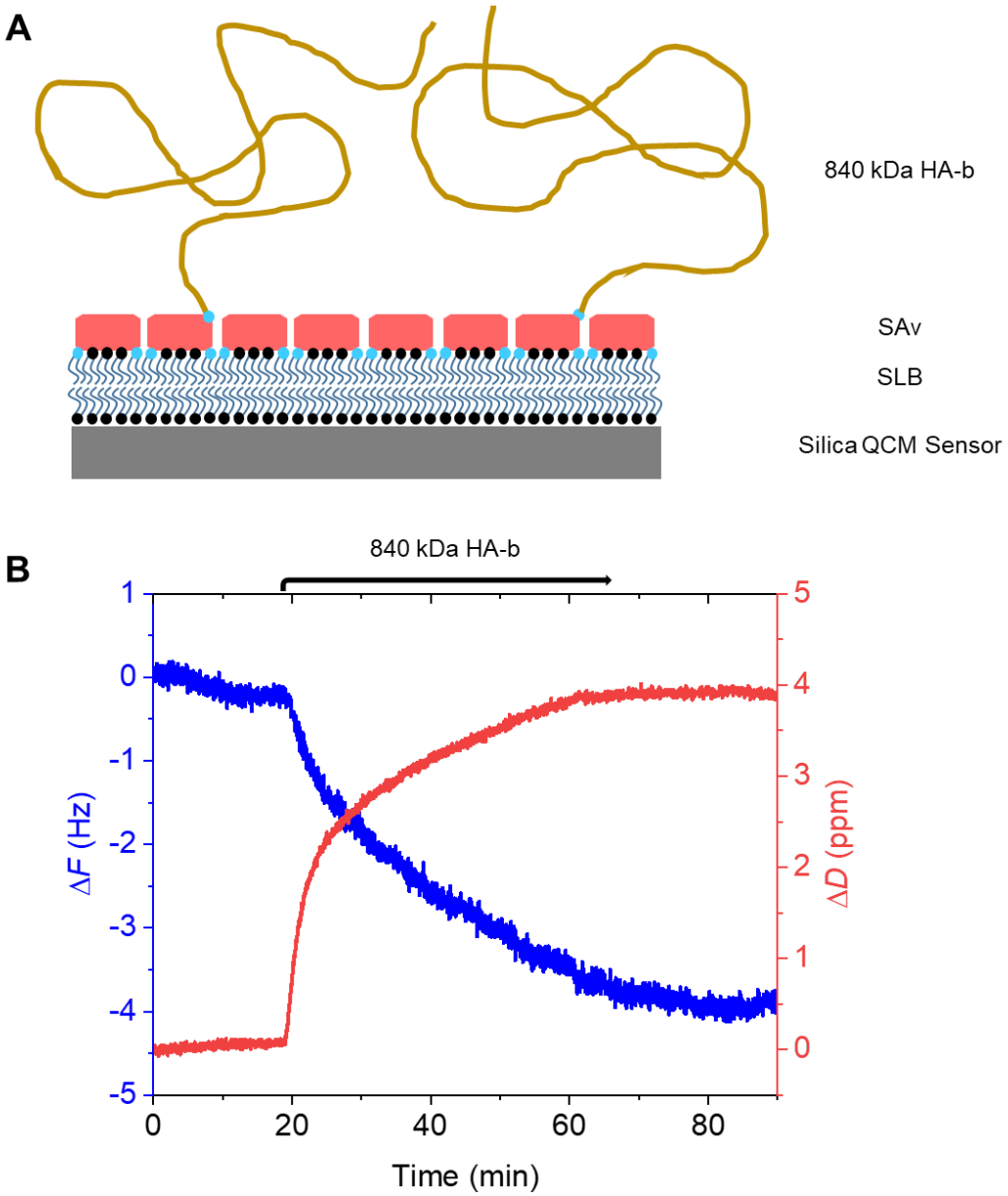


Figure 21. ***Formation of a High Molecular Weight Hyaluronan Brush****. A) A schematic of a high molecular weight HA brush on an SLB. Individual HA chains are spaced far apart from each other due to the electrostatic interactions between the individual HA chains. B) The frequency (ΔF) and dissipation (ΔD) changes that accompany the formation of a high molecular weight HA brush. Start and duration of incubation of respective materials are indicated by arrows above the graph. The SLB and SAv layers were formed as in Figure 18. Concentrations for incubation: SUV (5 mol-% DOPE-CAP-B + 95 mol-% DOPC) – 50 µg/ml, SAv – 20 µg/ml, HA-b (nominal M_W = 840 kDa) – 20 µg/ml. The fifth overtone is presented here, data was qualitatively comparable across all overtones.*

The spacing between HA molecules can be decreased by increasing the incubation period of the HA (121). In order to measure this, a technique is required that would allow the quantification of the number of HA chains attached to the surface. SE can do this as it can measure the Areal Mass Density (AMD) of an object on the surface. For these types of films, the anchor distance between HA chains is equivalent to the pore size of the matrix (119, 141). In order to analyse diffusion through an HA brush, the pore size must be greater than the size of the diffusing molecules. Therefore, the aim was to generate brushes with pore sizes greater than 50 nm.

SLBs with SAv can be assembled on SE silica wafers (Figure 22). On to this surface three different HA films of differing molecular weight (280, 520, and 840 kDa) were formed and the process measured by SE, to define what kinds of films form a pore size of around 50 nm. This is demonstrated through the data in Figure 23. As the molecular weight of the HA increases, the areal mass density achieved by the HA within the same period decreases. The initial binding rates are quite similar, this is because for the initial binding periods, the same amounts of material of each molecular weight. For HA 280 kDa, an AMD of 60 ng/cm^2 is achieved within 30 minutes, whereas, this value is only 30 ng/cm^2 for HA 840 kDa. The AMD relates directly to the spacing between the molecules as it relates to the molar surface density which can be converted to the root mean square (RMS) anchor distance (Section 3.2.10) (Figure 23B). For 280 kDa HA, the anchor distance becomes less than 50 nm within 5 minutes of incubation on the surface. Anchor distance for 520 kDa HA is around 50 nm within 10 minutes, and becomes 40 nm after one hour. This is too close to the pore size of interest therefore, is not suitable. For 840 kDa HA, the anchor distance remains above 50 nm for the entire incubation period, at around 60 nm at its most dense. The film generated with the largest molecular weight HA is the most suitable to produce matrices of pore sizes larger than the molecule of interest. Overall, by selecting the molecular mass and incubation time of HA, it is possible to tune the spacing between HA molecules within the film.

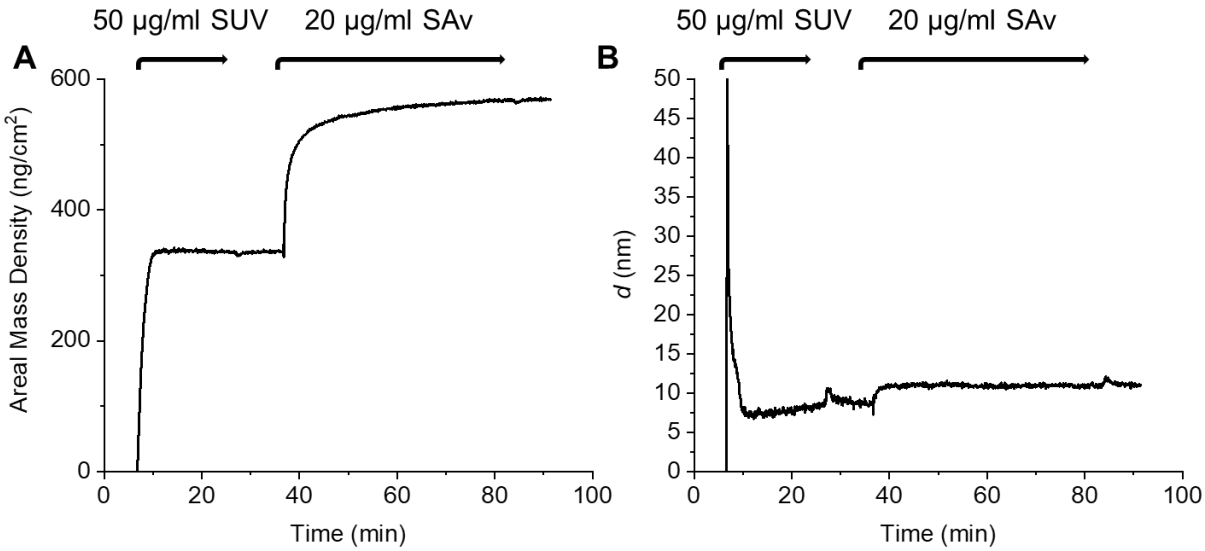


Figure 22. ***Formation of SLB and SAv Layers on Silica Wafers.*** *A) The areal mass density changes during the formation of an SLB and addition of SAv during an SE experiment. B) The thickness (d) changes to the surface during the SLB formation and SAv addition. Start and duration of incubation of respective materials are indicated by arrows above the graph. Concentrations for incubation: SUV (5 mol-% DOPE-CAP-B + 95 mol-% DOPC) – 50 µg/ml, SAv – 20 µg/ml.*

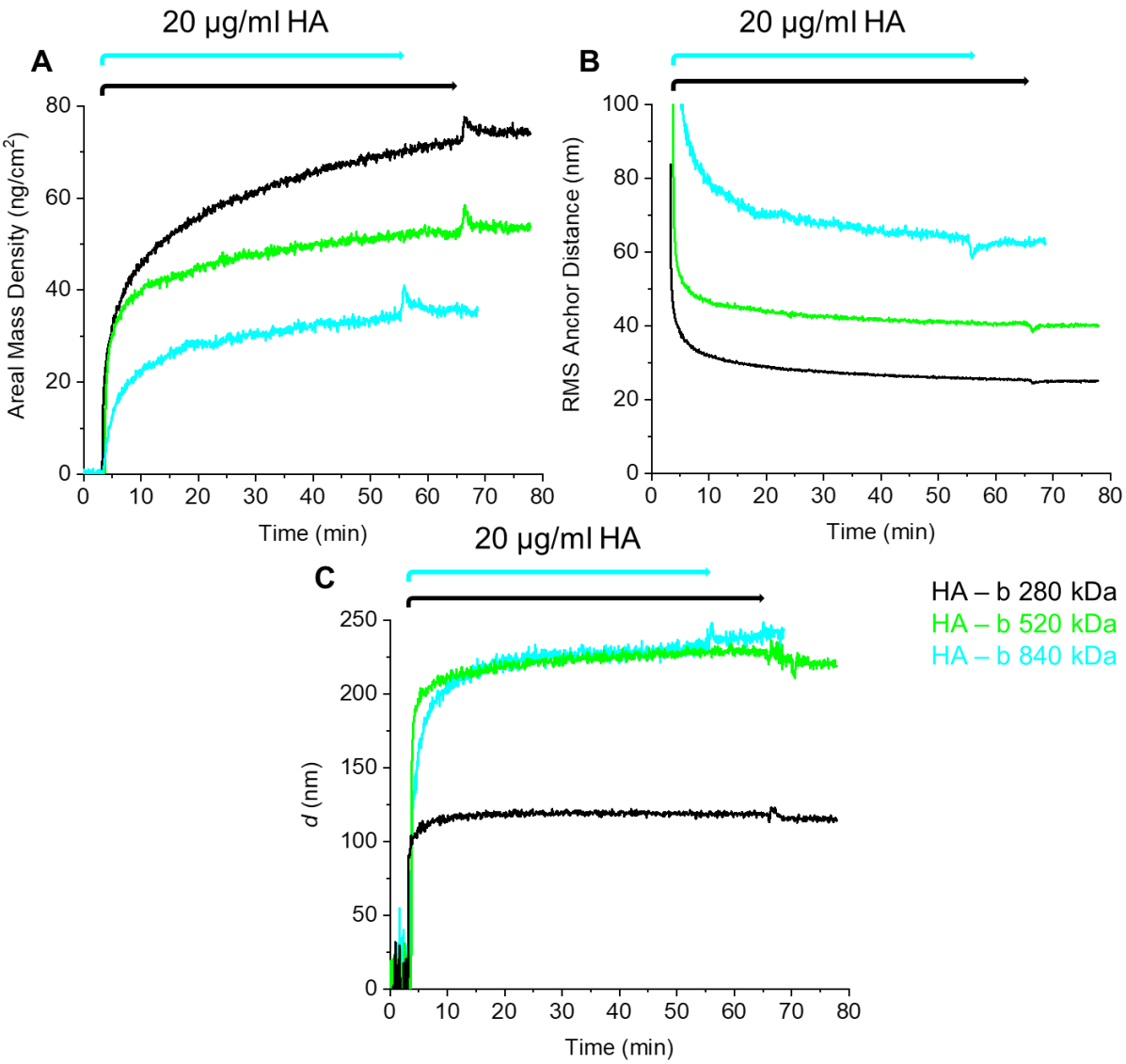


Figure 23. ***The RMS Anchor Distance Between Different Size HA Chains****. A) Areal mass density of HA-b on a SAv monolayer during incubation with 20 µg/ml HA-b polysaccharides of different molecular mass (280 kDa, 520 kDa and 840 kDa, colour coded as indicated). B) The anchor distance between HA chains over the incubation period. C) The thickness (d) of the HA layer of the film. These HA films were formed on the surfaces presented in Figure 22. Start and duration of incubation of respective materials are indicated by arrows above the graph.*

3.3.1.3 Models Inspired by Mucin-rich Glycocalyces

Other than films consisting of GAGs, films containing Gb_3 were also developed. Gb_3 is a glycosphingolipid that is present in cell membranes in a variety of mammalian tissues and is a receptor for the B sub unit of the Shiga toxin (128). The sugar moiety of Gb_3 consists of two galactose and one glucose residue (Figure 3). To investigate the interaction of Gb_3 with molecules in a model matrix without forming a bilayer of the sphingolipid itself, a polymer construct was made consisting of an HA

backbone, which was biotinylated on its reducing end, with the sugar moiety of the Gb_3 molecule grafted at onto it with 35% substitution (127).

A model matrix with this grafted molecule (HA-*g*-Gb_3) can be formed in a similar manner as the previous matrices and measured via QCM-D (Figure 24). SAv on SLB is formed in a similar manner as presented in Section 3.3.1.1, then HA-*g*-Gb_3 is applied resulting in a frequency change of -32 Hz and a dissipation change of 8 ppm. These values are congruent with previously demonstrated surfaces of this type (127). This highlights the possibility of versatility of these surfaces, the type of surface modulation described in the earlier parts of this section, can also be applied to this type of film.

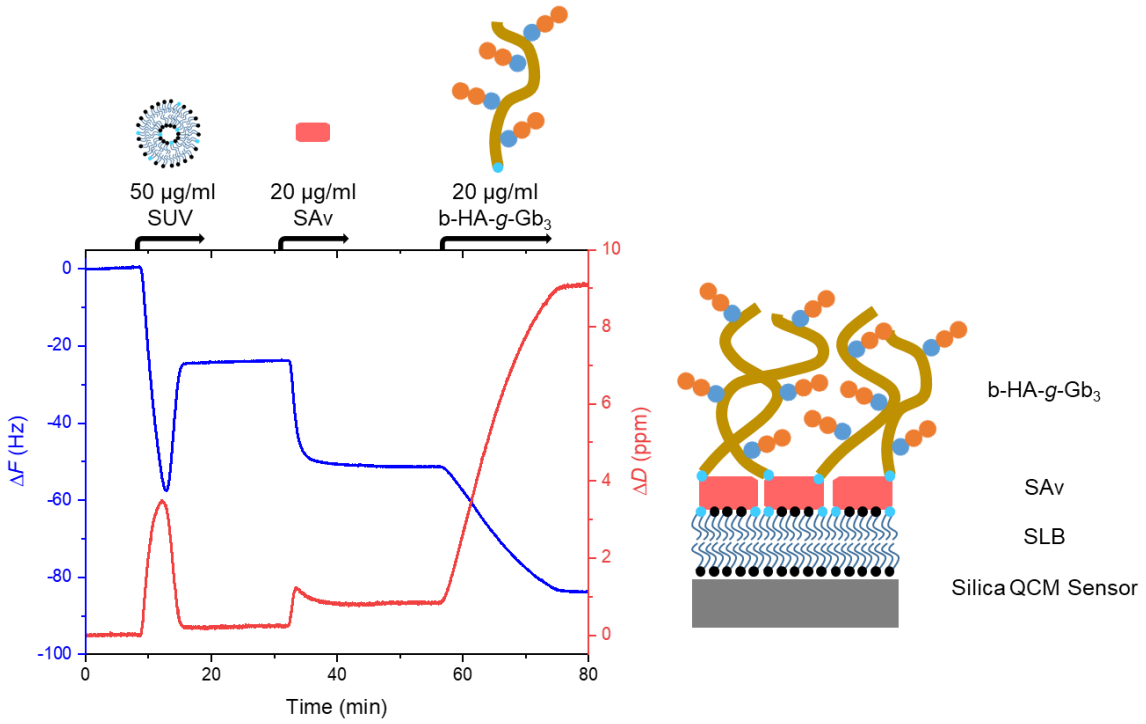


Figure 24. ***The Formation of Films of Mucin-like Structures, Monitored by QCM-D.*** *The frequency and dissipation changes that accompany the formation of a film consisting of a supported lipid bilayer, an intermediate SAv monolayer, and a layer of HA with grafted Gb_3 moieties (orange circles represent galatose, blue circles represent glucose). The start and duration of incubation of respective materials are indicated by arrows above the graph. Concentrations: SUV (5 mol-% DOPE-CAP-B and 95 mol-% DOPC) – 50 µg/ml, SAv – 20 µg/ml, (HA-g-Gb_3)-b – 20 µg/ml.*

3.3.2 Fluorescent Labelling of Diffusion Colloids

To trace biological colloid diffusion in model glycocalyces, a method to visualise the colloids is required. Fluorescence labelling of the biological colloids is the most compatible method with microscopy as it would allow the mobility of the molecules to be visualised.

3.3.2.1 Requirements on Colloids and Labels for Model Glycocalyx Binding and Diffusion Analyses

The aim for fluorescent labelling of the colloids is that the molecules are labelled site specifically with an appropriate fluorophore without affecting the functionality of the molecules. The term functionality includes that the molecule retains any of its innate ability to bind the target glycans, it does not introduce any nonspecific binding to other areas of the surface, and its size would not impact on the diffusivity of the colloids. This provided the reasoning for labelling site specifically with small molecule fluorophores. Site specific labelling would allow the position of the label to be defined and this can be chosen as far away as possible from the motifs required for binding within the molecule of interest (143). Small molecules were chosen as these are typically on nm length scales and therefore, would not significantly impact the hydrodynamic radius of the molecule (144).

The colloids chosen for fluorescent labelling were CXCL12, STxB, and EUVs. The first two interact specifically with glycan molecules with vastly different affinities, (nM and mM ranges, respectively) and have pertinent biological functions (41, 127). EUVs should be inert in a glycan rich extracellular matrix, and therefore, can be used to study the effect of the matrix pore size on the diffusion of molecules.

3.3.2.2 CXCL12 Chemokines

3.3.2.2.1 Labelling of CXCL12 on the N terminus Affects HS binding

3.3.2.2.1.1 Successful production and purification of CXCL12α and CXCL12γ

Chemokines are well documented HS binding partners and distribute within the glycocalyx (39). Consequently, this group of molecules were considered as models to investigate the diffusion of GAG binding molecules in GAG-rich matrices.

CXCL12 has multiple isoforms (α, β and γ) with differing affinities to HS resulting from additional amino acids at the C terminus, providing a set of molecules that can be readily compared (46). CXCL12α and CXCL12γ were selected as these are the most distinct from each other. CXCL12γ features an additional 11 amino acids (Figure 25A-B), which strongly enhances HS binding. The binding of CXCL12α and CXCL12γ to HS and heparin has been extensively characterised (125, 126, 145-147). CXCL12γ has been found to bind with 130-fold enhanced affinity compared to CXCL12α, and both isoforms have been shown to cross-link HS films (41). This prior knowledge made CXCL12 attractive as a model chemokine.

The aim thus was to produce fluorescently labelled CXCL12α and CXCL12γ isoforms without hindering their binding affinities to HS. The first step in the generation of these labelled colloids was to generate plasmids for production of histidine tagged forms of these proteins. The histidine tag allows for ease of purification via nickel affinity chromatography but also for labelling with Tris NTA conjugated fluorophores (132). The N terminus was chosen for placement of the His tag as the C terminus has been shown to be involved in HS interactions and the N terminus has been successfully used for chemokine labelling previously (125, 148). This is an example of site-specific labelling of a protein. Site-specific labelling has many advantages including compatibility with studying proteins in their native environment limiting the interference of the label with the proteins functions (143).

The pRSET A plasmid (Figure 17) was chosen as the vector due to its availability and versatile multiple cloning site (133). CXCL12α and CXCL12γ were amplified from their original plasmids via a PCR reaction (see Section 3.2.3.1), sub-cloned into pRSET A and transformed into *E. coli*. The transformed bacteria were selected for ampicillin resistance. Chosen bacterial colonies were sequenced via the T7 promoter upstream of the cloning site (see Section 3.2.3). The cloning of the genes into the plasmid was successful, as indicated by the plasmid containing the exact genetic sequences of the reference material (Figures S1 and S2). The final amino acid sequences, translated from the genetic sequence, for the two protein constructs are listed in Figure 25A-B. These contain the start codon (M), the N-terminal His_6 tag, and the native protein sequence.

The two protein isoforms were produced in BL21 *E. coli* strain and purified products were obtained by nickel affinity chromatography. Purity of the final products was assessed via SDS PAGE (Figure 25C). Both HisCXCL12α and CXCL12α wild-type were observed between 6 and 14 kDa, with HisCXCL12α showed a slightly larger molecular weight than its wild- type, which is consistent with the slightly larger molecular mass due to the additional amino acids (Figure 25C, gel on the left). The molecular weight of the wild-type is 8 kDa and the His tagged protein is 10 kDa. HisCXCL12γ migrates just above molecular weight marker 14 kDa (Figure 25C, gel on the right) which is slightly larger than its expected molecular weight (13 kDa). However, both CXCL12α and HisCXCL12α also migrate above their true molecular weight so this is likely an artefact of how CXCL12 moves through the SDS PAGE gel and not an indication of an incorrect molecular weight. There are slight shadows below the bands in the gel on the right hand side, which is not present on the band for HisCXCL12α in the gel on the left hand side made from the same protein stock. Therefore, these shadows are likely an artefact of the SDS PAGE and not other protein species. Due to the lack of visible contaminants within the protein sample as shown by the lack of additional protein bands at other molecular weights, the final products were judged to be of at least 90% purity.

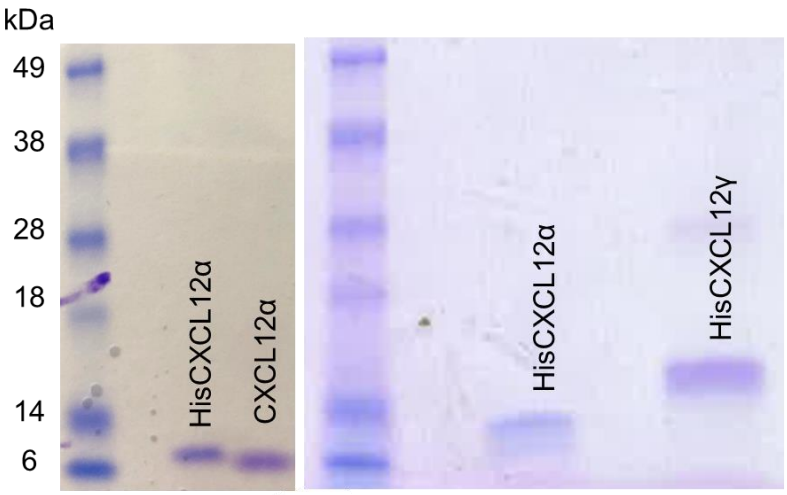
A HisCXCL12α

MRGSHHHHHHGMASMKPVSLSYRCPCRFFESHVARANVKHLK
ILNTPNCALQIVARLKNNNRQVCIDPKLKWIQEYLEKALNK

B HisCXCL12γ

MRGSHHHHHHGMASMKPVSLSYRCPCRFFESHIARANVKHLK
ILNTPNCALQIVARLKNNNRQVCIDPKLKWIQEYLEKALNKG
RREEKVGKKEKIGKKKRQKKRKAAQKRKN

C



D

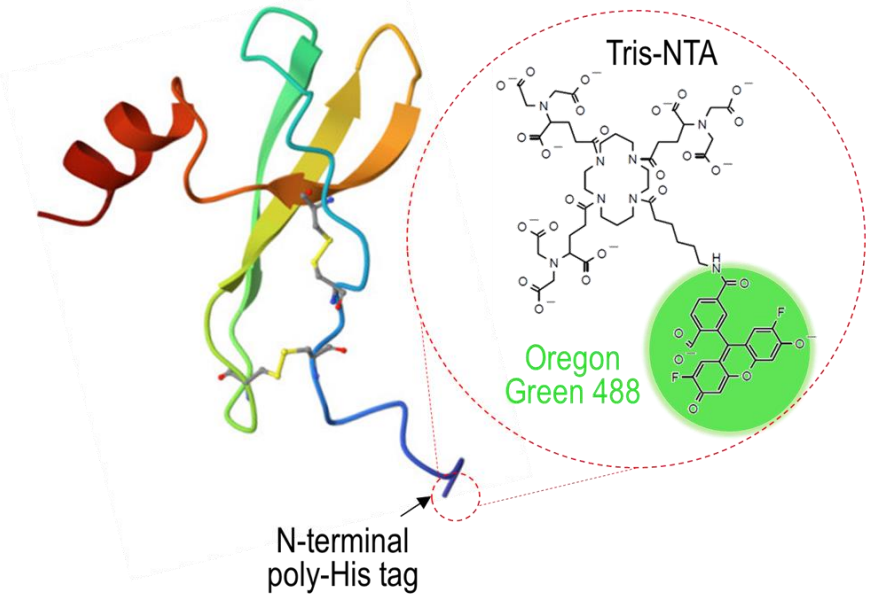


Figure 25. ***Production and Strategy for Labelling CXCL12****. A-B) Amino acid sequences (single letter code) of the two constructs, HisCXCL12α (A) and HisCXCL12γ (B). Red text represents the* His_6 *tag, blue text represents the wild-type protein sequence, and grey text represents amino acids that act as spacers between the other parts of the sequence. C) 12.5 % SDS PAGE analysis of the threeproteins following purification, stained by SeeBlue. The expected molecular masses are 8 kDa for CXCL12α (left image), 10 kDa for HisCXCL12α (left and right images), and 13 kDa for HisCXCL12γ (right image). D) Structure of CXCL12α (ribbon representation, adapted from (149)), and the location that the Tris NTA fluorophore, adapted from (132), will attach. The ball and stick amino acids shown here are the two disulfide bonds present in the protein. The histidine tag is not present in this representation of the structure. The structure of CXCL12γ is not shown here as the addition of the tags would appear at the same location.*

3.3.2.2.1.2 HisCXCL12γ shows modified HS binding compared to CXCL12γ

To assess functionality of the His_6 tagged CXCL12s, HS binding was tested by QCM-D analysis with a model glycocalyx. The HS model matrix formed of 12 kDa HS at the maximal surface coverage was formed and validated by QCM-D (Section 3.3.1). Upon addition of HisCXCL12γ to the HS film for 20 min, the frequency decreased by 30 Hz (without reaching equilibrium) and remained at this value upon rinsing with working buffer (Figure 26). This indicates that the protein does bind the film and remains stably bound despite the washing of the surface, consistent with the high affinity of CXCL12γ for HS (K_d = 1.5 nM) that was previously reported (126). However, previous work with CXCL12γ wild-type and a HS film of the same surface coverage and nominal molecular weight, showed equilibrium binding with a much smaller negative frequency change (ΔF = -10 Hz (41)). This reference did use half the concentration used in this assay. The 3-fold increase in frequency shift is too large to be explained simply by the slight increase in molecular mass of HisCXCL12γ due to the added His_6 tag or due to the doubling of the concentration. The dissipation decreased by 2 ppm upon initial binding of HisCXCL12γ, yet after reaching a minimum began to rapidly increase and continued to do so even upon rinsing of the surface in working buffer, reaching 9 ppm after 20 minutes of rinsing. The initial decrease is consistent with published data on wild-type CXCL12γ (41) and evidences HS cross-linking by HisCXCL12γ. However, in the previous work with the wild-type protein the dissipation decrease continued for the entirety of the incubation period and only a small increase (1 ppm) was observed upon rinsing (41). Clearly, the second phase of HisCXCL12γ binding, leading to a soft HS/protein film, is unexpected.

The responses seen in the frequency and dissipation shifts for HisCXCL12γ are unexpected and indicate that the protein does not bind HS in a comparable manner with the wild-type protein. This may be a consequence of that the histidine tag changes the interaction with the film or that the histidine tag

affects the folding of the protein. Another possible explanation is that the HisCXCL12γ protein not folding correctly and, therefore, not including the correct structural motif for binding. Chemokines are expressed as inclusion bodies and then must undergo a refolding process, as the folding process for this protein has occurred outside of its natural environment, it is possible that this has introduced some form of error (150). In either case, as the protein does not retain its HS binding functionality, the HisCXCL12γ construct was not taken further for diffusion analyses.

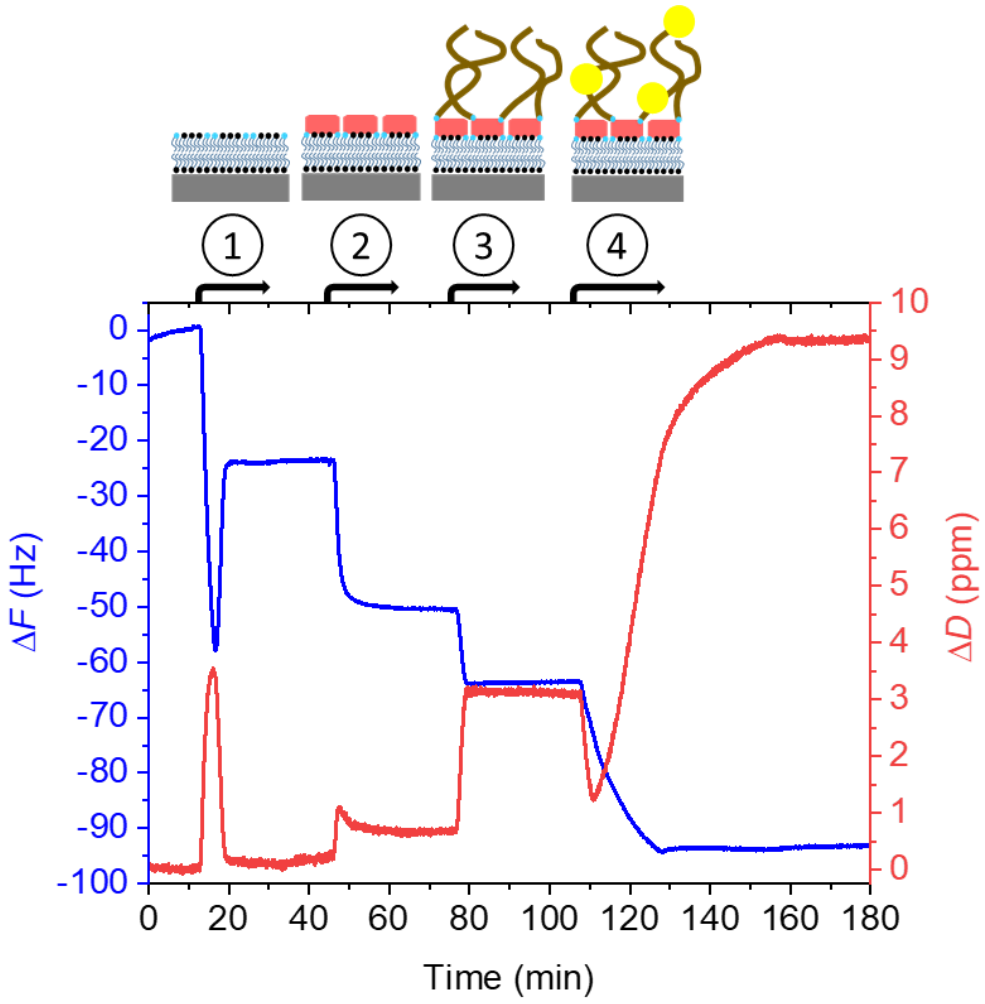


Figure 26. ***QCM-D Responses of HisCXCL12γ Binding to an HS Film.*** *Shown are the frequency (ΔF, blue) and dissipation (ΔD, red) changes that accompany HS film formation (reproduced from Figure 18) and CXCL12γ binding. Arrows indicate the start and duration of 1) 5% DOPE-CAP-B – 50 µg/ml, 2) SAv – 40 µg/ml, 3) HS-b (nominal M_W = 12 kDa) – 10 µg/ml, 4) HisCXCL12γ (yellow) – 0.8 µM. The fifth overtone is presented here, data was qualitatively comparable across all overtones.*

3.3.2.2.1.3 HisCXCL12α and CXCL12α bind similarly to HS films

In contrast to the γ isoform, the QCM-D responses for binding to the HS film were largely similar for the wild-type CXCL12α and HisCXCL12α (Figure 27). Binding rates were comparable, and frequency shifts reached equilibrium at Δ*F* = -10.5 for CXCL12α, and Δ*F* = -12.5 Hz for HisCXCL12α. These values

match well with the previously published data on CXCL12α binding so a saturated 12 kDa HS film (41). This indicates that the N-terminal His_6 tag had little to no impact on the HS binding properties of CXCL12α. The observed decrease in frequency is indicative of successful binding to HS, and the 2 Hz difference in the equilibrium frequency shift between wild-type CXCL12α and HisCXCL12α can be explained by the difference in the molecular weight of the two proteins. Due to the His_6 tag and linker, HisCXCL12α has approximately 2 kDa higher molecular weight compared to the untagged form, and frequency changes monitored by QCM-D are sensitive to the molecular mass of the object binding to the surface (94). More notably, a change in a proteins size can also change the amount of hydrodynamically couple solvent which can affect the frequency shift. The difference could also be due to minor differences in the concentration of active protein.

CXCL12α binding also induced decreases in dissipation, Δ*D* = -2 ppm for CXCL12α and Δ*D* = -2.5 ppm for HisCXCL12α, indicating that the addition of the His_6 tag did not impact on the HS crosslinking ability of CXCL12α. This is congruent with the previous crosslinking data obtained with CXCL12α on 12 kDa HS films. Overall, the functionality of HisCXCL12α is maintained in respect to HS binding.

3.3.2.2.1.4 Fluorescent labelling via the His_6 tag impairs HS binding of CXCL12α

Visualisation by fluorescence microscopy ultimately requires the addition of a fluorophore. The N-terminal His_6 tag in HisCXCL12α was used to attach a fluorophore via histidine-Ni^{2+}-NTA affinity. Tris-NTA Oregon Green 488 (132) was used as the fluorophore construct, to make OG488•HisCXCL12α (Figure 25D). The benefit of this system is that the protein does not require any additional modifications, the protein can simply be labelled by mixing prior to use, and has a lifetime of over an hour (132).

The QCM-D response to the binding of OG488•HisCXCL12α (labelled at a molar ratio of approximately 1:1) to HS indicated that the labelled protein bound HS to a similar extent as the wild-type protein (Δ*F* = -12 Hz and Δ*D* = -2 ppm). However, the binding rate was notably reduced, indicating that the fluorophore had an unexpected effect on HS binding.

In addition to testing the interaction of the protein with HS, OG488•HisCXCL12α was also applied to the SAv monolayer in order to ensure that the His_6 tag did not result in a non-specific binding interaction between the protein and SAv. No significant changes in frequency or dissipation were observed upon addition of OG488•HisCXCL12α to the SAv monolayer (Figure 29). There is a small change of ~1 Hz, but this is small and is reversible upon rinsing. Therefore, very limited nonspecific binding is occurring.

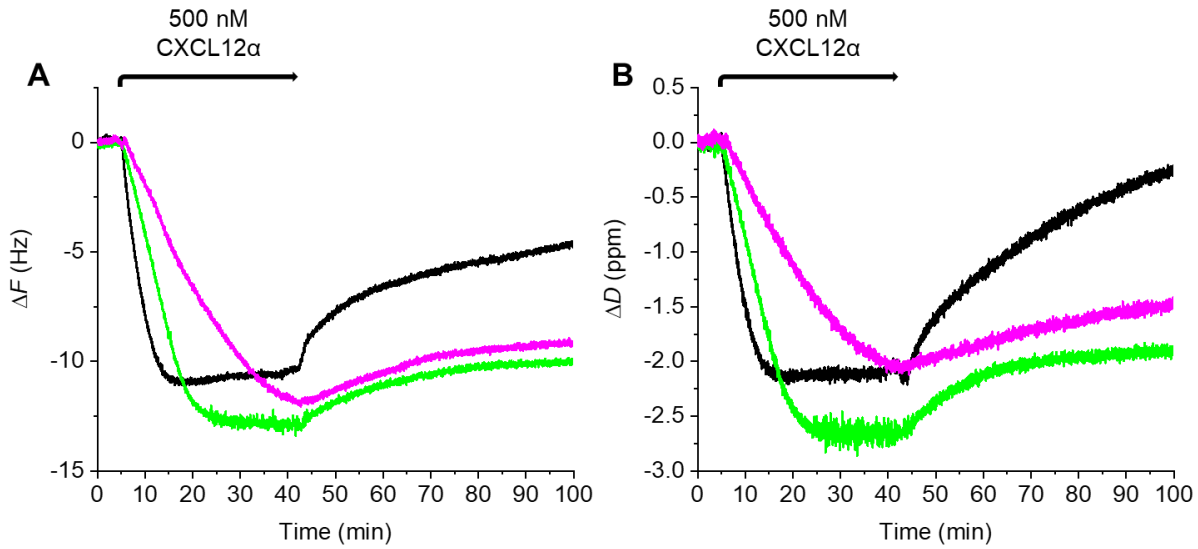


Figure 27. ***QCM-D Responses of Different CXCL12α Forms Binding to an HS Film.*** *A) Frequency shift (ΔF) responses to binding of wild-type CXCL12α (black), HisCXCL12α (green), and fluorescently labelled OG488•HisCXCL12α (1:1) (magenta) to HS films. B) Changes in dissipation (ΔD) due to binding. HS films formed in this experiment were comparable to those formed in Figure 18 (data not shown). Start and duration of incubation of the CXCL12α forms is indicated by arrows above the graph. Concentrations for incubation: SUV (5 mol-% DOPE-CAP-B + 95 mol-% DOPC) – 50 µg/ml, SAv – 20 µg/ml, HS-b (nominal M_W = 12 kDa) – 10 µg/ml, CXCL12 Forms – 500 nM. An equimolar mixing ratio was used for the protein and the fluorophore. The fifth overtone is presented here, data was qualitatively comparable across all overtones.*

To test if the slower binding response is due to the presence of unlabelled CXCL12α, OG488 and HisCXCL12 and were mixed in a range of molar ratios (from 0:1 to 5:1) and binding to HS films measured by QCM-D (Figure 28). Previous experiments were performed with OG488 and HisCXCL12α being mixed at a 1:1 ratio, but a small deviation of stock concentration or pipetting error could lead to the presence of unlabelled proteins. Testing Tris NTA Oregon Green 488 in molar excess would reveal whether the labelled protein is able to bind. Responses for 0:1 and 1:1 mixing ratios reproduced the previous observations (Figure 27), with a reduced binding rate but comparable equilibrium binding responses at 1:1 ratio compared to pure His_6CXCL12. The magnitude of the response is slightly larger owing to the increased concentrations used in this assay. Strikingly, no response at all was observed when the fluorophore was in excess (ratios 2:1 and 5:1). This indicates that OG488•HisCXCL12α is unable to bind HS, and that the slow binding response observed at a nominal 1:1 ratio is due to the presence of residual unlabelled HisCXCL12α.

Taken together, whilst the N-terminal His_6 tag alone does not result in a reduced functionality of CXCL12α, the further addition of a fluorophore OG488 to this site, forming OG488•HisCXCL12α, does

have a detrimental effect and abolishes the binding to HS. Therefore, this method has not resulted in the production of a fluorescently labelled protein that can be used for the study of diffusion in GAG-rich matrices.

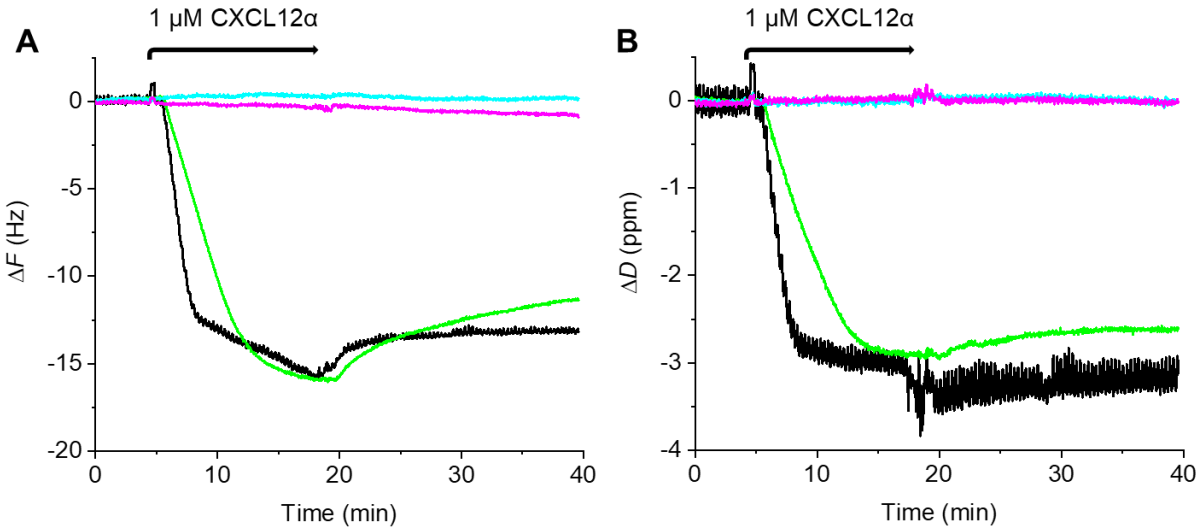


Figure 28. ***QCM-D Responses for Different Molar Ratios of OG488:HisCXCL12α Binding to HS Films.*** *A) Frequency shift (ΔF) responses for binding of OG488•HisCXCL12α at varying molar ratios to HS films: 0:1 (black), 1:1 (green), 2:1 (magenta), and 5:1 (cyan). B) Changes in dissipation (ΔD) due to binding. HS films formed in this experiment were comparable to those formed in Figure 18 (data not shown). Start and duration of incubation of CXCL12α is indicated by arrows above the graph. Concentrations for incubation: SUV (5 mol-% DOPE-CAP-B + 95 mol-% DOPC) – 50 µg/ml, SAv – 20 µg/ml, HS-b (nominal M_W = 12 kDa) – 10 µg/ml, CXCL12 – 1 µM. The fifth overtone is presented here, data was qualitatively comparable across all overtones. Note that this data set features some oscillatory noise (most pronounced for plain HisCXCL12α, but also appreciable for some other datasets); this is due to a different liquid flow control (peristaltic pump instead of syringe pump) being used, and whilst affecting the data quality does not affect the global trends seen.*

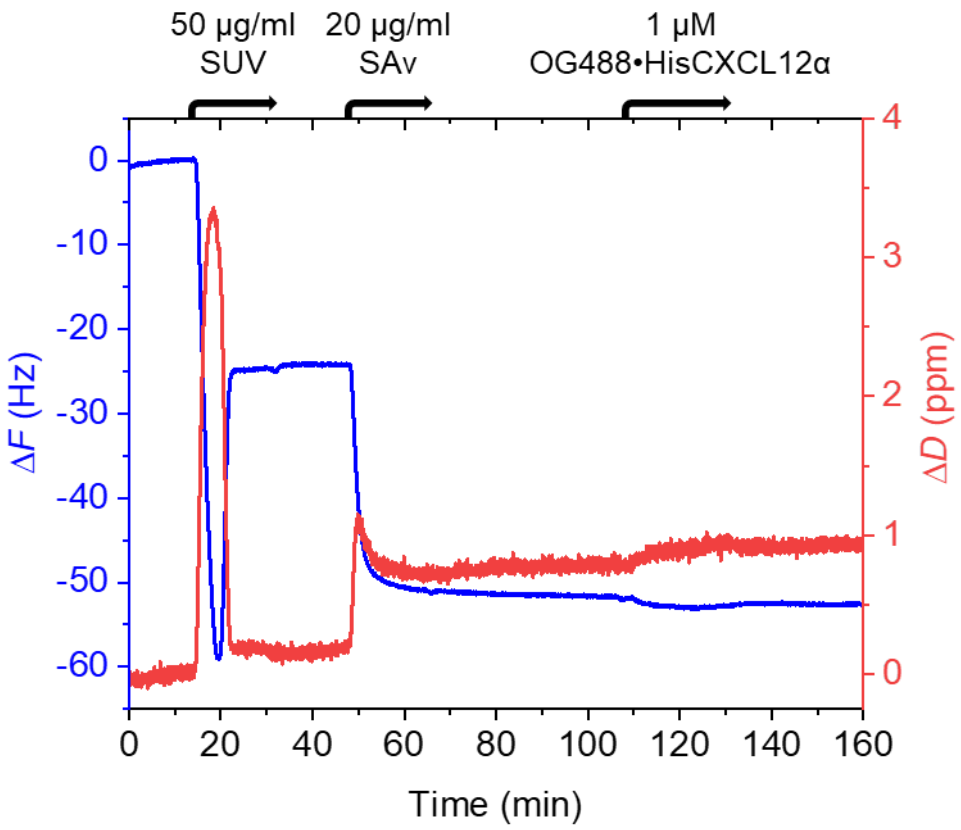


Figure 29. ***Nonspecific Binding of OG488•HisCXCL12α to SAv.*** *Shown are the frequency (ΔF, blue) and dissipation (ΔD, red) changes that accompany HS film formation (reproduced from Figure 18) and OG488•HisCXCL12α non-specific binding. Arrows indicate the start and duration of 5% DOPE-CAP-B – 50 µg/ml, SAv – 40 µg/ml, OG488•HisCXCL12α – 1 µM. The fifth overtone is presented here, data was qualitatively comparable across all overtones.*

3.3.2.2.2 Labelling of CXCL12α on the C terminus Affects HS binding

As previous assays had shown that labelling of CXCL12α at the N terminus can dramatically affect HS binding, other sites for labelling were considered. A labelled CXCL12α form is commercially available (from Almac) with Alexa Fluor 647 (AF647) site-specifically attached to a lysine residue, three amino acids from the C terminus and part of the native protein sequence. At the outset, this was not considered an ideal choice as it has been shown that the C terminus may be involved in HS binding for many chemokines, including CXCL12α (44, 55). However, following the results in Section 3.3.2, where a label on the N terminus affected binding despite no known role for the N terminus in HS binding, it was important to consider if the other end of the protein might be more amenable to labelling.

QCM-D was used to test for the binding of CXCL12α-AF647 to an HS film (Figure 30). At 500 nM, CXCL12α-AF647 bound to the HS film with an equilibrium frequency shift of -10 Hz, just 2.5 Hz less in magnitude than the wild-type protein. However, the binding rate was reduced by 2 fold, and dissociation was also enhanced, with binding being fully reversible for the labelled protein upon

rinsing in working buffer whereas the unlabelled CXCL12α retained a substantial amount of binding after 20 min of rinsing. There observations indicate that the affinity of CXCL12α-AF647 for HS is reduced compared to CXCL12α.

Despite the reduced affinity, CXCL12α-AF647 is able to cross-link HS as evidenced by the reduction in dissipation (by 1 ppm) upon protein binding. Any crosslinking achieved by the protein was also fully reversible, as observed through the dissipation shift to -1 ppm during incubation and back to 0 ppm upon rinsing. Compared to -2 ppm for the wild-type and an increase of 1 ppm after rinsing.

The nonspecific binding capacity of CXCL12α-AF647 to SAv was also tested (Figure 31). There were no changes in frequency or dissipation to the surface upon addition, indicating that there is no nonspecific interaction between CXCL12α-AF647 and the surface.

In summary, C-terminally labelled CXCL12α has the capacity to bind HS, but its interaction is altered by the label AF647, reducing the interaction affinity. Due to the ability of the protein to more readily dissociate in addition to the reduced binding rate, the equilibrium dissociation constant (K_d) of this protein to HS will be different, therefore, the diffusion within the HS matrix is likely to be altered. CXCL12α-AF647 thus proves sub-optimal to investigate the impact of GAG interactions on diffusion. See Chapter 5 for more details on the expected impact of the dissociation constant on diffusion in glycan-rich matrices.

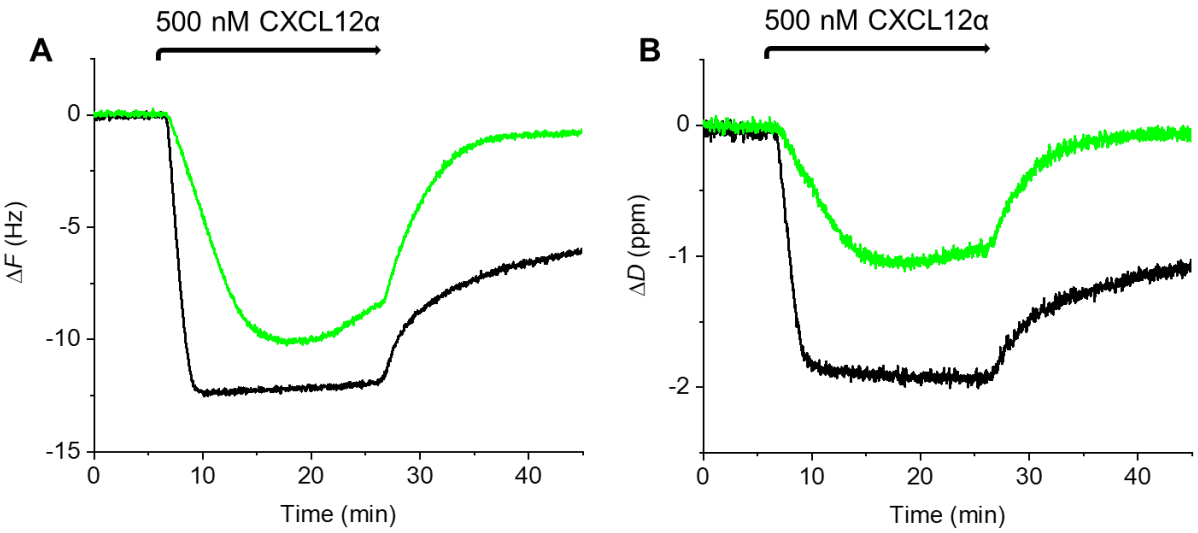


Figure 30. ***QCM-D Response for CXCL12α-AF647 Binding to an HS film*** *A) Frequency shift responses to binding of wild-type CXCL12α (black) and CXCL12α-AF6475 to HS films. B) Changes in dissipation due to binding. HS films formed in this experiment were comparable to those formed in Figure 18 (data not shown). Start and duration of incubation of CXCL12α is indicated by arrows above the graph. Concentrations for incubation: SUV (5 mol-% DOPE-CAP-B + 95 mol-% DOPC) – 50 µg/ml, SAv – 20 µg/ml, HS-b (nominal* M_W *= 12 kDa) – 10 µg/ml, CXCL12α – 500 nM. The fifth overtone is presented here, data was qualitatively comparable across all overtones.*

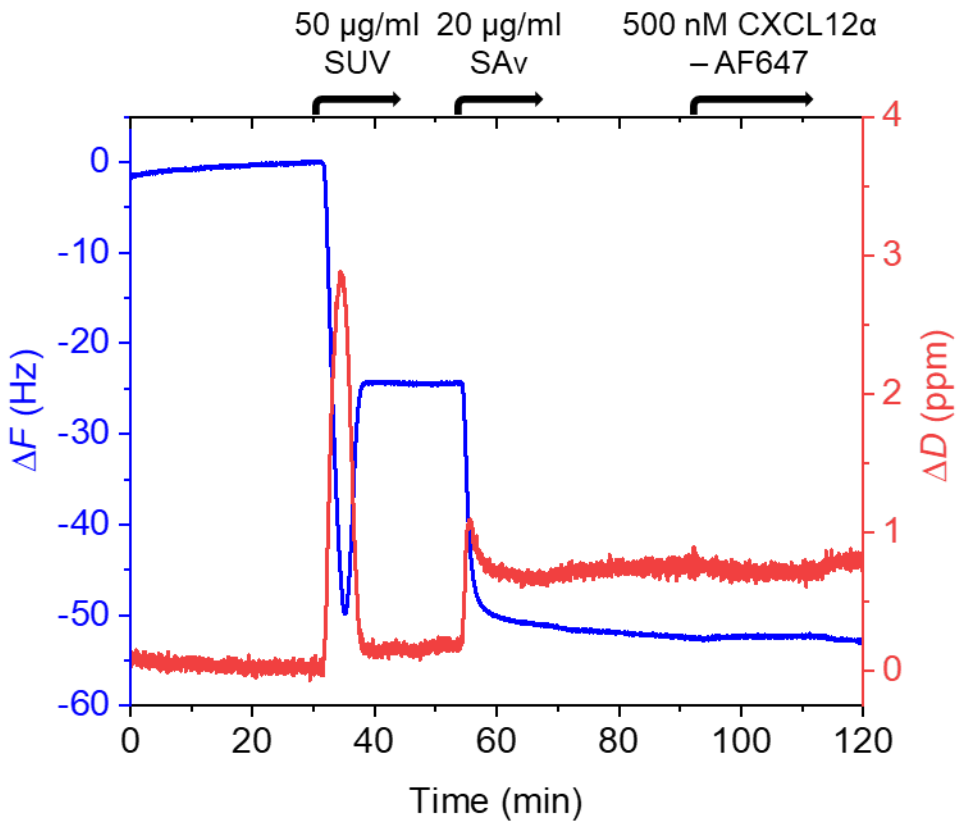


Figure 31. ***Nonspecific Binding of CXCL12α-AF647 to SAv.*** *Shown are the frequency (ΔF, blue) and dissipation (ΔD, red) changes that accompany HS film formation (reproduced from Figure 18) and OG488•HisCXCL12α non-specific binding. Arrows indicate the start and duration of 5% DOPE-CAP-B – 50 µg/ml, SAv – 20 µg/ml, CXCL12α-AF647 – 0.5 µM. The fifth overtone is presented here, data was qualitatively comparable across all overtones.*

3.3.2.3 Shiga Toxin

Chemokines are small proteins, consequently, added labels are more likely to be in close proximity of important functional domains on the protein. Larger, multimer proteins such as STxB may be more readily labelled without adverse effects due to a higher chance of being further from the important binding sites. A CXCL12 monomer has a size of around 2 nm and the pentamer of STxB has a diameter of 7 nm (41, 72). Therefore, STxB was selected as an alternative colloid to test for mobility in glycan-rich matrices upon fluorescent labelling.

Three different labelled STxB constructs were tested alongside unlabelled STxB: (1) His_6 tagged STxB (STxB-His), containing a polyhistidine tag on the C terminus of each of the 5 protomers in the pentamer, (2) wild-type STxB labelled via primary amines, (possible at Thr1, Lys8, Lys13, Lys23, Lys27, Lys53), with Alexa Fluor 488, either with one fluorophore per pentamer (20% labelled; $STxB\text{-}AF488_{20\%}$), or (3) with five fluorophores per pentamer (100% labelled; $STxB\text{-}AF488_{100\%}$), on average (127, 130,

131). STxB monomer has three binding sites for the Gb3 sugar moiety, all on the bottom face of the protein (Figure 32) (71, 151).

These molecules were tested by QCM-D for their binding to a mucin-like film containing the sugar moiety of the Gb_3 sphingolipid (Figure 33). The unlabelled protein bound to the film fully reversibly. An equilibrium frequency shift of -7 Hz was reached within 5 min of incubation, and the frequency rapidly returned to 0 Hz after rinsing with HBS. Moreover, there were no significant change to the dissipation and hence no strong cross linking of the film by the protein.

3.3.2.3.1 Labelling of STxB via NHS Ester Affects Gb_3 Binding

AF488 labelled StxB also bound to Gb_3 presenting films, albeit with distinct binding kinetics (Figure 33C-D). STxB-AF488 (20% and 100%) did not reach saturation within the timescale (20 min) of incubation. The AF488 label had a dose dependent effect on STxB binding to the Gb_3 presenting film. The rate of binding became slower as the amount of label on the protein increased. STxB-$AF488_{20\%}$ reached a final frequency shift of -14 Hz, and STxB-$AF488_{100\%}$ a final shift of -27 Hz. Both these constructs remained stably bound upon rinsing in working buffer.

This shows that the fluorophore changes both the extent to which the protein can bind to the glycan and also the ability of the protein to dissociate from it. One reasoning for this could be that although there are 5 lysine residues in a STxB monomer which may provide the primary amine, there is also the N terminal residue. The N terminus is in close proximity to the Gb_3 binding site (71). The N terminal residue is relatively easily accessible, which may increase the likelihood of the NHS-Ester reaction occurring at this site. If indeed the fluorophore attaches to the N terminus, the presence of a label in this location could provide steric hindrance to binding. Additionally, the maximum extent of labelling achieved was 5 labels per pentamer, if the labelling was possible on one of the lysine residues, it would be expected that a greater degree of labelling could be achieved as there would be more available primary amines that were labelled.

3.3.2.3.2 Labelling of STxB via C-terminal Polyhistidine Tag Affects Gb_3 Binding

StxB-His had a much steeper and greater decrease in frequency than unlabelled STxB, reaching a final frequency shift of -40 Hz (Figure 33A-B). Upon rinsing, only a partial increase of a quarter of the final frequency shift was observed. This shows that this protein bound more strongly than the wild-type. Furthermore, there was also a distinct decrease in dissipation indicating an increase in rigidity of the film. This is not seen in the wild-type protein binding and could indicate a different mode of binding. The polyhistidine tag for this protein is located at the C terminus, which is not known to be within proximity of the binding site (71, 130). Therefore, the reason for altered binding in this case is not clear.

Overall, these results demonstrate that it is not trivial to label STxB without impacting on its glycan binding function. Consequently, this protein was not pursued further. In light of consistent challenges with non-perturbing protein labelling, other non-protein colloids were considered instead.

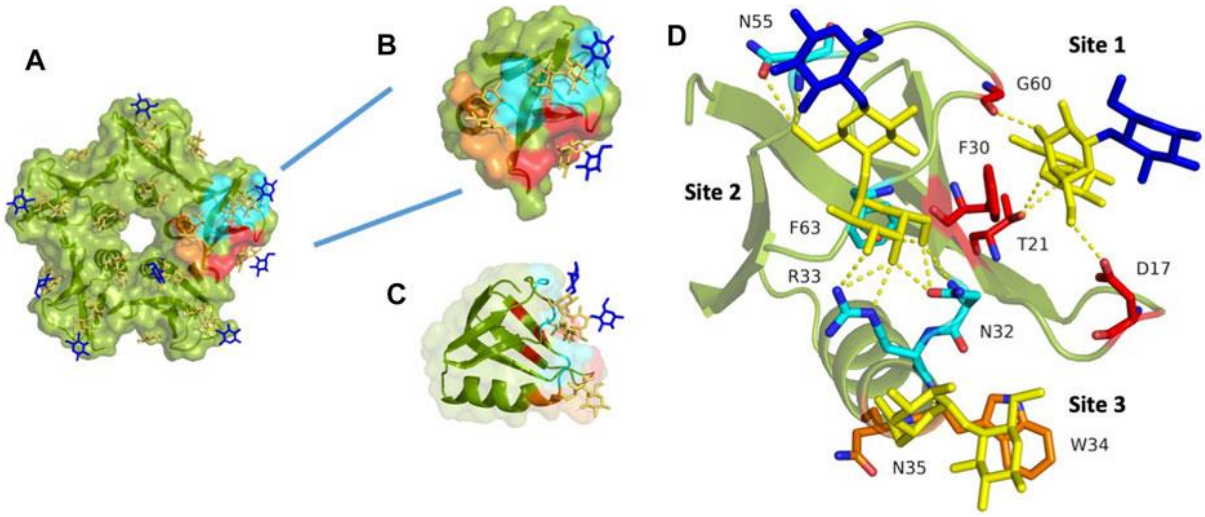


Figure 32. ***STxB and its Binding Sites for Gb_3.*** *A) The STxB pentamer with one monomer and its binding sites highlighted. B) Monomer STxB with bound Gb_3. C) The ribbon structure of the monomer STxB bound to Gb_3. D) The three binding sites in the monomer with both the interacting amino acid residues and Gb_3 in stick and a ball representation. Galactose is represented as yellow and glucose as blue. Taken from Ref. (151).*

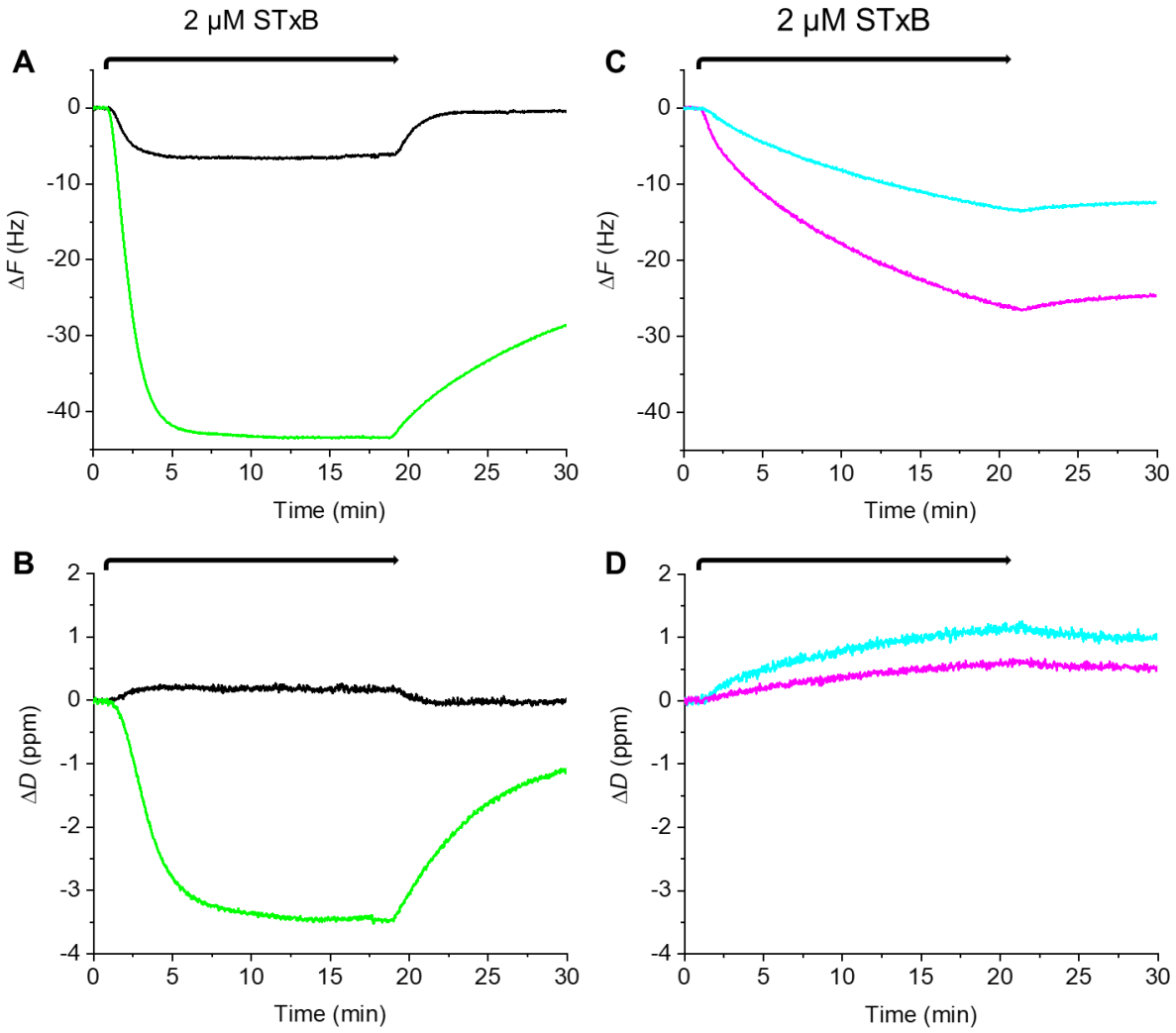


Figure 33. ***QCM-D Response of Different STxB Forms Binding to a Mucin-like Film.*** *A) and C) Frequency (ΔF) shift responses to binding of WT (black), His tagged (green), 100% labelled (cyan) and 20% labelled (magenta) STxB to a HA-g-Gb_3 film. B) and D) Dissipation (ΔD) shift responses due to the binding. The mucin-like film here consists of HA-g-Gb_3 monolayer on a supported lipid bilayer and Sav layer, consistent with Figure 24. Start and duration of incubation of respective materials are indicated by arrows above the graph. Concentrations for incubation: SUV (5 mol-% DOPE-CAP-B + 95 mol-% DOPC) – 50 µg/ml, SAv – 20 µg/ml, HS-b (nominal MW = 12 kDa) – 10 µg/ml, STxB – 2 µM (monomer). The fifth overtone is presented here, data was qualitatively comparable across all overtones.*

3.3.3 Fluorescently Labelled EUVs

Fluorescently labelled EUVs provide a visible colloid that can be used for single particle tracking due to their large size in comparison to proteins (30 and 50 nm). Their sizes are comparable to exosomes which need to traverse the glycocalyx to fuse with plasma membrane. The purpose of testing this EUVs is to investigate the impact of a glycocalyx with a defined pore size on the diffusion of inert molecules.

However, when the EUVs were applied to a SAv on SLB layer in QCM-D, the colloids bounds to the surface (Figure 34A). The frequency decreased by 10 Hz and the dissipation increased 2 ppm. These frequency and dissipation changes were stable upon rinsing indicating that these are not transient interactions. BSA is commonly used to passivated surfaces in QCM-D, it was applied to the surface after the formation of the SAv layer for 10 minutes (Figure 34B). BSA transiently changes the frequency and dissipation shifts but the surface returns to the previous baseline after rinsing. EUVs were then applied to the surface and stable frequency and dissipation shifts were observed, similar to the measurements without BSA (Figure 34B), although with a slightly attenuated binding (ΔF = -8 Hz and ΔD = 1.75 ppm).

An alternative method of passivation was used, by creating a layer of short HA chain. HA-b dp 15 (dp = degree of polymerisation and is equivalent to individual sugar units) was applied to the SAv layer (Figure 35) resulting in a frequency shift of -10 Hz and dissipation shift of 1.5 ppm. When EUVs were applied to this surface, there were no appreciable changes frequency or dissipation; therefore, the EUVs did not bind to this surface.

In this manner, an alternative method of passivation using a low molecular weight HA was created. As the planned use of EUVs was on surfaces of high molecular weight HA, which will have many biotin binding sites available after the film formation; the remainder of these sites can be filled with HA-b dp15 to prevent any non-specific interactions seen in Figure 34.

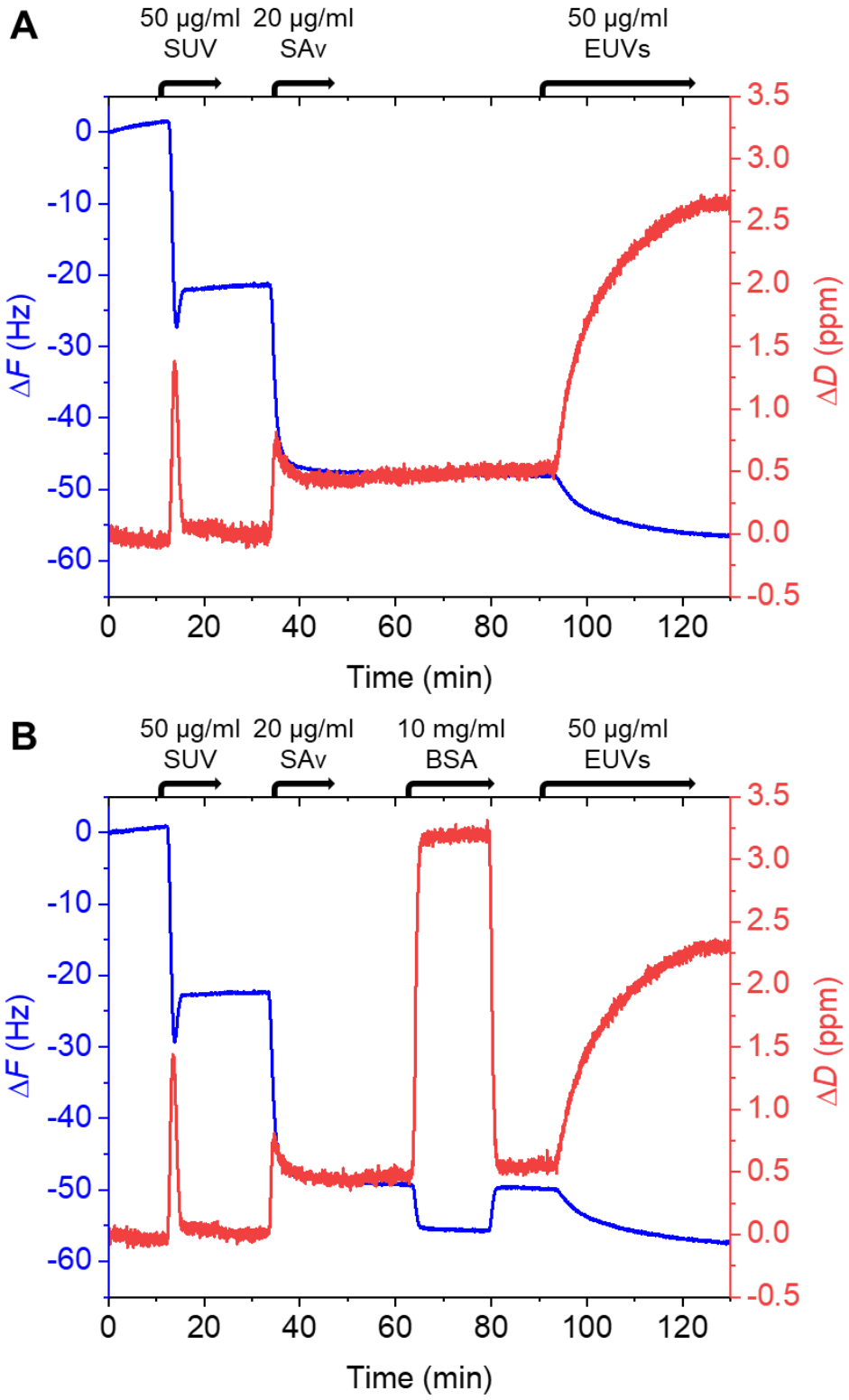

A
50 µg/ml SUV
20 µg/ml SAv
50 µg/ml EUVs
ΔF (Hz)
ΔD (ppm)
Time (min)
B
50 µg/ml SUV
20 µg/ml SAv
10 mg/ml BSA
50 µg/ml EUVs
ΔF (Hz)
ΔD (ppm)
Time (min)

Figure 34. ***Fluorescent EUVs Bind to SAv Monolayers.*** *Shown are the frequency (ΔF, blue) and dissipation (ΔD, red) changes that accompany SLB formation and SAv addition followed by the addition of EUVs (A) or passivation by BSA and then addition of EUVs (B). Arrows indicate the start and duration of 5% DOPE-CAP-B – 50 µg/ml, SAv – 20 µg/ml, BSA – 10 mg/ml, EUVs – 50 µg/ml. The fifth overtone is presented here, data was qualitatively comparable across all overtones. This data set was collected by Jelizaveta Pavljuk.*

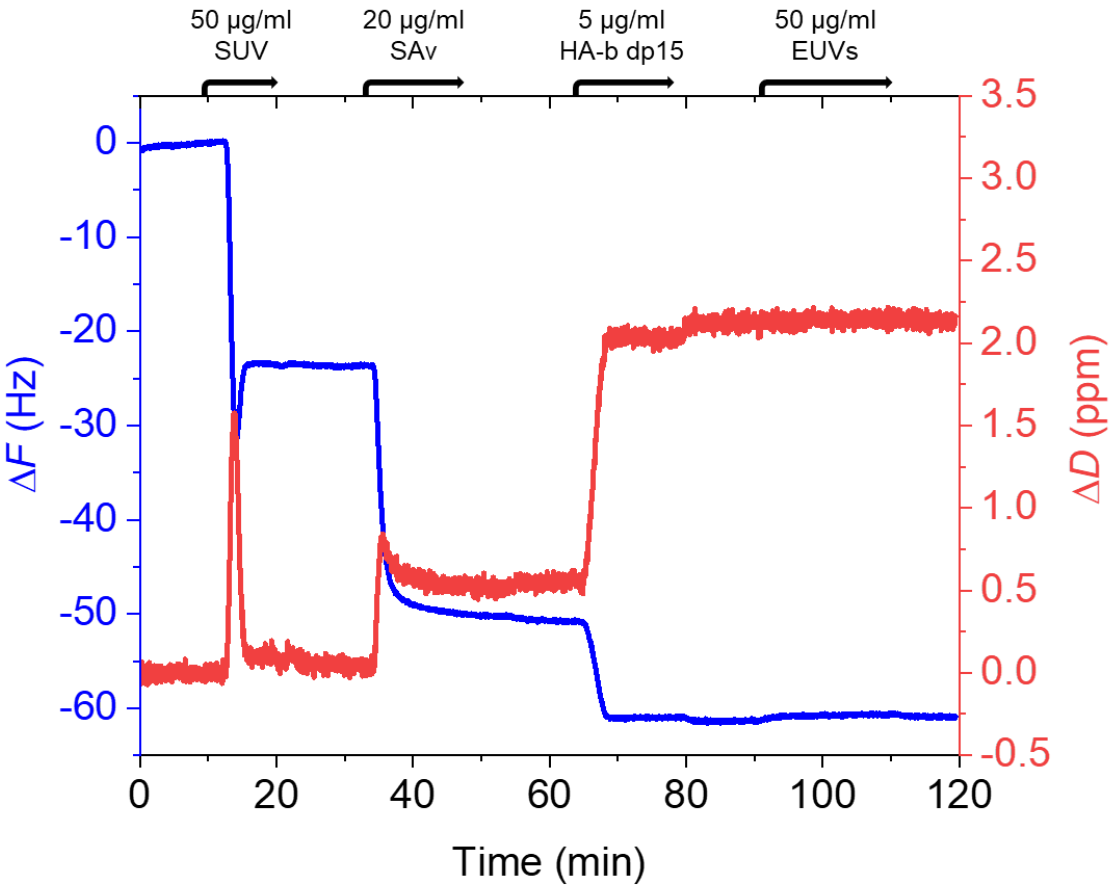


Figure 35. ***Fluorescent EUVs Do Not Bind HA-b dp15 Surfaces****. The frequency (ΔF, blue) and dissipation (ΔD, red) changes that accompany HA-b dp15 film formation followed by the addition of EUVs. Arrows indicate the start and duration of 5% DOPE-CAP-B – 50 µg/ml, SAv – 20 µg/ml, HA-b dp15 – 5 µg/ml, EUVs – 50 µg/ml. The fifth overtone is presented here, data was qualitatively comparable across all overtones. This data set was collected by Jelizaveta Pavljuk.*

3.3.4 Minute Defects in SLBs on Glass Affect the Interpretation of Protein Distribution Data

To study the diffusion of colloids in model matrices under microscopy, the HS films described in Section 3.3.1.1 were formed on glass surfaces following established protocols (41, 88) (Sections 3.2.7 and 3.2.9) before the addition of fluorescently labelled colloids. As part of the quality control of this, the SAv used to form the intermediate layer is labelled with Atto 565 (SAv-Atto565). This allows for

the lateral homogeneity of the surface coating, and the lateral mobility of SAv and any SAv-anchored glycans, to be assessed.

As part of the development of the fluorescence assay to colloid diffusion, OG488•HisCXCL12α was visualised by confocal microscopy on glycocalyx models made with 12 kDa HS-b (Figure 36A and B, left). Before data confirming that the fluorescently labelled chemokine did not bind HS, the appearance of OG488•HisCXCL12α on HS surfaces was interpreted as the formation of CXCL12α clusters (Figure 36A, left). This phenomenon was tentatively attributed to a sophisticated process of self-organisation of CXCL12α and HS, inspired by earlier data demonstrating that CXCL12α cross-links HS and suggesting that such a process is mediated by CXCL12α oligomerisation (38, 41, 100). However, subsequent controls revealed that the labelled OG488•HisCXCL12α does not bind HS (Figure 28), thus calling this interpretation into question. Moreover, when the labelled protein was applied to a plain SAv monolayer (with any anchored HS-b) and visualised via microscopy, a similar pattern was observed (Figure 36, right panel in both A and B). Upon closer inspection (Figure 36, white arrows), it was found that very small dark spots in the SAv-Atto565 layer correlated with the bright spots of OG488•HisCXCL12α accumulation. A plausible explanation for these effect is that minute defects in the supported lipid bilayer, exposing the glass surface beneath, enable the non-specific binding of OG488•HisCXCL12α to glass.

Further tests by epifluorescence microscopy confirmed that OG488•HisCXCL12α readily binds to a plain glass surface (Figure 37). This may be due to a charge interaction, given that glass surfaces carry some negative charges and CXCL12 is positively charged. This non-specific binding response could be reduced by passivation of the glass surface with casein prior to OG488•HisCXCL12α incubation. Casein passivation was also shown to reduce the visibility of the punctate pattern and the overall level of background fluorescence on SAv monolayers and HS films. These data clearly show that the non-specific binding of OG488•HisCXCL12α to defects in SLBs needs careful consideration in assay design, and that such undesired binding can be circumvented through Casein passivation.

It may here be noted that prior QCM-D analyses had found no significant binding of OG488•HisCXCL12α to SAv-on-SLB films on QCM-D sensors (Figure 29) prepared similarly to the SAv-on-SLB films on glass for microscopy analysis. There are two main reasons for this: the proportion of CXCL12 bound directly to the surface is very small, smaller than can be detected by the QCM-D, or that the surfaces formed are different. There has been some evidence to suggest that bilayer formation on glass is different to silica wafers (92) and this data may suggest that to be true. However, more evidence is required on this. Furthermore, the SLBs used in Figure 35, Figure 36 and Figure 37 had a 10% lower level of biotinylated lipids within the mixture. It is possible that the reduced coverage

of SAv leads to the underlying surface being more accessible for the chemokine and this is why the binding was not detected in the earlier experiment.

These data provided key evidence that inspired the experiment shown in Figure 28 which revealed that the fluorescent label on CXCL12α did perturb its binding to HS. These data also show that OG488•HisCXCL12α binds to glass, this may be due to electrostatic interactions as OG488•HisCXCL12α is positively charged and glass is negatively charged (152). This type of phenomenon may apply to other positively charged proteins, however, this is may not be a problem in every case. For this case, as the distribution of the CXCL12 was the key interest, it means that interpretation of the fluorescent signal is the key aspect of analysis. If the focus was on the mobility of the GAG chains, such as previous studies (38, 41, 100), the binding of protein to the glass is trivial as it does not impact on the mobility of the SLB and GAGs on the surface.

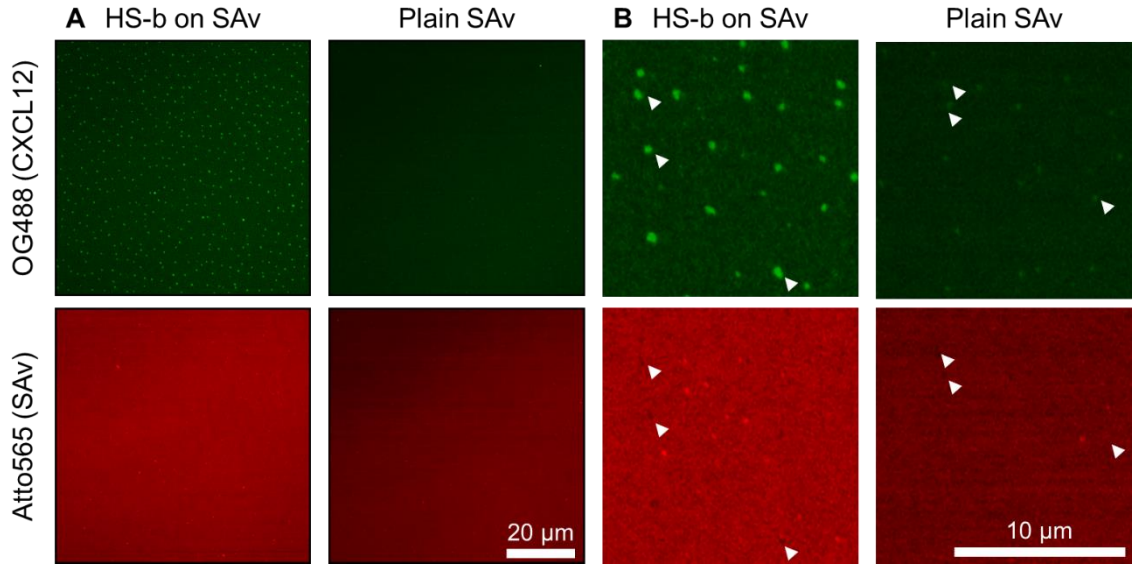


Figure 36. ***Airyscan Confocal Images of CXCL12α 'Clusters'.*** *A) Full field of view of OG488•HisCXCL12α on an HS film and a SAv monolayer. B) Zoomed in view of the images in A) to appreciate smaller features. OG488•HisCXCL12α is visible in the 488 illumination and SAv-Atto565 is visible in the 565 illumination. Image brightness and contrast have been modified to improve visibility, with consistency across images. OG488•HisCXCL12α was incubated at a concentration of 500 nM and rinsed with HBS before imaging. Supported lipid bilayers in this assay contain only 0.5 mol-% DOPE-CAP-B and 99.5 mol-% DOPC, resulting in approximately 50% coverage of SAv-Atto565; this conditions was chosen to avoid SAv crystallisation and thus maintain lateral mobility of SAv (and anchored HS-b).*

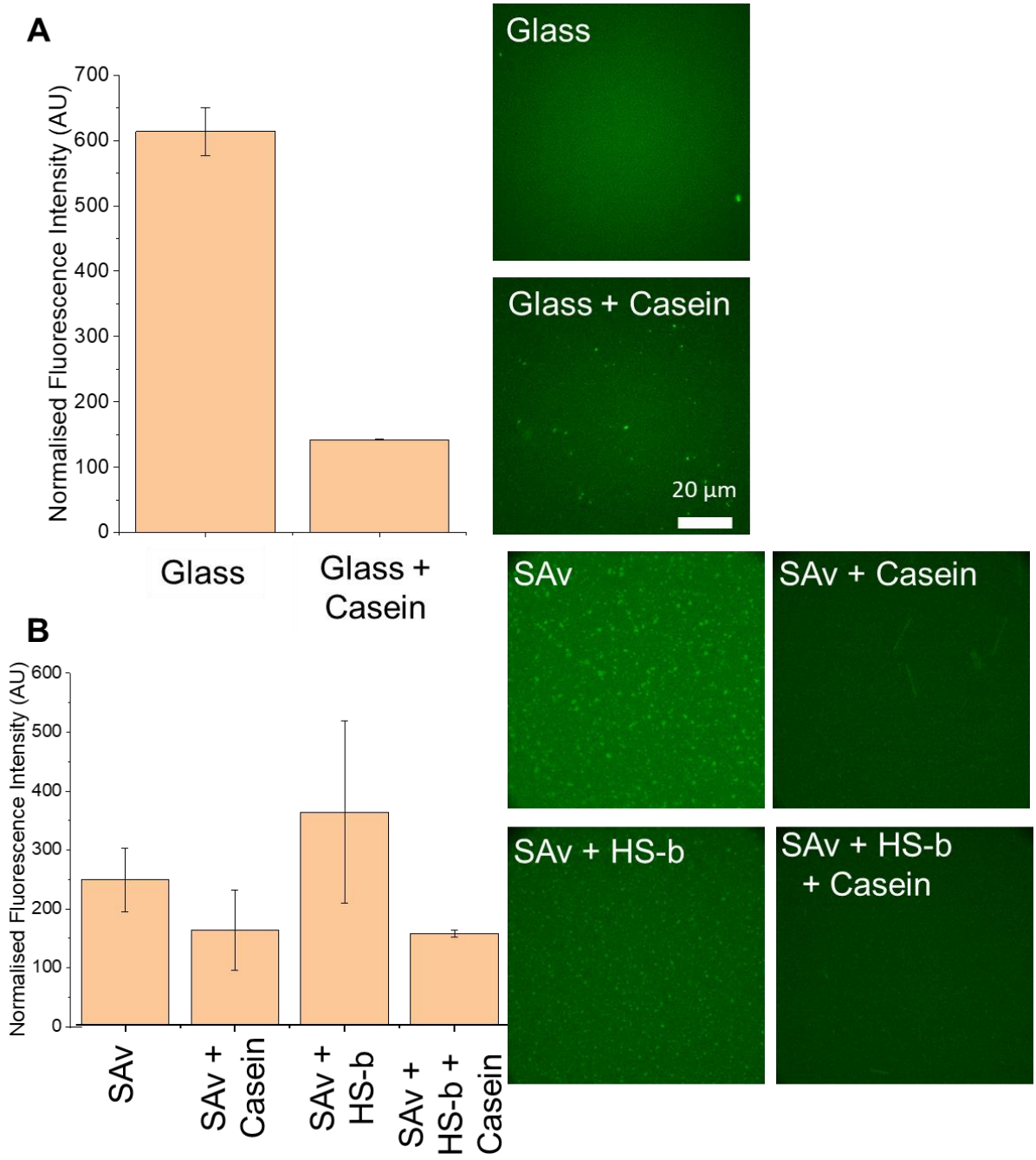

A
Normalised Fluorescence Intensity (AU)
700
600
500
400
300
200
100
0
Glass
Glass + Casein
Glass
Glass + Casein
20 µm
B
Normalised Fluorescence Intensity (AU)
600
500
400
300
200
100
0
SAv
SAv + Casein
SAv + HS-b
SAv + HS-b + Casein
SAv
SAv + Casein
SAv + HS-b
SAv + HS-b + Casein

Figure 37. ***Epifluorescence Microsocopy Analyses of OG488•HisCXCL12α on Glass.*** *A) Left, quantitative analysis of the 488 epifluorescence images (right). Condition 1 OG488•HisCXCL12α on glass, condition 2 is casein passivated glass. B) The same as above with OG488•HisCXCL12α applied to varying conditions: SAv monolayer, SAv monolayer passivated with casein, 12 kDa HS film, four 12 kDa HS film passivated with casein. Image brightness and contrast have been modified to improve visibility, with consistency across images. OG488•HisCXCL12α was incubated on the surface at a concentration of 500 nM and rinsed with HBS before imaging. SLBs were incubated for 30 min at 100 µg/ml, SAv was incubated for 20 mins at 40 µg/ml, HS-b for 20 mins at 10 µg/ml. Casein passivation was performed at 20 mg/ml for 10 mins. Error bars represent standard deviation, N = 3 areas within the same well. Bilayers formed in this experiment contain only 0.5% DOPE-CAP-B in order to allow for lateral bilayer mobility (as in Figure 36). The background intensity was subtracted to create the normalised fluorescence intensities.*

3.4 Discussion

Within this chapter, data has been presented showing the different types of model glycocalyces that can be formed, including HS and Gb3-linked films, the ways that they can be modulated and the information that can be extracted such as concentration, contaminants the number of disaccharides, film thickness, and the coverage of molecules on the surface. Three different colloids (including CXCL12s, StxB, and EUVs) were labelled with fluorescent tags and their suitability for investigating diffusion under different circumstances. Methods were generated for the passivation of surfaces to prevent non-specific binding on glass and SAv surfaces. The results also demonstrate that labelling biological colloids without perturbing their functions remains a challenge, and that analysis of data derived from such colloids needs to be cautious.

3.4.1 Generation of Different Glycocalyces

Three different model matrices were generated within this study a matrix of 12 kDa HS-b, matrices of 33 kDa HS-b with different percentage coverages of HS-b, and different molecular weight HA matrices with different anchor distances. All of these data are continuations of already published studies and reinforce ideas presented within them (88, 91, 101, 121, 141). These data also provide confidence in the designs of the matrices used later within this thesis, providing relevant controls and context to understand other data.

In Section 3.3.1.1.2, the surface coverage of 33 kDa HS-b was modulated by the addition of excess biotin. A new method was presented that allows for the calculation of the concentration of HS that has been applied to the surface. The percentage coverage should have scaled linearly with the maximal frequency shift achieved for different ratios of HS-b and biotin, but it did not. By altering the input concentration of HS-b which changes the estimated percentage coverage of HS, it was clear that the input concentration of HS was incorrect. This meant that the stock concentration of HS was also not correct. This highlights the importance of accurate concentrations of individual molecules and showed what the value should have been. Going forward, if the percentage coverage must be exact then it is worthy to define the concentration of the HS-b well beforehand.

Modulating the surface coverage of GAGs in the model matrices has many wide ranging uses but one that is relevant to immune system signalling is the being able to generate matrices that replicate immune states. Evidence suggests that proteoglycans in the ECM shed from endothelial cells during states of inflammation (37). Therefore, it would be possible to use the modulation of surface coverage to replicate these inflammation states and observe differences this impact has on the binding of molecules and their diffusion in future experiments.

The data in Section 3.3.1.1.1 showed that the length of HS chains has decreased over time. The molecular weight of HS had decreased from ~12 kDa to ~10 kDa over a period of 5 years. This is a significant change and is likely also applicable to other GAGs produced and stored in this way. This highlights that it may be worthy for others working with GAGs stored for long periods of time to do this analysis if the exact molecular weight or number of disaccharides is vital within the investigation parameters. The reasons for this degradation are not clear

3.4.2 Molecular Mechanisms for Altered Binding

This chapter has also highlighted the difficulty of maintaining the glycan binding capabilities of molecules once labelled for CXCL12 and STxB. These have wide implications for many facets of research.

The exact mechanism for the attenuation of HS binding for the labelled CXCL12α is not known. For the C terminally labelled CXCL12, it is unlikely to be the position of the label as the Histidine tag did not seem to affect binding, only the addition of the fluorophore itself. The Tris NTA fluorophore does have two negative charges within the Oregon Green motif (132). CXCL12 binds to HS through a BBXB amino acid motif, the basic amino acids are lysine and histidine, the latter of which can shift from being positively charged to neutral when the pH of the solution changes (52, 153). It is possible that the addition of negative charges within close proximity has changed the charge on the histidine residue and attenuate the BBXB motif that is required for binding.

The mechanisms for perturbation of the binding of HS for the N terminally labelled CXCL12α is less clear as the labelled protein does bind to HS, but in a different manner. Therefore, the binding is not eliminated but changed. The subsequent residues on the N terminus of CXCL12 isoforms that increase the affinity of the protein to HS (26). It is possible that the fluorophore occludes some residues but not others. Therefore, the protein may be able to bind due to the availability of some residues, but it cannot remain bound due to the unavailability of others. Furthermore, the protein is labelled on lysine residue 64, a change to residue 65 (alanine) results in the formation of a locked dimer (41). Dimerization increases the ability of CXCL12 to bind and crosslink HS (41), the labelled residue being in close proximity to the residues involved in dimerization could lead to the prevention of dimerization formation. Therefore, the CXCL12-AF647 may be analogous to a locked monomer form of CXCL12. A partial monomer form of CXCL12 does bind fully reversibly in a similar way as observed in Figure 30.

Due to the importance of glycan binding within this body of work, the controls for the usability of the binding molecules were tested specifically with a robust biophysical method and in an environment where there was little ambiguity for the reasoning behind the observed responses, due to the nature of the model extracellular matrix. In this case, it was observed clearly that the molecules would not

have the required capabilities for this study. However, considering that labelled molecules are frequently used for *in vitro* work, where there are many factors that may be at play that have not necessarily been considered. For example, Gutjahr *et al.* produced a study in which Atypical Chemokine Receptor 1 plays a role in the regulation of CXCL12 by using a fluorescently labelled protein on transfected MDCK cells (154). However, they had not tested for this labelled proteins binding to glycosaminoglycans. As the cells will produce their own pericellular matrix that contains GAGs, it is possible that this labelled CXCL12 has attenuated GAG binding, leading it to be more available for binding its other binding partners. This could lead to an increased binding to receptors than would be expected for wild-type chemokines and may skew results.

The mechanism behind the attenuated binding of the primary amine labelled STxB is likely due to the label position being the amino acid threonine 1. This amino acid is involved in the second binding site interactions with the Gb_3 sugar moiety (71). Although additional experiments would be required to verify this.

Furthermore, protein-glycan interactions are often largely influenced by hydrogen and van der Waals bonds (155). These are highly dependent on the environment such as pH and local charges, so it is very plausible that additional chemical groups in close proximity to binding sites could have effects on these components of protein-GAG binding. This also highlights the requirement for control experiments for testing labelled molecules in the exact environment that is under investigation. For example, Jabeguero *et al*., found that the His tagged form of STxB interacted as expected with a Gb_3 presenting supported lipid bilayer (124). However, this form of Gb_3 extends from the surface in a different way than the HA-g-Gb_3 tested here, as it is integrated into the lipid bilayer itself, indicating that the binding may also be orientation dependent (124, 127).

Overall, these data sets serve as a caution notice for others investigating GAG-binding proteins and attempting to label them. Although not a biological insight, it has multiple impacts on the interpretation of data, which is a nontrivial part of science.

3.4.3 The Importance of Defects in SLBs

Furthermore, this collection of data also reveals the importance of testing systems thoroughly through a variety of different measurements. In previous publications using a model ECM on glass for microscopy assays, the bilayer was assumed to be homogenous and covering the entire surface (41, 88). However, data revealed here showed that there are minute defects in the surface. These defects were not discovered earlier as standard confocal microscopy images do not reveal the very small defect areas, these were only observed with the increased resolution of the Airyscan method. This is not to say that this detail was overlooked. In fact, the previous studies may not have been impacted

by this phenomenon at all. These studies focused on the mobility of GAGs through the mobility of the SLB (41, 100). Minor defects in the bilayer do not affect the mobility of the surrounding molecules, the interpretation of these data remains the same regardless of the presence of minute defects. The correlation between the dark spots in the SAv monolayer and the bright spots caused by the fluorescently labelled CXCL12 was not revealed until careful investigation under airyscan confocal microscopy, a super resolution technique. However, without a fluorescent molecule that can bind to the glass surface and produce an unexpected pattern, these defects may have been left undiscovered. Along these lines, if there are minute defects in the bilayer and the molecules of interest do not bind them, this also does affect the interpretation of data. Therefore, there are cases where the defects are worth considering and cases where it is not. If the analysis of distribution data is to be undertaken, then this could introduce artefacts into the interpretation. If the molecule binds equally the surface and the binding partner and the type of analysis is independent of the locations of molecule and it does not affect other parameters, then this is not a concern. In the future, it would be pertinent to dedicate an investigation of what situations the minute defects would be of concern.

Overall, the data in this chapter has provided evidence on the robustness of glycan film formation on SLB surface and methods to modulate them. They also added evidence to show that parameters that directly affect the interpretation of data should be considered for control experiments before interpreting data as having biological significance. For example, if nonspecific binding of a fluorescent molecule will impact the interpretation of microscopy data then that binding should be investigated. However, the glycocalyx models shown here also highlight how many aspects of the models can be defined and modulated which gives an added element of control and certainty to the experiments, such as the exact defining of the polymer molecules through size and concentration, and the change in the coverage of the molecule on the surface. This chapter gives an indication of how depth and additional analysis can give information that is helpful and, sometimes, required to be able to interpret data fully and without bias. In addition to this, in this case, without performing additional tests, some of the data presented here would have implied that chemokines form dense clusters in the extracellular matrix, but considering the additional evidence, a false claim has been prevented.

Chapter 4: Plane Sphere Confinement Microscopy to probe Diffusion within Model Glycocalyces

4.1 Introduction

There are many types of biological colloids that diffuse through the ECM as part of their function and many of these colloids have been investigated using model matrices that are solvated films which tend to be tens to hundreds of nanometres thick (38, 41, 80, 88, 121). The model matrices allow for a strictly controlled environment of the type of matrix components present (GAGs of defined size and sulfation) and the density and concentration of the components. This is beneficial compared to analysis on tissues, the ECM is notoriously heterogeneous and therefore on tissues, it is difficult to define the exact components (4, 88). The particular ECM type that is of interest here is the glycocalyx, it is glycan rich and thin, providing barriers to cells. There are currently limited methods to analyse the diffusion within the glycocalyx and the mechanisms underlying diffusion are unknown.

In a standard confocal microscopy set up, the confocal depth is typically larger than the height of these films (122). This results in multiple types of movement occurring simultaneously in the detection volume (Figure 38). Firstly, the diffusion within the bulk solution, methods to analyse diffusion in solution are well established and information on this is readily accessible (156, 157). Secondly, the exchange between the bulk solution and the film. This is a parameter that may be of interest in some cases when considering the movement of a molecule into an area that differs from its source. Although, it is important to consider that bulk solution does not commonly exist *in vivo*. This type of movement has been previously considered and modelled in the context of polymer films (158). Furthermore, binding and unbinding rates of films have well established experimental methods such as QCM-D, SPR, and SE (38, 41, 104, 121, 159). Finally, diffusion within the film is the main parameter of interest. In standard microscopy, these three types of movement are difficult to separate, making it challenging to quantify in-film diffusion. This has led to the development of Plane Sphere Confinement Microscopy (PSCM).

In PSCM, a spherical surface with shallow curvature is brought into contact with the planar surface, to define a confined volume near the contact with a gradient of gap heights in the range of 10s to 100s of nanometres over lateral distance in the range of 10s to 100s of micrometres. The radius of curvature is large, enabling the formation of the shallow gradient. The planar surface and/or the curved surface are coated with the film of interest, and surface-to-surface contact results in a defined film compression gradient (Figure 38). This geometry causes bulk solution to be completely excluded for gap heights that are smaller than the film thickness. In this range of gap heights, analysis of lateral colloidal diffusion within the film as a function of film compression becomes possible. Yet, at the same time the film is in contact with the bulk solution at larger gap heights. In this manner, in-film diffusion of can be measured separately from bulk diffusion, whilst enabling equilibrium distribution of colloids between the film and the bulk solution.

A first version of PSCM was established recently (122), and applied to study the diffusion of globular proteins in brushes of intrinsically disordered protein domains rich in phenylalanine–glycine motifs (FG domains), a transport process that is important for nucleo-cytoplasmic exchange of macromolecules across the nuclear pore complex. The study demonstrated quantitation of the partitioning of fluorescently labelled colloids between the brush and the bulk solution as a function of film compression, and quantitation of the in-brush diffusion coefficient of the colloids by FRAP. This is the first, and so far the only application, of PSCM.

The first PSCM prototype (122) had a notable shortcoming. A micromanipulator with a long arm was used to approach the hemi-spherical cap of a glass rod (used as the curved surface) to the planar surface. This approach provided limited control on the compression force (and thus the exact geometry) of the plane-sphere contact. It also was prone to temporal perturbations of the plane-sphere interface (and thus local perturbation of the surface coating) by external noise and vibrations.

In this chapter, the main aims were to improve the PSCM design for robust use on glycan-rich model extracellular matrices, and to demonstrate the analysis of diffusion of a biological colloid within such a model matrix. This was achieved by selecting a model matrix that with features compatible with PSCM such that damage introduced to the system by the plane-sphere contact did not impact on the diffusion measurements, and changing the method of creating the contact between the curved and planar surfaces such that the compression force was well defined. As a proof-of-principle application, the diffusion of Extruded Unilamellar Vesicles (EUVs) within an HA brush was measured by single particle tracking as a function of the gap height (that is, HA brush compression).

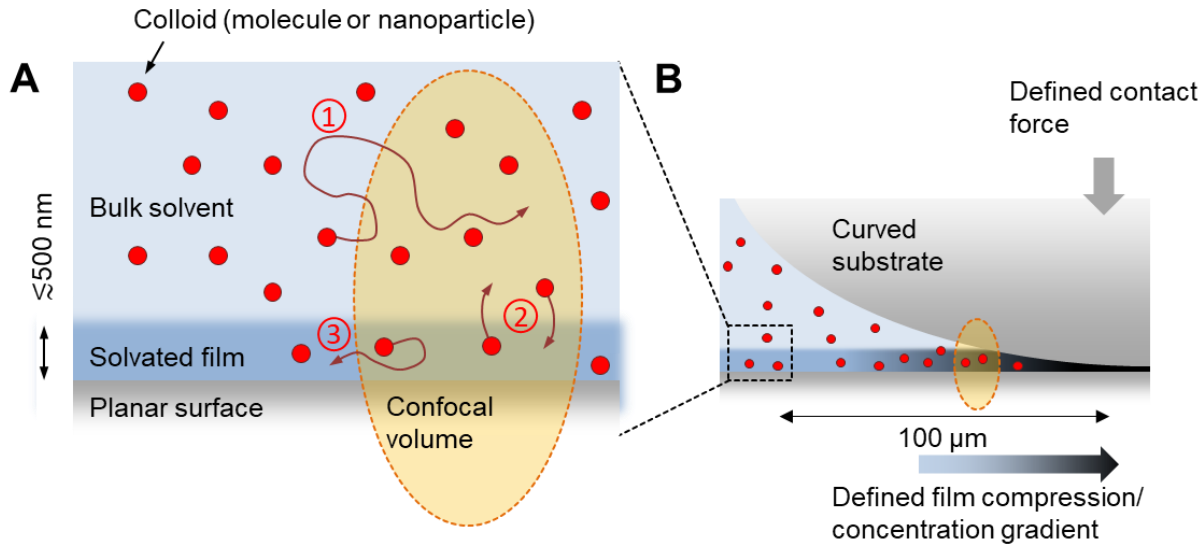


Figure 38. ***The Types of Diffusion Measured in Standard Microscopy on Thin Films, and How PSCM Enables Analysis of In-Film Diffusion.*** *A) A solvated film is formed on a planar surface, bulk solvent is present above the film and colloids are diffusing within (and partitioning between) the film and the bulk solvent. The different types of movement present are labelled: ① – free diffusion within the bulk solution, ② – exchange between the bulk solution and the film, ③ – diffusion with the solvated film. B) An image of a curved surface in contact with the planar surface, with one surfaces covered by a solvated film. Adapted from Ref. (122).*

4.2 Methods

4.2.1 Materials

EUVs containing 89 mol-% DOPC, 10 mol-% DOPS (Avanti) and 1 mol-% beta-BODIPY FL C12-HPC were produced in accordance with Section 3.2.10 and extruded with membranes of size 50 and 30 nm, EUVs are referred to by these sizes. SAv labelled with an Atto 565 fluorophore (SAv-Atto565) were sourced from Sigma-Aldrich. Glutaraldehyde was sourced from Merck. HA-b (840 kDa) was quasi-monodispersed with sizes of 280, 520, and 840 kDa and provided by Hyalose (Oklahoma City, OK, USA). HA-b dp15 was produced by Dhruv Thakar (CNRS, Grenoble, France).

4.2.2 Manufacture of Glass Rods with Hemi-spherical Caps

Glass rods with hemispherical caps were produced in-house. Long borosilicate glass rods (type 1 class A, VWR) of 3 mm radius were cut into Sections of 3 to 4 cm length. Each of the two blunt ends was molten through exposure to heat with an acetylene torch (Turbo Set 200INC, Oxyturbo) until a droplet formed. The rod Sections were left to cool down in ambient air, and cleaned with ultrapure water. The smoothness of the cap was previously established on a nm scale (122).

4.2.3 Assembly of a Motorised Cantilever for Gentle Plane-Sphere Approach

Materials for the motorised cantilever were purchased from Pimoroni Ltd (Sheffield, UK) and consisted of the following: Micro Metal Gearmotor (Extended Back Shaft) 1006:1, Micro Metal Gearmotor (Extended Back Shaft) 298:1, Pololu Universal Aluminium Mounting Hub for 3 mm Shaft #4-40 Holes, and 1x Micro Metal Gearmotor Bracket Pair. The cantilever itself was made from materials from LEGO (Billund, Denmark). These are shown in conjugation in Figure 39.

This was assembled by the by the Electronics Workshop at the School of Physics and Astronomy, University of Leeds. The two gearboxes were linked in series to allow a sufficiently slow movement of the lever arm with the set speed of the motor. A Tenma Power Supply 72-10480 (Tokyo, Japan) controlled the motor.

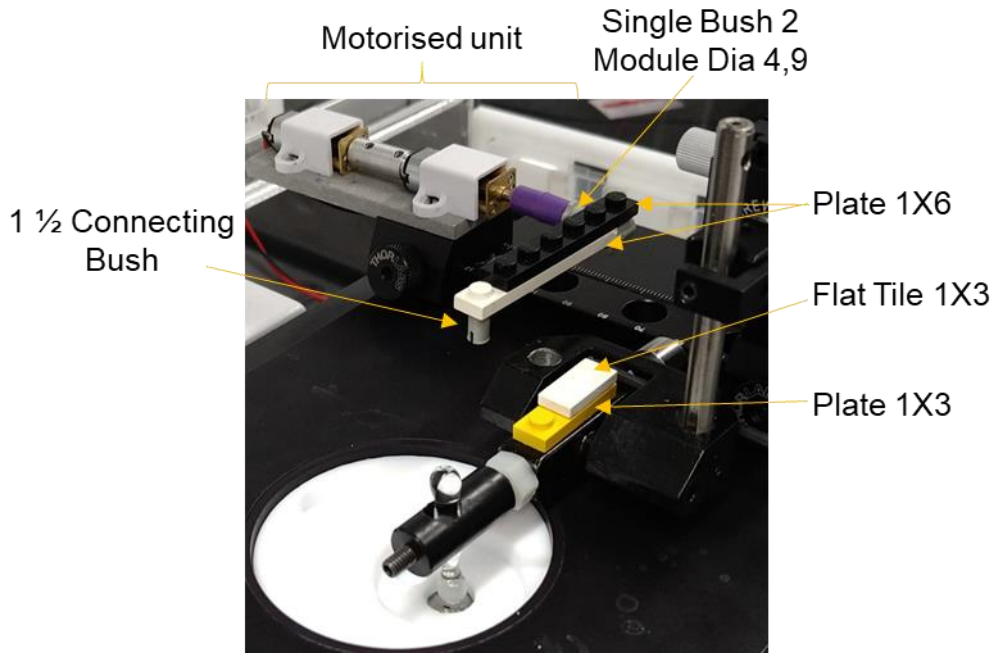


Figure 39. ***The PSCM Motorised Cantilever.*** *The motorised unit as it sits in conjugation with the rest of the PSCM set up as well as the cantilever (not in contact with beam mount). The Lego pieces that form the cantilever and attached to the beam mount are labelled.*

4.2.4 Dynamic Light Scattering (DLS)

DLS was used to quantify the hydrodynamic radius *r* and the size distribution of EUVs. Dynamic light scattering analyses the intensity of scattering signals from particles in solution. The intensity is fit with a temporal autocorrelation function which provides information on the diffusion coefficient of the particle, h allowing for a distribution of the hydrodynamic radius (*r*) to be calculated. This enables the production of histograms with intensity or number weighted values as a function of diameter in nm.

DLS analyses were performed by Dr Ralf P. Richter. EUVs were diluted to 50 µg/ml in HBS (filtered with 0.2 um pore size membrane) before DLS analysis. Experiments were performed with a Zetasizer Nano system (Malvern) in plastic cuvettes with a sample volume of approximately 1 mL, at a temperature of 23 °C. Three sets of data were acquired for each sample. All DLS data for EUVs could be well fitted as a monodisperse solution. The peak value and standard deviations reported here are based on number-weighted data.

4.2.5 Cleaning and Functionalisation of Surfaces

Glass rods with hemispherical caps were Piranha treated (1:3 (*v/v*) mixture of hydrogen peroxide and concentrated sulfuric acid), and exposed to UV/ozone for 30 minutes immediately prior to use.

Planar surfaces were formed as described in Sections 3.2.6 and 3.2.8 using a dedicated PSCM Teflon well that creates a single well of 300 µl. The Teflon well was cleaned and the glass coverslip mounted

to the Teflon well. The surface formation was then performed within the single well with concentrations and incubation times the same as those presented in Sections 3.2.6 and 3.2.8. The rinsing was performed with 10 times 600 µl to account for the additional volume in the well.

After surface functionalisation, the solution was exchanged with 10 mg/ml BSA in HBS. The Teflon well with the sample was installed into the PSCM unit on the microscope. The rod was then installed into the Force Exertion Unit (FEU). After installation of the rod, it was brought into contact with the BSA containing solution within the well and was incubated for 10 minutes to passivate the rod surface. The surfaces were then rinsed 15 times with HBS (600 µl) to deplete residual BSA from the solution.

4.2.6 Optical Microscopy

Fluorescence microscopy and reflection interference contrast microscopy (RICM) were performed with an Axio Observer 7 inverted epi-illumination microscope, equipped with an EC Plan NeoFluar 63x/1.25 Ph3 Antiflex Oil Objective (ZEISS) with a Hamamatsu Camera using OTOVAR 1 (Pixel size = 0.103 µm). Microscopy images were acquired in ZEN Blue (ZEISS). All microscopy images were analysed in Fiji ImageJ (139).

4.2.6.1 Fluorescence Microscopy

SAv-Atto565 was detected using LED illumination (25% intensity) at 555 nm with excitation filter 545-565 and emission filter 579-604 nm. EUV-BODIPY was detected using LED illumination (50% intensity) at 475 nm with excitation filter 450-490 nm and emission filter 500-550 nm. All fluorescence micrographs were acquired without camera binning, giving a scaling factor of 0.103 µm per camera pixel. The exposure time was set to 20 ms.

Time series for tracking of EUV diffusion were obtained at a rate of 16 frames per second, for 20 frames (1.25 s) or 200 frames (12.5 s).

4.2.6.2 Reflection Interference Contrast Microscopy

RICM images were obtained using LED illumination at 475 nm, 555 nm or 630 nm (as specified) and a dedicated reflector cube containing two cross-polariser filters and a 50/50 intensity beam splitter. Together with the quarter wave plate installed in the objective, the system of crossed polarisers filters reflected light and blocks scattered or background light thus maximising contrast (118). The aperture diaphragm was kept minimally open, to minimise the range of angles of light incidence. The field diaphragm was opened such that its borders were just about visible at the periphery of the image; the borders were used as a focusing aid.

4.2.6.3 Confocal Microscopy and Fluorescence Recovery After Photobleaching

Confocal images were obtained at the University of Leeds Bioimaging Facility, using a Zeiss LSM880 inverted Airyscan confocal microscope with ZEN software, and a Plan-Apochromat 40×/1.4 Oil DIC

M27 Objective (ZEISS). The pixel dwell time was 8.19 µs, image size was 256 × 256 pixels, and the scaling factor was 0.69 µm. Fluorophores (SAv-Atto565) were excited with the 561 nm laser at 1% of maximal intensity. The pinhole size was set to 198 µm, corresponding to 5 Airy units. For FRAP series, 60 images were taken with bleaching occurring after the third image. Bleaching was performed at 100% of maximal intensity (using the 'zoom bleach' option to maximise the bleaching rate), and the number of bleach iterations was 50.

4.2.7 Height analyses from RIC micrographs

4.2.7.1 Analyses of the thickness of surface coatings

Plain polystyrene beads of 25 µm diameter were used for colloidal probe RICM, to determine the thickness of glass coverslip coatings. The beads were injected into the HBS solution and left to sediment on the coating. The bead concentration was chosen such that individual beads could easily be found and visualised by RICM as a pattern of Newtonian rings. The effective distance of the bead from the coverslip was determined through analysis of the rings pattern with a custom algorithm (written by Dr. Delphine Débarre, Laboratory of Interdisciplinary Physics, University Grenoble-Alpes/CNRS, Grenoble, France) implemented in Labview, as described in detail in Ref. (121). In short, the fringe pattern around the centre of the bead is symmetric, this is exploited and used to create a radial intensity profile (after the centre of the bead is identified) and the intensity varies as a function of the distance from the centre of the bead (r_d) and is described by:

$$I(r_d) = A_1 e^{-\frac{r^2}{w_1^2}} + A_2 e^{-\frac{r^2}{w_2^2}} \cos(\phi_0 + \frac{2\pi n}{\lambda} \delta h(r_d)) \quad [4.1]$$

where A_1 and the exponential decay with w_1 describe the background signal, A_2 and the exponential decay with w_2 the envelope of the fringes, and the cosine term the oscillation of intensity as a function of r_d. n is the refractive index of the solution (1.334), λ is the wavelength of light, $\delta h(r_d)$ is the distance between the light reflected from the planar surface and the light reflected from the polystyrene bead, and ϕ_0 is the phase shift on reflection (π). In this case, as the polystyrene bead has a sufficiently large radius, $\delta h(r_d)$ can be described as (121):

$$\delta h(r_d) = 2h(0) + \frac{r_d^2}{R_p} - 0.75\frac{r_d^4}{R^3} \quad [4.2]$$

where R_p is the radius of the polystyrene bead. In the data fitting, A_1, A_2, w_1, w_2, $h(0)$ and R_p were adjustable parameters. However, R_p was fixed and a 'fudge factor' was introduced to account for incorrect focus and the difference between real and assumed radii. From this analysis, $h(0)$ provided an effective measure of the coating thickness. The numerical aperture enters in the fitting, but is not covered here.

4.2.7.2 *Quantifying the grafting distance of HA brushes from the brush thickness*

Root mean squared anchor distance between HA chains were calculated using the brush thickness determined by RICM, as described by Davies *et al.* (121):

$$\xi^2 = \frac{8}{\pi^2}\frac{pv}{b}\left(\frac{I_c}{H_0}\right)^3 \quad [4.3]$$

where $p = a/b = 13.9$ is a measure of the intrinsic chain stiffness (13.9), $v = 3.67$ nm^3 is the effective excluded volume per chemical monomer unit (the HA disaccharide), $b = 1.0$ nm is the contour length per chemical monomer unit, $I_c = b\,M_{polymer} / M_{monomer}$ is the contour length of the polymer (with $M_{polymer}$ = 840 kDa and $M_{monomer}$ = 378 Da, I_c = 2.22 µm), and H_0 is the measured thickness of the brush.

4.2.7.3 *Analysis of the effective height of plane-sphere contact in PSCM*

The effective height in the centre of contact between the planar surface and the hemispherical cap of the glass rod was determined using a custom algorithm (written by Dr. Saikat Jana) and implemented in MATLAB. The analysis algorithm was based on the same principles as those presented in Section 4.2.7.1, and comparative analysis with selected datasets indeed resulted in virtually identical results. This analysis also provides the centre position of the rod.

The effective height is negative as it is sensitive to the flex of the glass coverslip, it is dependent on the resting force of the hemispherical cap on the surface (122).

4.2.8 Determination of the Gap Height Profile in Plane-Sphere Confinement

The distance between the hemispherical gap and the planar surface for areas outside of the contact radius (gap height, h) were determined using Equation S6 in Frost *et al.* (122):

$$h(r_d, F) = \frac{1}{\pi R_{hc}}\left[(r_d{}^2 - 2r_c^2)\left(\frac{\pi}{2} - arcsin\frac{r_c}{r_d}\right) + r_c\sqrt{r_d^2 - r_c^2}\right] \quad [4.4A]$$

where r_c is the contact radius and F is the resting force at the contact area. The resting force is determined by the positioning of the counterweight. The contact radius is calculated by (122):

$$r_c(F) = \left(\frac{3FR_{hc}}{4E^*}\right)^{\frac{1}{3}} \quad [4.5]$$

where E^* is 35.56 GPa. The height can also be estimated by the following approximate equation, this is not accurate at small distances (a few nm) (122):

$$h(r_d, F) = \frac{r_d^2}{2R_{hc}} \quad [4.4B]$$

This analysis allows the locations within the image to be linked to their gap height.

4.2.9 Relating Effective Height to Resting Force in PSCM

The effective height of the hemispherical cap on the planar surface can be related to the resting force of the hemispherical cap in the following equation (122):

$$h_{eff} \approx -5.3\ nm \times \left(\frac{F}{mN}\right)^{\frac{2}{3}} \times \left[1 - 0.039\ \left(\frac{F}{mN}\right)^{\frac{2}{3}}\right] \qquad [4.6]$$

4.2.10 Tracking of Diffusion of Fluorescent EUVs

4.2.10.1 Pre-processing of Image Time Series

All images in a time series were pre-processed identically prior to particle tracking, using the Fiji routine: Trackmate. First, a circular area centred on the plane-sphere contact (determined as described in 4.2.8) and encompassing the desired gap height range was extracted from the images. The radius $r_{\max}$ of the circular area, commensurate with the desired maximal gap height $h_{\max}$, was here determined as $r_{\max} = \sqrt{2R_{\mathrm{hc}}h_{\max}}$. This step reduced the number of tracks to analyse, and thus sped up downstream data analysis. Second, the cropped images were processed to remove immobile particles using a method by Cosette *et al.* (160). Specifically, a median image of the entire time series was computed, and each individual image in the series was then divided by the median image.

4.2.10.2 Determination of EUV Diffusion Tracks

The series of pre-processed images were analysed using the Trackmate tracking algorithm in Fiji (116). Particles were identified using the Laplacian of Gaussian (LoG) detector using the size 1 µm and detection threshold at 0.002. These are parameters that allow the software to select particles in each frame according to the size and fluorescent intensity. The Linear Assignment Problem (LAP) tracker was used to generate tracks, with the maximum allowed movement distance between frames set to 4 µm. Gap closing was allowed for the same distance, in case of a particle missing in up to 1 frames. From the ensemble of tracks generated, the shorted tracks (that is, comprising 10 frames or less) were discarded.

4.2.10.3 Mean Square Displacement (MSD) Analysis of Diffusion Tracks

The remaining ensemble of tracks were analysed using the MSDAnalyzer algorithm in MATLAB (161), to obtain the MSD as a function of lag time τ, and a diffusion coefficient, *D*, per track. For tracks derived from series with 200 frames, the diffusion coefficient was calculated by linear fitting of the MSD (τ) data for $0 < \tau < 0.1\ \tau_{max}$ (with τ_{max} the maximal lag time for a given track). For tracks derived from series with only 20 frames, the range $0 < \tau < 0.18\ \tau_{max}$ was used for fitting. In addition to *D*, corresponding to the slope of the linear fit, the fit also produced the intercept (ε^2), a measure of the noise in particle positioning, and the coefficient of determination (R^2), a measure of the quality of the fit.

The data set of was refined by removing low quality tracks. Specifically, tracks with $R^2 < 0.8$ were discarded as poor fits. Further analysis revealed a rather large spectrum of ε^2 values in the remaining data set, indicating that the R^2 analysis alone with insufficient as a quality control. As a further measure, tracks with $\varepsilon^2 < -0.5\ \mu m^2$ and $\varepsilon^2 > 2.5\ \mu m^2$ were discarded.

In addition to the standard parameters output by the MSDAnalyzer, the mean position of each track (x_m, y_m) was also computed. From the mean position, the mean distance from the centre of plane-sphere contact (r_m) and the mean gap height (h_m) were then computed for each track. Tracks with $h_m > h_{max} - 50$ nm were discarded to avoid artefacts with tracks leaving or entering the analyse area.

4.3 Results

This results section has three main parts. The first, modification of the PSCM design that were made to improve its suitability for use on model glycocalyces. The second on the development of single particle tracking analysis for this system. The third, the effect of the pore size of the model HA matrix on the diffusion of EUVs.

4.3.1 Development of a PSCM Stage Insert with Improved Interface Stability and Quality

The first PSCM prototype (122) had drawbacks in terms of limited control over the resting force (and thus the exact geometry) of the plane-sphere contact, and damage to the interface increasing over time due to sensitivity to external vibrations, limiting the amount of data that can be acquired. A new PSCM stage insert aimed to resolve these limitations was designed and the new stage insert was then also used to develop experimental methods to minimise damage to the surface film, an effect that is particularly important for glycocalyx models which requires longer term measurement.

4.3.1.1 The New PSCM Stage Insert

The PSCM setup is now more compact to fit onto the microscope stage, and the force between the surfaces is controlled by a gravity driven counter-weight-balance system rather than a micromanipulator. The PSCM stage insert is schematically shown in (Figure 40A). It consists of an *xyz* positioning unit and a force exertion unit. The positioning unit allows the glass rod with the hemispherical cap to be positioned over the desired area of the sample. The force exertion unit (Figure 40B) contains a beam that can rotate freely about its roller bearing and holds the glass rod and the counterweight on opposing ends. A locking pin holds the beam in place until the desired time at which the hemispherical cap will be brought into contact with the planar surface. The PSCM stage insert can be easily mounted and is separated from the microscope stage, making this an accessory with any inverted microscope for desired use.

Another major benefit of the new PSCM stage insert is that the plane-sphere contact is temporally stable, allowing analyses of the confined region without lateral movement or a change in resting force over long times (minutes and even hours). The resting force at which the rod with hemispherical cap interacts with the planar surface is controlled by a counter-weight-balance system (Figure 41). At equilibrium, the mass of the counterweight and the mass of the glass rod balance each other such that the beam remains in a horizontal position. When the counter-weight is moved towards the pivot point, the effect of gravity on the glass rod is greater than on the counterweight resulting in the rod lowering and making contact with the surface. The resting force with which the glass rod presses onto the planar surface can be controlled by the mass of the counter-weight and its distance from the pivot. The counter-weight sits on a threaded portion of the beam, allowing easy adjustment of the resting force. Specifically, for a 3.5 g counterweight, one turn of the counterweight towards the pivot is equal

to 1 mN of added resting force. This was established by measuring the weight of the glass rod on the surface for subsequent turns away from the equilibrium position towards the pivot and converting the weight into force through the equation $F = mg$, where g is equal to 9.81 m s^{-2}.

The hemispherical cap resting on the surface produces a negative effective height between two objects. This is because the planar surface is a coverslip undergoes deformation as a result of the compressive force on the surface (122).

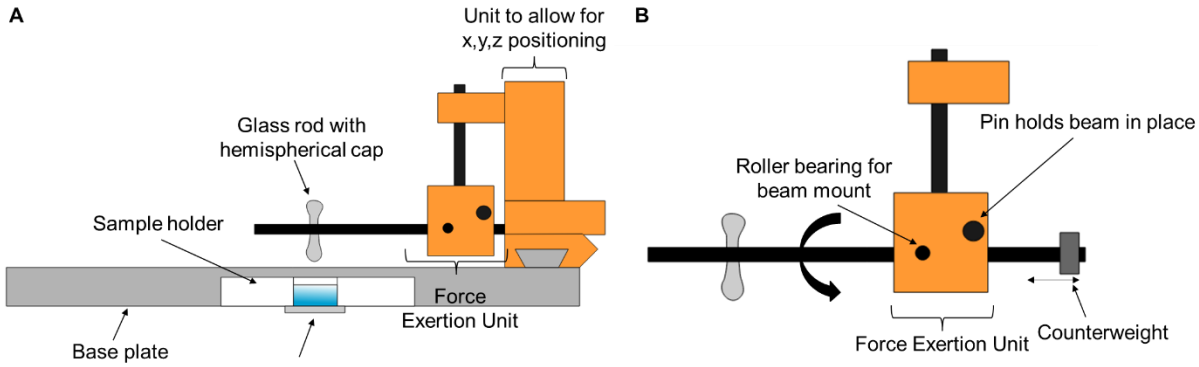


Figure 40. ***The PSCM Stage Insert.*** *A) A schematic of the PSCM stage insert installed in relation to the sample holder and functionalised surface. The xyz positioning unit with the force exertion unit is designed to slide onto the base plate, and holds the glass rod with hemispherical cap into place. B) Detailed view of the force exertion unit. The roller bearing allows the beam with the glass rod and counterweight on opposing ends to pivot freely, and the locking pin holds the beam in resting position prior to establishing plane-sphere contact.*

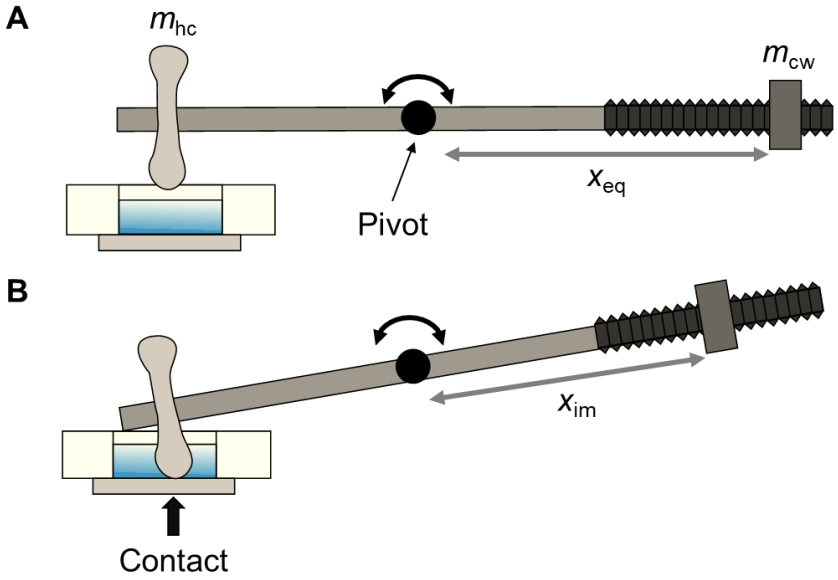


Figure 41. ***Resting Forces Are Set by a Counter-Weight-Balance System.*** *A) Schematic of the beam at equilibrium. The distance between the counterweight (of mass m_{cw}) and the rod with hemispherical cap (m_{hc}) with the pivot at the centre results in the beam resting with the ability to pivot to either side. B) Schematic of the beam in the imbalanced state. The counterweight has been turned towards the pivot, resulting in the lowering of the hemispherical cap causing a contact between the cap and the glass surface. The resting force of the cap is determined by the distance between the counterweight and the pivot (x_{im}). This mechanism was created by Dr Saikat Jana.*

4.3.1.2 Mitigating Damage to Functionalised Surfaces upon Plane-Sphere Contact Formation

Glycan-rich model matrices are soft and quite easily perturbed by mechanical forces. Resting forces in the mN range readily compress the model matrices to an extent that virtually all water is released in the plane-sphere contact area (122). An important consideration therefore was if parts of the model matrix near the contact area become damaged upon the plane-sphere contact. Previous PSCM study has only been performed on covalently bound molecular surfaces and it was not possible to study such an effect. Here, PSCM has been applied to these soft model matrices for the first time.

Damage was tested for by analysing the distribution of streptavidin around the contact region, this was made possible by using the SLB of model matrices (Section 2.1.1). The availability of fluorescent SAv and its intrinsic link to the other layers of the model matrix via the biotin-SAv interaction, the appearance of the fluorescent SAv can give an indication on the quality of the surface. A homogenous fluorescence distribution would indicate a homogenous bilayer (88).

Initial analysis of a SAv-on-SLB layer after a single contact with a bare rod with hemispherical cap showed that the SAv monolayer was substantially perturbed in the surrounding of the contact area (contact radius = 4.37 µm) (resting force 1.5 mN) (Figure 42A). The perturbation extended for a radius

of 25 µm in the x direction and 75 µm in the y direction corresponding to gap heights of up to 110 nm and 180 nm, respectively (calculated with equation 4.4). The x direction coordinates with the long beam mount of the PSCM unit. The model matrices of interest in this study range from heights of 10 nm and 400 nm, and the present damage would thus impact all or at least a substantial part of the confined region that excludes bulk solution. These data indicate that the impact of the rod on the planar surface leads to a level of damage that would severely perturb the analysis of colloid diffusion within the model matrix film. Several options were considered to reduce the level of damage.

4.3.1.2.1 Stabilising the Functional Surface by Streptavidin Crosslinking

Firstly, it was hypothesised that the damage may be accentuated by the fluidity of the SLB. The lipids in the SLB, and the associated SAv, are laterally mobile and, therefore, may be more easily displaced by the impact of shear forces. To limit this effect, SAv was crosslinked by glutaraldehyde (GTA), resulting in a two-dimensional network of chemically bonded SAv. The effectiveness of this approach in eliminating SAv mobility is demonstrated in Figure 43. Prior to GTA treatment, SAv fluorescence in a bleached area almost fully recovered within 80 s, whereas after GTA treatment, the bleached area appears largely similar immediately following bleaching and after 80 s (Figure 5). This clearly shows that the SAv has reduced mobility and therefore been crosslinked by the GTA.

The PSCM contact area of surfaces with crosslinked SAv was then analysed. The GTA crosslinking had an appreciable effect on the appearance of the contact area, and the damage caused by the contact. In a previous case, the GTA treatment led to a sharper boundary between the damaged area and undamaged area (Figure 42B) (contact radius = 4.32 µm). It also resulted in a decreased radius of damage around the contact area (Figure 44, (contact radius = 4.44 µm).) to around 40 µm diameter, in the x direction, which corresponds to a gap height of approximately 70 nm. This brings the range of accessible heights down and allows for films with heights above 70 nm to be studied. The combination of data in Figure 42 and Figure 44 show that the inter-sample variation is more important than the effect of GTA itself. Therefore, there clearly is potential for further improvement to improve on the repeatability of good plane-sphere contact.

Another interesting feature of the impact of the hemispherical cap on the surface is seen by observing the quality of the surface at the contact point after removing the cap (Figure 44B). The damaged area after removing the rod has a decreased fluorescence intensity than when the cap is in contact, this indicates that some of the fluorescent SAv has been transferred from the planar to the curved surface. As the SAv and SLB are intrinsically linked, this suggests that some lipid material has also been transferred to the curved surface. As the hemispherical cap is also made of glass, the same material as the planar surface that has been functionalised with an SLB, it is possible that the lipids that have been removed from the planar surface in the damaged areas interact with the glass hemispherical cap

in a similar way, forming a bilayer on the hemispherical cap surface. This should not impact the analysis of data in gap heights above the radius of damage. Furthermore, this could also be exploited by the formation of surfaces on the hemispherical gap, enabling the formation of a matrix that extends into the z direction.

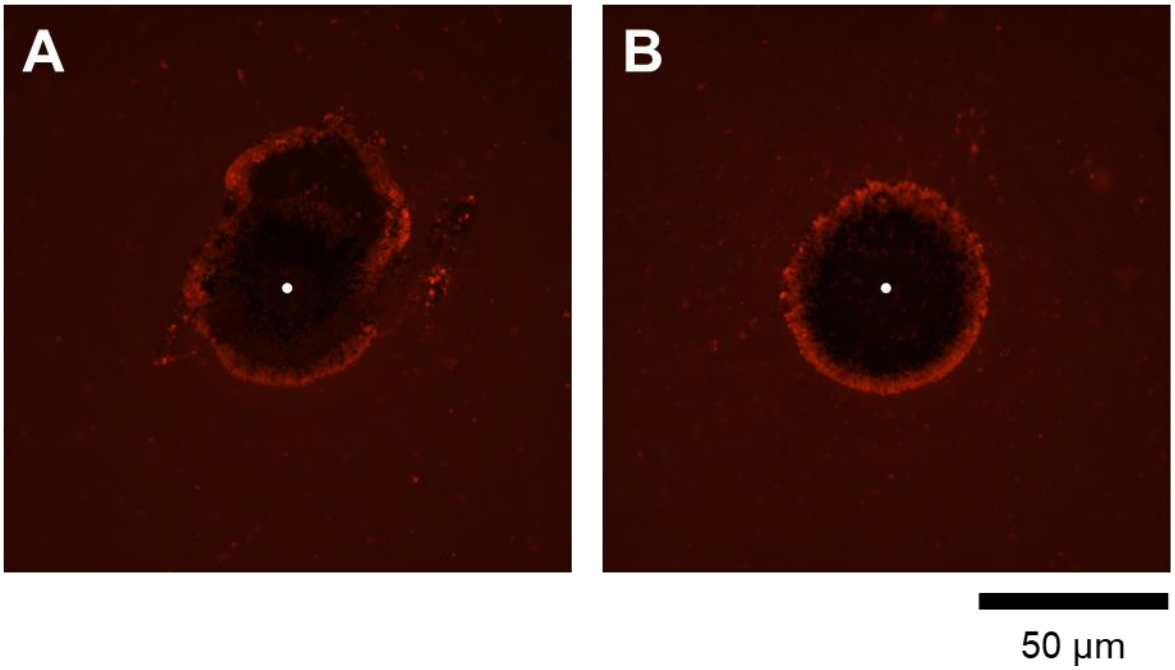


Figure 42. ***Epifluorescence Micrographs of Functionalised Surfaces after Plane-Sphere Contact Formation Reveal Defects.*** *A) Fluorescent SAv-on-SLB on a planar surface in contact with the hemispherical surface of a bare rod (the centre of contact is shown by the white dot). B) Same conditions as in (A), but with SAv cross-linked by GTA prior to contact formation. Surface formation included: SUVs – 100 µg/ml, 30 min, SAv-Atto565 – 40 µg/ml, 20 min, GTA – 1%, 10 min. The composition of the SLBs in these images are 5 mol % biotinylated lipids with 95 mol % DOPC. The resting force was 1.5 mN. These images are representative of a dataset of N ≥ 3.*

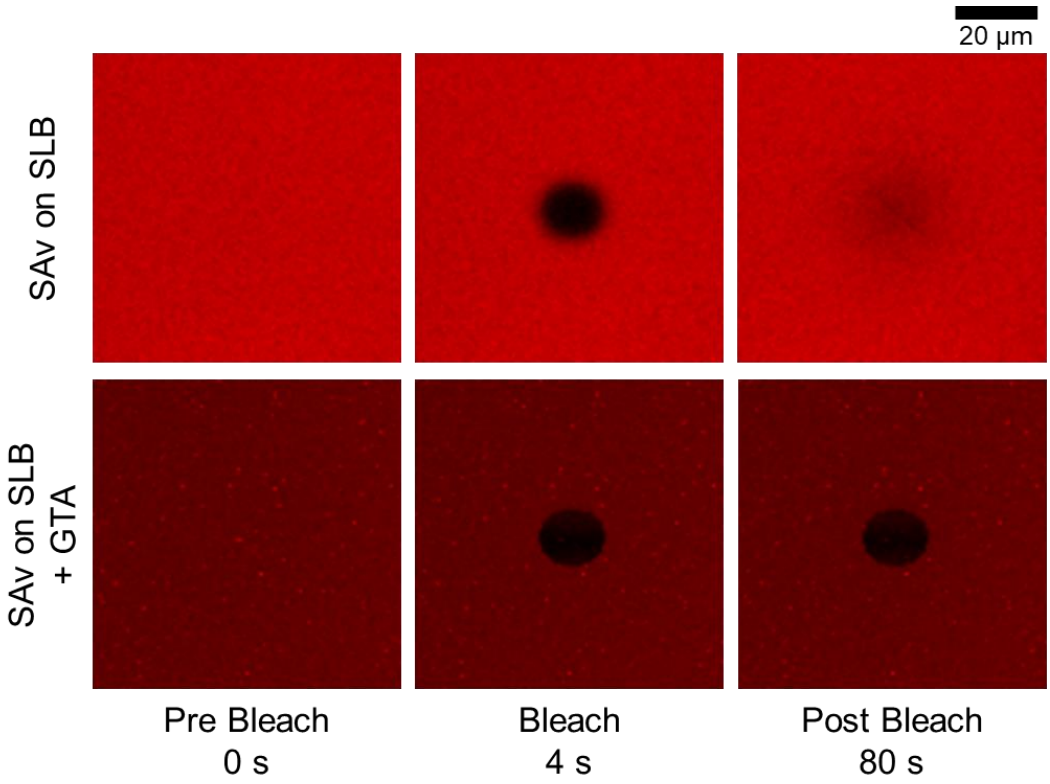


Figure 43. ***GTA crosslinks SAv Monolayers.*** *Confocal fluorescence images of monolayers of fluorescent SAv on an SLB without (upper panels) and with (lower panels) GTA treatment before bleaching (0 s), immediately after bleaching (4 s), and after a time period for recovery (80 s). The bleached region is visible by the decreased fluorescence intensity in the centre of the image (note that the bleached region is not a perfect circle in this particular experiment, owing to improper instrument calibration; this defect does not impact on the conclusions). Surface formation included: SUVs – 100 µg/ml, 30 min, SAv-Atto565 – 40 µg/ml, 20 min, GTA – 1%, 10 min. The composition of the SLBs in these images are 5 mol % biotinylated lipids in a DOPC background. These images are a representative data set of N = 3 independent measurements.*

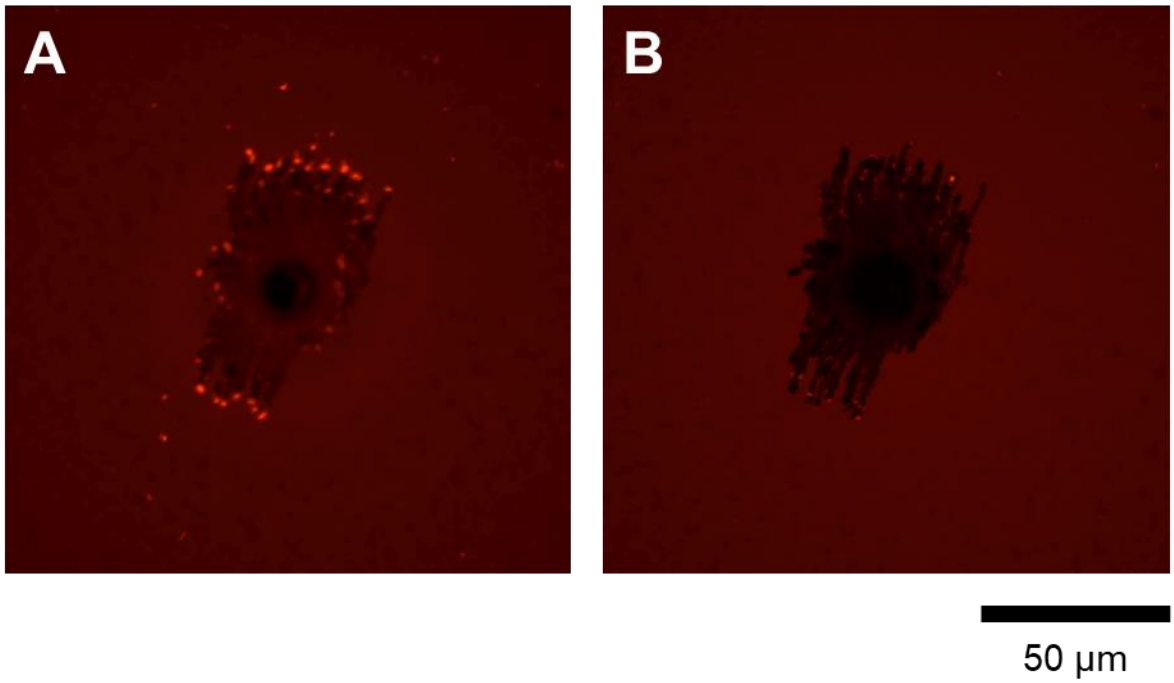


Figure 44. ***Epifluorescence Micrographs Reveal Transfer of SAv from the Planar to the Curved Surface.*** *The damage caused to a film consisting of a SLB made from 5 mol% biotinylated lipids and 95 mol-% DOPC, GTA treated SAv-Atto565, and HA-b dp 15 with the hemispherical cap in place (A) and removed (B). Surface formation included: SUVs – 100 µg/ml, 30 min, SAv-Atto565 – 40 µg/ml, 20 min, GTA – 1%, 10 min, HA-b dp15 – 50 µg/ml, 20 mins. The composition of the SLBs in these images are 5 mol % biotinylated lipids in a DOPC background. The brightness and contrast of these images has been modified to improve visibility of all the regions within the image.*

4.3.1.2.2 Reducing the Rate of Approach of the Curved Surface

Secondly, the rate of approach of the rod on the planar surface was considered. The movement of the rod towards the planar surface entails lateral shear force due to the expulsion of liquid between the two surfaces. Therefore, methods to decrease the rate of approach of the rod were considered. There is an intrinsic method to reduce the rate of approach, as it is affected by the counterweight (Figure 41) and damage to the surface is increased with increased resting force (data not shown). This is why 1.5 mN resting force was routinely used during experiments, it is a slow rate of approach but enough force to generate quality contacts.

To further reduce the rate of approach of the hemispherical cap, a motor controlled cantilever was added to the force exertion unit (Figure 45). The cantilever presses on the part of the beam that holds the counter-weight, keeping the beam in horizontal position and the rod away from the planar surface. The motor is then turned on to slowly raise the cantilever, allowing the beam to slowly become lowered. This method decreased the rate of rod approach, but should not affect the resting force that

the rod produces on the planar surface. With the cantilever in place, the rate of approach is 0.2 mm/s, without the cantilever the rate of approach is not steady, but can be described by 5 mm per 10 s.

A set of experiments with different set resting forces was performed to validate that the resting force is not affected by the addition of the cantilever. The counter-weight was used to set the resting force, and the motorised cantilever was used to lower a bare rod to a bare surface. Figure 46 demonstrates that the effective height, obtained through RICM analysis, became more negative as resting force was increased, from h_{eff} = -5 nm at F = 1.5 mN to h_{eff} = -18 nm at F = 6 mN. The experimental results (Figure 46, symbols) reproduce the theoretical predictions for the dependence of the effective height on resting force (Figure 46; solid line corresponds to Eq. 4.5, Section 4.2.9) reasonably well, indicating that the resting force is not impacted by the addition of the cantilever.

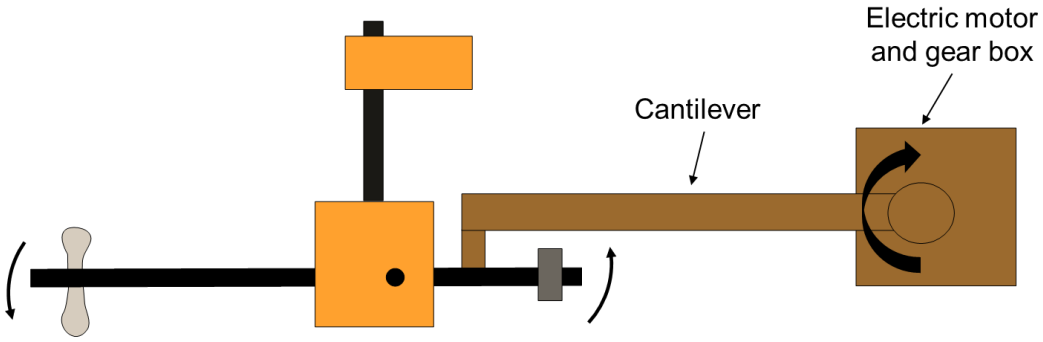


Figure 45. ***The Addition of a Motorised Cantilever to the PSCM Unit.*** *The addition of a motorised cantilever (brown) to the PSCM unit. The cantilever sits on the beam that holds the hemispherical cap and controls the tilt of the beam. The motor and gear box moves the cantilever slowly, allowing the beam to tilt more gradually than the removal of the pin.*

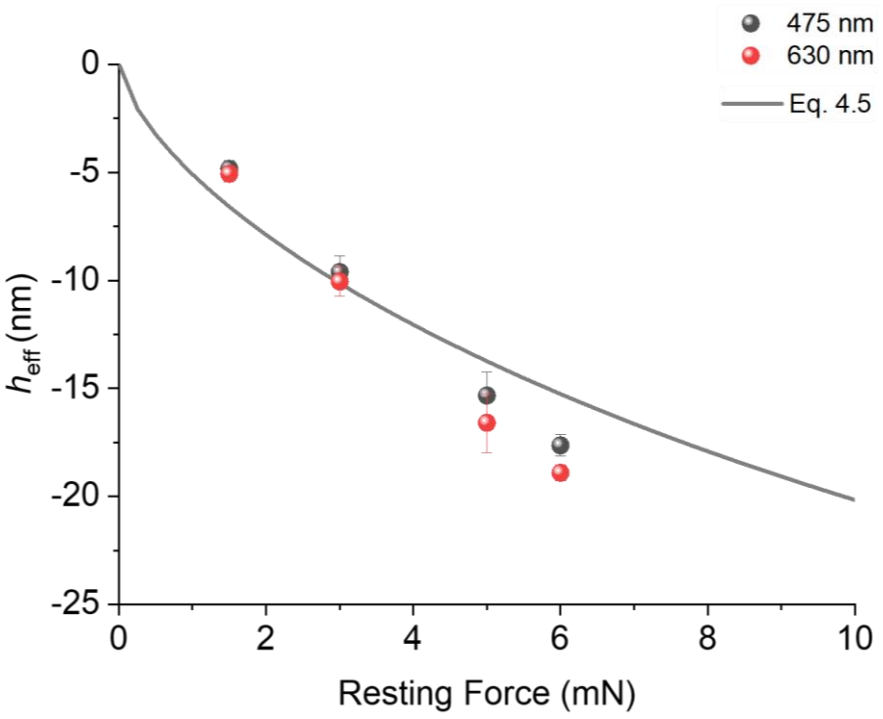


Figure 46. ***The Effective Height as a Function of the Set Resting Force is not Affected by the Cantilever.*** *Effective height h_{eff} determined from the RICM analysis of the hemispherical cap in contact with the surface, plotted against the resting force of the hemispherical cap on the planar surface as set by the counter-weight. Symbols with error bars show measured values of h_{eff} (mean ± SD for N = 3 independent contact measurements) at two different wavelengths (grey – 475 nm, red – 630 nm). The solid line is a prediction of values of h_{eff} according to Eq. 4.5 (122). The measurements were taken in HBS on clean glass (coverslip and rod) surfaces.*

Next, the impact of the cantilever on the quality of the plane-sphere contact in the presence of a surface coating was analysed (Figure 47). The coating here consisted of SLB, SAv, and HA dp15, and SLB, SAv, and HA 840 kDa, backfilled with HA dp15. It can be seen that the damage around the contact area is substantially reduced. In an ideal case (Figure 47A), the radius of the damaged area was just 10 µm, corresponding to a gap height of approximately 10 nm (contact radius = 4.44 µm). This would allow thin films of heights greater than 10 nm to be studied well without having to consider any of the damaged area. This is an improvement of seven times the scenario without the motorised cantilever. In another, less ideal case (Figure 47B), the damage extends to 20 µm, corresponding to heights of 70 nm (contact radius = 4.38 µm). Although supported lipid bilayers have been observed to be perturbed by forces in the nN range (162), HA films have been shown to withstand multiple, repeated compressions without any appreciable damage to the film (119). It is unclear what causes damage to both the HA film and the surface coverages underneath. Overall, however, the motorised cantilever

reduced the amount of damage caused to the surface coating and demonstrates the feasibility of near ideal contact with damage essentially confined to the contact area.

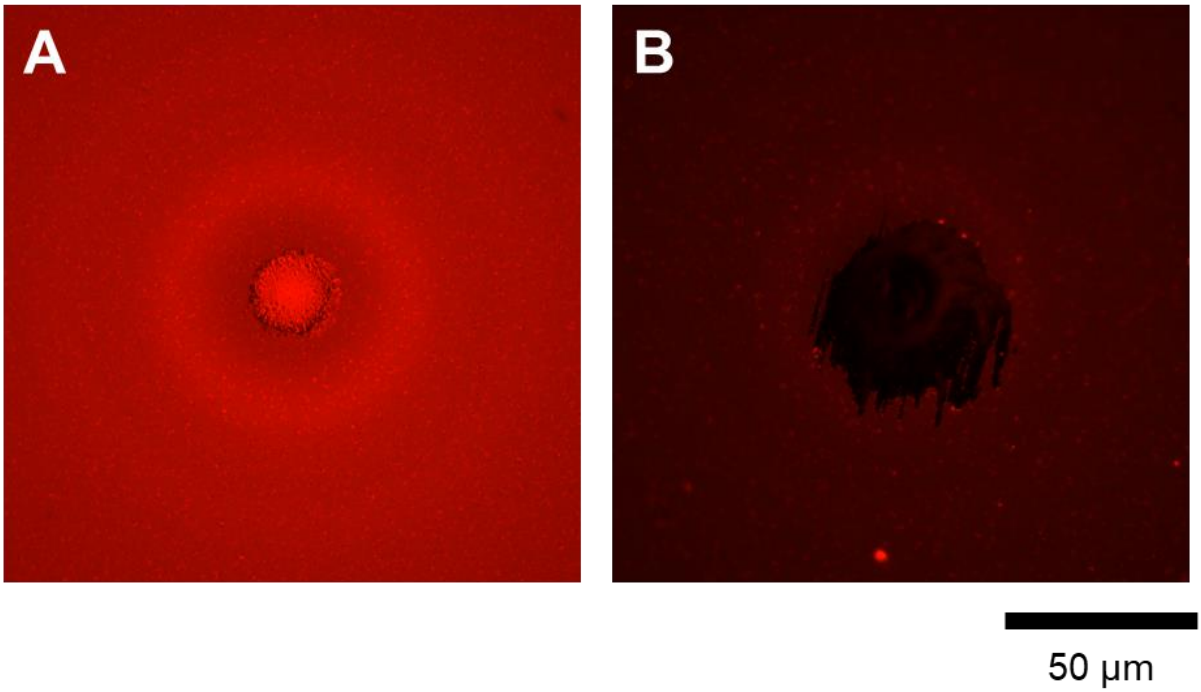


Figure 47. ***Damage to Functionalised Surfaces is reduced with the Motorised Cantilever****. A) Example epifluorescence micrograph of the contact region with a film consisting of a SLB with 5 mol-% biotinylated lipids and 95 mol-% DOPC, GTA treated SAv-Atto565, and HA-b dp 15 where the cap lowering was controlled with the motorised cantilever. B) Another example epifluorescence micrograph of the contact region with a film consisting of a SLB with 5 mol-% biotinylated lipids and 95 mol-% DOPC, GTA treated SAv-Atto565 and HA-b 840 kDa, backfilled with HA-b dp 15 where the cap lowering was controlled with the motorised cantilever. Surface formation included: SUVs – 100 µg/ml, 30 min, SAv-Atto565 – 40 µg/ml, 20 min, GTA – 1%, 10 min, HA-b 840 kDa – 20 µg/ml, 30 min, HA-b dp15 – 50 µg/ml, 20 mins.*

4.3.1.3 Reliability of the Calculated Effective Height

PSCM deploys RICM to evaluate the quality of the plane-sphere contact (Figure 48A) (122). Specifically, analysis of the fringe pattern provides a measure of the effective height h_{eff} at the centre of contact between the curved and planar surface. An aspect that required validation was if the image analysis routine provides a robust measure for h_{eff}. Of particular concern was if the focus position impacts on h_{eff}, as RICM images are typically acquired for two or three wavelengths simultaneously, the 63× antiflex objective used in this study has some minor chromatic aberrations over the wavelength range of interest (475 – 630 nm). To test for focus effects, the effective height was analysed for three wavelengths and over a *z* range of ± 1.5 µm relative to the optimal focus at each respective wavelength (475, 555, 630 nm) (Figure 48B).

The difference in effective height at the focal plane (for 555 nm) was 2 nm from the largest value (-11 nm at 475 nm) to the smallest value (-13 nm at 630 nm). The spread of heights across the wavelengths was greater (~2nm) below the focal plane and smaller (< 1 nm) above the focal plane. Typically, height differences of less than 2 nm are considered negligible (as established previously (122)), as these fall within this range, this leads to the conclusion that for differences in focal position of 1.5 µm, the output of the data will be reliable within 2 nm. Going forward, the focal position for one wavelength was determined, and this position was maintained across all wavelengths.

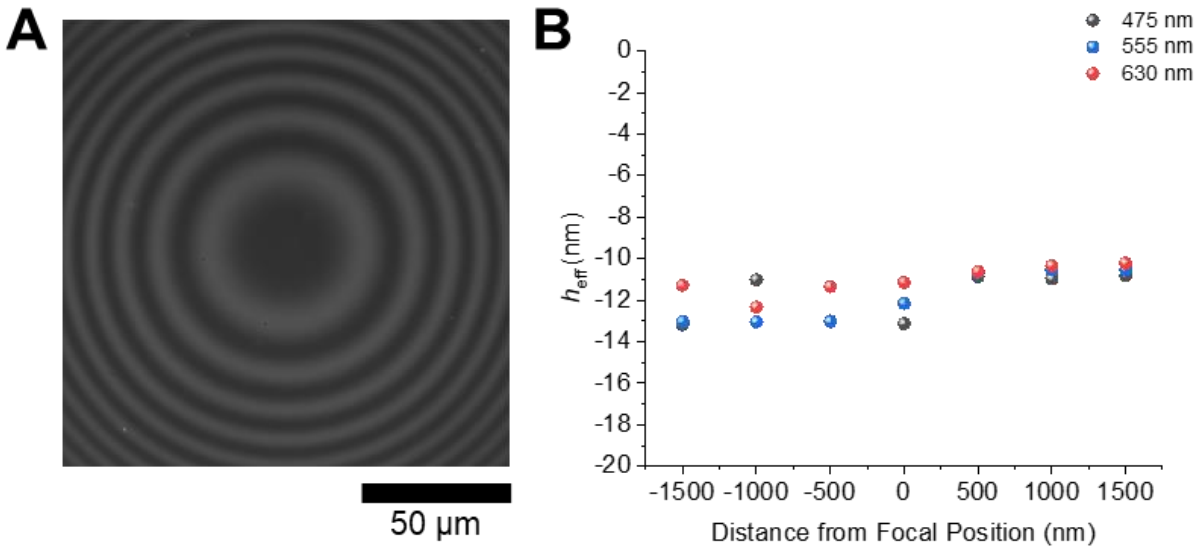


Figure 48. ***The Focus Position Has a Minor Effect on the Effective Height Measured by RICM.*** *A) Representative RIC micrograph (555 nm) of a quality contact between plain curved and planar surfaces. The quality contact is evidenced by good contrast between the sets of interference rings. B) Effective heights h_{eff} obtained for the same contact as a function of the focus position for three different wavelengths (colour coded as indicated). Conditions: bare glass coverslip and bare glass rod immersed in HBS; resting force: 3 mN. A representative data set is shown here; variations in effective height with focal position were comparable in two other data sets.*

4.3.1.4 Surface Coverage Impacts on the RICM Image and the Impact on the Effective Height

The effective height is calculated from the radial intensity profile of the RICM image. If there is damage at the plane sphere interface, this is visible in the RICM image (Figure 49A-B), this is present in the radial intensity profile in the form of an attenuation to the smoothness of the intensity curve. Although this gives another opportunity to appreciate the quality of the plane-sphere interface, it is possible that this impacts the fitting of the curve by the algorithm (described in Section 4.2.7). Therefore, the amount of damage to the surface may impact the calculated effective height. As additional surface covering increase the likelihood of damage, it is possible that different surface coverings may also impact on the calculated effective height. Therefore, the impact of different surface coverings and sub

sequential rod drops on different surfaces was investigated in regard to the calculated effective height.

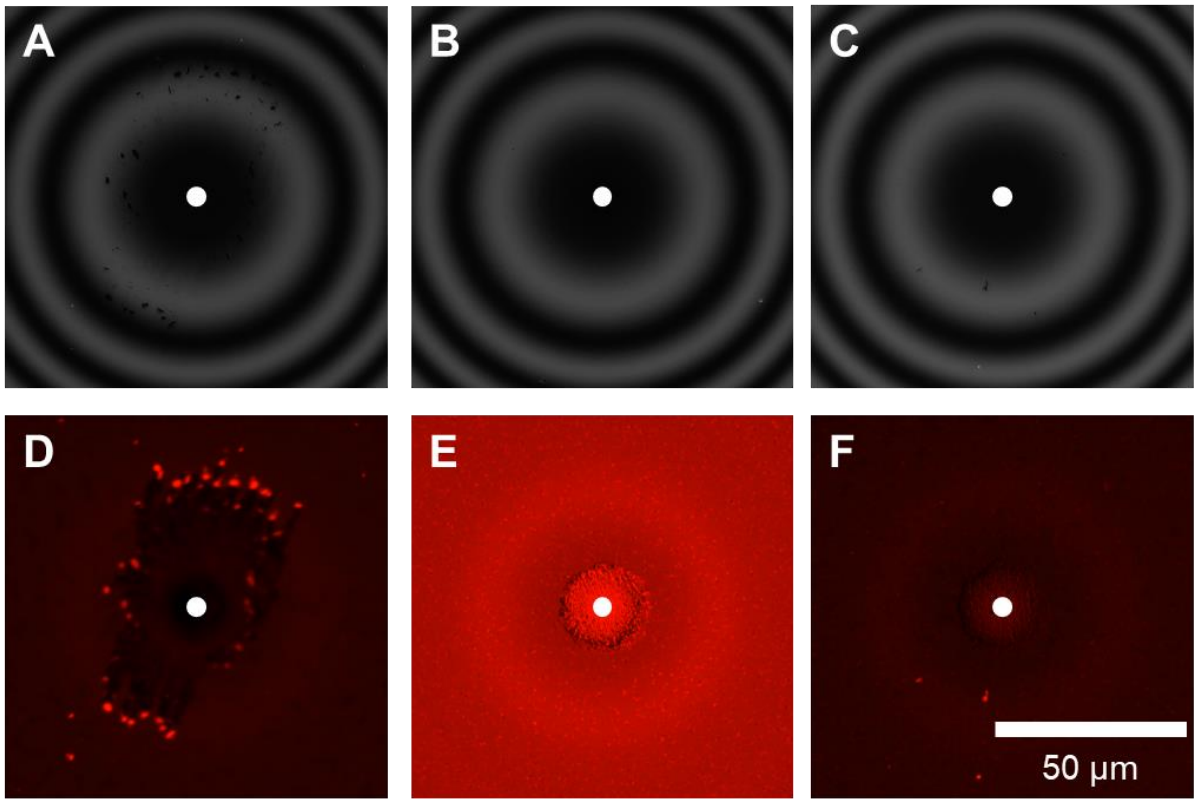


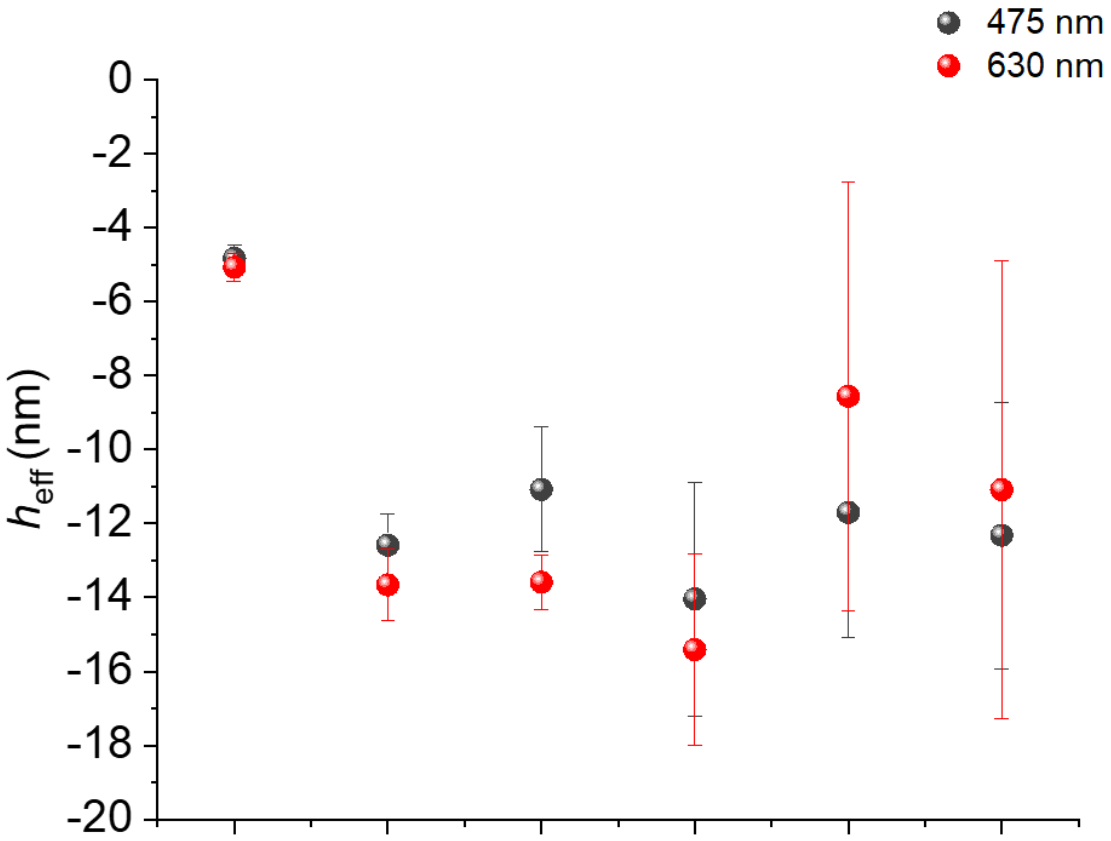
Figure 49. ***Surface Coverings Cause Changes to the Appearance of Newtonian Rings.*** *A-C) RICM image (acquired at λ = 630 nm) of a hemispherical cap in contact with an SLB, SAv-Atto565, HA-b dp15 surface. D-F) Epifluorescence micrograph of A-C). The white dot represents the centre of the ppoint of contact between the curved and planar surfaces. Surface formation for all images included: SUVs – 100 µg/ml, 30 min, SAv-Atto565 – 40 µg/ml, 20 min, GTA – 1%, 10 min, HA-b dp15 – 50 µg/ml, 20 mins.*

4.3.1.4.1 The Effect Model Matrix Surface Functionalisation Decreases Effective Height

To adapt this application for use in model glycalyces, the effective height at the plane-sphere interface was calculated for different functionalised surfaces of interest (Figure 50). The purpose of this was to assess the damage on the surface using the effective height as the representative parameter. The resting force was set to 1.5 mN. For two bare surfaces touching each other, the resulting effective height was -5 ± 0.5 nm (Figure 50). Additional surface coatings were found to decrease the effective height, by 7 nm on average (Figure 50). This countered initial expectations as additional material between the hemispherical cap and the planar surface would be expected to increase the distance between the two objects and increase the effective height.

It was also noticeable that, with additional surface coverings, the variations in the effective height increased. The variation for bare glass is only 0.5 nm, for SAv-on-SLB, it is 3 nm, and for an HA surface,

it is 12.5 nm. This could reflect that the degree of damage becomes more unpredictable with additional surface coverings, but it is not clear that this is the only parameter and there may be others that have not been identified. From this RICM analysis, one can conclude that the changes in effective gap height with surface functionalisation is generally small (<10 nm). The gap heights as calculated from the resting force and radius of the hemispherical cap, which assumes no surface coating and is not affected by the effective height. These may be assumed to be accurate even with a surface coating to approximately ± 10 nm.



Glass	✓	✓	✓	✓	✓	✓
SLB		✓	✓	✓	✓	✓
SAv			✓	✓	✓	✓
GTA				✓	✓	✓
HA					✓	
HS						✓

Figure 50. ***The Effect of Surface Coatings on the Effective Height Extracted from RICM Images.*** *The table below the graph indicate the components present on the surface, the y axis is the effective height calculated from RICM images from wavelengths of 475 nm (black) and 630 nm (red). The error bars represent standard deviation (N = 3 independent measurements). Surface formation included: SUVs – 100 µg/ml, 30 min, SAv-Atto565 – 40 µg/ml, 20 min, GTA – 1%, 10 min, HA-b 840 kDa – 20 µg/ml, 30 min, HS-b (33 kDa) – 10 µg/ml, 20 min.*

4.3.1.4.2 Subsequent Contacts Results in a Decreased Effective Heights for GAG Films

As the increased damage appears to substantially affect the effective height, this brings into question how subsequent contacts made with the same hemispherical surface and the contact area affect the effective height as it would be expected that increased damage would occur upon subsequent

contacts. For each surface explored in Section 4.3.1.4.1, contact was established 3 times subsequently by lifting and lowering the same rod and the effective height was calculated from the resulting RICM image (Figure 51). This was tested on multiple different surfaces that are of interest within model glycocalyces, an HS film as an example of a highly sulphated GAG film and an HA film as an example of a film of a higher molecule weight GAG.

For surfaces of SLBs, and GTA-cross-linked SAv on SLBs (Figure 51A-C), subsequent contacts did not change the effective height appreciably. All gap heights were within 10 nm of each other, and there was no clear trend with the number of contacts. For surfaces with GAG layers (Figure 51D-E), the effective height decreased with subsequent contacts. For the HS film (33 kDa), the mean effective height decreased from -12 nm for the first contact to -28 nm for the third contact. The variation in effective height also increased for subsequent contacts. For the HA film (840 kDa), the effective height decreased by 5 nm for each subsequent contact, although the variation was stable across contacts. This is consistent with the idea that the addition of GAGs to the surface increases the potential for damage on the surface as a result of plane-sphere contact. Additionally, by comparing the fluorescence micrographs of subsequent contacts for the SAv on SLB layer and the HA film (Figure 52), the amount of fluorescence at the contact point decreases much more for the HA film than for SAv in SLB layer, highlighting that more fluorescent material is removed after contact on the HA film.

Overall, these data indicate that subsequent contacts may change the level of damage on the surface and the calculated effective height for certain functionalised surfaces. Therefore, it is prudent to make only one contact with one specified interface. This is a drawback as it required multiple glass rods to be made and cleaned, which is time intensive. However, there is a possible work around for this. The PSCM set up allows the rod to be tilted so that a different angle of the hemispherical cap is facing downward and a new contact is made from a new interface, this was the method used to achieve the two interfaces in Figure 49B/E and C/F.

This Section has highlighted that the damage to the interface at plane-sphere contact results in a decreased effective height and that damage increases when GAG films are present. The reason for the increased damage when GAGs are present is unknown, but shows that the complexity of the interactions between these molecules at the interface results in unprecedented effects on the data analysis. Furthermore, an efficient way to produce quality contacts for experimentation was developed by tilting the rod slightly between contacts to reuse the same rod.

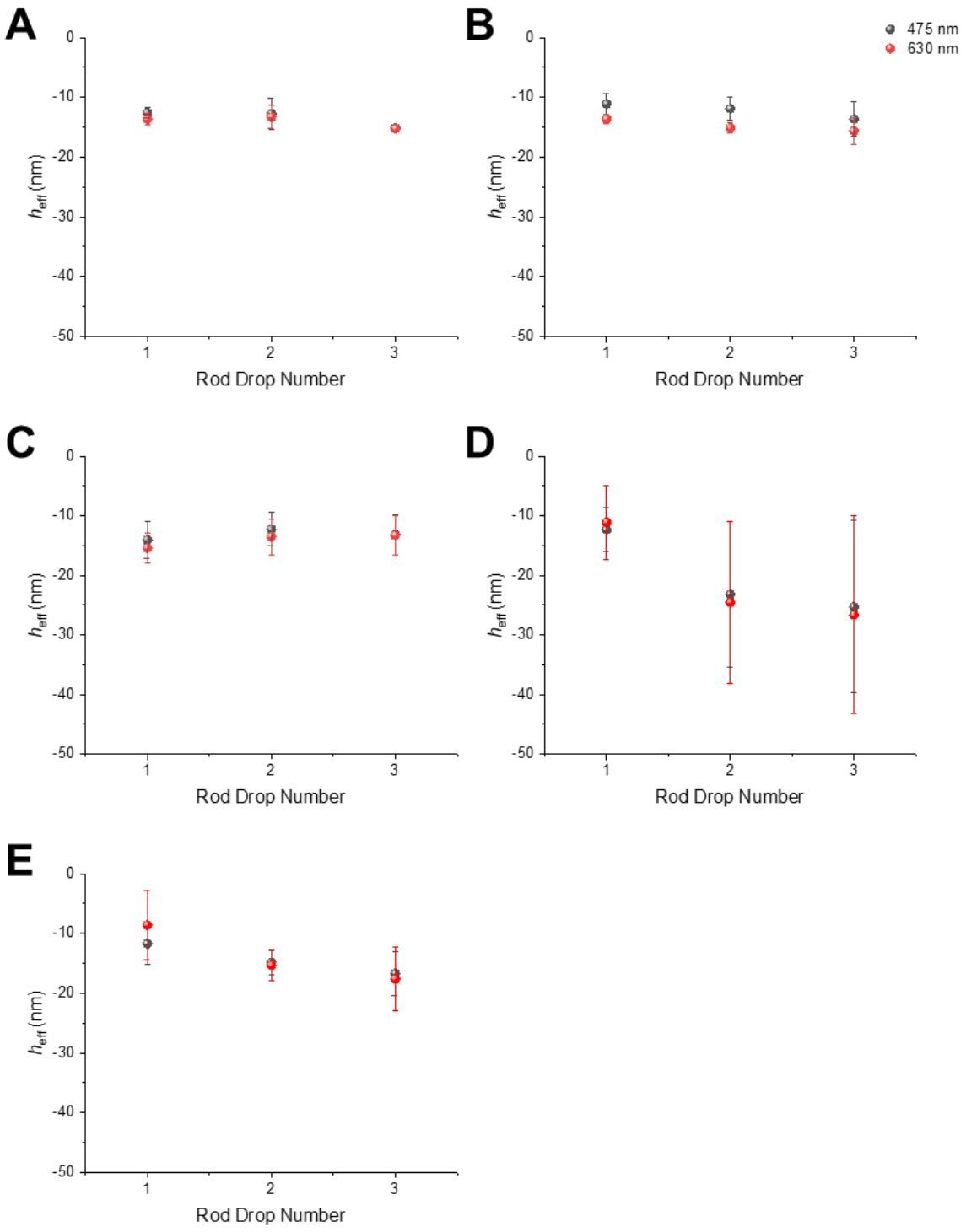


Figure 51. ***The Effect of Subsequent Rod Drops on the Effective Height Extracted from RICM Images.*** *Effective height h_{eff} (mean ± SD for N = 3 independent measurements) calculated from RICM images at wavelengths of 475 nm (black) and 630 nm (red) for 3 subsequent rod drops on an SLB (A), SAv on SLB (B), SAv on SLB with GTA crosslinking (C), SAv on SLB with GTA crosslinking plus 33 kDa HS-b film (D), SAv on SLB with GTA crosslinking plus 840 kDa HA-b film (E). Surface formation included: SUVs – 100 µg/ml, 30 min, SAv-Atto565 – 40 µg/ml, 20 min, GTA – 1%, 10 min, HA-b 840 kDa – 20 µg/ml, 30 min, HS-b (33 kDa) – 10 µg/ml, 20 min.*

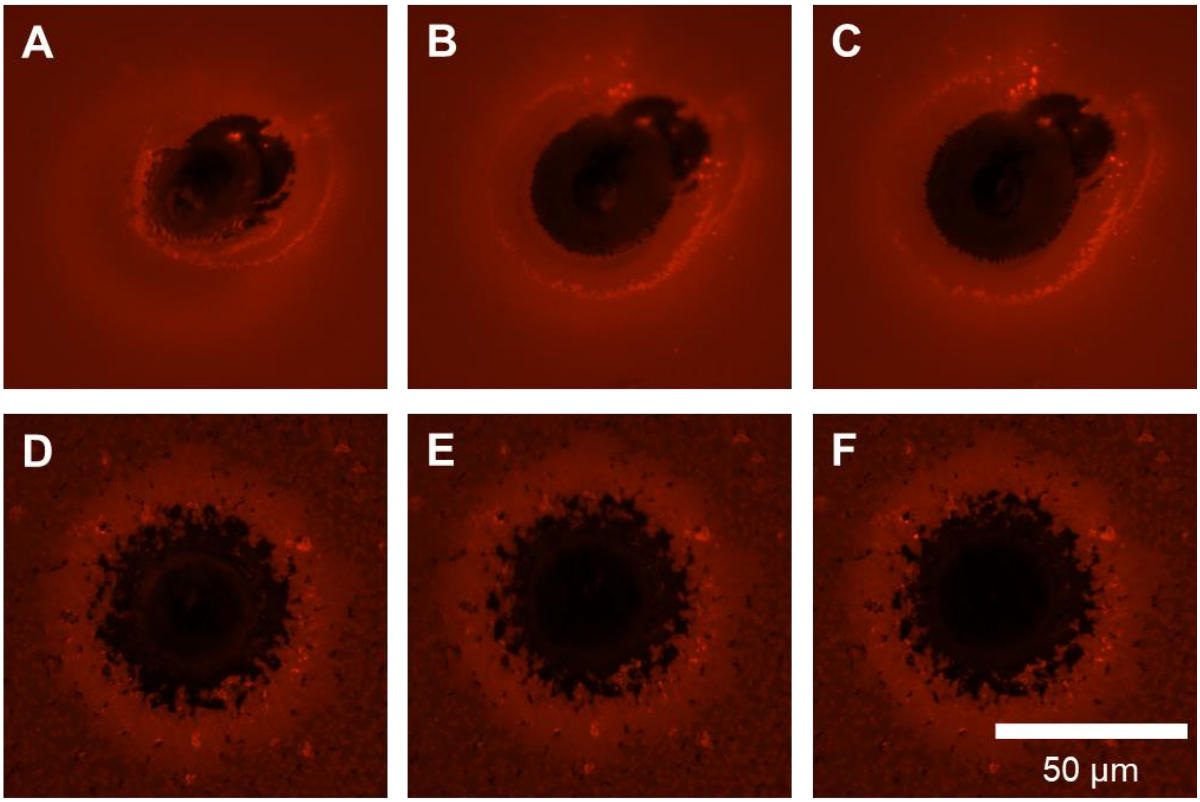


Figure 52. ***Changes to the Appearance of the Contact Point Following Subsequent Contacts.*** *A)-C) Example epifluorescence micrograph of the contact region with a film consisting of a SLB with 5 mol-% biotinylated lipids and 95 mol-% DOPC and SAv-Atto565 for the first (A), second (B), and third (C) contacts. D-E) Example epifluorescence micrograph of the contact region with a film consisting of a SLB with 5 mol-% biotinylated lipids and 95 mol-% DOPC, SAv-Atto565, HA-b 840 kDa for the first (D), second (E), and third (F) contacts. Surface formation included: SUVs – 100 µg/ml, 30 min, SAv-Atto565 – 40 µg/ml, 20 min, GTA – 1%, 10 min, HA-b 840 kDa – 20 µg/ml, 30 min, HA-b dp15 – 50 µg/ml, 20 mins.*

4.3.2 Developing a Workflow for Single Particle Tracking in PSCM

The previous application of PSCM used FRAP to assess the diffusivity of molecules within the confined space (122). However, the biological colloids that will be investigate here are fluorescent EUVs with diameters on the order of tens of nanometers and are, therefore, visible as single fluorescent particles. This enables the possibility for the use of single particle tracking to analyse the diffusion of the EUVs. An overview of the workflow is shown in Figure 53.

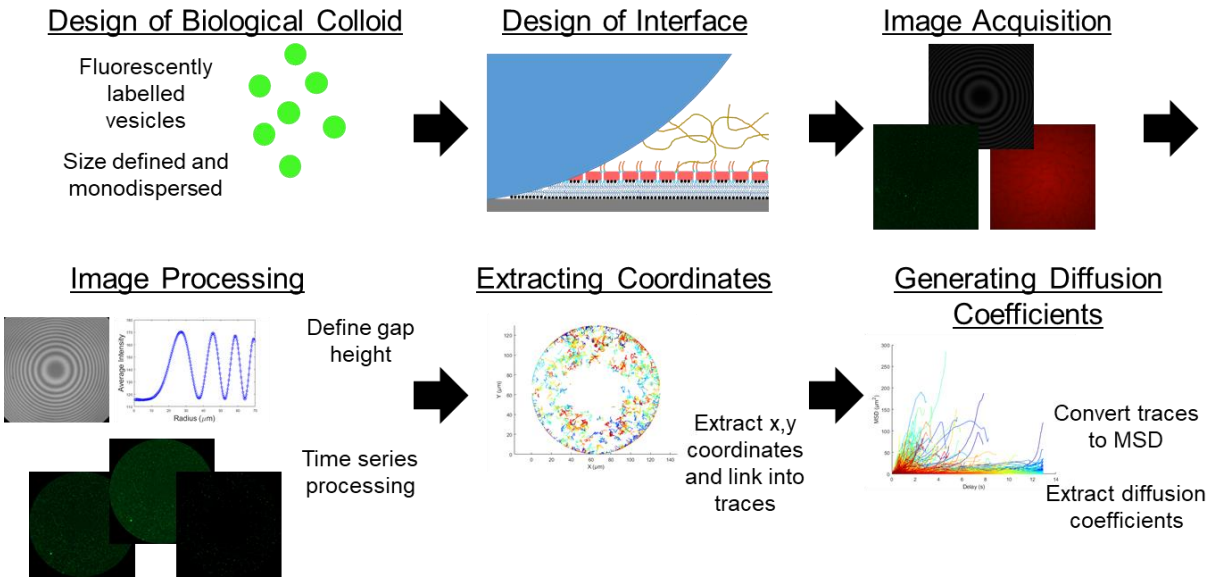


Figure 53. ***Workflow for SPT in PSCM.*** *The individual steps involved in designing and applying PSCM to trace single particles in model ECMs.*

4.3.2.1 Overview of the Data Analysis Steps

The overall approach to the analysis of the diffusion of EUVs was to capture images series over an approximately 240 x 240 μm^2 area around the region of plane-sphere contact over a time period long enough to view appreciable diffusion without excessive photobleaching. The resulting image series were then processed to include gap heights of interest and remove background fluorescence. The single particle tracking was then completed via Trackmate in Fiji (116), this produced the x and y coordinates of individual locations of particles in individual tracks. These coordinates were then input into a modified MATLAB script that isolated the MSD, diffusion coefficient, average location, and approximate gap height of individual tracks. The diffusion coefficient was then analysed with respect to the gap height.

4.3.2.2 Establishing an Example Data Set

EUVs containing the fluorescent molecule BODIPY were used as the EUVs are size defined and appear as single particles under fluorescence microscopy. The surfaces chosen were HA-b dp15 films, as the control non-brush surface that the EUVs do not interact with (established in Section 3.3.1.2, Figure 54A), and HA- b (840 kDa) films, for the diffusion with a model glycocalyx with a defined pore size (established in Section 3.3.3, Figure 54B). The fluorescent SAv was used as a readout for the quality of the surface functionalisation (Figure 54C), the surface is homogenous with an even distribution of SAv 2D crystals on the surface. SAv crystals are an artefact of using 5 mol-% biotinylated lipids, it does not have an effect on the system other than to decrease the mobility of the SLB. The SAv is crosslinked by GTA to prevent diffusion of the film in this assay, therefore, the impact of the SAv crystals is eliminated.

Plane-sphere contact was made resulting in quality interfaces (Figure 54D) and the EUVs around the contact point were visualised (Figure 54E). The EUVs used contained 1% BODIPY containing lipids, resulting in the ability to fluoresce under 488 nm wavelength illumination. The size of EUVs were both 30 and 50 nm. Some EUVs were immobile, as can be seen by the narrow and circular spots, whereas, the mobile particles appear more deformed, this is due to the movement of the EUVs during the image capture. The immobile EUVs are attached to the hemispherical cap, this is due to the interaction between the lipids and the glass surface. These particles were removed during analysis.

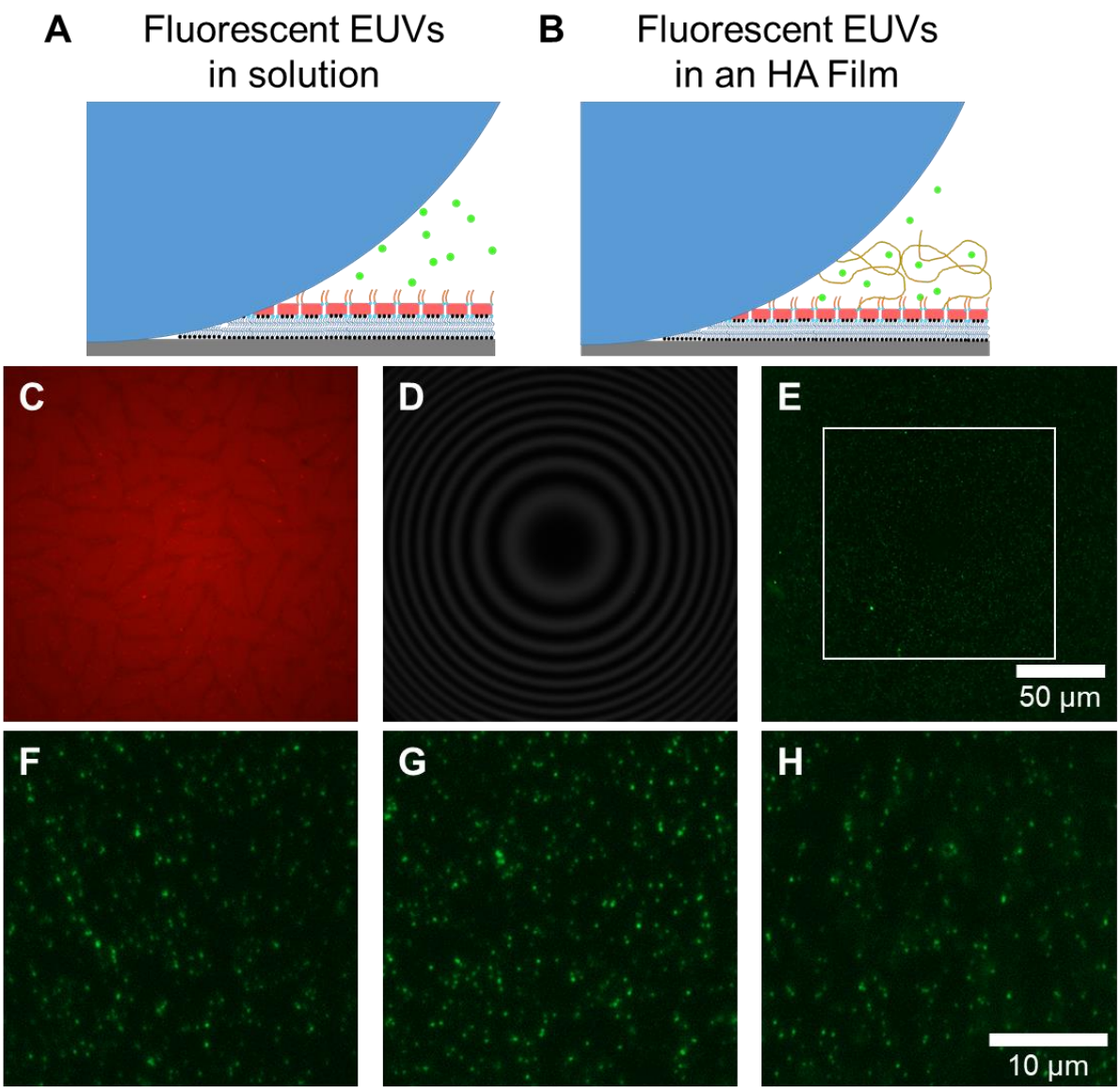


Figure 54. ***An Overview of an Example Data Set.*** *A-B) A schematic of the two interfaces under investigation for diffusion in solution (A) and in HA films (B). C) A fluorescent micrograph (565 illumination) to show the quality of the SAv in the surfaces under investigation. D) A representative RIC micrograph of a quality interface. E) A representative fluorescent micrograph (488 illumination) for the distribution of fluorescent EUVs around the contact point (centre). The white square represents the part of this image that is also shown in Figure 55A. F-H) Zoomed in micrographs from Sections of E). C-H) Surface formation included: SUVs – 100 µg/ml, 30 min, SAv-Atto565 – 40 µg/ml, 20 min, GTA – 1%, 10 min, HA-b dp15 – 50 µg/ml, 20 min, 50 nm EUVs – 0.94 nM.*

4.3.2.3 Pre-processing of Image Time Series

Two pre-processing steps proved necessary to enable the robust tracking of particles. Firstly, the images in the time series were cropped, as shown in Figure 55A. Only the region around the contact

area with gap heights up to 800 nm was retained, to reduce the data input and speed up downstream analysis.

Secondly, the cropped images were processed to remove background including immobile objects. This was achieved using a method previously established by Cosette *et al.* (160), which relies on the pixel-by-pixel division of each image by the median projection of the time series. In the median projection of the time series (Figure 55B), the background and the immobile particles are clearly visible as a homogenous intensity and sharp bright spots, respectively. In contrast, the processed images (Figure 55C) shows the mobile particles on a dark background. This made individual particles easily detectable by eye, increased the reliability of the tracking procedure, and increased the ease with which the downstream particle selection and tracking algorithms could be optimised by manually checking the validity of selected particle selections and tracks.

There is a visible rim of increased fluorescence intensity in Figure 55C. This artefact caused particles to be detected around the entire rim of the image. To avoid propagation of artefacts, all tracks with mean positions located at gap heights within a 50 nm range of the maximal height were removed from the final data set. This also ensures that tracks that leave or enter through the boundary are not included, as this would result in the inclusion of many incomplete tracks.

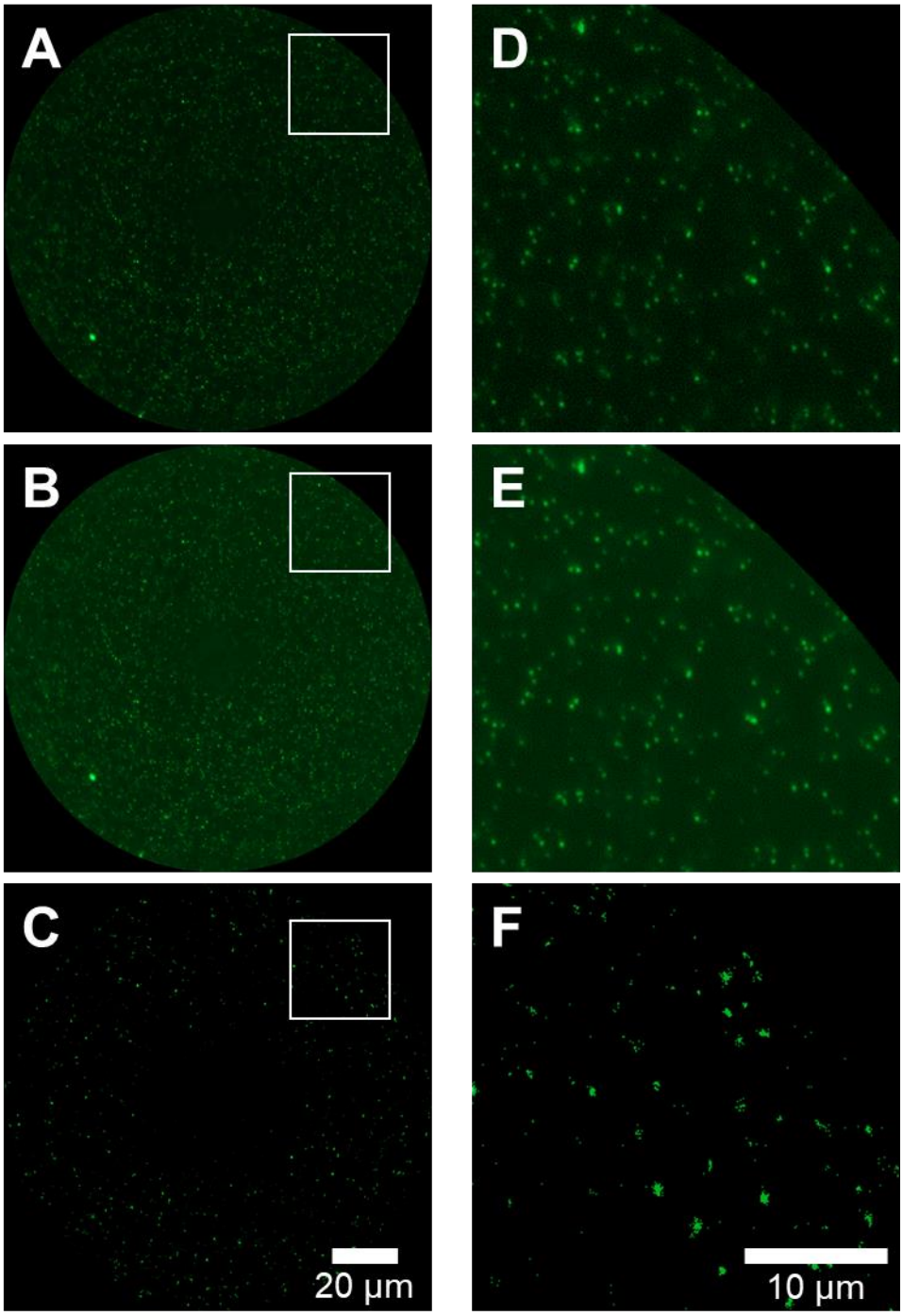


Figure 55. ***The Pre-Processing of Time Series for SPT.*** *A) One frame of the original time series of epifluorescence images of EUVs (cropped around the contact point, original image Figure 54E). B) The median projection of all frames within the time series. C) The image shown in A) after pixel-by-pixel division by the median image shown in B). D-F) Zoomed in sections for A-C), represented in the latter by white squares.*

4.3.2.4 Extraction of Diffusion Tracks and their Mean Square Displacement Analysis

Diffusion tracks were extracted using Trackmate in Fiji Image J (116). Single particles were selected based on their size and fluorescent intensity for each individual frame of the image series. The

individual particles were then linked using the LAP tracker (116). The details are presented in Section 4.2.10.2. Any tracks with less than 10 points were discarded, as these were deemed too short to produce reliable diffusion coefficients from the MSD analysis. Figure 56A visualises all the tracks (10,797 in total) obtained for the example data set.

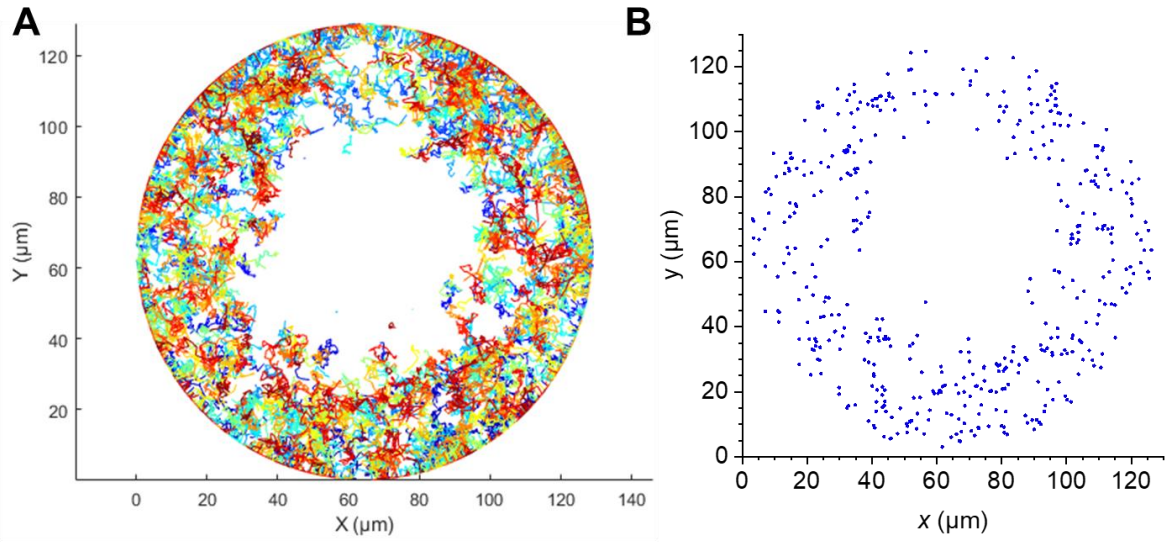


Figure 56. ***Validation of the Processing of MSDAnalyser Output.*** *A) The original output of all tracks from the example data set plotted by their x and y coordinates (retrieved from MATLAB MSD analyser). B) Plot of the mean x and y coordinates of each valid track, following the curation criteria.*

From the individual x and y coordinates, the mean square displacement (MSD) is calculated and plotted against the delay time (Figure 57). The first ~20% of each MSD plot was fit to a linear equation with an intercept (ε^2) and a gradient. The gradient is equal to the diffusion coefficient of that particle. Both of these values were exported along with a value for the degree of quality of fit (R^2). The intercept value also provides an idea of the goodness of fit. The specified details are presented in Section 4.2.10.3.

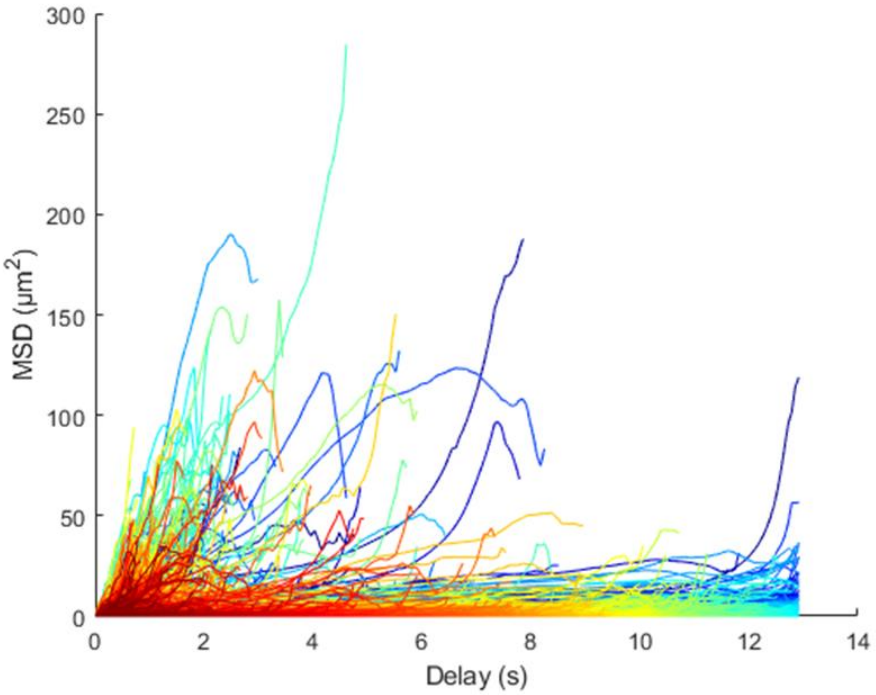


Figure 57. ***MSD Plot of Single Particle Tracking Data.*** *A graph of the MSD as a function of the delay time for the single particle tracks extracted from time series (retrieved from MATLAB MSD analyser).*

4.3.2.5 Curation of the MSD Analysis Output

The data set obtained from the MSDAnalyzer was curated to remove low quality data. Firstly, all tracks with a mean gap height position within 50 nm of the cut off height were excluded. Secondly, all tracks with too low R^2 values from the linear fit to the MSD *vs.* τ data ($R^2 < 0.8$) were discarded, as these represented poor fits and thus may have an unreliable diffusion coefficient. Thirdly, tracks with too low and too high intercept values from the linear fit to the MSD vs. τ data were discarded, as these are likely to represent poor track data. Specifically, the range $-0.5\ \mu m^2 < \varepsilon^2 < 2.5\ \mu m^2$ was retained, considering that the expected tracking accuracy (roughly equivalent to the MSD during the exposure time of 20 ms) is on the order of $\varepsilon^2 \sim 1\ \mu m^2$ and allowing (somewhat arbitrarily) an error of $\pm 1.5\ \mu m^2$. In Figure 58, the ε^2 values are plotted as a function of the diffusion coefficients. These data demonstrate that there is no obvious correlation between ε^2 and D within the selected ε^2 range, and that the exact choice of the ε^2 range boundaries does not impact on the mean value for the diffusion constant. Figure 59 shows that the ε^2 values vary over a rather wide range. These variations give an indication of the accuracy in the fitting of MSD *vs.* lag time traces. Apparently, the fitting is not entirely robust, which means that large datasets are required in order to generate accurate average values for D and ε^2.

Table 5. ***Percentage of Tracks Remaining at Different Quality Control Steps.***

Quality Control Step	Percentage of Tracks Remaining
Removal of tracks near boundary	41%
Removal of low R^2 values	21%
Removal of out of range ε^2 values	13%

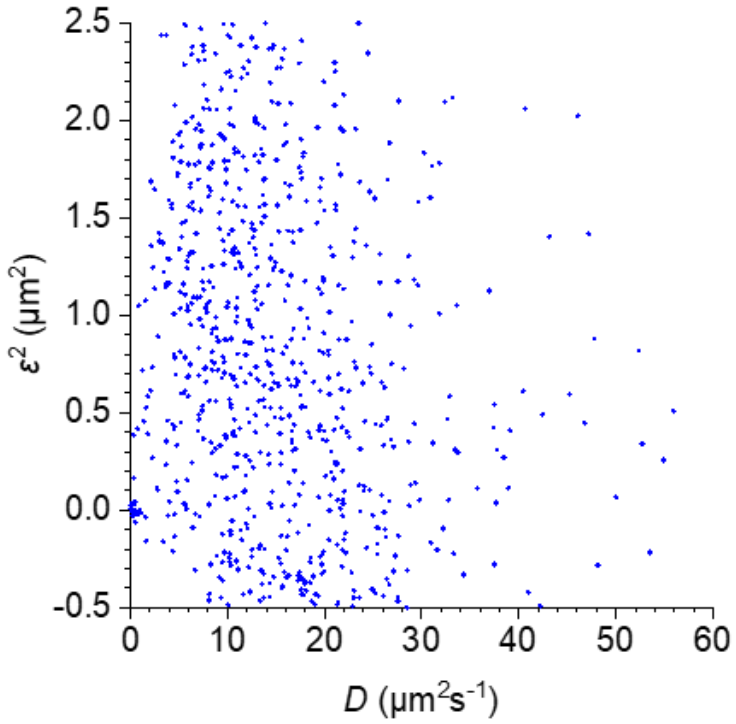


Figure 58. ***ε² and D Values Do not Correlate in the selected ε² range.*** *Shown are ε^2 as a function of D for all tracks retained from the example data set after curation, for the entire gap height range (A) and for gap heights larger than 500 nm (B).*

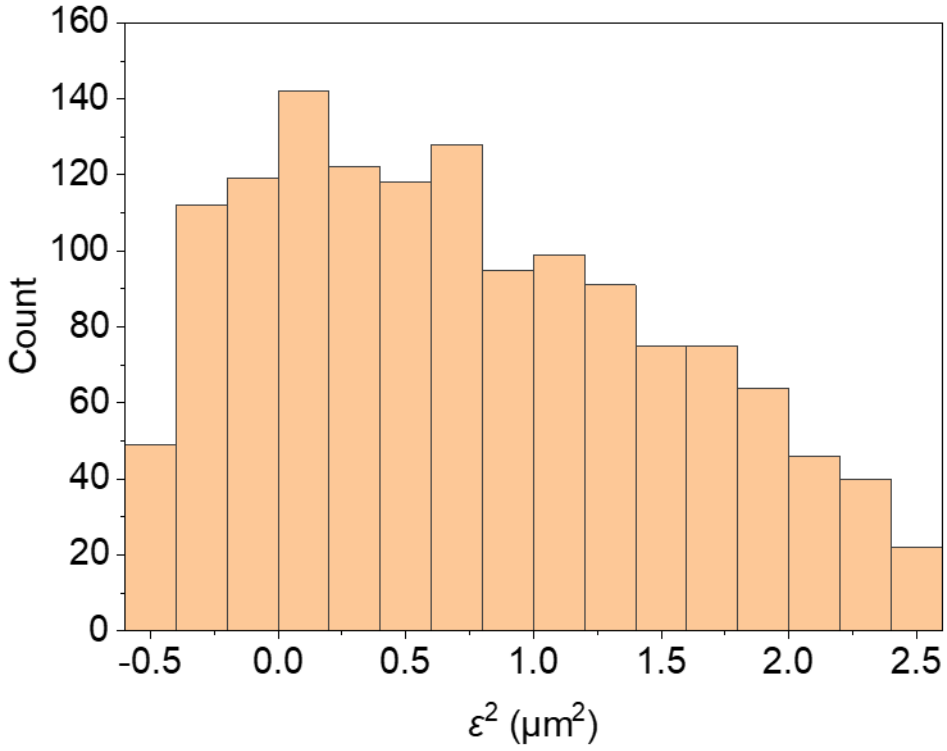


Figure 59. ***The Distribution of ε² Values.*** *A) The distribution of ε^2 (over all gap heights) in a histogram shows the positioning error ε^2 (equivalent to the MSD in the limit of zero lag time) as a function of the gap height.*

The total number of tracks retained after curation was 1397, corresponding to 13% of the total track number. This is a rather small proportion, indicating that most of the tracks were discarded in the curation process. To test if the data curation introduced any bias in the location of validated tracks, the plot of all original tracks (Figure 56A) was compared to the mean *x* and *y* positions of the final validated tracks (Figure 56B). One can see that the main features are maintained across the two maps. For example, a region without tracks between the coordinates *x* = 100 to 120 µm and *y* = 40 to 60 µm, a singular spot at x = 55 µm and y = 45 µm, and another oval shaped region without tracks at x = 60 µm and y = 220 µm, are discernible in both images. This comparative analysis also demonstrates that the mean *x* and *y* coordinates have been computed correctly.

Overall, these data collectively show that the image pre-processing, track generation, MSD analysis and output curation process provided a data set of several hundred validated tracks, with their mean position and their diffusion constants, covering the full range of gap heights.

4.3.3 Proof-of-Principle Application: Analysing EUV Diffusion in Confined Solution and in HA Brushes

This section focuses on the analysis of diffusion coefficients for EUVs in confined solution and in HA brushes. The analysis of diffusion in confined solution acts as a critical control to observe the effects

of the effects of the confined space on the diffusion of the EUVs without the presence of the HA brush. The analysis of diffusion in the HA brush shows how the pore size of a brush impacts on the diffusion of inert molecules through it.

4.3.3.1 Quantifying the Hydrodynamic Size of EUVs

The hydrodynamic size and size distribution of EUVs, which will influence the diffusion of EUVs and subsequent analysis, were first determined by dynamic light scattering (DLS; Figure 60). Two EUV preparations were analysed, which were made with the same lipid mixture (DOPC:DOPC:Bodipy-PC at 89:10:1 molar ratio) but extruded membranes with different pore size (50 nm or 30 nm diameter). The DLS data demonstrated both EUV preparations to be monodisperse, with a polydispersity index of 0.1 or less (Figure 60C). The number weighted average sizes (with standard deviation) were 63 ± 16 nm for EUVs extruded at 50 nm, and 42 ± 11 nm for EUVs extruded at 30 nm (Figure 60D). The standard deviations are around 30% of the mean values, and provide a sense of the size variation that is typical for EUV preparations. In the following the EUVs will be denoted by the size of the pores through which they were extruded, despite their hydrodynamic diameter being slightly higher.

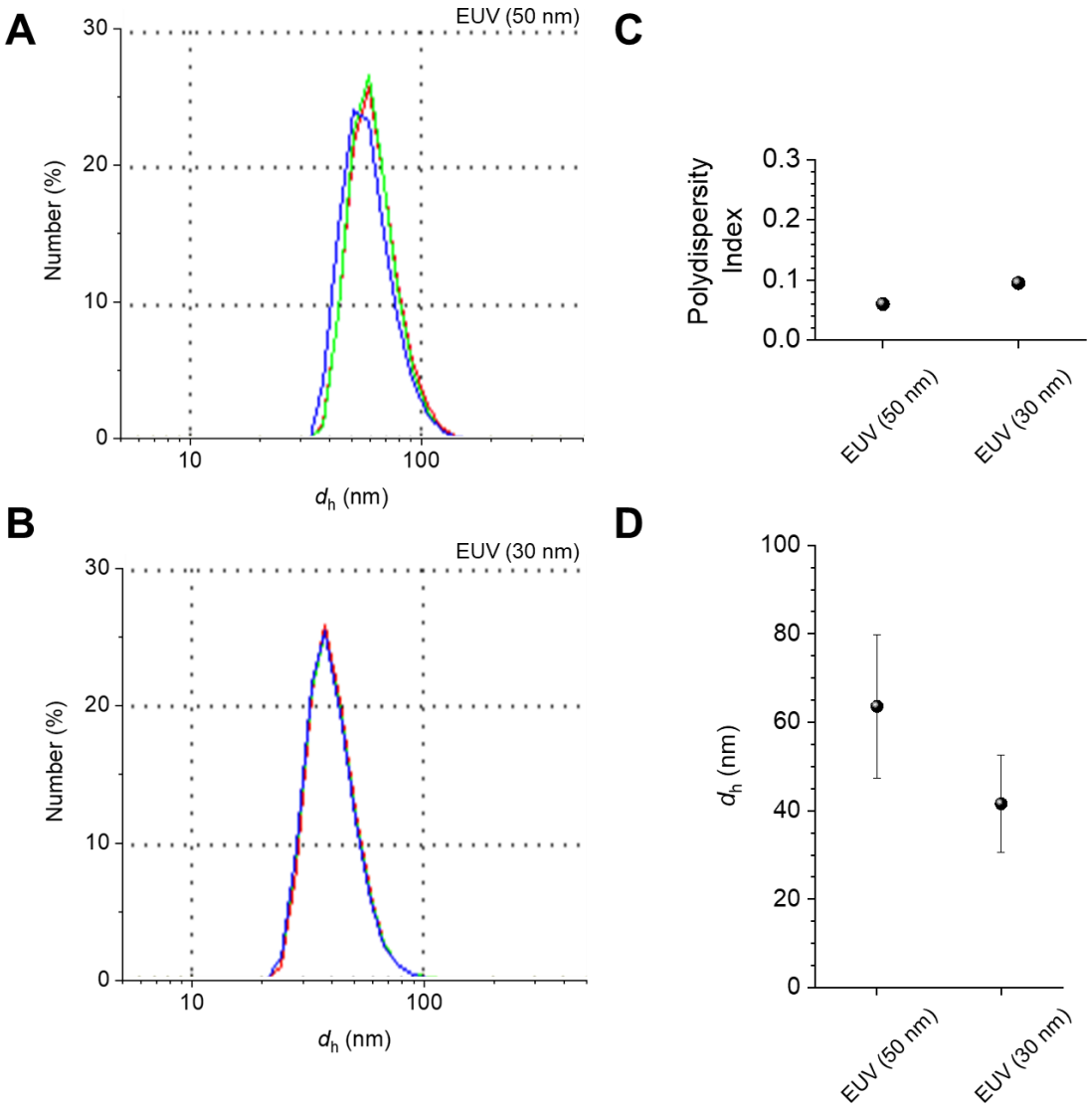


Figure 60. ***DLS Analysis of the Size of EUVs.*** *A-B) Number-weighted histograms of the hydrodynamic diameter d_h of 50 nm (A) and 30 nm (B) EUVs, as determined by DLS. Three data sets are shown (coloured in blue, green and red) for each EUV size, acquired sequentially with the same sample. C) Resulting polydispersity indices. D) Resulting hydrodynamic diameters (mean ± population standard deviation). This analysis was performed by Dr Ralf P Richter.*

4.3.3.2 Analysis of EUVs in Confined Solution

4.3.3.2.1 Quantifying EUV Diffusion in Confined Solution

50 nm EUV (BODIPY containing) diffusion in confined solution was studied by PSCM with a passivated surfaces to minimise EUV binding. The planar surface was passivated with a biotin-presenting SLB, a dense SAv monolayer, and a brush of short (7.5 nm long) HA chains (HA-b dp 15). The hemispherical cap on the glass rod was passivated with BSA. EUVs were injected prior to formation of the plane-sphere contact.

Image time series were processed according to the workflow described in Section 4.3.2 to extract EUV diffusion constants as a function of mean track position. The mean gap height for each track was obtained from the distance of the mean track position from the centre of plane-sphere contact, and the gap height profile calculated according to Eq. [4.4]. Diffusion constants were binned over height intervals of 50 nm, and are plotted as mean with standard error of the mean as a function gap height in Figure 61A.

A clear trend can be observed. The diffusion constant of 50 nm EUVs increases with gap height and reaches a plateau at a gap height of approximately 500 nm. This behaviour qualitatively aligns with trends reported by others for the diffusion of colloids confined between two parallel walls (163-165). Specifically, the plateau above 500 nm can be identified as the diffusion in unconfined bulk solution. At decreasing gap heights, the vicinity of the walls induces a viscous drag that progressively slows diffusion. The transition between bulk diffusion and slowed diffusion occurs at a gap height that is 7 to 8 times larger than the EUV diameter, consistent with findings for other particles confined between walls (163). Figure 62 shows a histogram of the bulk diffusion constants for all EUVs in areas with > 500 nm gap height, that is, the EUVs that effectively experience bulk diffusion. The data are rather well fitted by a Gaussian distribution, with a mean and standard deviation of 13.9 $\pm$ 7.4 $\mu m^2 s^{-1}$. It is notable that the mean obtained from the histogram is somewhat lower than any of the mean values shown in Figure 61A for gap heights above 500 nm. Apparently, a small population of outliers with very high diffusion coefficients (seen in Figure 62) skews the averages in this case. The mean of 13.9 $\mu m^2 s^{-1}$ is of the expected order of magnitude albeit somewhat larger than the diffusion coefficient that the Stokes-Einstein relation ($D = \frac{k_B T}{6\pi\eta r}$) predicts for a particle (D = 7.6 $\mu m^2 s^{-1}$ for a colloid with 63 nm in hydrodynamic diameter at temperature T = 20 °C and viscosity η = 0.9 mPa s). The reason for this remains unclear. However, the here presented data provides good evidence that changes in the diffusion of particles can be reliably quantified.

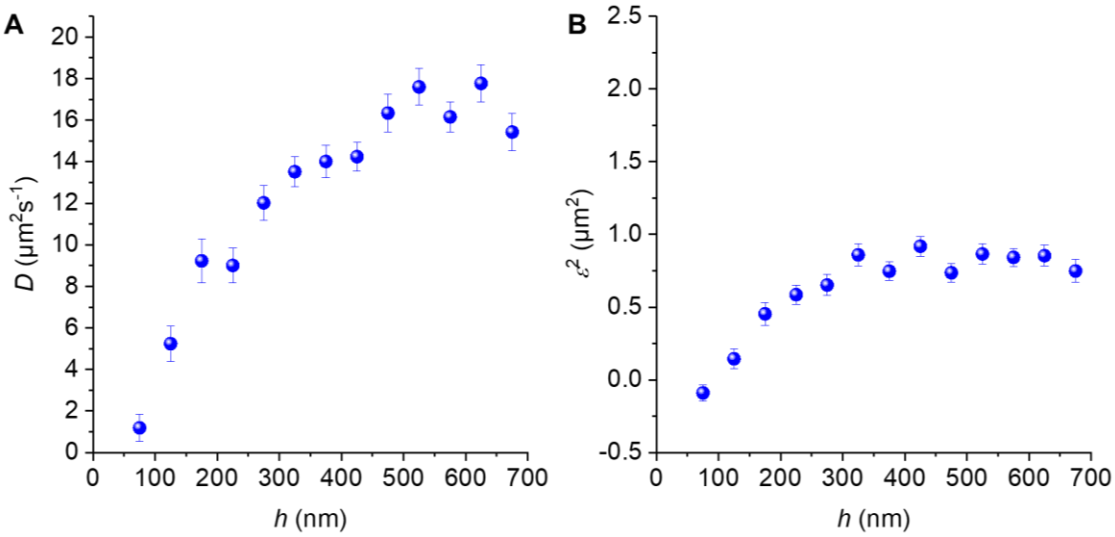


Figure 61. ***Effect of Confinement on the Diffusion of EUVs****. A) Diffusion coefficient D of EUVs as a function of gap height. B) Positioning error ε^2 as a function of gap height. Mean values ± standard errors of the mean are provided (from a total of N = 1397 individual tracks). EUVs were present at a concentration of 0.94 nM in HBS.*

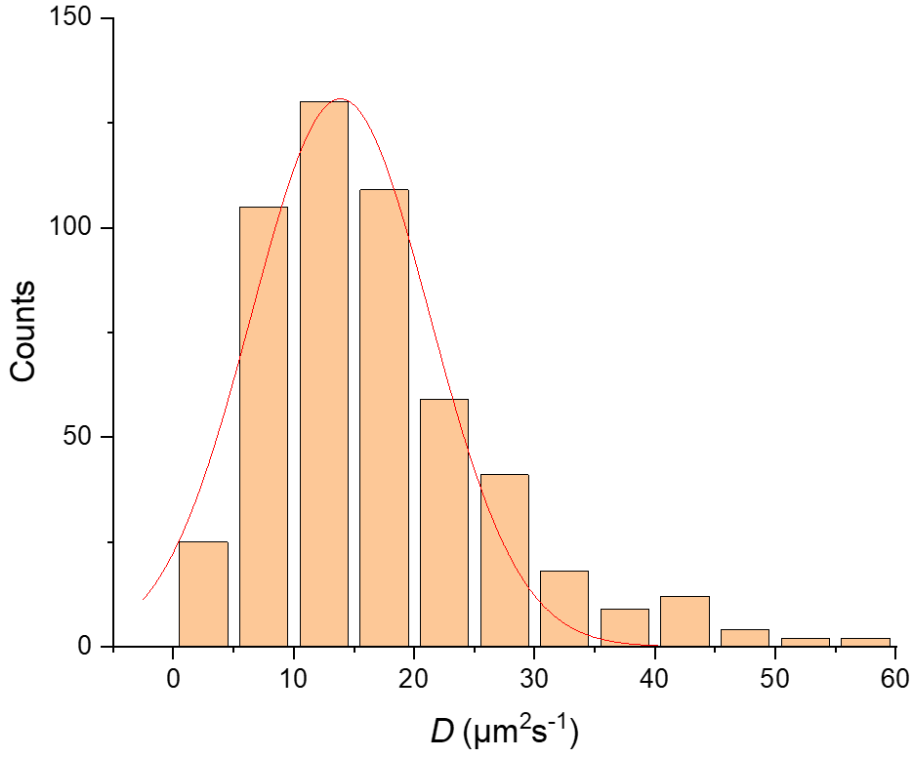


Figure 62. ***Population Analysis of Diffusion of EUVs in the Bulk Solution.*** *A histogram of the diffusion coefficients obtained from diffusion tracks at gap heights greater than 500 nm (N = 516; data as in Figure 61). A Gaussian curve is fit to the data (red line), giving D = 13.9 ± 7.4 $\mu m^2 s^{-1}$ (mean ± SD).*

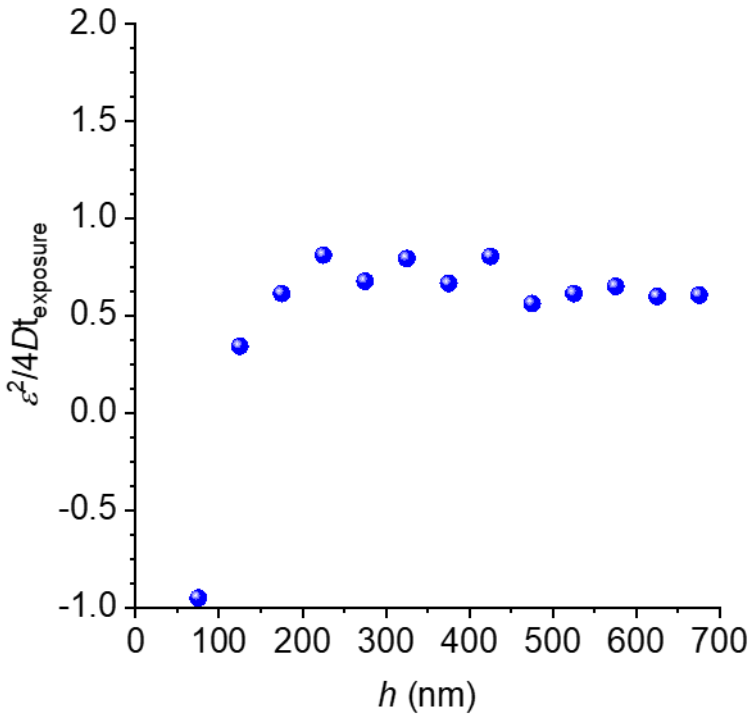


Figure 63. ***ε^2 / 4Dt$_{exposure}$ as a function of gap height.*** *The data from Figure 61B modulated to show the effect of exposure time.*

There is a correlation between ε^2 and gap height (Figure 61B), with D and ε^2 showing similar trends. For 2D diffusion, assuming that the exposure time is the main source of positioning error, and it can be expected that $\varepsilon^2 \approx 4D\mathrm{t}_{\mathrm{exposure}}$ (according to the Einstein-Smoluchowski equation)(18). A plot of $\varepsilon^2/4Dt_{exposure}$ shows that the values for most gap heights are around 0.7 (Figure 63), this is close to the value of 1, the expected value. This highlights that for most gap heights, the main source of error for positioning of particles was the exposure time. For low gap heights (75 nm), this is not the case and there may be another source of error present.

4.3.3.2.2 Estimating Number Distributions of EUVs in Confined Solution

The number distribution of EUVs as a function of gap height is also a parameter of interest, as it gives an indication of the penetration of EUVs into smaller gaps. The number of valid tracks at a specified height range may be used as a proxy for the number of particles. Figure 64A shows the number of valid tracks *N* as a function of gap height. It can be seen that the number of tracks gradually increases with gap height from 1 in the gap height range 50 to 100 nm to approximately 50 for gap heights above 350 nm.

The number of tracks can be converted to a concentration (Figure 64B) in terms of number per volume by:

$$c_{\text{number}} = \frac{N}{V_{\text{eff}}} \approx \frac{N}{\pi R(h-d)\Delta h} \quad [5]$$

where V_{eff} is the effective volume (accounting for volume exclusion at the wall), d = 63 nm is assumed for EUV size, and R = 2.7 mm is the radius of the rod. This number concentration can be further converted to a molar concentration by dividing c_{number} by Avogadro's constant (Figure 64C). The concentration of EUVs calculated in this manner give values in the range of 0.2 to 0.8 nM, which is of the same order of magnitude as the EUV concentration in the bulk solution (0.94 nM).

This comparison suggests that the number of valid tracks represents the number of EUVs rather well. However, it should be stressed that (with the exception of gap heights below 100 nm) the number of valid tracks decreases monotonically (and close to linearly) with gap height, whereas a constant EUV concentration is expected across the full height range. The decreasing track concentration with gap height may be due to tracks going out of the measured range and therefore, being removed as a part of the quality control routine used. Going forward, using the track concentration before the quality control may be better at estimating the concentration of the EUVs, however, this may also add in other artefacts.

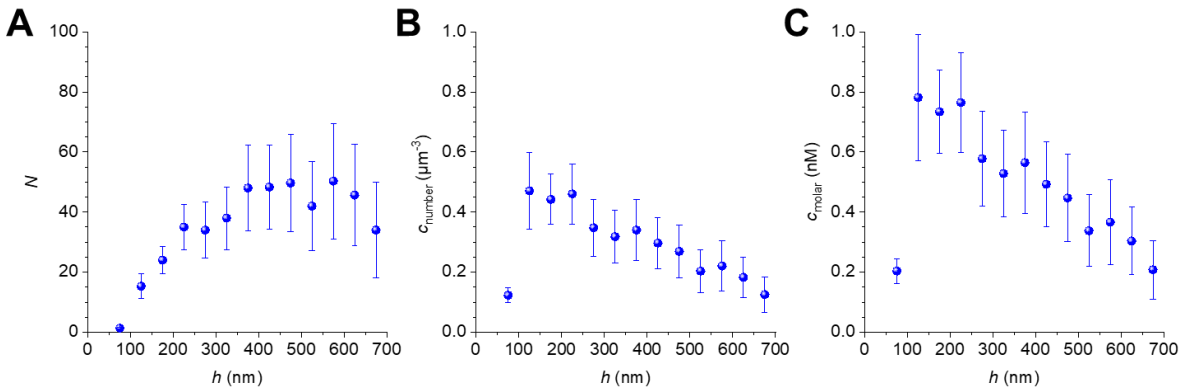


Figure 64. ***Distribution of Tracks within the Confined Space.*** *A) Number of valid tracks N (within 50 nm gap height intervals) as a function of gap height. B) Number concentration of valid tracks, calculated from (A) according to Eq. [4.5], as a function of the gap height. C) Molar concentration of valid tracks as a function of the gap height. Mean values ± standard errors of the mean are presented (total of N = 1397 tracks, from the same dataset as in Figure 61).*

4.3.3.3 Analysis of EUVs in an HA Brush

4.3.3.3.1 HA Brush Design

To analyse the diffusion of the EUVs within an HA brush, the brush must be able to accommodate the EUVs. The EUVs used here are do not bind to HA, as shown in Section 3.3.3. For colloids that do not interact with brushes, the penetration into the brush is primarily dictated by the size of the colloid

relative to the mesh size of the brush (166). Colloids smaller than the mesh size can penetrate the brush quite easily, whereas larger colloids may be quite strongly excluded. For the purposes of demonstrating PSCM in a glycocalyx model, the aim was to design a brush with a mesh size comparable to the EUV diameters (that is, 30 to 80 nm, see Section 4.3.3.1).

The mesh size of HA brushes can be tuned through the size of the HA polymers and their incubation conditions (121, 141). Large molecular weight HA (840 kDa) was used as they do not saturate binding sites and have root mean square anchor distances on the order of tens of nm. An incubation period of 30 min and a concentration of 20 μg/ml was selected based on the root mean square anchor distance larger than 60 nm obtained in SE experiments (Section 3.3.1.2).

The mesh size of the HA brush was determined indirectly: RICM analysis with microbeads provided a measure of the HA brush height ; from the brush height and HA size, the root mean square (rms) anchor spacing between HA polymers was estimated using previously established theory (see Section 4.2.7.1); further, the anchor spacing in brushes is equivalent to the mesh size, to a good approximation (121). Figure 65 shows the heights measured by RICM for control surfaces and surfaces with a brush made from HA-b (840 kDa). Plain glass (Figure 65A) exhibited a mean height very close to zero (h = -1.4 ± 3.5 nm; Figure 65D) as expected for direct contact between the glass and the microbead. The height increased only marginally for films of HA-b dp15 on a SAv-on-SLB coating (h = 6.6 ± 4.4 nm; Figure 65D), broadly consistent with the expected length of the HA oligosaccharide (given that 1 disaccharide is approximately 1 nm and there are 15 monosaccharide units in HA dp15). As expected, the height of the HA-b (840 KDa) film was much larger. A mean height of h = 415 ± 13.6 nm translates to an approximate rms anchor distance, and thus an approximate mesh size, of 80 ± 4 nm. The value is approximate though and may vary by around 10% due to the approximate values of the input parameters. However, considering the estimate in comparison to the size of the EUVs as determined by DLS, one can hypothesise that both EUV types will be able to penetrate this type of brush.

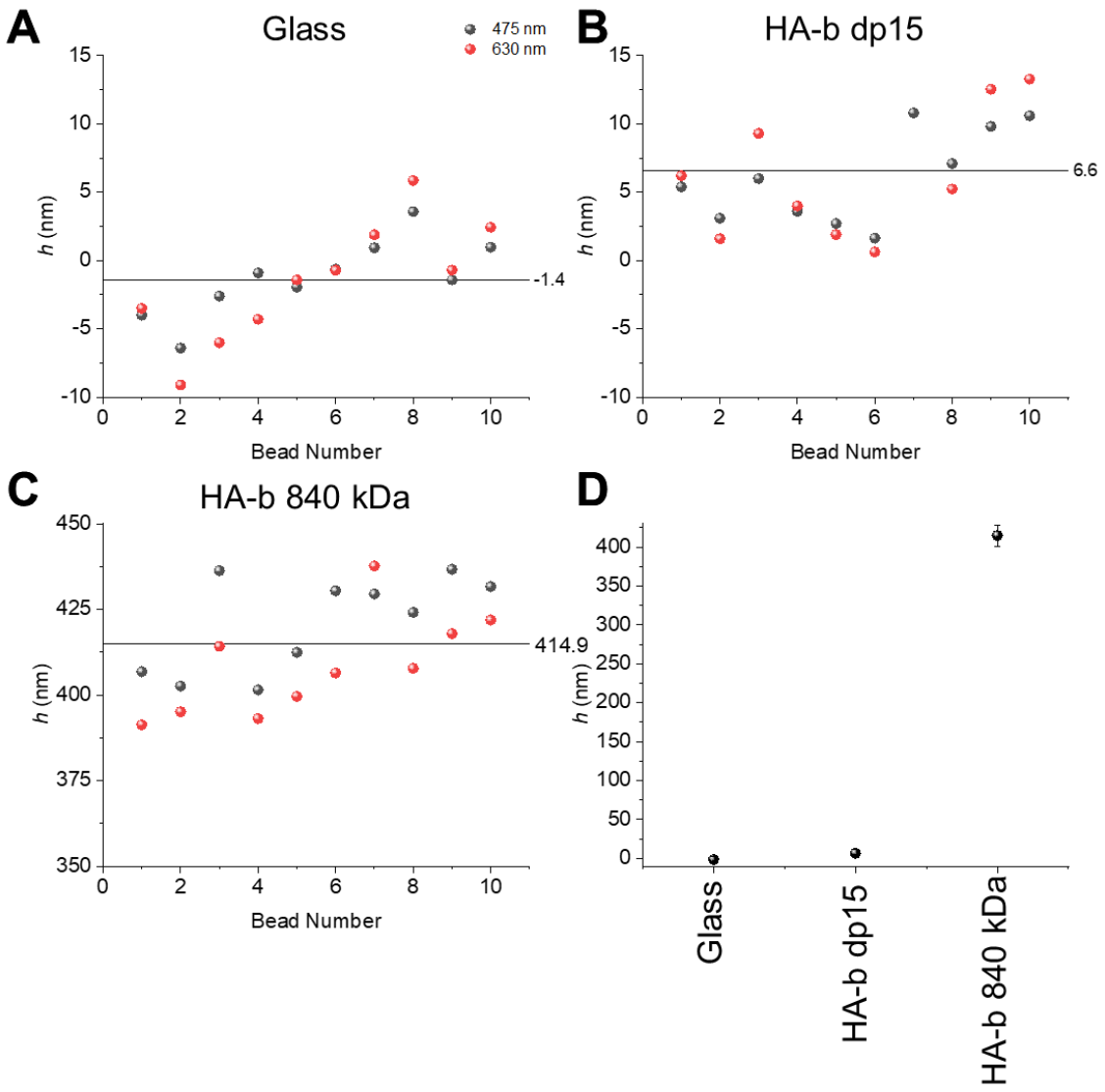


Figure 65. ***Height of HA Brush and Control Surfaces, as Measured by RICM****. The height measured with RICM of polystyrene microbeads on the surface of plain glass (A), an HA-b dp15 film on SAv-on-SLB (B), and an HA-b (840 kDa) film on SAv-on-SLB backfilled with HA-b dp15 (C). Measurements were taken for 10 beads (polystyrene in HBS, 25 µm) at wavelengths of 475 nm (black symbols) and 630 nm (red symbols). The average height for each surface is represented by the horizontal line. D) Mean heights with standard deviations obtained from the data in (A-C). Surface formation included: SUVs – 100 µg/ml, 30 min, SAv-Atto565 – 40 µg/ml, 20 min, GTA – 1%, 10 min, HA-b (840 kDa) – 20 µg/ml, 30 min,HA-b dp15 – 50 µg/ml, 20 min).*

4.3.3.3.2 Quantifying Diffusion of EUVs in an HA Brush

Both 30 nm EUVs and 50 nm EUVs (see Section 4.3.3.3.1) were used to study EUV diffusion in the 840 kDa HA brush. As in the previous analysis of EUV diffusion in confined solution, the HA brush on the planar glass surface was backfilled with HA-b dp15, and the hemispherical cap of the glass rod was passivated with BSA, to minimise non-specific binding of EUVs to the surfaces. EUVs were injected

prior to formation of the plane-sphere contact. The diffusion of EUVs in areas up to gap heights of 1 µm (that is, comprising the brush only areas up to ~400 nm gap height and also areas that included some bulk solution) was then analysed (Figure 66).

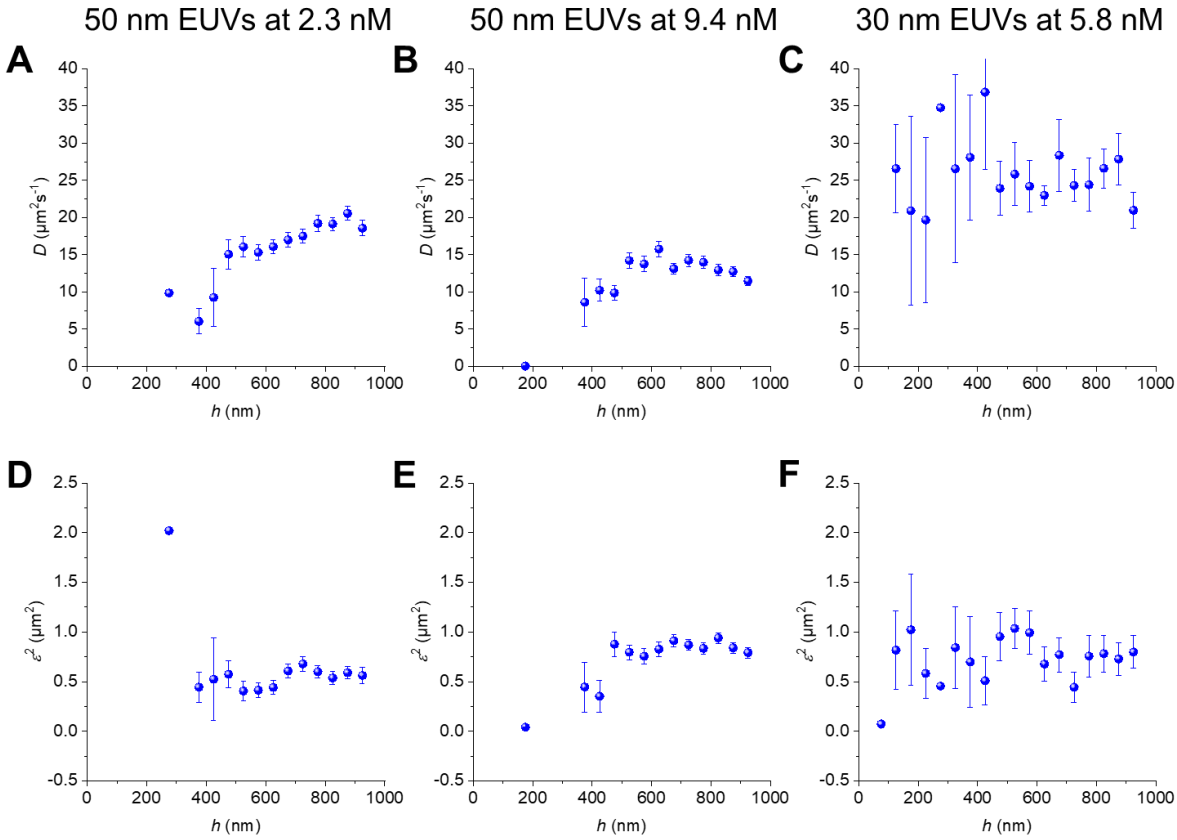


Figure 66. ***Effect of an HA Brush on the Diffusion of EUVs.*** *A-C) Diffusion coefficients of EUVs as a function of gap height for an 840 kDa HA brush. D-F) ε^2 values as a function of gap height for an 840 kDa HA brush. A) and D) 50 nm EUVs at a concentration of 2.3 nM. B) and E) 50 nm EUVs at a concentration of 9.4 nM. C) and F) 30 nm EUVs at concentration of 5.8 nM. Mean values and standard errors of the mean are presented (N = 939 in A) and D), N = 1656 in B) and E), N = 240 in C) and F)).*

For 50 nm EUVs, the diffusion constant in HA brushes was clearly reduced for gap heights below 400 (Figure 66A-B) as compared to diffusion in confined solution (Figure 61A). It is notable that only a few EUVs could be detected within the HA brush. This shows that the EUVs only penetrated with difficulty into the partially compressed HA brush. There are no mobile EUVs below gap heights of 200 nm, whereas without the HA brush, the EUVs were mobile down to gap heights of 75 nm. This clearly shows that the presence of the HA brush affects the ability of the EUVs to diffuse. This observation does lead to the question over how to discriminate EUVs that are trapped in the brush from those that are non-specifically bound to the surface. Observing the time series before and after processing (as achieved in Figure 55) showed that particles that had limited mobility to that of small vibrations were

maintained after processing. Particles that were totally immobile were not retained, it is difficult to discriminate by eye if these immobile particles are trapped in the brush and those non-specifically bound. Though, a quantification of the number of immobile particles could provide some insight if they differ between the two data sets. However, using this type of analysis, it is difficult to say if these values are actually significantly different or part of normal variations in non-specifically bound EUVs.

It should here be noted that the mesh size of the HA brush will decrease as the brush becomes increasingly compressed in smaller gap heights (122). To a first approximation, the mesh size is inversely proportional to the HA concentration, this is has been used within the literature, for example in Ref. (158). This implies that at a gap height of ~200 nm the mesh size would decrease by twofold (to 40 nm) compared to the average mesh size (80 nm) at its unperturbed height (~400 nm). The lack of penetration and mobility at gap heights below ~200 nm thus, is consistent with steric constraints imposed by the HA meshwork.

The diffusion of the 30 nm EUVs did not show any clear trends (Figure 66C). Whilst diffusion values scattered more than for 50 nm EUVs, the averages tended to remain unchanged even for gap heights down to 200 nm. The 30 nm EUVs were able to penetrate even smaller gap heights, between 100 and 150 nm, broadly consistent with their smaller size. The ε^2 data show similar correlations to gap height as *D* (Figure 66D-F), this is similar to the correlations in solution. Therefore, the same assumptions in the positioning error can be made here as in Section 4.3.3.2.1, that the exposure time is the main source of error in the positioning. Overall, these data demonstrate how the HA brush can sensitively affect EUV diffusion as a function of EUV size and brush compression.

Diffusion of EUVs in the solution above the HA film, essentially bulk solution, was also analysed through histograms (Figure 67). For 50 nm EUVs at the lower concentration (Figure 67A) the diffusion constant obtain via a Gaussian fit (D = 16.8 ± 8.6 $\mu m^2\ s^{-1}$) was congruent with the diffusion coefficient at large enough gap heights without the brush (D = 13.9 ± 7.4 $\mu m^2 s^{-1}$, see Figure 62). The increase in concentration from 2.3 nM to 9.4 nM led to a reduction in diffusion in the bulk of 7.9 ± 6.8 $\mu m^2 s^{-1}$, this could be due to molecular crowding decreasing the mobility of the molecules. This is unexpected as the concentrations used here are low such that the effective volume fractions of the EUVs are small and molecular crowding should be negligible. Therefore, this is unlikely the explanation. Surprisingly, the 30 nm EUVs had two populations of diffusion coefficients, a first and slightly larger population at 14.5 ± 5.8 $\mu m^2 s^{-1}$ and a second the slightly smaller population at 36.4 ± 8.2 $\mu m^2 s^{-1}$. It is unclear why this would be the case, but it could be that one population is diffusing through the brush and another is purely in bulk solution.

These values were compared to the Stokes-Einstein diffusion coefficients calculated based on the hydrodynamic diameters measured by DLS (Figure 67D). All experimental values are somewhat larger than the theoretically expected values in bulk solution. It is unclear why this is the case. Despite this systematic difference, and as mentioned earlier (see Section 4.3.3.2.1), this data is still successful in showcasing the impact of the HA brush on the diffusion of the EUVs.

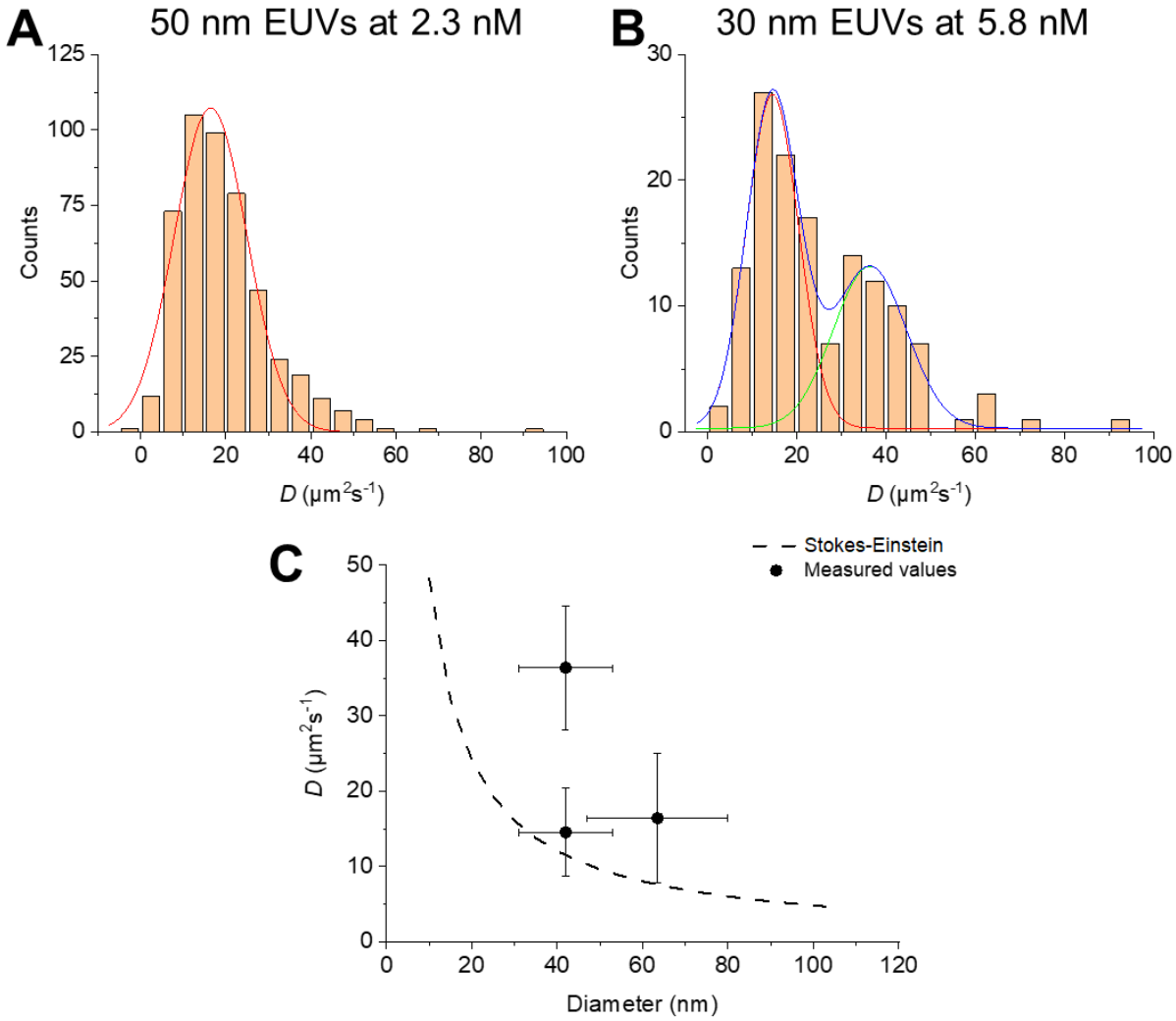


Figure 67. ***Population Analysis of Diffusion of EUVs above (and within) the HA Brush****. Histograms of the diffusion coefficients of 50 nm EUVs at 2.3 nM (A) (N = 484) at gap heights greater than 750 nm, and 30 nm EUVs at 5.8 nM (B) (N = 137) at gap heights greater than 650 nm. Lines are Gaussian fits with one (A) or two (B) peaks to the data. C) Comparison of the mean diffusion coefficients (obtained from A-B) as a function of diameter of 50 nm EUVs at 2.3 nM and 30 nm EUVs at 5.8 nM. The dotted line represents the values expected according to the Stokes-Einstein relation (Section 5.2.2) using T = 293 K and η = 8.9 × 10-4 Pa·s. The error bars represent population standard deviations.*

4.4 Discussion

The main results of this chapter are:

- The new PSCM stage insert enhanced control over the compression force and provided stable plane-sphere interfaces. The addition of a motorised cantilever to control the rate of approach of the curved surface, and crosslinking of the SAv layer holding the model glycocalyx, helped to reduce (and in the ideal case virtually eliminated) damage to the functionalised surface in the vicinity of the contact area.
- A workflow for single particle tracking in PSCM was developed and validated.
- As a proof-of-principle application, the diffusion of non-sticky EUVs in confined solution and in an HA brush was successfully quantified.

4.4.1 Further Improvements

The developments produced within this chapter can now be applied to model glycocalyces and to reliably study films with a height of 70 nm, as this is the most reproducible limit of damage that can be achieved. This is applicable for studies on the ECM as many HA based model matrices are focused on films of 250 nm or more (91, 104, 121). It is also clearly possible to limit the damage to gap heights of 10 nm, highlighting there is still room for development to make this more reliably reproduced. This would require the interface to be more extensively studied to reveal exactly why some cases result in more damage than others do. If indeed the addition of polymers to the surface does increase the damage area due to the inherent nature of the polymers, it may be possible to crosslink the polymers themselves in order to increase their resistance. However, crosslinking of polymer will have an effect on the diffusivity of particles through them if the particle is similar in size to the pore size generated (167, 168). If the particles are smaller than this, it may be a viable option.

Previously, there was no method for SPT of PSCM data. The data here present a clear method for SPT from PSCM data, creating a method to study diffusion of particles that are visible in fluorescent microscopy within a polymer brush. This is an area that lacks robust methods; the data within this chapter has created a method to fill this gap. Although the initial tracking of the particles was a method that has a lot of similarities to other microscopy outputs (85, 116, 169), PSCM presents the unique challenge of having to be aware of the exact position of the particles throughout the tracking period, relative to the contact point and the gap between the two surfaces, for stringent analysis. The development of the workflow, by modifying the MSDAnalyzer, allowed the diffusion coefficient to be extracted along with the mean position and its corresponding gap height much increased the speed of the analysis. All the important parameters are calculated in one place and are kept together. This is vital as with single particle tracking, there are often very large data sets and to do such analysis individually would be a tedious process. This aspect was the main challenge of this analysis, each

individual track had large amounts of information associated with it that needed to be retained for the objective analysis. This is unique to PSCM, and separates it from other microscopy techniques. A current drawback is that, although the analysis method works robustly, many manual steps are required. This adds an appreciable amount of time to the analysis. In the future, it may be possible to generate a macro within Fiji ImageJ that can perform all pre-processing steps automatically for multiple image sets. However, this would need to be stringently tested as errors in the pre-processing do influence the tracking procedure.

Thus, the tools for experimentation and data analysis presented here provide key methods that have been missing within the field of diffusion analysis within extracellular matrices.

4.4.2 Implications on the Impact of an HA brush on Diffusion

The technique developments were not the only key result in this chapter. The PSCM method was applied to a model ECM for the first time and the diffusion of EUVs was measured. The effect of the confinement between two surfaces and the addition of an HA brush on the diffusion coefficient of EUVs compared to the diffusion in solution. Confinement impacted on diffusion up to gap heights of 300 nm and the HA film impacted on diffusion up to heights of 500 nm. This is in alignment with published literature on Brownian motion in confined space and the diffusion of particles through polymer matrices with defined pore sizes (163, 166, 167). These data also highlight that affinity to glycosaminoglycans or other glycocalyx components is not the only thing that can influence on the diffusion of biological colloids, the pore size will also impact on the diffusion.

Although the bulk diffusion coefficients were higher than the values predicted by the Stokes-Einstein relation, the results as a comparison of diffusion within a brush and in solution effectively show that the HA brush decreased the mobility of the individual particles. One could expect that the differences in diffusion between the two different sizes of the EUVs would be the same if the EUVs had shown a diffusion coefficient closer to the Stokes-Einstein value in solution.

Furthermore, there are biological implications for the decreased diffusion coefficient of the EUVs within the HA brush. The extracellular matrix can be considered as a filtering system where the individual components guide what material is able to enter different types of matrices (170). The data presented here show that the matrix can effectively exclude particles of specific size and slow their diffusion so that they cannot penetrate further and interact with molecules in other areas. This is also congruent with the idea that the endothelial glycocalyx sheds glycosaminoglycans during extreme immune events which could allow larger biological colloids, such as cells, to penetrate the matrix (37, 49). Other types of extracellular matrix may also have different pore sizes that aligns with their function, and this could be related to their GAG composition (22).

On the whole, these data have contributed to both method development for other studies on diffusion in the ECM, but also to biological understanding by providing evidence that an HA matrix can restrict diffusion.

4.4.3 Future Applications

PSCM can be used for many applications. In particular, one application that would complement the results shown here would be to vary the pore size of the matrix over a wide range to include those that have been observed in different types of matrices and to use a greater range of EUVs to cover the range of protein sizes in the ECM. Performing the same analysis as that shown here, it would be possible to describe what the pore size matrix effects, including the different size ranges of the biological colloids within the matrix. This would provide a good idea of the level of base diffusion within the ECM before adding in the complexity that affinity to the matrix would add. This would also be a good way to validate simulation studies on the effect of pore size on diffusion (167).

PSCM may also be used to investigate the exchange between bulk solution and the matrix. As presented in Figure 38, there is an exchange between the bulk solution and thin films when thin films are present on surfaces. This exchange is governed by diffusion into the film. A recent publication has investigated a way to model the entry of particles with a polymer film (158). PSCM has the features that would enable this type of diffusion to be measured directly. Therefore, it would be possible to confirm the theoretical predictions within Ref. (158) by recreating the system that is described within it.

Overall, there are many possibilities for the application of PSCM for the studies of diffusion and this chapter provides the critical experimental and analytical tools that would allow these applications to have impact on research on diffusion.

Chapter 5: An Analytical Model for Biological Colloid Diffusion in a Sticky Polymer Matrix

5.1 Introduction

The diffusion of biological colloids in the extracellular matrix was once believed to be a result of passive diffusion, that is, molecules diffuse through the ECM unhindered as if they were free in solution (171). However, the ECM is filled with many polymers such as glycosaminoglycans (GAGs) which form crucial parts of this intercellular space and regulate the functions that are performed there (2). Many GAGs interact specifically with signalling proteins. A good illustration of this is that the presence of glycosaminoglycans is required for the correct distribution and diffusion of chemokines (26) or that glypicans (HS proteoglycans) are required for the correct diffusion of Hedgehog (a morphogen) and regulate proper development of different body parts, such as the wing disc in *Drosophilia* and nervous system in mammals (79). These types of data provide the information required to understand how the glycan components of the extracellular matrix control the distribution and destination of proteins in the ECM.

There are few studies that have investigated diffusion of molecules in the ECM (83, 168, 169, 172, 173) and fewer focusing specifically on GAG binding molecules (40, 63-65, 85). The results are insightful, but span a large range of values (Table 6) which creates difficulty in attempts to link the similarities between the systems. For example, Sun *et al.* measured the mobility of growth factors on the pericellular matrix of fibroblast cells with FRAP and analysed the differences extensively, but stopped short of describing the diffusion coefficient (65). A diffusion coefficient value allows diffusion to be compared across multiple studies with greater ease. The qualitative analysis of FRAP studies can be informative but it is difficult to compare that type of analysis with other methods to measure diffusion. Miller *et al.* provides values for the diffusivity of chemokines using single molecule tracking of CXCL12 in murine lymph node tissue, but the investigation into the effects of the relationship between HS and CXCL13 on this diffusivity is limited (85). A summary of measured diffusion coefficients for studies on GAG binding proteins are presented in Table 6.

There are a number of studies that focus on a theoretical prediction of diffusion of inert molecules through polymer matrices (166, 167, 174). These studies describe how molecules would diffuse through polymer matrices of defined pore size, but in these cases there are no interactions between the polymers and the diffusing molecules. They simply describe the effects of steric hindrances on diffusion and focuses on cases were the pore size of the matrix, and the diffusing molecule are of similar size. However, the glycocalyx has a pore size 5 times greater than the typical size of a signalling protein (29 nm vs 5 nm) (43, 175). Laktionov *et al.* describes the entry of colloids into polymer films for which they have a defined affinity, which is a similar case as what might be found between GAGs and their binding partners in an ECM (158). However, there are some assumptions made in this model that do not align with the reality of GAG-binding proteins and GAGs. For example, Laktionov *et al.*

assumes the interaction site on the colloid are spread over the entire surface, but for GAG binding proteins, the protein will have one or more specific binding sites that interact with specific binding sites on GAGs. Therefore, although some aspects of the Laktionov model are similar, there are some key differences which make it unable to describe the diffusion of GAG binding proteins in a GAG-rich matrix context.

Within this chapter, the aim is to generate a theoretical model that describes the diffusion of a macromolecule within a matrix of sticky polymers. The model focuses on the single point interactions, that can be defined by a dissociation constant, between biological colloids and polymers and how this would affect the time the colloid spends immobile (bound) in the ECM. This was achieved with the effective diffusion coefficient relying on the Stokes-Einstein diffusion coefficient, the concentration of binding sites, and the dissociation constant of the macromolecule to the polymer. This model neglects steric hindrance effects and the role of multivalency. Predictions of the model were compared to experimental values pertaining to GAG-protein interaction systems. This was successful in the cases, with more simple interaction systems, indicating that this model is a good first step in describing macromolecular diffusion in polymer matrices, but there is still a greater layer of complexity that remains to be elucidated.

Table 6. ***A Selection of Dissociation Constants for Proteins and their Measured Diffusion Coefficients.*** *The experimental values for K_d and diffusion from a variety of different studies using differing systems and methods of measurement.*The diffusion coefficient of the largest fraction of different mobile fractions.*

Protein	**GAG**	K_d	**Source**	**Measured Matrix Diffusion Coefficient**	**Source**
FGF2	HS	23.6 ± 2.2 nM	(176)	0.6 ± 1 $\mu m^2 s^{-1}$	(176)
		800 ± 600 nM	(40)	0.00015 – 0.25 $\mu m^2 s^{-1}$	(40)
FGF1	HS	0.4 – 8.6 µM	(61)	0.22 $\mu m^2 s^{-1}$	(8)
CXCL13	HS	19 nM	(10)	6.6 ± 0.4 $\mu m^2 s^{-1}$	(85)
CXCL12α	HS	200 ± 14 nM	(126)	None	N/A
CXCL12γ	HS	1.5 ± 0.2 nM	(126)	None	N/A
	DS	4.8 ± 0.04 nM			
Interferon (IFN) γ	HS	1.5 nM	(177)	None	N/A
Halo-GFP	None	N/A	N/A	28 ± 1* $\mu m^2 s^{-1}$	(169)

5.2 Results

5.2.1 An analytical model of macromolecular diffusion in a sticky polymer matrix

5.2.1.1 Defining the interaction scenario

The interaction scenario considered in this model is schematically described in Figure 68. The biological colloids diffused through the matrix of thickness ~ 100 nm and pore size ~30 nm, the colloid itself has an average size of 5 nm and interacts site specifically with the polymer. The main feature of the model is that random diffusion of the macromolecule is interrupted by attractive interactions within the polymer matrix. The polymer matrix is assumed to be quite open, with a typical pore size, ξ, much larger than the hydrodynamic radius, r, of the diffusing macromolecule ($\xi >> r$). Under these conditions, the effect of steric hindrance due to the polymer matrix on the rate diffusion compared to plain bulk solution is minor, and is here neglected.

Herein, an effective diffusion coefficient in the polymer matrix is derived. It represents the average rate of movement at a scale much larger than the distance between individual binding sites in the matrix, and considers how transient sticking to the polymer matrix modulates the random diffusion in the solution that pervades the matrix. Therefore, the terminal diffusion coefficient is the main parameter of interest.

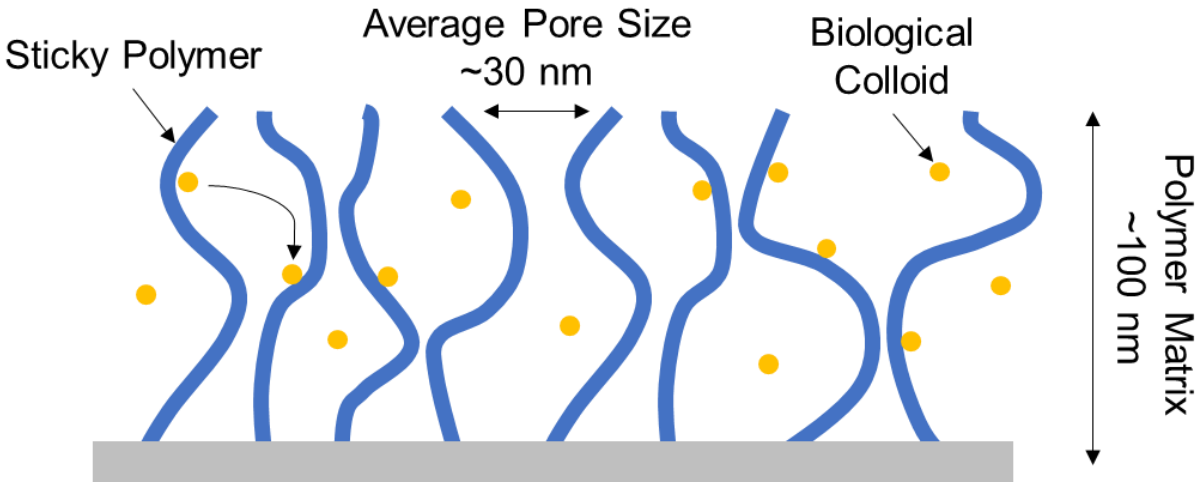


Figure 68. ***The Diffusion Process in a Sticky Polymer Matrix****. Biological colloids diffuse within the matrix by passing from binding site to binding site on the polymer chains.*

5.2.1.2 Defining the interaction between macromolecule and polymer

The interaction strength (affinity) between the molecule and the polymer is described by the dissociation constant K_{d}. The dissociation constant in turn is the ratio of the dissociation rate constant k_{off} and the association rate constant k_{on}:

$$K_{\mathrm{d}} = \frac{k_{\mathrm{off}}}{k_{\mathrm{on}}}. \qquad [5.1]$$

Following work by Svante Arrhenius, the individual rate constants can be linked to the activation energies for unbinding and binding (178). k_{off} and k_{on} are here expressed in units of s^{-1} and $s^{-1}M^{-1}$, respectively, and K_d thus has units of M.

The interactions considered here are monovalent, the molecule has a single binding site on its surface that interacts with the polymer. The binding of this molecule to the polymer should also not substantially affect the properties of the matrix. Though this may not be true for many GAG interactions, considering the interactions as monovalent in the first instance allows for the model to be built on later to include more complex interactions.

5.2.1.3 Defining diffusion in plain solution and in the polymer matrix

Brownian motion refers to the free diffusion of a macromolecule in solution, driven by random collisions with surrounding molecules. The rate of diffusion is defined by the thermal energy k_BT (which are the Boltzmann constant and temperature, in Kelvin, respectively), the hydrodynamic radius r of the macromolecule, and the viscosity η of the solution, through the Stokes-Einstein equation (17):

$$D = \frac{k_B T}{6\pi\eta r}. \qquad [5.2]$$

It is important that the radius here is defined as the hydrodynamic radius, this allows for different shaped molecules to be considered. Proteins are not strictly spheres and, therefore, do not have a strict radius.

Because Brownian motion is random in all directions, we cannot directly measure distance moved, but rather express the level of movement by the mean square displacement (MSD, $\langle x^2 \rangle$). MSD and diffusion can be linked by the Einstein-Smoluchowski equation (18):

$$\langle x^2(t) \rangle = 2nDt, \qquad [5.3]$$

where n is the number of dimensions of the system in which the molecule is diffusing, and t is the time frame over which the diffusion is considered.

The Einstein-Smoluchowski equation is not only valid in bulk solution. It also adequately describes the diffusion of a macromolecule in our open polymer matrix, over times and distances that are too short for the macromolecule to bind to the matrix.

The Einstein-Smoluchowski equation also captures the effective diffusion of macromolecules in the sticky polymer matrix over long times and distances. However, the effective diffusion coefficient D_{eff} is now defined by a sequence of periods of diffusion between polymer strands interspersed by periods of immobility due to sticking to a polymer stand:

$$D_{\mathrm{eff}} = \frac{\langle x^2 \rangle}{2n\tau_{\mathrm{T}}}. \qquad [5.4]$$

Here, the terminal relaxation time τ_{T} refers to a long time scale, that is, sufficient for both diffusion and sticking periods to occur.

5.2.1.4 A Theoretical Model of Diffusion in a Sticky Matrix

In order to derive the effective diffusion coefficient for a macromolecule in a sticky yet open polymer matrix, a few additional assumptions are made:

1. There is no change to polymer distance and number of binding sites: The concentration of binding sites (c_{bs}) in the polymer matrix remains constant throughout the diffusing time of the molecule, and the diffusion coefficient of the polymer is zero. However, the results should provide a good approximation even for mobile polymers as long as the diffusion coefficient of the matrix polymers is small compared to D_{eff}.

2. There is no bulk solvent flow within the system: Convective transport is ignored, and all molecular displacement is due to the intrinsic diffusion of the macromolecule.

3. The concentration of the diffusing molecule is constant: The matrix considered here is two dimensional, for simplicity but likely applicable to 3D matrices, with no source or sink of the molecule and the concentration of this molecule remains constant over the time considered and diffusion of the molecule is not dependent on a concentration gradient.

4. The concentration of the diffusing molecule is low in comparison to the total concentration of binding sites. This assumption is made in order to ensure that the concentration of free binding sites is not much smaller than the total concentration of binding sites.

The two distinct and alternating phases of movement in the matrix can now be considered explicitly. A molecule may be either bound to a polymer site and thus effectively immobile, or unbound and free to diffuse in the solvent spaces within the matrix until it binds a new polymer site. Both these phases have their characteristic durations (τ_{bound} and τ_{unbound}, respectively), defining the total time for a cycle of bound and unbound phases as $\tau_{\mathrm{cycle}} = \tau_{\mathrm{bound}} + \tau_{\mathrm{unbound}}$.

The Einstein-Smoluchowski equation links the mean square displacement $\langle x^2 \rangle$ to time. Whilst the molecule is unbound:

$$\langle x^2 \rangle = 2nD_{\mathrm{matrix}}\tau_{\mathrm{unbound}}, \qquad [5.5A]$$

where D_{matrix} is the diffusion rate within the solvent spaces of the matrix. For an open matrix, D_{matrix} is effectively described by the Stokes-Einstein diffusion rate ($D_{\mathrm{matrix}} = D$; Equation 5.2).

On the other hand:

$$\langle x^2 \rangle = 2nD_{\mathrm{eff}}\tau_{\mathrm{cycle}}. \qquad [5.5B]$$

As there is no additional movement during the bound phase, D_{eff} is the effective diffusion coefficient of the macromolecule as it moves through the sticky polymer matrix.

Equations 5.5A-B lead to:

$$\frac{D_{\mathrm{eff}}}{D_{\mathrm{matrix}}} = \frac{\tau_{\mathrm{unbound}}}{\tau_{\mathrm{cycle}}} = \frac{\tau_{\mathrm{unbound}}}{\tau_{\mathrm{unbound}}+\tau_{\mathrm{bound}}} = \left(1 + \frac{\tau_{\mathrm{bound}}}{\tau_{\mathrm{unbound}}}\right)^{-1}. \qquad [5.6]$$

The characteristic duration of the bound phase is defined by the dissociation rate constant, k_{off}, as:

$$\tau_{\mathrm{bound}} = \frac{1}{k_{\mathrm{off}}}. \qquad [5.7A]$$

The characteristic duration of the unbound phase is defined by the association rate constant, k_{on}, and the concentration of binding sites in the matrix, c_{bs}, as:

$$\tau_{\mathrm{unbound}} = \frac{1}{c_{\mathrm{bs}}k_{\mathrm{on}}}. \qquad [5.7B]$$

Inserting Equations 5.7A-B into Equation 5.6 gives:

$$\frac{D_{\mathrm{eff}}}{D_{\mathrm{matrix}}} = \left(1 + \frac{c_{\mathrm{bs}}k_{\mathrm{on}}}{k_{\mathrm{off}}}\right)^{-1}. \qquad [5.8]$$

Recognising the dissociation constant, Equation 5.1, gives:

$$D_{\mathrm{eff}} = \frac{D_{\mathrm{matrix}}}{1+{}^{c_{\mathrm{bs}}}/_{K_{\mathrm{d}}}}. \qquad [5.9]$$

This final equation predicts that the effective diffusion coefficient of a molecule is proportional to the product of the diffusion rate in the matrix and depends on the ratio of the concentration of binding sites and the dissociation constant. It is interesting that only the equilibrium constant, and not the rate constants individually, is significant for the diffusion, but does emphasise that the affinity of the interaction is paramount in this system.

Two extreme cases are noteworthy. If the concentration of binding sites is very small ($c_{\mathrm{bs}} \ll K_{\mathrm{d}}$), then the $c_{\mathrm{bs}}/K_{\mathrm{d}}$ ratio can be neglected and Equation 5.9 becomes:

$$D_{\mathrm{eff}} \approx D_{\mathrm{matrix}}. \qquad [5.10A]$$

This is a trivial result. On the other hand, if the concentration of binding sites is much larger than the dissociation constant ($c_{\mathrm{bs}} \gg K_{\mathrm{d}}$), then:

$$D_{\mathrm{eff}} \approx D_{\mathrm{matrix}}\, K_{\mathrm{d}}/c_{\mathrm{bs}}. \qquad [5.10B]$$

Overall, the main results are that the diffusion of biological colloids in sticky polymer matrices can be described by Equations 5.9 and 5.10. Allowing the diffusion to be described with simple knowledge of the colloid and the interaction system.

5.2.1.5 Extensions to the Model

5.2.1.5.1 Effect of Steric Hindrance on Diffusion

There are scenarios where steric effects need to be considered, in such situations where the size of the colloid approaches the average pore size of the matrix. Any steric effects will be imposed on D_{matrix}, maintaining the validity of Equation 5.9 as long as the binding of the colloid to the polymer meshwork does not affect the meshwork itself. The effects of steric hindrance can be incorporated into the model via D_{matrix}. This can be achieved using the approach by Cai *et al.*, where the diffusion of particles larger than the pore size of the matrix is dependent on the effective viscosity, which relies on the correlation length of the polymer, diffusion of particles much greater than the pore size is dependent on the bulk viscosity of the polymer solution (166). Therefore, this allows the incorporation of steric effects into the model.

5.2.1.5.2 Effect of High Concentration of Macromolecules on Diffusion

The impact of concentration on diffusion should also be considered. The Stokes-Einstein diffusion coefficient is independent on concentration, but Equation 5.9 includes the concentration of binding sites as a factor that will affect the effective diffusion in the matrix. There may be scenarios where the concentration of the diffusing molecules is high, resulting in the occupation of a sizeable fraction of the binding sites in the matrix. This results in an effective decrease in the concentration of binding sites, increasing the value of D_{eff}. This is biologically relevant as typically for cellular responses, a critical concentration of receptors must be occupied to trigger the response downstream within the cell (53, 179). Therefore, in certain circumstances, the concentration of free binding sites may be a better measurement than the concentration of binding sites alone in order to predict the effective diffusion.

5.2.1.5.3 Effect of Multivalent Binding on Diffusion

Many molecules have the ability to bind simultaneously to multiple different binding sites (180, 181). Multivalent binding is often a contributing factor for enhanced strength of binding and, therefore, can increase the residence time (τ_{bound}) of the molecule to the polymer. This would ultimately affect the effective diffusion coefficient. This is particularly relevant for the extracellular matrix as it harbours

multiple interaction pairs that have multiple sites for interaction between them (22, 41, 48, 86, 159, 182). For example, many chemokines have the ability to multimerise and crosslink HS chains, this indicates multiple different interaction points for these molecules (38, 41, 48, 100).

To a first approximation, if there is one K_{d} value for the interaction between the polymer and the colloid that is not linked to a specific binding site (affinity) but rather encompasses the binding between the two partners as a whole (avidity), one may assume that Equations 5.9 and 5.10 could provide a good estimate for the effective diffusion coefficient.

In fact, there is evidence that multiple binding sites can decrease the residence time of a molecule (183). The proximity of binding sites with different affinities can encourage the molecule to 'hop' between binding sites resulting in the decreased residence time of each individual binding site. However, whether this would increase the diffusion coefficient overall would require specific experimental investigation.

5.2.2 Exploring Quantitative Predictions of the Analytical Model

The following Section aims to analyse the values that the model predicts for different GAG matrices and GAG-binding proteins. Therefore, both the general input parameters for Stokes-Einstein diffusion and the input parameters specific to certain systems must be defined.

5.2.2.1 Parameters for Stokes-Einstein Diffusion

The Stokes-Einstein equation (Equation 5.2) comprises three parameters that influence *D*. With the Boltzmann constant (k_B = 1.38 × 10^{-23} J K^{-1}) and room temperature (T = 293 K), the thermal energy is k_BT = 4.0 × 10^{-21} J. This was selected as most measurements for effective diffusion discussed within this study occurred at room temperature. The changes to thermal energy at body temperature (310 K) are negligible (k_BT = 4.0 × 10^{-21} J) and therefore, these predictions should be correct at this temperature also. For this reason also, the viscosity was selected as that of water at room temperature (η = 8.9 × 10^{-4} Pa·s). Viscosity increases with temperature and would be 6.9 × 10^{-4} Pa·s at body temperature. Overall, the diffusion coefficient at body temperature values is only 1.36 times greater than the values at room temperature and are, therefore, broadly comparable.

The type of molecules considered here are proteins and their shape is best described by the third parameter, the hydrodynamic radius *r*. This can be calculated using the translational diffusion coefficient, working backwards from the diffusion coefficient via Equation 5.2 (184), this gives a good indication of how the diffusion coefficient is dependent on the hydrodynamic radius. This relies on having a measurement of the diffusion coefficient under specified conditions such as in solution with a known viscosity and set temperature. This can be achieved via Dynamic Light Scattering (DLS) where the light scattering caused by the interaction between the solvent and the molecule of interest as it

diffuses through the solution (156). Another way to determine the hydrodynamic radius is to determine the radius of gyration through small angle X-ray scattering (SAXS) by using the intensity of the scattered radiation and Guinier plot (185). The radius of gyration can then be translated to the hydrodynamic radius by considering the theory surrounding spherical proteins (186). The hydrodynamic radius can also be determined by nuclear magnetic resonance (NMR) spectroscopy (43, 187). However, the hydrodynamic radius of proteins can be estimated based on the primary structure. Wilkins *et al.* provide a method to calculate the hydrodynamic radius of a protein based on the number of amino acid residues within the sequence (187):

$$r = 4.75\text{Å}\ (N^{0.29}), \qquad [5.11]$$

where *N* is the number of amino acid residues. This equation is applicable for folded, globular proteins. This method has been tested to work experimentally for chemokines: CXCL7 (formally Neutrophil Activating Protein-2, NAP-2) and a CXCL7 isoform (Thrombocidin-1, TC1) with the calculated and measured hydrodynamic radii differing by 0.1 nm (43). Therefore, this method for calculating the hydrodynamic radius was used for the predictions within this study as they are all generally comparable with chemokines.

A number of the proteins considered here had additional tags that may affect the hydrodynamic radius of the molecule as a whole. For PEGylated proteins, the hydrodynamic radius is taken as the cubed root of the volume that each individual molecule occupies, which is defined as the hydrodynamic radius cubed (188).

The hydrodynamic radii and Stokes-Einstein diffusion coefficient *D* of proteins and their labelled counterparts are displayed in Table 7 and Table 8, respectively.

Table 7. ***Hydrodynamic Radii (r) of Proteins of Interests and their Labels****. All hydrodynamic radii of proteins, in their monomeric state, were calculated with equation 5.12 (187). Total hydrodynamic radius was calculated as described in (188).*

Protein Construct	Protein Hydrodynamic Radius (nm)	Label Hydrodynamic Radius (nm)	Total Hydrodynamic Radius (nm)
CXCL12α	1.6	-	1.6
CXCL12γ	1.8	-	1.8
CXCL13 – AF647	1.7	1.2 (144)	1.9
FGF2 – Au NP	2.0	5.0 (40)	5.1
Halo FGF1	2.0	2.5	2.9
Halo FGF2	2.0	2.5	2.9

Table 8. ***The Diffusion Coefficients (D) of Proteins and Protein Constructs.*** *These values were calculated using the Stokes-Einstein equation (Equation 5.2) using the hydrodynamic radii in Table 7.*

Protein Construct	D ($\mu m^2 s^{-1}$)
CXCL12α	149.8
CXCL12γ	134.7
CXCL13	140.2
CXCL13 – AF647	128.3
FGF1	121.2
FGF2	117.6
FGF2 - Au NP	47.2
Halo tag FGF1	84.3
Halo tag FGF2	83.4

5.2.2.2 Interaction Parameters

In order to apply Equation 5.9 to specific molecules, two specific values are required: the equilibrium dissociation constant K_d and the concentration of binding sites c_{bs}. The equilibrium dissociation constant must be measured or calculated from experimental data (189). The K_d of two interacting molecules can be measured by the concentration of free ligand when half of the binding sites are saturated (190, 191). These can be measured in various ways such as isothermal titration calorimetry, titration enzyme-linked immunosorbent assay, and surface plasmon resonance. These are typically robust values and are generally comparable across techniques (190, 191). However, for GAG-binding proteins the measurements of K_d are far from simple. The heterogeneity of GAGs themselves means that the affinity of one protein to one specific GAG is dependent on that GAG's composition, including length, sulfation, etc. (155).

The concentration of binding sites is ECM-type dependent and will be explored in relation to specific molecules. In many cases, there is not a measurement for how many GAG binding sites are present, this is due to the heterogenous nature of GAGs and that often the exact binding sites of molecules on GAGs are not well defined (22, 39, 155). The length of GAGs considered here is variable and, typically, a certain number of disaccharides is required for the binding of GAG-binding proteins, for example 6 disaccharides are required for the binding of CXCL12α (88). Therefore, as a preliminary estimate, the number of binding sites on an individual GAG chain is considered as at least one, making the concentration of GAGs equal to the concentration of binding sites.

5.2.2.3 Relevant Ranges of K_d and c_{bs} in GAG-rich ECMs

The concentration of binding sites in GAG-rich ECMs is dependent on the GAG composition of the ECM, which is notoriously heterogeneous and differs between tissues and states (9). For model systems, it is possible to estimate the concentration of binding sites through the biophysical methods

of SPR, QCM-D, and SE (Section 5.2.3.1.1) (88). There are also studies that have defined the concentration of GAGs and the number of binding sites (Sections 5.2.3.2.1, 5.2.3.2.2.1, and 5.2.3.2.3) (40, 176, 192). These values typically range from low µM for native ECMs to low mM for model ECMs. Table 6 shows that the dissociation constants for GAG-protein interactions, the affinities span the full nM and lower µM range. Both of the concentration of binding sites and the affinity span three orders of magnitude across different examples, highlighting the degree of variety in the system and the diffusion coefficients that may be possible.

By considering different interaction scenarios, the impact of the above parameters can be deduced (Figure 69). An increase in the concentration of binding sites from low µM range to low mM decreases the ratio of D_{eff} to D_{matrix}, indicating a decrease in D_{eff}, with the same trend at different dissociation constants (Figure 69A). An increase in the dissociation constant, which represents a decrease in affinity, increases the ratio of D_{eff} to D_{matrix}, indicating that D_{eff} becomes closer to the diffusion coefficient unaffected by binding (Figure 69B). These graphs show how the D_{eff} to D_{matrix} ratio are affected by ranges of c_{bs} and K_d that are biologically relevant.

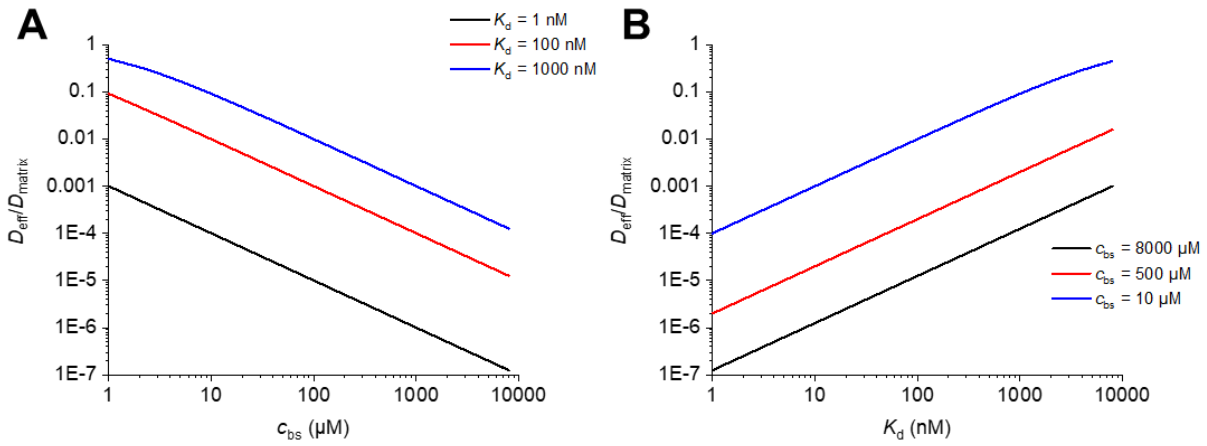


Figure 69. ***The Effect of c_{bs} and K_d on D_{eff}/D_{matrix}.*** *A) A log-log plot of D_{eff}/D_{matrix} as a function of c_{bs}. B) A log-log plot of D_{eff}/D_{matrix} as a function of K_d. D_{matrix} was estimated as 100 µm^{2}s^{-1}.*

5.2.3 Review of Literature Data in Light of the Analytical Model

5.2.3.1 Diffusion in Defined Model Matrices and Comparison to Experimental Data

Within this Section, the model matrices previously defined by Migliorini *et al.* (88) are considered in comparison to the model to verify the validity of the model.

5.2.3.1.1 Diffusion of CXCL12 Isoforms

To investigate the parameters that are present in Equation 5.9, this is best accomplished within a system in which these parameters are well defined.

The model glycocalyx interaction system generated by Migliorini *et al.* 2014 (88) represents the desired level of control, see Section 2.1.1. In an HS film formed on a dense SAv monolayer (on SLBs with 5 mol-% biotinylated lipids), considering that all biotin binding sites on SAv are saturated, and the area occupied by SAv is 36.4 nm^2, and the residual valency of SAv is 1.74 (as established in (193)), the projected area occupied by HS is 21 nm^2. With a film thickness of 11 nm, the volume occupied by each HS molecule is 230 nm^3. Using Avagadro's number, this converts to a molarity of 7.2 mM. It is also possible through the methods described in Section 3.3.1.1.2, to control the surface coverage of HS and hence, modulate the concentration of HS within the system (91). Migliorini *et al.* 2014, estimated that 6 disaccharides were available per individual CXCL12α and that the average number of disaccharides per HS was 10. Therefore, the assumption of at least one binding site per HS chain has been used. Here, the concentration of binding site range of 1 to 8 mM is considered.

In order to consider the impact that the affinity of molecules for GAGs would have on the diffusion, two isoforms of CXCL12 were selected: α and γ. There is previous research on the interaction between CXCL12 and HS and well documented dissociation constants for isoforms α (200 nM) and γ (1.5 nM) (129). Migliorini *et al.* 2014 found two different K_d values of 130 nM and 73 nM for CXCL12α binding to HS, this could point to a multivalent interaction (88). The effective diffusion coefficient was calculated for these two molecules over a range of concentration of binding sites, the results are shown in Figure 70.

For both protein isoforms (CXCL12α and γ), values calculated from Equations 5.9 and 5.10B are effectively superimposed on the graph, with differences between the values around 0.01% of the values themselves. This is because c_{bs} is six orders of magnitude greater than the K_d values and the c_{bs}/ K_d ratio is over 30,000 times greater than 1.

CXCL12γ has a predicted effective diffusion coefficients below 2×10^{-4} $\mu m^2 s^{-1}$ for the full range of concentrations considered here. This is congruent with the greater affinity that the γ isoform has for HS and the data that indicates that GAGs can cause an accumulation of this isoform (126). At the maximal concentration of binding sites possible for the model system, the mobility of the γ isoform is 2.5×10^{-5} $\mu m^2 s^{-1}$. Given that the free diffusion of CXCL12γ would be 135 $\mu m^2 s^{-1}$, the predicted effective diffusion coefficient is seven orders of magnitude different. This is a dramatic reduction in the level of diffusion.

For CXCL12α, Figure 70A shows a substantial decrease in the diffusivity with increasing HS density. At 0.4 mM HS (corresponding to 25% of maximal HS coverage, 25% of the maximal concentration), the effective diffusion coefficient is 0.0075 $\mu m^2 s^{-1}$. At maximal HS coverage, the effective diffusion coefficient is 0.037 $\mu m^2 s^{-1}$. These data show how the decreased affinity of this isoform increase the

diffusion coefficient in comparison to the γ isoform. Comparing the different measured K_d (from Migliorini *et al.* (88) and Laguri *et al.* (129)) (Figure 70B), at maximal HS density, the diffusion coefficients at these increased affinities are 0.0014 and 0.0024 $\mu m^2 s^{-1}$. These are among the same order of magnitude as the dissociation constant 200 nM. These changes in the diffusion coefficient have a relatively small despite covering the range of 73 to 200 nM.

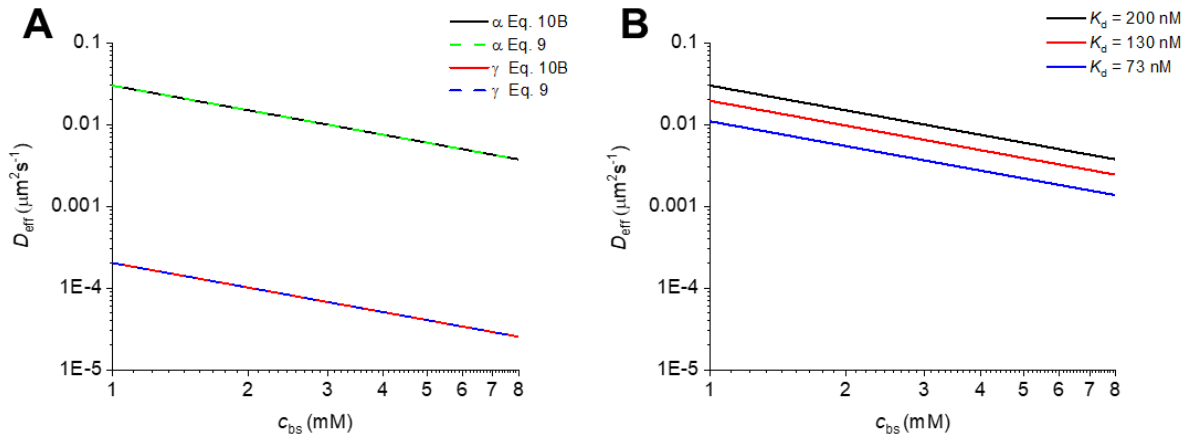


Figure 70. ***Effective Diffusion Coefficients of CXCL12α and CXCL12γ as a Function of the Concentration of HS****. A) The effective diffusion coefficient calculated by Equation 5.9 (dashed) and Equation 5.10B (solid) plotted as function of c_{bs} for CXCL12α (black, green) and CXCL12γ (red, blue) for K_d values 200 nM and 1.5 nM, respectively. B) The effective diffusion coefficient calculated by Equation 5.10B for CXCL12α at a variety of K_d values including those found within this model system (88).*

5.2.3.1.2 Diffusion of Halo-FGF1

In addition to CXCL12, the validity of the model has also been verified for FGF1. The thesis of Aïseta Baradji tested the diffusion of Halo FGF1 on model ECMs as described in Sections 2.1.1 and 5.2.3 (8). The FGF1 was tagged with a fluorophore through a halo protein tag was applied to HS rich model matrices and the diffusion measured through FRAP. The fluorescence recovery of Halo FGF1 (Figure 71) resulted in a measured diffusion coefficient of 0.22 $\mu m^2 s^{-1}$. The validation of Halo FGF1 binding to a model HS film via QCM-D is presented in Figure S3, the frequency and dissipation shifts between the wild-type and Halo tagged protein are comparable when considering for the extra mass attached to the Halo tagged protein.

Using the known values for the concentration of binding sites within these model matrices (7.2 mM) and a dissociation constant of FGF1 for HS (8.6 μM), the predicted diffusion coefficient using Equation 5.10B for this situation is 0.10 $\mu m^2 s^{-1}$. This is along the same order of magnitude as the measured diffusion coefficient and indicates that the model is successful in generating an approximate diffusion coefficient for this setting. The free diffusion of Halo-FGF1 is 84 $\mu m^2 s^{-1}$ (Table 8), the reduction in

diffusion here is less than CXCL12 (~380 fold for FGF1 *vs.* ~14,000 fold for CXCLα), but this aligns with the reduced affinity of FGF1 to HS in comparison to CXCL12.

In Figure 71, the effective diffusion coefficient as a function of the concentration of binding sites is shown. The trend here shows a range of diffusion coefficients similar to those observed in Figure 70, albeit with a greater degree of mobility. For the range of concentration of binding sites that could easily be probed in the model matrices, D_{eff} ranges from 0.10 to 0.70 $\mu m^2 s^{-1}$. This indicates that FGF1 in an HS matrix is a good choice for measuring the diffusion of a GAG-binding protein in a model GAG-rich matrix. Furthermore, the exact measured value is included within this range and using the measured value, it is possible to reveal the concentration of binding sites that is associated with this value by reading off the graph. The effective diffusion at a concentration of 3.3 mM correlates well with the measured value (Figure 71). This could indicate that there are less than 1 binding site for FGF1 per HS chain for this type of HS, although this would be unlikely for the size of HS used in this experiment.

Within the thesis, the diffusion of Halo FGF1 on the surface of HaCaT was also probed by FRAP (Figure 72) (8). HaCaT cells are keratinocytes which have been used in studies focusing on differentiation and previously used for testing the effectiveness of FGF isoforms (194, 195). Therefore, the matrix formed by these cells would be expected to interact with FGF1 in a way that the *in vivo* ECM would interact with FGF1. The amount of fluorescence recovery of Halo FGF1 on the HaCaT surface was very similar to the fluorescence recovery of FGF1 on the model matrix. Although a diffusion coefficient for this data could not be generated, the similarity between the recovery curves would indicate that the coefficient is reasonably similar to the measured value 0.22 $\mu m^2 s^{-1}$ (8). Consequently, as the theoretical model was able to describe the diffusion coefficient on the model ECM, it should also describe the diffusion coefficient for FGF1 on the HaCaT cells, on the order of 0.1 $\mu m^2 s^{-1}$ if there are similarities in the input numbers.

Overall, the Baradji thesis provides complementary experimental data for the theoretical model for diffusion of signalling proteins in GAG rich model matrices.

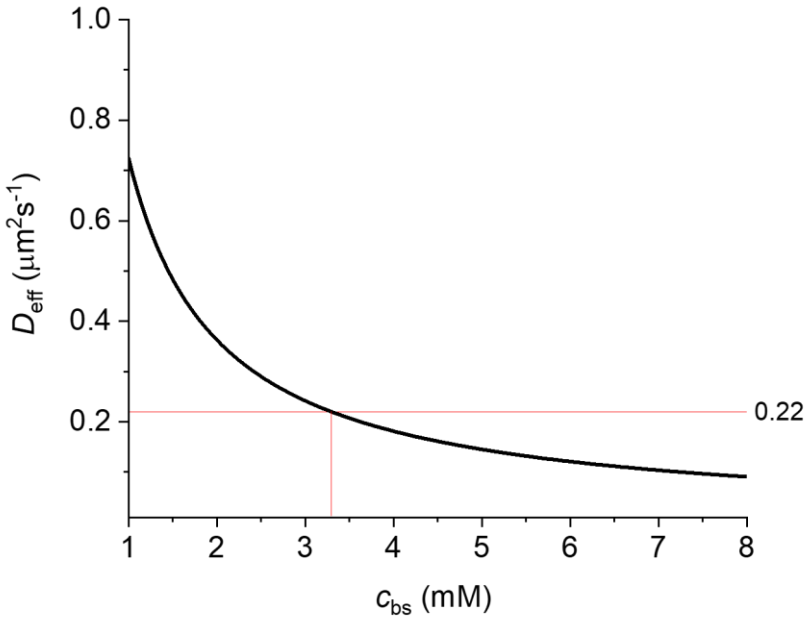


Figure 71. ***The Effect of the Concentration of Binding Sites the Effective Diffusion Coefficient of Halo FGF1 in an HS Model Matrix.*** *A) The effective diffusion coefficient as a function of the concentration of HS binding sites assuming a K_d of 8.6 µM. The horizontal red line indicates the area on the line that relates to the measured D_{eff} of 0.22 $\mu m^2 s^{-1}$. D_{eff} was calculated using Equation 5.10B.*

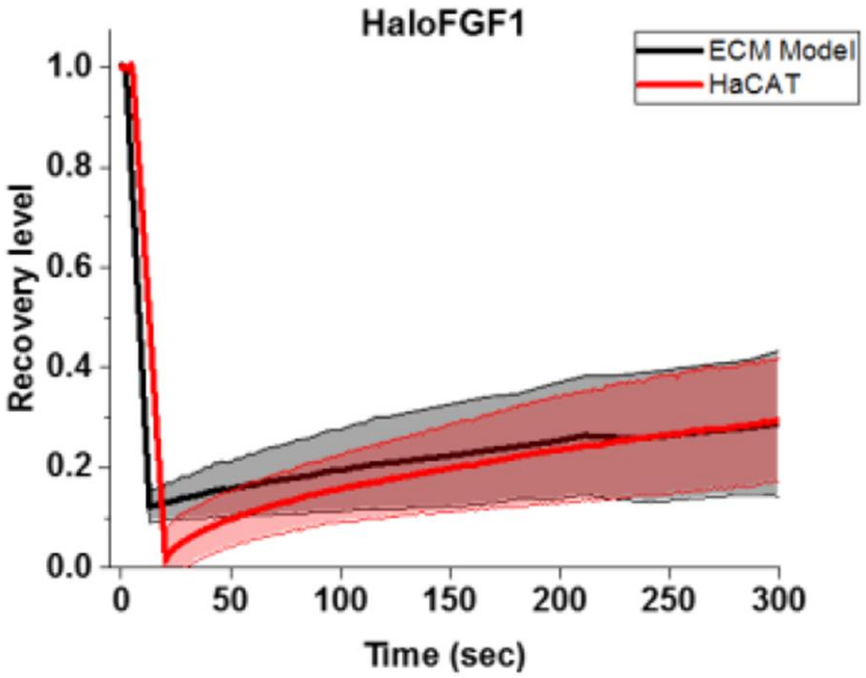


Figure 72. ***Fluorescence Recovery After Photobleaching of FGF2 on an HS Film and HaCAT Cells.*** *The average amount of fluorescence recovery for Halo FGF2 on an ECM model consisting of an HS film (black) and on the pericellular matrix of HaCaT keratinocytes (red). Halo FGF1 was incubated on HS films at a concentration of 0.28 µM and on HaCaT cells at a concentration of 2 nM. The HS films in this assay were formed under the following conditions SUV (5 mol-% DOPE-CAP-B + 95 mol-% DOPC) – 50 µg/ml, SAv – 20 µg/ml, HS-b (Nominal M_w = 12 kDa) – 5 µg/ml. This film was formed on acid cleaned glass slides. Details on this method are in Section 3.2.8. Shaded areas represent the standard deviation, N ≥ 4. Taken from Ref. (8).*

5.2.3.2 Comparison to Experimental Data: in vitro

Within this Section, diffusion data collected from extracellular matrices generated from tissues and cells are compared to this analytical model, providing an opportunity to assess the suitability of the model to the complexity of *in vitro* extracellular matrices.

5.2.3.2.1 Comparison to Experimental Data: CXCL13 diffusion in HS-rich lymphatic ECM

Although there is no experimental evidence of CXCL12 diffusion in a model ECM or an *in vitro* matrix, Miller *et al.* have traced the diffusion of another chemokine, CXCL13, in the lymph node ECM (85). CXCL13 has a similar shape and affinity to HS as CXCL12 and therefore, provides a good comparison to investigate if the model stands at a system of this complexity. The measurement of CXCL13 diffusion was achieved using FRAP and single particle tracking of CXCL13 labelled with Alexa Fluor 647 (CXCL13–AF647) on murine lymph node tissue sections. The most relevant result from this study to this thesis was a diffusion coefficient of 6.6 $\mu m^2 s^{-1}$ for CXCL13 in the lymph node. The estimated value using the

theoretical model (Equation 5.9) was 0.93 $\mu m^2 s^{-1}$; the values used for this are shown in Table 9. There is only a seven fold difference between the estimated and measured values. Equation 5.10B is not as well suited to this case as with the model matrices as the ratio between the concentration of binding sites and the dissociation constant is lower and therefore the discrepancy between the values calculated from the two equations is larger.

The input parameters (c_{bs} and K_d) for this case were extracted from separate sources. The concentration of binding sites was taken as the HS concentration (2.6 μM) that was use in a previous study surrounding chemokine gradient formation (192). This value was estimated but found to work well with a computational model and therefore appears to be an appropriate estimate for HS concentration. This value is also a thousand fold lower than the value in Section 5.2.3.1 and may represent the lower end of the range of c_{bs}. The K_d was taken from an NMR study on the HS and CXCL13 (10), it does not represent the interaction between HS in the lymph node and CXCL13–AF647. However, as observed in Section 5.2.3.1.1, a difference within a few tens of nM for the K_d does not appreciably impact the D_{eff}. The exact description of the HS in the lymph node is lacking, making it difficult to be certain that this K_d will represent this interaction well. The role of oligomerisation of CXCL13 in HS binding has also been ignored for the sake of simplicity.

A key piece of information for this study is that the CXCL13–AF647 used was sourced from Almac, just as the CXCL12α–AF647 in Section 3.3.2.2. In this previous section, the interaction between CXCL12 and HS was more transient when labelled in this way with this fluorophore. It seems possible that this label has a similar effect on CXCL13 and changes the K_d of the interaction. As previously mentioned, the K_d value used for estimations was not necessarily representative of the interaction between this labelled version of the chemokine and the HS present in the lymph node. The discrepancies in these may explain the different between the theoretical prediction and the measured value.

Overall, Miller *et al*. has provided a robust number for comparison and although there is a factor of seven difference between the predicted value and the measured value, this is reasonable considering the error on the input parameters and the simplifications that have been made with the input parameters. It highlights that a rough estimate can be made with the model even if the input parameters do not thoroughly describe the interaction taking place.

Table 9. ***Parameters to Calculate the Effective Diffusion Coefficient of CXCL13 in the Lymph Node.*** *D_{eff} was calculated from the parameters included in the table using Equation 5.9. Reference (192) was chosen for the concentration of HS binding sites in the lymph node as it provides a substantiated estimate for the HS concentration. Reference (10) provides an in depth analysis into the interaction between HS and CXCL13, including NMR data for an appropriate K_d.*

Parameter	Value	Source
D_{matrix}	128 $\mu m^2 s^{-1}$	Table 8
c_{bs}	2.6 µM	(192)
K_d	19 nM	(10)
D_{eff}	0.93 $\mu m^2 s^{-1}$	Calculated using Equation 5.9

5.2.3.2.2 Comparison to Experimental Values: Fibroblast Growth Factor

There are a number of published and unpublished data that dissect the diffusion of the FGF in ECM. This provides an opportunity for the comparison of this data to predictions of the analytical model. FGF1 and FGF2 are analysed, they have very different ranges in affinity for HS (nM and µM respectively) and should provide an *in vitro* comparison on the effect of the affinity on diffusion.

5.2.3.2.2.1 FGF2 Diffusion in Endothelium Basement Membrane

Dowd *et al.* investigated the diffusivity of FGF2 through the Descement's Membrane (DM). The DM is a specialised basement membrane of corneal endothelial cells. It contains collagen, laminins, and perlecan (176, 196). Perlecan is a heparan sulfate proteoglycan commonly found within basement membranes, and has been found to promote DM regeneration following injury. The authors presumed perlecan to act as the main HS source within the DM.

The diffusion of radioactive labelled FGF2 was measured by examining the flux of the FGF2 concentration through the DM as a function of time (176). Although the authors were unable to measure the diffusion coefficient of labelled FGF2 at physiological conditions due to the molecules not reaching steady state, they could quantify the diffusion coefficient under alternative conditions such as with an excess of unlabelled FGF2 in solution. This could entail competition for binding sites, lowering the effective concentration of binding sites (Section 5.2.1.5.2). This analysis produced a diffusion coefficient of 0.53 $\mu m^2 s^{-1}$. Overall, the concluded effective diffusion coefficient of FGF2 was quoted as 0.6 $\mu m^2 s^{-1}$. Dowd *et al.* also determined the K_d of FGF2 binding to the HS found within the DM as 23.6 nM by quantifying the amount of FGF2 bound to extracted HS, and the concentration of HS to lie in the range from 6.5 to 26 µM, this was determined using the molecular weight of the extracted HS and the purification yield (176).

Figure 73A shows the diffusion coefficients predicted according to Equation 5.9 and 5.10B using the above values. Equations 5.9 and 5.10B gave virtually identical results, which is expected since

$c_{\mathrm{bs}}/K_{\mathrm{d}} \gg 1$ (i.e., in the range of 275 to 1100). The range of the diffusion coefficients calculated falls between 0.43 and 0.11 $\mu m^2 s^{-1}$, this is slower than the predicted diffusion coefficient from Dowd *et al.* but is within the same order of magnitude.

However, there are mitigating factors that are worth considering. Firstly, the measured values of the key equation parameters. The measured value of the HS-FGF2 K_d falls within the range of a high affinity binding site of FGF2 to HS (22 to 30 nM) that was found in an alternative study, indicating that the value found by Dowd *et al.* is reproducible (61). The K_d calculated by Dowd *et al.* was achieved by rapid gel filtration with HS purified from the DM, which quantifies the amount of FGF2 bound to HS. The concentration of HS was calculated by calculating the purified yield of the extraction of HS from the DM and using the molecular mass of the extracted HS (42 kDa) (176). This produced a large range of error from 6.5 to 26 µM, but this is accounted for in Figure 73. However, relating the concentration of HS to the concentration of binding sites is difficult; Figure 73A assumes that there is one FGF2 binding site per HS molecule. However, Dowd *et al.* states that there are four FGF2 molecules bound to each HS molecule and that the concentration of HS binding sites is four times the molar concentration of HS (176). The calculated effective diffusion coefficients for this concentration range are shown in Figure 73B, these diffusion coefficients are all below 0.1 $\mu m^2 s^{-1}$ for the concentration range (26 to 104 µM). This is a factor of 60 different from the measured value.

Another factor to consider is the reference molecule, interleukin-1β (IL-1β), the effective diffusion coefficient for this molecule within the DM was 0.66 $\mu m^2 s^{-1}$ which is very close to the values for FGF2 (176). IL-1β is of a similar size and shape to FGF2 and so according to the Stokes-Einstein equation, their diffusion coefficients in solution should be broadly similar. However, IL-1β cannot bind HS and, therefore, in the matrix it should diffuse in a similar way to its diffusion in solution, but this is not the case, it has a much lower diffusion coefficient. However, the effect of the pore size does not explain for the discrepancy between the measured and calculated values as the calculated values are further slower than the measured values. Furthermore, there are several conditions tested in the paper which could prevent HS binding of FGF2 (use of non-heparin binding FGF2 and the addition of protamine sulfate), but the diffusion coefficient remains within the same order of magnitude (176). Furthermore, this type of ECM may prevent measurements. Therefore, it is possible that there are other factors affecting the diffusion, such as the pore size of the matrix, but more experimental investigation would be required to reveal this information. The authors of this work do emphasise the importance of steric effects, therefore, perhaps, a better value for D_{matrix} is also required for this case.

Overall, the study by Dowd *et al.* has provided some experimental data that can be explained by the equation derived in this thesis, but there remain uncertainties, such as the validity of certain input parameters, that require further investigation to illuminate whether or not these values are robust.

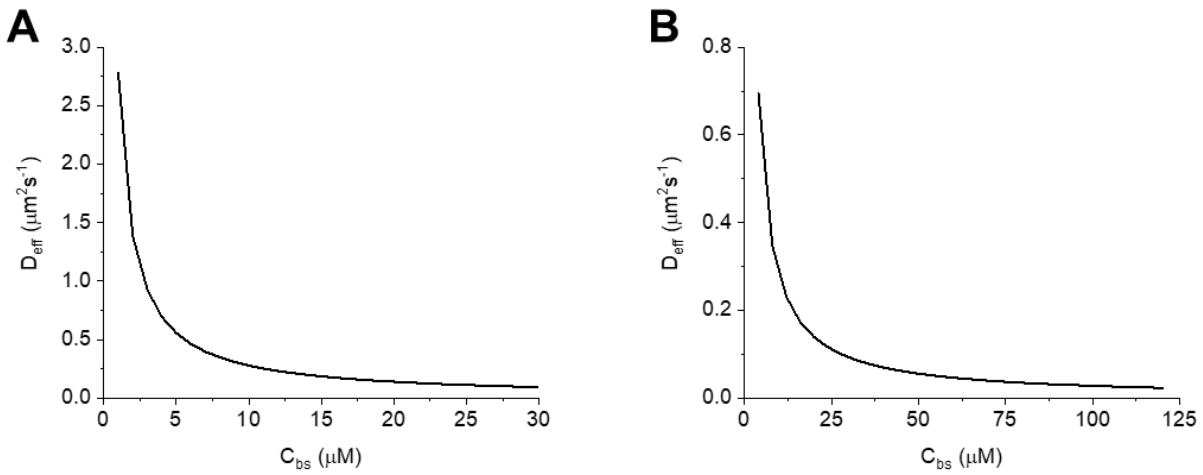


Figure 73. ***Effective Diffusion Coefficient of FGF2 in Descement's Membrane as a Function of the Concentration of HS Sites.*** *A) The effective diffusion coefficient calculated by Equation 5.9 plotted as a function of the concentration of HS sites, assuming one binding site per HS chain. B) The effective diffusion coefficient calculated by Equation 5.9 plotted as a function of the concentration of HS sites, assuming four binding site per HS chain. According to the parameters measured in Dowd* et al. *(176).*

5.2.3.2.3 Diffusion of FGF2 in the Fibroblast Pericellular Matrix

A couple of studies have focused on FGF2 and its relationship with HS and the resulting impacts on FGF diffusion (40, 65). Within these studies, they have utilised Rama 27 fibroblast generated pericellular matrices as their interaction platform.

In the 2012 study, Duchesne *et al.* quantified the number of heparan sulfate sites on the Rama 27 cells as 3×10^6 per cell (40). In order to make this number compatible with Equation 5.9, the concentration of binding sites must be expressed in a molar quantity. This was achieved by calculating the volume that the pericellular matrix of an individual Rama 27 cell occupies. Vasquez *et al.* have presented data that indicates the surface area of a fibroblast 7.44×10^{-5} cm^2 (197). This can be converted to volume of the matrix per cell by multiplying the thickness of the extracellular matrix, as defined by Duchesne *et al.* (1 HS chain ≈ 100 nm), making the volume of the pericellular matrix of a Rama 27 fibroblast 7.44×10^{-13} dm^3 (40). The number of HS binding sites presented on the surface of a Rama 27 fibroblast was 3×10^6 and is converted to 4.98×10^{-18} moles using Avogadro's number. This makes the concentration of HS sites within the Rama 27 fibroblast pericellular matrix 6.7 µM.

Duchesne *et al.* also provides a K_d for FGF2 to the HS sites present in the fibroblast pericellular matrix as 0.8 µM, this was achieved using a LIGAND program and it is likely representative of the system (40). The standard error of the mean for the K_d was 75%, though this is likely more representative of the degree of heterogeneity of the FGF2-HS interactions than the quality of the data. This dissociation constant is not specific to a particular binding site on FGF2 and is below the previously established ranges for the K_d for the interaction between FGF2 and HS, a low affinity site of 47 to 320 nM and a high affinity site of 22 to 30 nM (61). 0.8 µM may reflect the avidity of the FGF2 for the HS rather than the affinity. It is also possible that the type of HS measured in each experiment was different in regards to sulfation composition and size and that the HS present in the fibroblast matrix is a type that lacks certain modifications that give FGF2 a greater affinity. Nonetheless, this value has been used as the starting point for the calculations of the effective diffusion coefficient as it specific to the situation for the pericellular matrix.

Duchesne *et al.* measured the diffusion coefficient using a single gold nanoparticle tagged to each FGF2 and using photothermal heterodyne imaging (PHI) (40). This allows for the acquisition of single particle tracks and the generation of mean square displacement as a function of lag time, from which the diffusion coefficient was determined.

The results from the estimation of the diffusion coefficients of FGF2 can be seen in Table 10. The K_d value from Duchesne *et al.* generated a D_{eff} that was 20 times greater than the largest D_{eff} measured. Using an alternative K_d that was successful for Dowd *et al*., a smaller diffusion coefficient was calculated; 0.17 $\mu m^2 s^{-1}$. This is within the same order of magnitude as the measured value. However, this value is only one of a range of values presented in this publication, with values grouped into five distinct categories. These different categories may be due to differences in local ECM composition and this can be related to Equation 5.9 by modifications on the concentration of binding sites or the affinity. Duchesne *et al.* does state that the speed limit for the tracker is 0.2 $\mu m^2 s^{-1}$ and that results may be skewed to slower diffusing particles, this may explain why the predicted coefficients are larger than the measured values. It is also equally possible that the input parameters are not correct.

The number of HS binding sites within the fibroblast pericellular matrix was calculated via a competition assay using heparin. Heparin is an analogue to heparan sulfate, it is often used as a substitute for this in experiments, but it is not entirely the same (145). It is possible that in some cases the FGF2 may bind HS over heparin and that these binding sites may not have accounted for in the number of HS binding sites for FGF2. This could lead to the value of 6.7 µM being an underestimate. The binding sites that are accounted for and those not accounted for may have different affinities. Therefore, it is possible that the different groups of mobility correspond to different dissociation

constants for different HS sites. This information could be input into the model to calculate the diffusion coefficients of different groups.

Another study on the same type of matrices, Sun *et al*., measured mobility of FGFs by FRAP (65). The half time of recovery from photobleaching can be converted to a diffusion coefficient following the Soumpasis method (198). In this study, FGF1 and FGF2 were tagged with a fluorophore through a halo protein tag (as described in Section 5.2.3.1.2) and the measured diffusion coefficients show a greater discrepancy to the calculated values than the previous study. These values were 0.029 and 0.067 $\mu m^2 s^{-1}$, for FGF1 and FGF2 respectively. This could again be due to, as previously mentioned, the unsuitability of FRAP to give reliable diffusion coefficients for values lower than 0.1 $\mu m^2 s^{-1}$(199), but given that the estimate for FGF1 is 4.75 $\mu m^2 s^{-1}$, this would indicate that these low results are more than an artefact of the analysis method.

One interesting result from Sun *et al*. is that FGF1 is more mobile than FGF2. This is the inverse of what is predicted by Equation 9 and against the idea that a greater affinity for GAGs would reduce mobility. This could be due to similar artefacts as those that are described in Chapter 3, that the label has impacted on the interaction between the molecule and the GAG. However, these protein constructs were tested for their biological activity on fibroblasts and produced similar intracellular responses as the wild-type (195). Another possible reason for a lower FGF1 diffusion coefficient and discrepancy with the calculated and measured values could be that it is possible that the number of binding sites on the GAG chains for FGF2 and FGF1 are not comparable. There may be a greater number of binding sites for FGF1 than FGF2 as this would result in a lower diffusion coefficient for FGF1. However, this would require further detailed experimentation to provide justification for this.

Overall, these data indicate that the level of complexity within certain biological matrices may introduce sizeable differences between calculated and measured effective diffusion coefficients.

Table 10. ***The Calculated Diffusion Coefficients and the Measured Diffusion Coefficients for FGF.*** *The K_d values for FGF1 were taken from (61). The K_d for FGF2 were taken from (40, 176). D_{eff} was calculated from Equation 9. The measured diffusion coefficient for FGF2 – Au NP was taken from the group of slow directed diffusion on living cells in reference (40). The measured diffusion coefficient for the halo tagged FGF constructs was calculated from the half time of recovery during FRAP (65) and was calculated with the Soumpasis method (198). The c_{bs} used for these calculations was 6.7 µM.*

Protein Construct	K_d (nM)	Calculated D_{eff} ($\mu m^2 s^{-1}$)	Measured D_{eff} ($\mu m^2 s^{-1}$)
FGF2 – Au NP	800	5.03	0.25
	23.6	0.17	
Halo tag FGF2	800	8.90	0.067
	23.6	0.29	
Halo tag FGF1	8600	47.39	0.029
	400	4.75	

5.3 Discussion

Overall, this chapter has introduced a new analytical model to predict the effective diffusion coefficient of molecules within a sticky yet open polymer matrix. The model clearly shows that the affinity of the molecule to the polymer has the greatest effect on the diffusion of molecule within that polymer rich matrix. The model was used to generate predictions for the effective diffusion coefficient for different molecules and GAG-rich matrices in order to compare with measured data. Some of these results reinforced the model, and some showed that there were things left to decipher. The diffusion of FGF2 in the model matrix and the diffusion of CXCL13 in the lymph node fit well with the predictions with the model. However, the diffusion of FGF1 and FGF2 in pericellular matrices did not match well with the predictions of the model.

5.3.1 Validity of the Model for Model Matrices

The model was first applied to the model ECMs to CXCL12 in the absence of experimental data, considering what the diffusion of different isoforms of CXCL12 could look like (Section 5.2.3). This highlighted that the range of diffusion coefficients that the model could probe would be difficult to measure with the most readily accessible method of diffusion measurement, FRAP. This is due to the diffusion coefficient values being below what can be reliably measured. This highlights the importance of choosing a molecule that is suitable to the techniques, or *vice versa*, being used, under a different technique the diffusion of CXCL12 might be more easily measured. This highlights one of the possible uses for this theoretical model - as a first approximation to select the most appropriate method for measuring diffusion.

The model was also applied to the data acquired by Aïseta Baradji (Section 5.2.3.1.2) for Halo FGF1 in an HS rich model matrix ($D_{measured}$ = 0.22 $\mu m^2 s^{-1}$). The model predicted a value on the same order of magnitude. Upon closer investigation of the measured diffusion coefficient appeared to match a slightly lower concentration of binding sites than originally estimated. This may showcase a method to estimate the concentration of binding sites for the molecule within the system, given that there is no other aspect of the system that could impact on the diffusion of FGF1. This highlights how the model can be used to predict parameters beyond the effective diffusion. It also highlights that the model has correctly described diffusion in this case.

Baradji also investigated the diffusion of Halo FGF2, but found no measurable diffusion of the molecule. This is congruent with what the model found for CXCL12 in the model matrix. Indeed, the predicted diffusion coefficient for Halo FGF2 in this matrix is 0.0003 $\mu m^2 s^{-1}$ (data not shown). Further highlighting the importance of selecting techniques that are compatible with the molecules of interest.

Additionally, the model shows that affinity of the polymer has the greatest impact on the predicted diffusion coefficient. However, as has been discussed throughout this chapter, this is difficult to define for GAG binding interactions. This may be the main factor that prevents the model from being valid in comparison to experimental data. Highlighting an area of GAG research that still has many research gaps within the context of diffusion and GAG-binding interactions.

5.3.2 Validity of the Model for *In Vitro* Matrices

The *in vitro* matrices are those that have been generated as part of the cellular or tissue function. Predictions from the theoretical model were also compared with diffusion coefficients from GAG-rich matrices generated by cells, pericellular coats and lymph node tissue. For all of these matrices, there was a certain error applied to each of the input parameters. Some of the discrepancies in the predicted and measured values could be explained by the errors in these parameters. This highlights that the model may provide better predictions if more accurate details about the matrices are present.

One prominent factor is the binding sites that exist on heparan sulfate. HS is a heterogeneous molecule with non-uniform sulfation (22). Chemokines require a certain number of disaccharides present in order to bind HS and will only bind to oligosaccharides derived from it if a certain number of disaccharides is present (41). There are still some unknown motifs and structures on GAGs that can bind specific proteins (200). Consequently, it is difficult to define how many binding sites for a protein exist on a GAG chain. As the concentration of binding sites is a key element to this theoretical model, its application is limited if accurate estimates for the number of binding sites on GAGs are not present. This provides compounding evidence for the need to further study the structure of GAGs and how they bind to proteins.

Another factor is the overall affinity and avidity of protein and GAG interactions. In Duchesne *et al.,* a K_d for the interaction between FGF2 and the HS binding sites in the pericellular matrix, this is not referred to as belonging to any specific binding sites on FGF2 (40). In other data, FGF2 was shown to have multiple HS binding sites with different affinities (61). Therefore, this indicates that the K_d for FGF2 against HS in the pericellular matrix of fibroblast cells is not a measure of affinity, but rather of avidity. It is not clear if the model will perform correctly with this type of input as the K_d. Among the systems discussed here, there is evidence to suggest that all the molecules described by bind to GAGs in more than one way and therefore, they are all likely to be somewhat affected by multivalency. The best example of a single point binding molecule to GAGs would likely be a nanoparticle that is designed to function as such (83). Further experiments would be required to tease out whether the equations shown here or different equations would be more suitable in this case.

5.3.3 Experimental Design for Further Verification

There are certain aspects of the model that remain to be verified with experimental data. The exact effects of the parameters of K_d and c_{bs} have not been experimentally measured, the model would benefit from having experimental data to provide the validity on the theoretical predictions. This section focuses on the design of experiments to address these uncertainties.

5.3.3.1 The Effect of Varying the Concentration of Binding Sites on D_{eff}

Using the methods presented in Kirichuck *et al.* and Section 3.3.1.1.2, it is possible to modulate the surface coverage of GAGs in the model matrix (91). This would modulate the concentration of GAGs and therefore, the concentration of binding sites. The aim of this would be to create a graph similar to Figure 70, with the equation plotted as a line and the measured values at a series of intervals (e.g. 0 mM, 0.4 mM, 0.8 mM, and 1.6 mM). If the measured values fell within a range close to the predicted values, this would provide excellent evidence in favour of this theoretical model. A good choice for a protein to use for this test would be Halo FGF1 as this is already validated to work well with the model ECM and has a range of predicted effective diffusion coefficients that would fit well with the FRAP method (8).

5.3.3.2 The Effect of Multivalency on D_{eff}

As addressed previously, the effect of multivalency and multiple binding sites on diffusion may not be reflected in theoretical model presented here. In order to decipher the effect that these may have on diffusion an experiment is required. The best way to do this would be in the well-controlled environment of the model matrix with a defined number of GAGs in the system with a protein with known multiple binding sites for the GAG. If a protein with two different binding sites was being tested, for example, three separate forms of this protein would be tested: wild-type, binding site one mutant, and binding site two mutant. Each individual mutant should have diffusion coefficients that are well described with the theoretical model. Through the comparison of these two results and the result from the wild-type, it might be possible to reveal how multiple binding sites affect the diffusion coefficient.

FGF2 may make a good choice for this as its HS binding sites have been well defined with K_d ranges for each one (61), but due to its slow diffusion, FRAP may not be the best analysis method. Techniques such as FCS may be more appropriate for the diffusion range that FGF2 may cover (201).

Chapter 6: General Discussion and Conclusions

6.1 Summary of Results

The main results of this thesis can be summarised by four main statements:

1. Working with model systems and labelled molecules presents unique challenges that can be overcome by circumventive measures. Glycan binding molecules do not retain their ability to binding glycans and model systems can introduce the possibility of nonspecific binding.
2. Plane sphere confinement microscopy (PSCM) can be successfully applied to model glycocalyces with additional modifications.
3. The pore size of hyaluronan (HA) matrices impacts on the diffusion of inert colloids.
4. Diffusivity of biological colloids in a sticky yet open polymer matrix can be estimated from the affinity of the interaction between the polymer and the colloid, and the concentration of binding sites for the colloid in the matrix.

The overall research question in this thesis was about the biophysical mechanisms that underlie diffusion in the extracellular matrix (ECM). This mechanism must include how biological colloids interact with the ECM, which has been demonstrated extensively, but the impact of these interactions on the diffusion coefficient is not defined.

The main bottleneck for this research question within the field is the lack of tools for investigation. Within this thesis, model systems and microscopy tools have been further developed to help address the biophysical mechanisms that underlie diffusion. Model ECMs can be generated to defined the pore size and the number of binding sites available for glycan binding molecules and PSCM can be applied to these systems in order to measured diffusion within the model ECMs alone.

The benefits of using model systems is that the glycan content can be strictly controlled. However, it can involve the introduction of additional molecules and surfaces that are not present *in vivo* and the exclusion of some that are. In the process of this development, a key artefact that appeared multiple times was the issue of non-specific binding. This included both non-specific binding to molecules that form part of the model ECM such as the SAv layer (Section 3.3.3) and binding to materials used as part of the setup such as the underlying glass support (Sections 3.3.4 and 4.3.2.3). Through the development of passivation procedures or subtraction of data, these non-specific binding issues were mitigated. However, their pervasiveness within these model systems does merit more consideration.. These results highlight that particular care needs to be taken when designing model matrices and labelled colloids, to mitigate for non-specific binding and other secondary effects.

The analytical model in Chapter 5 can describe diffusion of biological colloids in model matrices for which the glycan content and the interaction between the glycan and the colloid is defined. On the other hand, the difficulty in defining some of the parameters of *in vitro* matrices, such as the

concentration of GAG binding sites and the affinity of proteins to the types of GAGs in those matrices, presented its own unique challenges. Considering the effect that these parameters have on diffusion, the defined model matrices generated here allow these to be more accurately defined and provide a better method to investigate the underlying biophysical and biochemical mechanisms on diffusion. The results in this thesis show how this can be done.

This thesis has highlighted three main factors that affect diffusion of biological colloids in the ECM: the matrix pore size, the affinity of the biological colloid to the matrix, and the number of binding sites for the colloid within the matrix. The theoretical model brings these factors together to represent their influence on diffusion in the ECM, providing a method for the prediction of biological colloid diffusion within ECMs.

6.2 Integrating Experimental and Theoretical Tools

The experimental and theoretical tools produced in Chapters 4 and 5, respectively, can now be used in tandem by comparing measurements to predictions. The two different approaches can complement one another in other areas. As discussed in Chapter 5, the diffusion of a biological colloid through a sticky polymer matrix is determined as a modification of the Stokes-Einstein diffusion by the dissociation constant and the concentration of binding sites. On the other hand, the diffusion of colloids through a non-sticky polymer matrix is impacted by the pore size of the matrix (166). In the analytical model, the Stokes-Einstein diffusion can be replaced by the diffusion as modulated by the pore size.

However, predicting the diffusion coefficient of a colloid entrapped in a non-sticky matrix with a defined pore size is also non-trivial. The experimental tools developed here can fill this knowledge gap, by performing experiments that such as those in Chapter 4. The effect of pore size on the diffusion of an inert biological colloid was measured. The methods produced in Chapter 4 provides a way to generate the diffusion coefficients required for specific matrices under investigation using the model in Chapter 5. By testing the diffusion of an inert probe of the same size as the protein of interest within a matrix with the pore size of interest, the diffusion coefficient as a function of the pore size can be measured. This would allow for a more accurate D_{matrix} value for the analytical model, generating a better estimated value of D_{eff}.

Additionally, these challenges could be addressed by developing and testing new and refined theoretical models that can predict diffusion under conditions that are not covered by the current model. Such as the question of multivalent interactions or the presence of more than one interacting polymer.

Furthermore, the results in Chapters 3 and 4 also allow for the formation of defined model matrices that have more defined input parameters for the theoretical model in Chapter 5. In this manner, all the results from this thesis can work in conjunction to address the question of the biological colloid diffusion in GAG-rich matrices.

6.3 Future Work in the Field

6.4 How to Label Glycan-binding Proteins Wisely?

The results in Chapter 4 showed that multiple different methods of fluorescent labelling on different glycan-binding proteins change the way the proteins interacted with their glycan partners, highlighting that care should be taken when labelling colloids that interact through multiple weak interactions with glycans. The exact mechanisms for this is unclear but it is possible that there is a feature of the protein-glycan interaction that plays a critical role. Especially considering that for CXCL12-AF647 and labelled STxB, the labelled proteins still interacted with the glycan, but the affinity of the interaction had changed. Dietz et al. found a similar phenomenon, the addition of the fluorophore Cyanine5 to the 3' end of an oligonucleotide caused the K_d of the interaction with the complementary strand to increase by a factor of 100 in comparison to the label on the 5' end (202). The authors of this study postulate that the location of the fluorophore is the key aspect that impacts on the ability of the fluorophore to change the affinity of the native interactions. This was demonstrated by carefully designing a fluorescent label for a protein using knowledge of the binding site location and observing a difference of less than 1 nM in the K_d of the labelled and unlabelled proteins (202).

However, for the N-terminal method of fluorescent labelling for CXCL12 (Section 3.3.2.2.1.4), this location should not impact on the GAG-binding capabilities of CXCL12 as it is not close to any identified GAG binding sites (46, 145). This leaves two possibilities: there are additional HS-binding sites on CXCL12 that have not been identified or the location of the fluorophore is not the only aspect of the labelling that can impact on the interactions of the labelled molecule. The first possibility could be correct as many GAG binding proteins have more than one interaction site, but considering that the histidine tag at this location did not impact on the protein interaction with HS (Section 3.3.2.2.1.3) this seems unlikely. The second possibility would require a more extensive review of differentially labelled proteins and their subsequent binding abilities. If a protein labelled with the same fluorophore on different sites, with all labels having a similar impact on binding then there must be something about the fluorophore itself impacting on the interaction that is independent from the location it is place on.

Hughes *et al.* performed a comparative study on 32 fluorophores and their interaction with lipid bilayers due to evidence that there is some interaction between the two (203). The results of this study were inconclusive in terms of what properties of the fluorophore led to an interaction between the fluorophore and the bilayer and the resounding recommendation was that future studies should

consider the controls required to test the impact of the addition of a fluorophore on the system. While the performance of such controls is good scientific practice and should be not be bypassed, the impact of fluorophores on protein-glycan interactions may be more predictable than the impact of fluorophores on lipid membranes. Protein-glycan interactions tend to have subtle characteristics including electrostatics and hydrogen bonding (23, 24, 71). Therefore, a systematic review on fluorescent labelling of glycan-binding proteins, analogous to the Hughes *et al.* study, could be extremely beneficial. This type of investigation could reveal key insights on the mechanisms underlying protein-glycan interactions and would also provide a databank of fluorescently labelled proteins that do not impact on the GAG-binding capabilities of the protein. This type of analysis would be key in progressing scientific research on glycan binding proteins by providing reagents that can be used across a variety of different experimental methods, such as those generated and utilised within this thesis.

6.4.1 What is the Pore Size in the Glycocalyx?

The pore size of the endothelial glycocalyx has previously been assumed as 7 nm, due to the size of the protein albumin and the assumption that the glycocalyx must exclude this protein (13). However, this value does not have any experimental data to provide credibility and would cause the endothelial glycocalyx to exclude a majority of the biological colloids that may distribute and diffuse within it. Sun *et al.* used electron microscopy to show that the average pore size in murine enterocyte glycocalyx is approximately 30 nm (204). This study focused on one type of glycocalyx and considering that the composition of glycocalyces differs upon location and in different states, the pore size of ECMs is likely to have a range of values (2, 15, 28). Furthermore, synthetic matrix scaffolds often used in matrix research have pore sizes on the order of tens of microns, indicating the diverse field of matrix research (81). The model HA matrices produced in Section 3.3.1.2 have pore sizes that are much closer to the measurement of Sun *et al.* and therefore may produce matrices that are more replicative of the biological scenario than other types. Overall, however, studies into producing accurate and repeatable measurements of the pore size in different glycocalyces would benefit research into processes in the ECM given the effect that pore size has on diffusion as highlighted by the effect of pore size on the diffusion of EUVs and the role of the pore size in the analytical model.

6.4.2 What is the Role of the Diffusion Coefficient in Gradient Formation?

Most signalling molecules in the ECM form gradients in order to generate diffusion toward the source of the molecules (36, 51, 53, 55, 80, 172, 205, 206). Many of these studies on gradient formation have emphasised the importance of the interaction with HS. In order to form these gradients, the molecules must diffuse from the source. Considering the role of HS in gradient formation and the interaction of many signalling molecules (chemokines, growth factors, etc.) with HS and the relationship between

HS interactions and diffusion (40, 41, 65). The diffusivity of signalling molecules in specified matrices must be a part of the underlying mechanisms of gradient formation. This is covered in Fick's laws of diffusion, gradient formation rates and gradient shape can be predicted if certain conditions, such as the rate of colloid production, are known (207). As shown in Sections 5.2.3.1 and 5.2.3.2.2.1, the effective diffusion coefficient scales with the concentration of binding sites in the matrix. Changes in concentration of binding sites with the ECM is likely one of the major driving forces for gradient formation. This would include the effective lowering of the concentration of binding sites as a result of occupation by molecules.

Mapping the different diffusion coefficients of a signalling molecule across tissues from source to sink may reveal the mechanisms behind the formation of gradients. This could be achieved by measuring the diffusion of the molecule in defined model matrices that recapitulate the features of different matrices that the gradients covers using the methods developed in this thesis. Understanding the mechanisms underlying gradient formation may help in cases where there is aberrant recruitment of cells due to the incorrect distribution of signalling molecules such as autoimmune diseases (208).

6.5 Conclusions

To conclude, the results in this thesis provide experimental and theoretical methods to investigate the diffusion of biological colloids in model ECMs. They have also highlighted key parameters which underlie the molecular/physical mechanisms for diffusion and what further areas of investigation are required in order to fill the remaining gaps of knowledge.

References

1. Cruz Walma DA, Yamada KM. The extracellular matrix in development. Development. 2020;147(10):dev175596.

2. Frantz C, Stewart KM, Weaver VM. The extracellular matrix at a glance. Journal of Cell Science. 2010;123(24):4195-200.

3. Karamanos NK, Theocharis AD, Piperigkou Z, Manou D, Passi A, Skandalis SS, et al. A guide to the composition and functions of the extracellular matrix. FEBS. 2021;288(24):6850-912.

4. Theocharis AD, Skandalis SS, Gialeli C, Karamanos NK. Extracellular matrix structure. Advanced Drug Delivery Reviews. 2016;97:4-27.

5. Sutherland TE, Dyer DP, Allen JE. The extracellular matrix and the immune system: A mutually dependent relationship. 2023;379(6633):eabp8964.

6. Akhmanova M, Osidak E, Domogatsky S, Rodin S, Domogatskaya A. Physical, Spatial, and Molecular Aspects of Extracellular Matrix of In Vivo Niches and Artificial Scaffolds Relevant to Stem Cells Research. Stem cells international. 2015;2015:167025.

7. McDonald KK, Cooper S, Danielzak L, Leask RL. Glycocalyx Degradation Induces a Proinflammatory Phenotype and Increased Leukocyte Adhesion in Cultured Endothelial Cells under Flow. PLoS One. 2016;11(12):e0167576.

8. Baradji A. Interactions of fibroblast growth factors with glycosaminoglycan brushes and the pericellular matrix. [PhD]: University of Liverpool; 2017.

9. Silva JC, Carvalho MS, han X, Xia K, Mikael PE, Cabral JMS, et al. Compositional and structural analysis of glycosaminoglycans in cell-derived extracellular matrices. Glycoconjugate Journal. 2019;36(2):141-54.

10. Monneau YR, Luo L, Sankaranarayanan NV, Nagarajan B, Vivès RR, Baleux F, et al. Solution structure of CXCL13 and heparan sulfate binding show that GAG binding site and cellular signalling rely on distinct domains. Open Biology. 2017;7(10).

11. Woodcock TE, Woodcock TM. Revised Starling equation and the glycocalyx model of transvascular fluid exchange: an improved paradigm for prescribing intravenous fluid therapy. British Journal of Anaesthesia. 2012;108(3):384-94.

12. Reitsma S, Slaaf DW, Vink H, van Zandvoort MA, oude Egbrink MG. The endothelial glycocalyx: composition, functions, and visualization. Pflugers Archiv. 2007;454(3):345-59.

13. Arkill KP. A Reinterpretation of Evidence for the Endothelial Glycocalyx Filtration Structure. Frontiers in Cell and Developmental Biology. 2021;9:734661.

14. Sieve I, Münster-Kühnel AK, Hilfiker-Kleiner D. Regulation and function of endothelial glycocalyx layer in vascular diseases Vascular Pharmacology. 2018;100:26-33.

15. Zeng Y. Endothelial glycocalyx as a critical signalling platform integrating the extracellular haemodynamic forces and chemical signalling. Journal of Cellular and Molecular Medicine. 2017;21(8):1457-62.

16. Neves MI, Araújo M, Moroni L, da Silva RMP, Barrias CC. Glycosaminoglycan-Inspired Biomaterials for the Development of Bioactive Hydrogel Networks. Molecules. 2020;25(4):978.

17. Einstein A. Investigations on the Theory of the Brownian Motion [PhD]: University of Zürich 1905.

18. Islam MA. Einstein–Smoluchowski Diffusion Equation: A Discussion. Physica Scripta. 2004;70:120-5.

19. Wijmans J, Baker R. The solution-diffusion model: a review Journal of Membrane Science. 1995;107(1-2):1-21.

20. Nitsche JM. Cellular Microtransport Processes: Intercellular, Intracellular, and Aggregate Behavior. Annual Review of Biomedical Engineering. 1999;1:463-503.

21. Wiegel FW. Diffusion and the physics of chemoreception. Physics Reports. 1983;95(5):283-319.

22. Perez S, Makshakova O, Angulo J, Bedini E, Bisio A, de Paz JL, et al. Glycosaminoglycans: What Remains to Be Deciphered? JACS Au. 2023;3(3):628-56.

23. Ricard-Blum S, Pérez S. Glycosaminoglycan interaction networks and databases. Current Opinion in Structural Biology. 2022;74:102355.

24. Gómez Toledo A, Sorrentino JT, Sandoval DR, Malmström J, Lewis NE, Esko JD. A Systems View of the Heparan Sulfate Interactome. 2021;69(2):105-19.

25. Alotaibi Faizah S, Alsadun Marim MR, Alsaiari Sarah A, Ramakrishnan K, Yates Edwin A, Fernig David G. Interactions of proteins with heparan sulfate. Essays in Biochemistry. 2024.

26. Monneau Y, Arenzana-Seisdedos F, Lortat-Jacob H. The sweet spot: how GAGs help chemokines guide migrating cells. Journal of Leukocyte Biology. 2015;99(6):935-53.

27. El Masri R, Crétinon Y, Gout E, Vivès RR. HS and Inflammation: A Potential Playground for the Sulfs? Frontiers in Immunonology. 2020;11.

28. Zeng Y, Ebong EE, Fu BM, Tarbell JM. The Structural Stability of the Endothelial Glycocalyx after Enzymatic Removal of Glycosaminoglycans. PLoS One. 2012;7(8).

29. Zhang T, de Waard AA, Wuhrer M. The Role of Glycosphingolipids in Immune Cell Functions. Frontiers in Immunology. 2019;10.

30. Schnaar RL, Sandhoff R, Tiemeyer M, Kinoshita T. Glycosphingolipids. In: Varki A, Cummings R, Esko J, editors. Essentials of Glycobiology. 4th Edition ed. Cold Spring Harbor, NY, USA: Cold Spring Harbor Laboratory Press; 2022.

31. Marangon D, Boccazzi M, Lecca D, Fumagalli M. Regulation of Oligodendrocyte Functions: Targeting Lipid Metabolism and Extracellular Matrix for Myelin Repair. Journal of clinical medicine. 2020;9(2).

32. García-Hevia L, Muñoz-Guerra D, Casafont Í, Morales-Angulo C, Ovejero VJ, Lobo D, et al. Gb3/cd77 Is a Predictive Marker and Promising Therapeutic Target for Head and Neck Cancer. 2022;10(4):732.

33. Ogemdi IK. Properties and Uses of Colloids: A Review. Colloid and Surface Science. 2019;4(2):24-8.

34. Anderson JL. Transport Mechanisms of Biological Colloids. Annals of the New York Academy of Sciences. 1986;469(1):166-77.

35. Bandzerwicz A, Gadomska-Gajadhur A. Into the Tissues: Extracellular Matrix and Its Artificial Substitutes: Cell Signalling Mechanisms. Cells. 2022;11(5).

36. Cosgrove J, Novkovic M, Albrecht S, Pikor NB, Zhou Z, Onder L, et al. B cell zone reticular cell microenvironments shape CXCL13 gradient formation Nature Communications. 2020;11.

37. Derler R, Gesslbauer B, Weber C, Strutzmann E, Miller I, Kungl A. Glycosaminoglycan-Mediated Downstream Signalling of CXCL8 Binding to Endothelial Cells. International Journal of Molecular Sciences. 2017;18(12).

38. Gray AL, Karlsson R, Roberts ARE, Ridley AJL, Pun N, Khan B, et al. Chemokine CXCL4 interactions with extracellular matrix proteoglycans mediate widespread immune cell recruitment independent of chemokine receptors. Cell Reports. 2023;42(1).

39. Proudfoot AEI, Johnson Z, Bonvin P, Handel TM. Glycosaminoglycan Interactions with Chemokines Add Complexity to a Complex System. Pharmaceuticals. 2017;10 (3).

40. Duchesne L, Octeau V, Bearon RN, Beckett A, Prior IA, Lounis B, et al. Transport of Fibroblast Growth Factor 2 in the Pericellular Matrix is Controlled by the Spatial Distribution of its Binding Sites in Heparan Sulfate PLoS Biology. 2012;12(9).

41. Migliorini E, Thakar D, Kuhnle J, Sadir R, Dyer DP, Li Y, et al. Cytokines and growth factors cross-link heparan sulfate. Open Biology. 2015;5(8).

42. Lortat-Jacob H. The molecular basis and functional implications of chemokine interactions with heparan sulfate. Current Opinion in Structural Biology 2009;19(5):543-8.

43. Nguyen LT, Kwakman PHS, Chan DI, Liu Z, de Boer L, Zaat SAJ. Exploring Platelet Chemokine Antimicrobial Activity: Nuclear Magnetic Resonance Backbone Dynamics of NAP-2 and TC-1. Antimicrobial Agents and Chemotherapy. 2011;55.

44. Vanheule V, Boff D, Mortier A, Janssens R, Petri B, Kolaczkowska E, et al. CXCL9-Derived Peptides Differentially Inhibit Neutrophil Migration In Vivo through Interference with Glycosaminoglycan Interactions. Frontiers in Immunology. 2017;8.

45. Hughes CE, Nibbs RJB. A guide to chemokines and their receptors. FEBS Journal 2018;285(16):2944-71.

46. Jannssens R, Struyf S, Proost P. The Unique Structural and Functional Features of CXCL12. Cellular and Molecular Immunology. 2018;15(4):299-311.

47. Hardy D, Fefeu M, Besnard A, Briand D, Gasse P, Arenzana-Seisdedos F, et al. Defective angiogenesis in CXCL12 mutant mice impairs skeletal muscle regeneration. Skeletal Muscle. 2019;9(1).

48. Giblin SP, Ranawana S, Hassibi S, Birchenough HL, Mincham KT, Snelgrove RJ, et al. CXCL17 binds efficaciously to glycosaminoglycans with the potential to modulate chemokine signaling. 2023;14.

49. Graham GJ, Handel TM, Proudfoot AEI. Leukocyte Adhesion: Reconceptualizing Chemokine Presentation by Glycosaminoglycans. Trends in Immunology. 2019;40(6):472-81.

50. Sepuru KM, Rajarathnam K. Structural basis of chemokine interactions with heparan sulfate, chondroitin sulfate, and dermatan sulfate. Journal of Biological Chemistry. 2019;294(43):15650-61.

51. Massena S, Christoffersson G, Hjertstrom E, Zcharia E, Vlodavzky I, Ausmees N, et al. A chemotactic gradient sequestered on endothelial heparan sulfate induces directional intraluminal crawling of neutrophils. Blood. 2010;116(11):1924-31.

52. Rueda P, Richart A, Récalde A, Gasse P, Vilar J, Guérin C, et al. Homeostatic and Tissue Reparation Defaults in Mice Carrying Selective Genetic Invalidation of CXCL12/Proteoglycan Interactions. Circulation. 2012;126(15):1882-95.

53. Schwarz J, Bierbaum V, Hauschild R, Brown M, de Vries I, Leithner A, et al. Dendritic Cells Interpret Haptotactic Chemokine Gradients in a Manner Governed by Signal-to-Noise Ratio and Dependent on GRK6 Current Biology. 2017;27(9):1314-35.

54. Schwarz J, Bierbaum V, Merrin J, Frank T, Hauschild R, Bollenbach T, et al. A microfluidic device for measuring cell migration towards substrate-bound and soluble chemokine gradients. Scientific Reports. 2016;6.

55. Weber M, Hauschild R, Schwarz J, Moussion C, de Vries I, Legler DF, et al. Interstitial Dendritic Cell Guidance by Haptotactic Chemokine Gradients. Science. 2013;339(6117):328-32.

56. Sarris M, Masson J-B, Maurin D, Van der Aa LM, Boudinot P, Lortat-Jacob H, et al. Inflammatory Chemokines Direct and Restrict Leukocyte Migration within Liver Tissues as Glycan-Bound Gradients. Current Biology. 2012;22(24): 2375-82.

57. Beenken A, Mohammadi M. The FGF family: biology, pathophysiology and therapy. Nature Reviews Drug Discovery. 2009;8(3):235-53.

58. Hui Q, Jin Z, Li X, Liu C, Wang X. FGF Family: From Drug Development to Clinical Application. International Journal of Molecular Sciences 2018;19(7).

59. Yun Y-R, Eun Won J, Jeon E, Lee S, Kang W, Jo H, et al. Fibroblast Growth Factors: Biology, Function, and Application for Tissue Regeneration. Journal of Tissue Engineering. 2010.

60. Adrian E, Treľová D, Filová E, Kumorek M, Lobaz V, Poreba R, et al. Complexation of CXCL12, FGF-2 and VEGF with Heparin Modulates the Protein Release from Alginate Microbeads. Int J Mol Sci. 2021;22(21).

61. Rahmoune H, Chen H-L, Gallagher JT, Rudland PS, Fernig DG. Interaction of heparan sulfate from mammary cells with acidic fibroblast growth factor (FGF) and basic FGF. Regulation of the activity of basic FGF by high and low affinity binding sites in heparan sulfate. Journal of Biological Chemistry. 1998;273(13):7303-10.

62. Pye DA, Vivès RR, Hyde P, Gallagher JT. Regulation of FGF-1 mitogenic activity by heparan sulfate oligosaccharides is dependent on specific structural features: differential requirements for the modulation of FGF-1 and FGF-2. Glycobiology. 2000;10(11):1183-92.

63. Duchesne L, Gentili D, Comes-Franchini M, Fernig DG. Robust Ligand Shells for Biological Applications of Gold Nanoparticles. Langmuir. 2008;24(23):13572-80.

64. Nieves DJ, Li Y, Fernig DG, Lévy R. Photothermal raster image correlation spectroscopy of gold nanoparticles in solution and on live cells. Royal Society Open Science. 2015;2.

65. Sun C, Marcello M, Li Y, Mason D, Lévy R, Fernig DG. Selectivity in glycosaminoglycan binding dictates the distribution and diffusion of fibroblast growth factors in the pericellular matrix. Open Biology. 2016;6(3).

66. Bhattacharya M, Horswill AR. The role of human extracellular matrix proteins in defining Staphylococcus aureus biofilm infections. FEMs Microbiology Reviews. 2024;48(1).

67. Siggins MK, Sriskandan S. Bacterial Lymphatic Metastasis in Infection and Immunity. 2022;11(1):33.

68. Vaca DJ, Thibau A, Schütz M, Kraiczy P, Happonen L, Malmström J, et al. Interaction with the host: the role of fibronectin and extracellular matrix proteins in the adhesion of Gram-negative bacteria. Medical Microbiology and Immunology. 2019;209:277-99.

69. Odumosu O, Nicholas D, Yano H, Langridge W. AB Toxins: A Paradigm Switch from Deadly to Desirable. Toxins. 2010;2(7):1612-45.

70. Gerling-Driessen UIM, Hoffmann M, Schmidt S, Snyder NL, Hartmann L. Glycopolymers against pathogen infection. Chemical Society Review. 2023;52:2617-42.

71. Ling H, Boodhoo A, Hazes B, Cummings MD, Armstrong GD, Brunton JL, et al. Structure of the Shiga-like Toxin I B-Pentamer Complexed with an Analogue of Its Receptor Gb3. Biochemistry. 1998;37(7):1777-88.

72. Pezeshkian W, Gao H, Arumugam S, Becken U, Bassereau P, Florent J-C, et al. Mechanism of Shiga Toxin Clustering on Membranes. ACS Nano. 2017;11(1):314-24.

73. Murzin AG. OB(oligonucleotide/oligosaccharidebinding)-fold: common structural and functional solution for non-homologous sequences. EMBO. 1993;12(3):861-7.

74. Arif S, Moulin VJ. Extracellular vesicles on the move: Traversing the complex matrix of tissues. European Journal of Cell Biology. 2023;102(4).

75. Sariano PA, Mizenko RR, Shirure VS, Brandt AK, Nguyen BB, Nesiri C, et al. Convection and extracellular matrix binding control interstitial transport of extracellular vesicles. Journal of Extracellular Vesicles. 2023;12(4).

76. Nikoloff JM, Saucedo-Espinosa MA, Kling A, Dittrich PS. Identifying extracellular vesicle populations from single cells. Proceedings of the National Academy of Sciences. 2021;118(38).

77. McGough IJ, Vincent J-P. Exosomes in developmental signalling. Development. 2016;143(14):2482-93.

78. Stapornwongkul KS, Vincent J-P. Generation of extracellular morphogen gradients: the case for diffusion. Nature Reviews Genetics. 2021;22(6):393-411.

79. Han C, Belenkaya TY, Wang B, Lin X. Drosophila glypicans control the cell to cell movement of Hedgehog by a dynamin independent process Development. 2004;131(3):601-11.

80. Grude F, Froese J, Manikowski D, Di Iorio D, Grad J-N, Wegner S, et al. Hedgehog is relayed through dynamic heparan sulfate interactions to shape its gradient. Nature Communications. 2023;14.

81. Murphy CM, O'Brien FJ. Understanding the effect of mean pore size on cell activity in collagen-glycosaminoglycan scaffolds. Cell Adhesion & Migration. 2010;4(3):377-81.

82. Zhao C, Si Y, Zhu S, Bradley K, Taha AY, Pan T, et al. Diffusion of Protein Molecules through Microporous Nanofibrous Polyacrylonirile Membranes. ACS Applied Polymer Materials. 2021;3(3):1618 - 27.

83. Le Goas M, Testard F, Taché O, Debou N, Cambien B, Carrot G, et al. How Do Surface Properties of Nanoparticles Influence Their Diffusion in the Extracellular Matrix? A Model Study in Matrigel Using Polymer-Grafted Nanoparticles. Langmuir. 2020;36(35):10460-70.

84. Tomasetti L, Liebl R, Wastl DS, Breunig M. Influence of PEGylation on nanoparticle mobility in different models of the extracellular matrix. European Journal of Pharmaceutics and Biopharmaceutics. 2016;108:145-55.

85. Miller H, Cosgrove J, Wollman AJM, Taylor E, Zhou Z, O'Toole PJ, et al. High-Speed Single-Molecule Tracking of CXCL13 in the B-Follicle. Frontiers in Immunology. 2018;9(1073).

86. Rhodes JM, Simons M. The extracellular matrix and blood vessel formation: not just a scaffold. Journal of Cellular and Molecular Medicine. 2007;11(2):176-205.

87. McCabe MC, Saviola AJ, Hansen KC. Mass Spectrometry-Based Atlas of Extracellular Matrix Proteins across 25 Mouse Organs. Journal of Proteome Research. 2023;22(3):790-801.

88. Migliorini E, Thakar D, Sadir R, Pleiner T, Baleux F, Lortat-Jacob H, et al. Well-defined biomimetic surfaces to characterize glycosaminoglycan mediated interactions on the molecular, supramolecular and cellular levels. Biomaterials. 2014;35(32):8903-15.

89. Paradiso F, Serpelloni S, Francis LW, Taraballi F. Mechanical Studies of the Third Dimension in Cancer: From 2D to 3D Model. 2021;22(18):10098.

90. Sánchez-Romero N, Schophuizen CMS, Giménez I, Masereeuw R. *In vitro* systems to study nephropharmacology: 2D versus 3D models. European Journal of Pharmacology. 2016;790:36-40.

91. Kirichuk O, Srimasorn S, Zhang X, Roberts ARE, Coche-Guerente L, Kwok JCF, et al. Competitive Specific Anchorage of Molecules onto Surfaces: Quantitative Control of Grafting Densities and Contamination by Free Anchors. Langmuir. 2023;39(50):18410-23.

92. Richter R, Mukhopadhyay A, Brisson A. Pathways of Lipid Vesicle Deposition on Solid Surfaces: A Combined QCM-D and AFM Study. Biophysical Journal. 2003;85(5):3035-47.

93. Thakar D, Migliorini E, Coche-Guerente L, Sadir R, Lortat-Jacob H, Boturyn D, et al. A quarts crystal microbalance method to study the terminal functionalisation of glycosaminoglycans. Chemical Communications. 2014;50(96):15148-51.

94. Reviakine I, Johannsmann D, Richter RP. Hearing What You Cannot See and Visualising What You Hear: Interpreting Quartz Crystal Microbalance Data from Solvated Interfaces. Analytical Chemistry 2011;83(23):8838-48.

95. Chen JY, Penn LS, Xi J. Quartz crystal microbalance: Sensing cell-substrate adhesion and beyond. Biosensors and Bioelectronics. 2018;99:593-602.

96. Chen Q, Xu S, Liu Q, Masliyah J, Xu Z. QCM-D study of nanoparticle interactions. Advances in Colloid and Interface Sicence. 2016;233:94-114.

97. Horst RJ, Katzourakis A, Mei BT, de Beer S. Design and validation of a low-cost open-source impedance based quartz crystal microbalance for electrochemical research. HardwareX. 2022;12:e00374.

98. Rodahl M, Hook F, Krozer A, Brzezinski P, Kasemo B. Quartz crystal microbalance setup for frequency and Q-factor measurements in gaseous and liquid environments. Review of Scientific Intruments. 1995;66(7).

99. Sauerbrey G. The use of quartz oscillators for weighing thin layers and for microweighing. Zeitschrift fuer Physik. 1959;155:206-22.

100. Dyer DP, Migliorini E, Salanga CL, Thakar D, Handel TM, Richter RP. Differential structural remodelling of heparan sulfate by chemokines: the role of chemokine oligomerization. Open Biology. 2016;7(1).

101. Srimasorn S, Souter L, Green DE, Djerbal L, Goodenough A, Duncan JA, et al. A quartz crystal microbalance method to quantify the size of hyaluronan and other glycosaminoglycans on surfaces. Scientific Reports. 2022;12.

102. Keller CA, Kasemo B. Surface specific kinetics of lipid vesicle adsorption measured with a quartz crystal microbalance. Biophysical Journal. 1998;75(3):1397-402.

103. Richter RP, Hock KK, Burkhartsmeyer J, Boehm H, Bingen P, Wang G, et al. Membrane-Grafted Hyaluronan Films: A Well-Defined Model System of Glycoconjugate Cell Coats. Journal of the American Chemical Society. 2007;129(27):5306-7.

104. Baranova NS, Inforzato A, Briggs DC, Tilakaratna V, Enghild JJ, Thakar D, et al. Incorporation of Pentraxin 3 into Hyaluronan Matrices Is Tightly Regulated and Promotes Matrix Cross-linking. Journal of Biological Chemistry. 2014;289(44):30481-98.

105. Bally M, Block S, Höök F, Larson G, Parveen N, Rydell GE. Physicochemical tools for studying virus interactions with targeted cell membranes in a molecular and spatiotemporally resolved context. Analytical and bioanalytical chemistry. 2021;413(29):7157-78.

106. De Feijter JA, Benjamins J, Veer FA. Ellipsometry as a tool to study the adsorption behaviour of synthetic and biopolymers at the air-water interface. Biopolymers. 1978;17(7):1605-826.

107. Garcia-Caurel E, De Martino A, Gaston J-P, Yan L. Application of Spectroscopic Ellipsometry and Mueller Ellipsometry to Optical Characterization. Applied Spectroscopy. 2013;67:1-21.

108. Eisele NB, Frey S, Piehler J, Görlich D, Richter RP. Ultrathin nucleoporin phenylalanine–glycine repeat films and their interaction with nuclear transport receptors. EMBO Reports. 2010;11(5):366-72.

109. Campoy-Quiles M, Alonso MI, Bradley DDC, Richter LJ. Advanced Ellipsometric Characterisation of Conjugated Polymer Films. Advanced Fuctional Materials. 2013;24(15):2116-34.

110. Nag N, Sasidharan S, Saudagar P, Tripathi T. Fundamentals of spectroscopy for biomolecular structure and dynamics. In: Saudagar P, Tripathi T, editors. Advanced Spectroscopic Methods to Study Biomolecular Structure and Dynamics: Academic Press; 2023. p. 1-35.

111. van der Meulen SA, Dubacheva GV, Dogterom M, Richter RP, Leunissen ME. Quartz Crystal Microbalance with Dissipation Monitoring and Spectroscopic Ellipsometry Measurements of the Phospholipid Bilayer Anchoring Stability and Kinetics of Hydrophobically Modified DNA Oligonucleotides. Langmuir. 2014;30(22):6525-33.

112. Jonkman J, Brown CM, Wright GD, Anderson KI, North AJ. Tutorial: guidance for quantitative confocal microscopy. Nature Protocols. 2020;15:1585-611.

113. Li Y, Dick WA, Tuovinen OH. Fluorescence microscopy for visualization of soil microorganisms—a review. Biology and Fertility of Soils. 2004;39(5):301-11.

114. Day CA, Kang M. The Utility of Fluorescence Recovery after Photobleaching (FRAP) to Study the Plasma Membrane. Membranes. 2023;13(5).

115. Demchenko AP. Photobleaching of organic fluorophores: quantitative characterization, mechanisms, protection. Methods and Applications in Fluorescence. 2020;8(2).

116. Tinevez J-Y, Perry N, Schindelin J, Hoopes GM, Reynolds GD, Laplantine E, et al. TrackMate: An open and extensible platform for single-particle tracking. Methods. 2017;115(15):80-90.

117. Wang Z, Wang X, Zhang Y, Xu W, Han X. Principles and Applications of Single Particle Tracking in Cell Research. Small. 2021;17(11).

118. Limozin L, Sengupta K. Quantitative Reflection Interference Constrast Microscopy (RICM) in Soft Matter and Cell Adhesion. ChemPhysChem. 2009;10(16):2752-68.

119. Attili S, Richter RP. Combining Colloidal Probe Atomic Force and Reflection Interference Contrast Microscopy to Study the Compressive Mechanics of Hyaluronan Brushes. Langmuir. 2012;28(6):3206-16.

120. Rädler J, Sackmann E. On the measurement of weak repulsive and frictional colloidal force by reflection intereference contrast microscopy. Langmuir. 1992;8(3):749-1032.

121. Davies HS, Baranova NS, El Amri N, Coche-Guérente L, Verdier C, Bureau L, et al. An integrated assay to probe endothelial glycocalyx-blood cell interactions under flow in mechanically and biochemically well-defined environments. Matrix Biology. 2019;78-79:47-9.

122. Frost R, Débarre D, Jana S, Bano F, Schünemann J, Görlich D, et al. A Method to Quantify Molecular Diffusion within Thin Solvated Polymer Films: A Case Study on Films of Natively Unfolded Nucleoporins. ACS Nano. 2020;14(8):9938-52.

123. Thakar D, Dalonneau F, Migliorini E, Lortat-Jacob H, Boturyn D, Albiges-Rizo C, et al. Binding of the chemokine CXCL12α to its natural extracellular matrix ligand heparan sulfate enables myoblast adhesion and facilitates cell motility. Biomaterials. 2017;123:24-38.

124. Jabeguero D, Siukstaite L, Wang C, Mitrovic A, Pérez S, Makshakova O, et al. Enzymatic Glyco-Modification of Synthetic Membrane Systems. Biomolecules. 2023;13(2).

125. Connell BJ, Sadir R, Baleux F, Laguri C, Kleman J-P, Luo L, et al. Heparan sulfate differentially controls CXCL12α- and CXCL12γ-mediated cell migration through differential presentation to their receptor CXCR4. Science Signaling. 2016;9(452).

126. Laguri C, Sadir R, Rueda P, Baleux F, Gans P, Arenzana-Seisdedos F, et al. The Novel CXCL12γ Isoform Encodes an Unstructured Cationic Domain Which Regulates Bioactivity and Interaction with Both Glycosaminoglycans and CXCR4. PLoS One 2007;2(10).

127. Saltor Núñez L. Mucin-like glycocalyx modules for creating complex artificial glycocalyxes: University of Leeds; 2023.

128. Celi AB, Goldstein J, Rosato-Siri MV, Pinto A. Role of Globotriaosylceramide in Physiology and Pathology. 2022;9.

129. Laguri C, Sapay N, Simorre JP, Brutscher B, Imberty A, Gans P, et al. 13C-Labeled Heparan Sulfate Analogue as a Tool To Study Protein/Heparan Sulfate Interactions by NMR Spectroscopy: Application to the CXCL12α Chemokine. Journal of the American Chemical Society. 2011;133(25):9642-5.

130. Danielewicz N, Rosato F, Tomisch J, Gräber J, Wiltschi B, Striedner G, et al. Clickable Shiga Toxin B Subunit for Drug Delivery in Cancer Therapy. ACS Omega. 2023;8(17):15406-21.

131. Schubert T, Sych T, Madl J, Xu M, Omidvar R, Patalag LJ, et al. Differential recognition of lipid domains by two Gb3-binding lectins. Scientific Reports. 2020;10.

132. Lata S, Gavutis M, Tampé R, Piehler J. Specific and Stable Fluorescence Labeling of Histidine-Tagged Proteins for Dissecting Multi-Protein Complex Formation. Journal of the American Chemical Society. 2006;128(7):2365-72.

133. Invitrogen. pRSET A, B, and C - For high-level expression of recombinant proteins in E. coli. 2010.

134. Scientific TF. Thermo Scientific Phusion High-Fidelity DNA Polymerase https://assets.thermofisher.com/TFS-Assets/LSG/manuals/MAN0012393_Phusion_HighFidelity_DNAPolymerase_UG.pdf2018 [

135. Scientific TF. T_m Calculator https://www.thermofisher.com/uk/en/home/brands/thermo-scientific/molecular-biology/molecular-biology-learning-center/molecular-biology-resource-library/thermo-scientific-web-tools/tm-calculator.html [

136. QIAGEN. QIAquick® Spin Handbook. 2020.

137. QIAGEN. QIAprep® Miniprep Handbook. 2020.

138. Jing W, Haller FM, Almond A, De Angelis PL. Defined megadalton hyaluronan polymer standards. Analytical Biochemsitry. 2006;355(2):182-8.

139. Schindelin J, Arganda-Carreras I, Frise E, Kaynig V, Longair M, Pietzsch T, et al. Fiji: an open-source platform for biological-image analysis. Nature Methods. 2012;9:676-82.

140. Richter RP, Rodenhausen KB, Eisele NB, Schubert M. Coupling Spectroscopic Ellipsometry and Quartz Crystal Microbalance to Study Organic Films at the Solid-Liquid Interface. In: Hinrichs K, Eichhorn K-J, editors. Ellipsometry of Functional Organic Surfaces and Films. 52. Heidelberg, Germany: Springer; 2013. p. 223-48.

141. Attili S, Borisov OV, Richter RP. Films of End-Grafted Hyaluronan Are a Prototype of a Brush of a Strongly Charged, Semiflexible Polyelectrolyte with Intrinsic Excluded Volume. Biomacromolecules. 2007;13(5):1466-77.

142. Information NCfB. PubChem Compound Summary for CID 5288499, Heparin disaccharide I-S. 2024 [Available from: https://pubchem.ncbi.nlm.nih.gov/compound/Heparin-disaccharide-I-S.

143. Zhang G, Zheng S, Liu H, Chen PR. Illuminating biological processes through site-specific protein labeling. Chemical Society Review. 2015;44(11):3405-17.

144. Jung C, Lee J, Kang M, Kim SW. Measurement of the Temperature-dependent Diffusion Properties of Nanoparticles by Using Fluorescence Correlation Spectroscopy. Journal of the Korean Physical Society 2014;65(7):1083-9.

145. Murphy JW, Cho Y, Sachpatzidis A, Fan C, Hodson ME, Lolis E. Structural and Functional Basis of CXCL12 (Stromal Cell-derived Factor-1α) Binding to Heparin. Journal of Biological Chemistry 2007;282(13):10018-27

146. Sadir R, Imberty A, Baleux F, Lortat-Jacob H. Heparan Sulfate/Heparin Oligosaccharides Protect Stromal Cell-derived Factor-1 (SDF-1)/CXCL12 against Proteolysis Induced by CD26/Dipeptidyl Peptidase IV. Journal of Biological Chemsitry. 2004;279(42):43854-60.

147. Spiller S, Panitz N, Limasale YDP, Atallah PM, Schirmer L, Bellman-Sickert K, et al. Modulation of Human CXCL12 Binding Properties to Glycosaminoglycans To Enhance Chemotactic Gradients. ACS Biomaterials Science & Engineering. 2019;5(`0):5128-38.

148. Kawamura T, Stephens B, Qin L, Yin X, Dores MR, Smith TH, et al. A General Method for Site Specific Fluorescent Labeling of Recombinant Chemokines. PLoS One 2014;9(1).

149. Crump MP, Gong J-H, Loetscher P, Rajarathnam K, Amara A, Arenzana-Seisdedos F, et al. Solution structure and basis for functional activity of stromal cell-derived factor-1; dissociation of CXCR4 activation from binding and inhibition of HIV-1. The EMBO Journal 1997;16:6996-7007.

150. Allen SJ, Hamel DJ, Handel TM. A rapid and efficient way to obtain modified chemokines for functional and biophysical studies. Cytokine. 2011;55(2):168-73.

151. Siukstaite L, Imberty A, Römer W. Structural Diversities of Lectins Binding to the Glycosphingolipid Gb3. 2021;8.

152. Xia Z, Williams ER. Protein-Glass Surface Interactions and Ion Desalting in Electrospray Ionization with Submicron Emitters. Journal of the American Society for Mass Spectrometry. 2017;29:194-202.

153. Berg JM, Tymoczko JL, Gatto Jr. GJ, Stryer L. Biochemistry. Eighth ed. New York, NY: W. H Freeman & Company; 2015.

154. Gutjahr JC, Crawford KS, Jensen DR, Naik P, Peterson FC, Samson GPB, et al. Dimeric form of CXCL12 binds to atypical chemokine receptor 1. Science Signalling. 2021;14(696).

155. Bu C, Jin L. NMR Characterization of the Interactions Between Glycosaminoglycans and Proteins. Frontiers in Molecular Biosciences. 2021;8.

156. Stetefeld J, McKenna SA, Patel TR. Dynamic light scattering: a practical guide and applications in biomedical sciences. Biophysical Reviews. 2016;8(4):409-27.

157. Maguire C, Rösslein M, Wick P, Prina-Mello A. Characterisation of particles in solution – a perspective on light scattering and comparative technologies. Science and Technology of Advanced Materials. 2018;19(1):732-45.

158. Laktionov MY, Zhulina EB, Klushin L, Richter RP, Borisov OV. Selective Colloid Transport across Planar Polymer Brushes. Macromolecular Rapid Communications. 2023.

159. Djerbal L, Vivès RR, Lopin-Bon C, Richter RP, Kwok JCF, Lortat-Jacob H. Semaphorin 3A binding to chondroitin sulfate E enhances the biological activity of the protein, and cross-links and rigidifies glycosaminoglycan matrices. BioRxiv. 2019.

160. Cosette J, Moussy A, Paldi A, Stockholm D. Combination of imaging flow cytometry and time-lapse microscopy for the study of label-free morphology dynamics of hematopoietic cells. Cytometry A. 2017;91(3):254-60.

161. Tarantino N, Tinevez J-Y, Crowell EF, Boisson B, Henriques R, Mhlanga M, et al. TNF and IL-1 exhibit ubiquitin requirements for inducing NEMO-IKK supramolecular structures. Journal of Cell Biology. 2014;204(2):231-45.

162. Garcia-Manyes S, Sanz F. Nanomechanics of lipid bilayers by force spectroscopy with AFM: A perspective. Biochimica et Biophysica Acta - Biomembranes. 2010;1798:741-9.

163. Benesch T, Yiacoumi S, Costas T. Brownian motion in confinement. Physical Review E. 2003;68(2).

164. Faucheux LP, Libchaber AJ. Confined Brownian motion. Physical Review E. 1994;49(6):5158-63.

165. Lin B, Yu J, Rice SA. Direct measurements of constrained Brownian motion of an isolated sphere between two walls. Physical Review E. 2000;62(3):3909-19.

166. Cai L-H, Panyukov S, Rubinstein M. Mobility of Nonsticky Nanoparticles in Polymer Liquids Macromolecules. 2011;44(19):7853-63.

167. Cho HW, Kim H, Sung BJ, Kim JS. Tracer Diffusion in Tightly-Meshed Homogenous Polymer Networks: A Brownian Dynamics Simulation Study. Polymers. 2020;12(9).

168. Burla F, Sentjabrskaja T, Pletikapic G, van Beugen J, Koenderink GH. Particle diffusion in extracellular hydrogels. Soft Matter. 2020;16(5):1366-76.

169. Kuhn T, Landge AN, Mörsdorf d, Coßmann J, Gerstenecker J, Čapek D, et al. Single-molecule tracking of Nodal and Lefty in live zebrafish embryos supports hindered diffusion model. Nature Communications. 2022;13.

170. Lieleg O, Baumgärtel RM, Bausch AR. Selective Filtering of Particles by the Extracellular Matrix: An Electrostatic Bandpass. Biophysical Journal. 2009;97(6):1569-77.

171. Schwank G, Dalessi S, Yang S-F, Yagi R, de Lachapelle AM, Affolter M, et al. Formation of the Long Range Dpp Morphogen Gradient. PLoS Biology. 2011;9(7).

172. Carrell SN, O'Connell MD, Jacobsen T, Pomeroy AE, Hayes SM, Reeves GT. A facilitated diffusion mechanism establishes the *Drosophila* Dorsal Gradient. Development. 2017;144(23):4450-61.

173. Lippert A, Janeczak AA, Fürstenburg A, Ponjavic A, Moerner WE, Nusse R, et al. Single-Molecule Imaging of Wnt3A Protein Diffusion on Living Cell Membranes. Biophysical Journal. 2017;113(12):2762-7.

174. Erbas A, Olvera de la Cruz M, Marko JF. Receptor-Ligand Rebinding Kinetics in Confinement. Biophysical Journal. 2019;116(9):1609-24.

175. Kong P, Dong J, Li W, Li Z, Gao R, Liu X, et al. Extracellular Matrix/Glycopeptide Hybrid Hydrogel as an Immunomodulatory Niche for Endogenous Cardiac Repair after Myocardial Infarction. Advanced Sciences. 2023;10 (23).

176. Dowd CJ, Cooney CL, Nugent MA. Heparan Sulfate Mediates bFGF Transport through Basement Membrane by Diffusion with Rapid Reversible Binding. Journal of Biological Chemistry. 1999;274(8):5236-44.

177. Lortat-Jacob H, Kleinman HK, Grimaud JA. High-affinity binding of intereferon-gamma to a basement membrane complex (matrigel). The Journal of Clinical Investigation. 1991;87(3):878-83.

178. Arrhenius S. Über die Dissociationswärme und den Einfluss der Temperatur auf den Dissociationsgrad der Elektrolyte. Zeitschrift für Physikalische Chemie. 1889;4(1):96-116.

179. Menko AS, Boettiger D. Occupation of the Extracellular Matrix Receptor, Integrin, Is a Control Point for Myogenic Differentiation Cell. 1987;51:51-7.

180. Haag R. Multivalency as a chemical organization and action principle. Beilstein Journal of Organic Chemistry. 2015;11:848-9.

181. Cyrillus T, Zhixin, Meyer AS. A general model of multivalent binding with ligands of heterotypic subunits and multiple surface receptors. Mathematical Biosciences. 2021;342.

182. Ziegler A, Seelig J. Binding and Clustering of Glycosaminoglycans: A Common Property of Mono- and Multivalent Cell-Penetrating Compounds. Biophysical Journal. 2008;94(6):2142-9.

183. Vauquelin G, Charlton SJ. Exploring avidity: understanding the potential gains in functional affinity and target residence time of bivalent and heterobivalent ligands. British Journal of Pharmacology. 2013;168(8):1771-85.

184. Nesmelova IV, Melnikova DL, Ranjan V, Skirda VD. Chapter 4 - Translational diffusion of unfolded and intrinsically disordered proteins. In: Uversky VN, editor. Progress in Molecular Biology and Translational Science. 166. Netherlands: Academic Press; 2019. p. 85-108.

185. Lattman EE. Small angle scattering studies of protein folding. Current Opinion in Structural Biology. 1994;4(1):87-92.

186. Nygaard M, Kragelund BB, Papaleo E, Lindorff-Larsen K. An Efficient Method for Estimating the Hydrodynamic Radius of Disordered Protein Conformations. Biophysical Journal. 2017;113:550-7.

187. Wilkins DK, Grimshaw SB, Receveur V, Dobson CM, Jones JA, Smith LJ. Hydrodynamic Radii of Native and Denatured Proteins Measured by Pulse Field Gradient NMR Techniques. Biochemistry. 1999;38(50):16424-31.

188. Molek JR. Ultrafiltration of Pegylated Proteins [PhD]: Pennsylvania State University 2008.

189. Pääkkönen J, Jänis J, Rouvinen J. Calculation and Visualization of Binding Equilibria in Protein Studies. ACS Omega. 2022;7(12):10789-95.

190. Day YSN, Baird CL, Rich RL, Myszka DG. Direct comparison of binding equilibrium, thermodynamic, and rate constants determined by surface- and solution-based biophysical methods. Protein Science 2002;11(5):1017-25.

191. Eble JA. Titration ELISA as a Method to Determine the Dissociation Constant of Receptor Ligand Interaction. Journal of Visualised Experiments. 2018;132.

192. Stine CA, Munson JM. Autologous Gradient Formation under Differential Interstitial Fluid Flow Environments. Biophysica. 2022;2(1):16-33.

193. Dubacheva GV, Araya-Callis C, Geert Volbeda A, Fairhead M, Codée J, Howarth M, et al. Controlling Multivalent Binding through Surface Chemistry: Model Study on Streptavidin. Journal of the American Chemical Society. 2017;139(11):4157-67.

194. Wilson VG. Growth and Differentiation of HaCaT Keratinocytes. In: Turksen K, editor. Epidermal Cells. Methods in Molecular Biology. New York, NY: Springer; 2014. p. 31-41.

195. Sun C, Li Y, Taylor SE, Mao X, Wilkinson MC. HaloTag is an effective expression and solubilisation fusion partner for a range of fibroblast growth factors. PeerJ. 2015;3.

196. de Oliveira RC, Wilson SE. Descemet's membrane development, structure, function and regeneration. Experimental Eye Research 2020;197.

197. Vasquez C, Siddiqui RA, Moreno AP, Berbari EJ. A fibroblast-myocyte model which accounts for slow conduction and fractionated electrograms in infarct border zones. Computers in Cardiology; Memphis, TN, USA2002. p. 245-8.

198. Soumpasis DM. Theoretical analysis of fluorescence photobleaching recovery experiments. Biophysical Journal. 1983;41(1):95-7.

199. Deshcout H, Hagman J, Frannson S, Jonasson J, Rudemo M, Lorén N, et al. Straightforward FRAP for quantitative diffusion measurements with a laser scanning microscope. Optics Express. 2010;18(22):22886-905.

200. Severin IC, Soares A, Hantson J, Teixeira M, Sachs D, Valognes D, et al. Glycosaminoglycan analogs as a novel anti-inflammatory strategy. Frontiers in Immunology. 2012;3.

201. Hung JJ, Zeno WF, Chowdhury AA, Dear BJ, Ramachandran K, Nieto MP, et al. Self-diffusion of a highly concentrated monoclonal antobody by fluorescene correlation spectroscopy: insight into protein-protein interactions and self-association. Soft Matter. 2019;15(33):6660-76.

202. Dietz MS, Wehrheim SS, Harwatdt M-LIE, Niemann HH, Heilemann M. Competitive Binding Study Revealing the Influence of Fluorophore Labels on Biomolecular Interactions. Nano Letters. 2019;19(11):8245-9.

203. Hughes LD, Rawle RJ, Boxer SG. Choose Your Label Wisely: Water-Soluble Fluorophores Often Interact with Lipid Bilayers. PLOS One. 2014;9(2).

204. Sun WW, Krystofiak ES, Leo-Macias A, Cui R, Sesso A, Weigert R, et al. Nanoarchitecture and dynamics of the mouse enteric glycocalyx examined by freeze-etching electron tomography and intravital microscopy. Communications Biology. 2020;3.

205. Hof DJ, Versteeg EMM, van der Lest CHA, Daamen WF, van Kuppevelt TH. A versatile salt-based method to immobilise glycosaminoglycans and create growth factor gradients. Glycoconjugate Journal. 2019;36:227-36.

206. Kilb MF, Engemann VI, Siddique A, Stark RW, Schmitz K. Immobilisation of CXCL8 gradients in microfluidic devices for migration experiments. Colloids and Surfaces B: Biointerfaces. 2021;198.

207. Parlato M, Murphy W. Soluble Molecule Transport Within Synthetic Hydrogels in Comparison to the Native Extracellular Matrix. In: Connon CJ, Hamley IW, editors. Hydrogels in Cell-Based Therapies: The Royal Society of Chemistry; 2014. p. 1-30.

208. Gschwandtner M, Strutzmann E, Teixeira MM, Anders HJ, Diedrichs-Möhring M, Gerlza T, et al. Glycosaminoglycans are important mediators of neutrophilic inflammation in vivo. Cytokine. 2017;91:65-73.

Appendix

Supplementary Figures

```
Clone     TTCTCATCATCATCATCATCATGGTATGGCTAGCATGAAACCGGTGAGCCTGAGCTATCG 120
αref      -------------------------------------AAACCGGTGAGCCTGAGCTATCG  23
                                                 **********************

Clone     CTGCCCGTGCCGCTTCTTTGAAAGCCATGTGGCCCGCGCGAACGTGAAACATCTGAAAAT 180
αref      CTGCCCGTGCCGCTTCTTTGAAAGCCATGTGGCCCGCGCGAACGTGAAACATCTGAAAAT  83
          ************************************************************

Clone     TCTGAATACGCCGAACTGTGCCCTGCAGATTGTTGCCCGCCTGAAGAACAATAACCGCCA 240
αref      TCTGAATACGCCGAACTGTGCCCTGCAGATTGTTGCCCGCCTGAAGAACAATAACCGCCA 143
          ************************************************************

Clone     AGTGTGCATTGATCCGAAACTGAAATGGATTCAGGAATATCTGGAAAAAGCGCTGAACAA 300
αref      AGTGTGCATTGATCCGAAACTGAAATGGATTCAGGAATATCTGGAAAAAGCGCTGAACAA 203
          ************************************************************

Clone     ATAACCATGGAATTCGAAGCTTGATCCGGCTGCTAACAAAGCCCGAAAGGAAGCTGAGTT 360
αref      A------------------------------------------------------------ 204
          *
```

Figure S1. ***DNA of Sequence CXCL12α Cloned into pRSET A.*** *The clone line is the DNA sequence of the results of the DNA cloning of CXCL12α cloned into pRSET A at the multiple cloning site. The αref (reference) line is the DNA sequence of CXCL12α. Asterisks indicate matching nucleic acids between both lines. A, T, G, and C represent adenine, thymine, guanine, and cytosine respectively.*

```
Clone     CATCATCATCATCATGGTATGGCTAGCATGAAACCAGTCAGCCTGAGCTACCGATGCCCC     120
γref      ---------------------------ATGAAACCAGTCAGCCTGAGCTACCGATGCCCC     33
                                      ********************************

Clone     TGCCGGTTCTTCGAGAGCCACATCGCCAGAGCCAACGTCAAGCATCTGAAAATCCTCAAC     180
γref      TGCCGGTTCTTCGAGAGCCACATCGCCAGAGCCAACGTCAAGCATCTGAAAATCCTCAAC     93
          ************************************************************

Clone     ACTCCAAACTGTGCCCTTCAGATTGTTGCACGGCTGAAGAACAACAACAGACAAGTGTGC     240
γref      ACTCCAAACTGTGCCCTTCAGATTGTTGCACGGCTGAAGAACAACAACAGACAAGTGTGC     153
          ************************************************************

Clone      ATTGACCCGAAATTAAAGTGGATCCAAGAGTACCTGGAGAAAGCTTTAAACAAGGGGCGC    300
γref       ATTGACCCGAAATTAAAGTGGATCCAAGAGTACCTGGAGAAAGCTTTAAACAAGGGGCGC    213
           ************************************************************

Clone      AGAGAAGAAAAAGTGGGGAAAAAAGAAAAGATAGGAAAAAAGAAGCGACAGAAGAAGAGA    360
γref       AGAGAAGAAAAAGTGGGGAAAAAAGAAAAGATAGGAAAAAAGAAGCGACAGAAGAAGAGA    273
           ************************************************************

Clone      AAGGCTGCCCAGAAAAGGAAAAACTAGCCATGGAATTCGAAGCTTGATCCGGCTGCTAAC    420
γref       AAGGCTGCCCAGAAAAGGAAAAACTAG-------------------------------    300
           ***************************
```

Figure S2. ***DNA Sequence of CXCL12γ Cloned into pRSET A.*** *The clone line is the DNA sequence of the results of the DNA cloning of CXCL12γ cloned into pRSET A at the multiple cloning site. The γref (reference) line is the DNA sequence of CXCL12γ. Asterisks indicate matching nucleic acids between both lines. A, T, G, and C represent adenine, thymine, guanine, and cytosine respectively.*

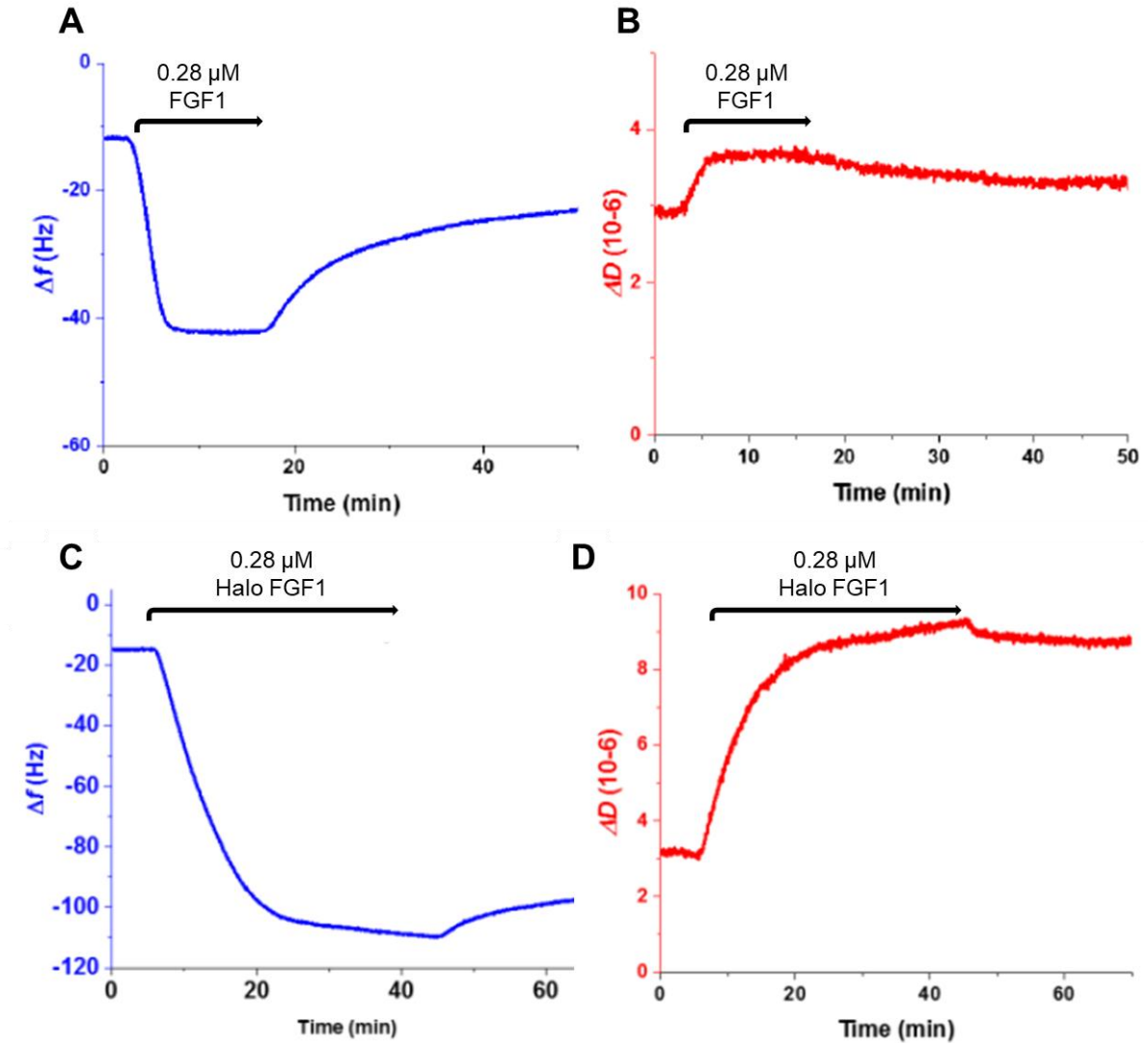


Figure S3. ***QCM-D Responses to FGF1 and Halo FGF1 Binding to an HS Film****. A) and C) Changes in frequency (ΔF) following incubation of WT FGF1 (A) and Halo FGF1 (C) to 12 kDa HS Films. B) and C) Changes in dissipation (ΔD) following incubation of WT FGF1 (B) and Halo FGF1 (D) to 12 kDa HS Films. Arrows above the graph indicate start and duration of incubation of FGF1 and Halo FGF1. Concentrations for incubation: SUV (0.5 mol-% DOPE-CAP-B + 99.5 mol-% DOPC) – 50 µg/ml, SAv – 20 µg/ml, HS-b (Nominal M_w = 12 kDa) – 5 µg/ml, FGF1 and Halo FGF1 – 0.28 µM. Adapted from (8).*